



DIGITAL ACCESS TO SCHOLARSHIP AT HARVARD

Rapid Climate Change in the Cenozoic: Insights from Geochemical Proxies

The Harvard community has made this article openly available. [Please share](#) how this access benefits you. Your story matters.

Citation	No citation.
Accessed	February 17, 2015 12:50:19 AM EST
Citable Link	http://nrs.harvard.edu/urn-3:HUL.InstRepos:13064985
Terms of Use	This article was downloaded from Harvard University's DASH repository, and is made available under the terms and conditions applicable to Other Posted Material, as set forth at http://nrs.harvard.edu/urn-3:HUL.InstRepos:dash.current.terms-of-use#LAA

(Article begins on next page)

HARVARD UNIVERSITY
Graduate School of Arts and Sciences



DISSERTATION ACCEPTANCE CERTIFICATE

The undersigned, appointed by the

Department of Earth and Planetary Sciences

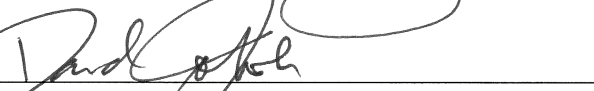
have examined a dissertation entitled
"Rapid Climate Change in the Cenozoic: Insights from
geochemical proxies"

presented by Sierra Victoria Petersen

candidate for the degree of Doctor of Philosophy and hereby
certify that it is worthy of acceptance.

Signature 

Typed name: Prof. Daniel Schrag

Signature 

Typed name: Assoc. Prof. David Johnston

Signature 

Typed name: Prof. Eli Tziperman

Date: August 18, 2014

**Rapid Climate Change in the Cenozoic: Insights from
geochemical proxies**

A dissertation presented

by

Sierra Victoria Petersen

to

The Department of Earth and Planetary Sciences

in partial fulfillment of the requirements

for the degree of

Doctor of Philosophy

in the subject of

Earth and Planetary Sciences

Harvard University

Cambridge, MA

August 2014

© 2014 Sierra Victoria Petersen

All rights reserved.

Rapid Climate Change in the Cenozoic: Insights from geochemical proxies

ABSTRACT

Studying the mean state and variability of past climate provides important insight into the dynamically coupled climate system, directly aiding projections of future climate. Reconstruction of past climate conditions can be achieved using geochemical proxies including the novel clumped isotope paleothermometer. In this thesis I use multiple proxies to study climate variability during the last glacial period and at the onset of Antarctic glaciation.

Greenland ice cores record repeated millennial-scale fluctuations in climate during the last glacial period known as Dansgaard-Oeschger (DO) cycles. We measure $\delta^{18}\text{O}$ of bulk sediment and planktonic foraminifera (*Neogloboquadrina Pachyderma*) in sediment cores from the North Atlantic to investigate fluctuations in sediment properties on the timescale of DO cycles. We find evidence of episodic deposition of carbonate ice-rafted debris near Iceland. Integrating these observations with published data and modeling studies, we propose a new hypothesis to explain DO cycles. We suggest that a large ice shelf in the Nordic Seas acted in concert with sea ice to set the slow and fast timescales of DO cycles. The ice shelf was periodically removed by subsurface warming with the timescale of shelf regrowth setting the duration of each interstadial.

We utilize the clumped isotope proxy to reconstruct the climate history during a key period of the Cenozoic – the onset of Antarctic glaciation. To facilitate this work, a new inlet is developed to streamline sample preparation and reduce sample size requirements. We decrease the required sample size from 5-8mg to 1-2mg per replicate, while still achieving

external precision of 0.005-0.010‰, equivalent to previous methods. This new capability increases the range of possible applications for the clumped isotope paleothermometer, specifically in the field of paleoceanography. We apply the clumped isotope paleothermometer to thermocline-dwelling foraminifera (*Subbotina angiporoides* and *Subbotina utilisindex*) from the Southern Ocean core ODP689 across the Eocene-Oligocene transition. With the clumped isotope paleothermometer we separate the contributions of near-surface temperature change and ice sheet growth on the ~1‰ increase in $\delta^{18}\text{O}$ observed in planktonic foraminifera from this site. We measure no change in temperature, and $0.8 \pm 0.2\text{‰}$ change in $\delta^{18}\text{O}_{\text{sw}}$, equivalent to 124-140% of the modern Antarctic ice sheet volume.

Table of Contents

Front Matter

Abstract	iii
Table of Contents	v
List of Figures	viii
List of Tables	x
List of Equations	xi
Acknowledgements	xii

Chapter 1. Introduction

1.1 The Study of Past Climate	1
1.2 Geochemical Proxies	2
1.2.1 Stable isotopes and notation	3
1.2.2 The oxygen isotope paleothermometer	4
1.2.3 The clumped isotope paleothermometer	5
1.3 Cenozoic Climate Change	7
1.3.1 The Eocene-Oligocene transition	8
1.3.2 Millennial-scale variability within Pleistocene glacial climate	9
1.4 Summary of Thesis Chapters	10
References	11

Chapter 2. A new mechanism for Dansgaard-Oeschger cycles

Abstract	15
2.1 Introduction	16
2.2 Rapid Climate Change in Greenland Ice Cores	16
2.3 Previous Hypotheses for DO Cycles	20
2.4 A New Hypothesis for DO Cycles	23
2.5 Discussion	25
2.6 Conclusions	29
Acknowledgments	30
References	30

Chapter 3. Evidence for Dansgaard-Oeschger cycles in sediment cores from the northern North Atlantic and Irminger Basin

Abstract	39
3.1 Introduction	40

3.1.1	Identification of Heinrich events and other Dansgaard-Oeschger stadials	41
3.1.2	Motivation for stable isotopes of bulk sediment carbonate	44
3.2	Materials	46
3.2.1	Sediment core selection	46
3.2.2	Sediment core sampling	46
3.3	Measurement Techniques	48
3.3.1	Bulk sediment	48
3.3.2	Sieved size fractions	48
3.3.3	Foraminifera	48
3.4	Results – Bulk Sediment Stable Isotopes	49
3.4.1	KN42, near the IRD belt	49
3.4.2	KN55, moving north of the IRD belt	53
3.4.3	EW1 and KN70, off the coast of Iceland	56
3.4.4	EW6, EW8, and KN84, the Denmark Strait	59
3.5	Results – Sieved Size Fractions	69
3.6	Results – Planktonic Foraminifera	74
3.7	Conclusions	76
	Acknowledgements	77
	References	77

Chapter 4. Clumped isotope measurements of small (1mg) carbonate samples using a high-efficiency dual-reservoir technique

Abstract	80
4.1 Introduction	81
4.2 Methods and Materials	84
4.2.1 Standard materials	84
4.2.2 Sample preparation	87
4.2.3 Mass spectrometry	88
4.3 Results	93
4.3.1 Demonstration of yield at small sample sizes	93
4.3.2 Diagnosing an unknown fractionation	96
4.3.3 Correction for a fractionation in Δ_{47} and Δ_{48}	99
4.3.4 Corrected carbonate data	104
4.4 Discussion	108
4.4.1 Precision and sample size	108
4.4.2 Detecting contaminated samples	109
4.4.3 A lower limit on sample size	110
4.5 Conclusions	112
Acknowledgements	113
References	113

Chapter 5. Application of the clumped isotope paleothermometer to foraminifera across the Eocene-Oligocene transition

Abstract	116
5.1 Introduction	117
5.1.1 Ice growth on Antarctica during the EOT	118
5.1.2 Temperature change across the EOT	119
5.1.3 Possible causes of the EOT	122
5.1.4 Determination of temperature change using clumped isotopes	124
5.2 Methods and Materials	125
5.2.1 Site ODP 689	125
5.2.2 Sample preparation	127
5.2.3 Clumped isotope measurement and data correction	128
5.3 Results	130
5.3.1 $\delta^{18}\text{O}$ and $\delta^{13}\text{C}$	130
5.3.2 Δ_{47} across the EOT	132
5.3.3 Temperature	134
5.2.4 $\delta^{18}\text{O}_{\text{sw}}$ across the EOT	134
5.4 Discussion	137
5.4.1 Comparison to temperature estimates from other proxies	137
5.4.2 Lack of temperature change at ODP689	139
5.4.3 Extremely high $\delta^{18}\text{O}_{\text{sw}}$ values	140
5.4.4 Choice of clumped isotope calibration line	142
5.4.5 Comparison to Mg/Ca data	143
5.4.6 Possible vital effects in <i>Subbotina</i> spp.	146
5.4.7 Influence of changing $[\text{CO}_3^{2-}]$ on ice volume estimates	148
5.5 Conclusions	149
Acknowledgements	150
References	150

Appendix A1. Additional Sediment Core Data from Chapter 3 158

Appendix A2. Discussion of Shot Noise Limit with Decreasing Beam Intensity 161

Appendix A3. Error Propagation in the Clumped Isotope Absolute Reference Frame Correction and Δ_{48} Correction 164

Appendix A4. Supplemental Figures for Chapter 4 172

Appendix A5. Choice of Group Fit vs. Individual Fit for the Δ_{48} Correction 181

List of Figures

Figure 1.1 $\delta^{18}\text{O}$ of benthic foraminifera over the Cenozoic	8
Figure 1.2 $\delta^{18}\text{O}$ of benthic foraminifera over four Pleistocene glacial-interglacial cycles and over the Eocene-Oligocene transition	9
Figure 1.3 $\delta^{18}\text{O}$ of ice from Greenland Ice Sheet from 0-65ka	10
Figure 2.1 Comparison of proxies showing DO variability in the Nordic Seas vs. Heinrich variability in the IRD belt	18
Figure 2.2 Schematic of proposed DO oscillation mechanism	22
Figure 3.1 Published records of IRD content in North Atlantic cores	42
Figure 3.2 Published records of $\delta^{18}\text{O}_{\text{Nps}}$ in North Atlantic cores	43
Figure 3.3 Map of core locations	47
Figure 3.4 $\delta^{18}\text{O}_{\text{bs}}$ and $\delta^{13}\text{C}_{\text{bs}}$ vs. Depth in core KN42	50
Figure 3.5 %CaCO ₃ vs. Depth in core KN42	50
Figure 3.6 $\delta^{18}\text{O}_{\text{bs}}$ and $\delta^{13}\text{C}_{\text{bs}}$ vs. Depth in core KN55	54
Figure 3.7 Comparison of %CaCO ₃ in cores KN55 and ODP 982	54
Figure 3.8 $\delta^{18}\text{O}_{\text{bs}}$, $\delta^{13}\text{C}_{\text{bs}}$, and %CaCO ₃ vs. Depth in core EW1	57
Figure 3.9 $\delta^{18}\text{O}_{\text{bs}}$, $\delta^{13}\text{C}_{\text{bs}}$, and %CaCO ₃ vs. Depth in core KN70 and comparison to %CaCO ₃ in core KN72	58
Figure 3.10 $\delta^{18}\text{O}_{\text{bs}}$, $\delta^{13}\text{C}_{\text{bs}}$, and %CaCO ₃ vs. Depth in core KN84	61
Figure 3.11 $\delta^{18}\text{O}_{\text{bs}}$, $\delta^{13}\text{C}_{\text{bs}}$, and %CaCO ₃ vs. Depth in core EW8	65
Figure 3.12 $\delta^{18}\text{O}_{\text{bs}}$, $\delta^{13}\text{C}_{\text{bs}}$, and %CaCO ₃ vs. Depth in core EW6	66
Figure 3.13 %CaCO ₃ vs. Depth in EW6 and EW8 showing correlations	68
Figure 3.14 $\delta^{18}\text{O}_{\text{bs}}$ vs. Depth in EW6 and EW8 showing correlations	68
Figure 3.15 $\delta^{18}\text{O}_{\text{bs}}$ and %CaCO ₃ vs. Depth in EW6 showing correlations	69
Figure 3.16 $\delta^{18}\text{O}_{\text{bs}}$, $\delta^{13}\text{C}_{\text{bs}}$, and %CaCO ₃ vs. Depth for bulk sediment and sieved size fractions in core EW6 and Weight % in each size fraction	71
Figure 3.17 $\delta^{18}\text{O}_{\text{bs}}$, $\delta^{13}\text{C}_{\text{bs}}$, and %CaCO ₃ vs. Depth for bulk sediment and sieved size fractions in core EW8 and Weight % in each size fraction	73
Figure 3.18 $\delta^{18}\text{O}_{\text{bs}}$, $\delta^{13}\text{C}_{\text{bs}}$, $\delta^{18}\text{O}_{\text{Nps}}$, and $\delta^{13}\text{C}_{\text{Nps}}$ vs. Depth for EW8	75
Figure 4.1 Diagram of new high-efficiency, dual-reservoir sample preparation inlet	86
Figure 4.2 Typical m/z 47 beam intensity in two different measurement configurations	91
Figure 4.3 Two indicators of sample yield	92
Figure 4.4 Correlation between Δ_{48} and $\Delta_{47\text{-raw}}$ for four sample types	94
Figure 4.5 Correlation between sample size and magnitude of fractionation	95
Figure 4.6 Diagram of correction method, shown for RTG points from February to March 2014	101
Figure 4.7 Fully corrected Δ_{47} vs. Sample size, divided into 0.1mg mass bins	107
Figure 5.1 $\delta^{18}\text{O}$ vs. Age for <i>S. angiporoides</i> and <i>S. utilisindex</i> samples compared to published data	131

Figure 5.2 $\delta^{13}\text{C}$ vs. Age for <i>S. angiporoides</i> and <i>S. utilisindex</i> samples compared to published data	132
Figure 5.3 Δ_{47} vs. Age	133
Figure 5.4 Temperature across the EOT, calculated using two different calibration equations	135
Figure 5.5 $\delta^{18}\text{O}$, Temperature, and calculated $\delta^{18}\text{O}_{\text{sw}}$ across the EOT	136
Figure 5.6 Comparison of Δ_{47} -temperatures and temperatures estimated from other proxies at nearby sites	140
Figure 5.7 Comparison of $\delta^{18}\text{O}$, Δ_{47} and published Mg/Ca records from ODP689	144
Figure A1.1 $\delta^{18}\text{O}_{\text{bs}}$, $\delta^{13}\text{C}_{\text{bs}}$, and %CaCO ₃ vs. Depth in core KN53	158
Figure A1.2 $\delta^{18}\text{O}_{\text{bs}}$, $\delta^{13}\text{C}_{\text{bs}}$, and %CaCO ₃ vs. Depth in core KN57	159
Figure A1.3 $\delta^{18}\text{O}_{\text{bs}}$, $\delta^{13}\text{C}_{\text{bs}}$, and %CaCO ₃ vs. Depth in core KN63	160
Figure A2.1 Comparison of theoretical shot noise limit and measured errors	163
Figure A4.1 Diagram of 10mL reservoir attached to the reference bellows	172
Figure A4.2 Δ_{48} vs. $\Delta_{47\text{-raw}}$ and Δ_{48} and $\Delta_{47\text{-RFAC}}$ for CM2 and RTG over four measurement periods	173
Figure A4.3 $\delta^{18}\text{O}$ and $\delta^{13}\text{C}$ vs. Δ_{48} for CM2 and RTG	174
Figure A4.4 Residual yield vs. Δ_{48}	175
Figure A4.5 Tests of reference gas run as a sample under three different configurations	176
Figure A4.6 Δ_{48} vs. $\Delta_{47\text{-raw}}$ and Δ_{48} and $\Delta_{47\text{-RFAC}}$ for CM2 and RTG corrected using standard gases run in a narrow size range	177
Figure A4.7 $\Delta_{47\text{-RFAC}}$ and $\Delta_{47\text{-corr}}$ vs. Sample size for CM2, RTG, and NBS19	178
Figure A4.8 Δ_{48} vs. $\Delta_{47\text{-raw}}$ showing seven contaminated samples	180
Figure A5.1 δ^{48} vs Δ_{48} for NBS19 samples run in meas. per. #4 showing group fit and individual fit lines	182
Figure A5.2 Δ_{48} vs. $\Delta_{47\text{-RFAC}}$ for NBS19 samples run in meas. per. #4 showing group fit and individual fit lines	183
Figure A5.3 δ^{48} vs Δ_{48} for NBS19 samples run in meas. per. #3 showing group fit and individual fit lines	184
Figure A5.4 Δ_{48} vs. $\Delta_{47\text{-RFAC}}$ for NBS19 samples run in meas. per. #3 showing group fit and individual fit lines	186
Figure A5.5 Point-by-point comparison of CM2 and RTG samples corrected using the group vs. individual fit methods	188
Figure A5.6 Comparison of binned averages of CM2 and RTG corrected using the group vs. individual fit methods	189

List of Tables

Table 3.1 Locations and other information for cores measured in this study	47
Table 4.1 Comparison of slopes fit individually and together to data shown in Figure 4.4	94
Table 4.2 Summary of carbonate data measured in this study	105
Table 4.3 Summary of NBS19 data, corrected and uncorrected	105
Table 5.1 Summary of measured temperature changes and calculated $\delta^{18}\text{O}_{\text{sw}}$ increases from published studies	122
Table 5.2 Datum levels and assigned ages used to create ODP689 age model	126
Table 5.3 Sampled depth horizons and calculate ages	126
Table 5.4 Calculated ice growth for a variety of scenarios	138
Table A4.1 Slopes and intercepts with error for Δ_{48} vs. $\Delta_{47\text{-raw}}$ and $\Delta_{47\text{-RFAC}}$ for CM2 and RTG through four measurement periods	173
Table A4.2 Slopes and intercepts with error for Δ_{48} vs. $\Delta_{47\text{-raw}}$ and $\Delta_{47\text{-RFAC}}$ for CM2 and RTG in meas. per. #2, using only data from a narrow size range	177
Table A4.3 Summary of all data, separated by mass bin, uncorrected and corrected using two methods	179
Table A5.1 Comparison of raw and corrected NBS19 points using group vs. individual fit methods for measurement period #4	183
Table A5.2 Comparison of raw and corrected NBS19 points using group vs. individual fit methods for measurement period #3	186

List of Equations

Equation 1.1 Definition of delta notation	3
Equation 1.2 $\delta^{18}\text{O-T}$ equilibrium equation of <i>Kim and O'Neil</i> [1997]	4
Equation 1.3 $\delta^{18}\text{O-T}$ equilibrium equation of <i>Leng and Marshall</i> [2004]	5
Equation 1.4 Theoretical definition of Δ_{47}	6
Equation 1.5 Practical definition of Δ_{47}	6
Equation 4.1 Definition of Δ_{47}	82
Equation 4.2 Calculation of $\Delta(\Delta_{48})$	100
Equation 4.3 Calculation of “true Δ_{48} ”	100
Equation 4.4 Correction of Δ_{47} for Δ_{48} fractionation	103
Equation A2.1 Theoretical shot noise definition	161
Equation A2.2 Practical shot noise definition	161
Equation A2.3 Relationship between $V_{44\text{-average}}$ and $V_{47\text{-initial}}$	162
Equation A2.4 Relationship between $V_{47\text{-initial}}$ and Mass of carbonate reacted	162
Equations A3.1 – A3.5 Five steps of Δ_{47} correction	164
Equations A3.6 – A3.7 Two error propagation identities	166
Equations A3.8 – A3.12 Intermediate error propagation equations	166
Equation A3.13 Final error propagation equation	168
Equation A3.14 Calculation of covariance coefficient, r	169
Equations A3.15 – A3.17 Calculation of the covariance and transformation matrices	170
Equations A3.18 – A3.19 Error equations on “true Δ_{48} ” and corresponding δ^{48}	171

Acknowledgements

Thanks to my advisor: Dan, you let me meander my way to projects that piqued my interest and let me explore. You taught me how to be a critical scientist and to never forget the big picture. I am especially grateful for how supportive you've been to me while I try and bring my career and life plans into alignment.

Thanks to my committee members and other faculty: Eli, Dave, and Peter, you have read patiently through quals proposals and thesis drafts, and have given me good feedback through the whole process. Francis, I really appreciate the opportunities you gave me early in grad school to do field work in Death Valley and the amazing Yukon Territories. I will never forget Diamond Tooth Gurtie's. Finally, Jerry, you have been an amazing mentor and supporter every step of the way, and have given (and will hopefully continue to give) me great career advice (and tell the best stories).

Thanks to my collaborators: Peter Clark, it was a pleasure to work with you on the DO hypothesis and to have you in the office next door at various points. Peter deMenocal, you (and other at the Core Repository) welcomed me to Lamont and taught me how to sample sediment cores.

Thanks to lab managers and friends: Greg, thanks for helping me build CISI and bring her to life. Sarah, thanks for making the many long lab hours of the past year more bearable. Thanks also to fellow graduate students Kate, Justin, and Emmy, for making sure I wasn't the only one in the lab. Andy and Erin, you have been very helpful with 253 discussions and trouble shooting. Valerie and Florence, without you there would not have been as much data in this thesis. Thanks also to Jeremy Shakun, for teaching me to pick forams.

Thanks to the EPS department: You made grad school as fun as it could be, through amazing field trips (Iceland, Death Valley/Yosemite, Canadian Rockies, Spain) and fun department events. To the department (Sarah, Chenoweth, Bridget, and Marjorie) and

group (Jen, Denise) administrators, thanks for making things run as smoothly as possible. A special thanks to Hillary for making my two years as department TF a blast!

Thanks to my fellow Schrag group members: Former and current Schrag group members (Tom, Kate, Katie, Julie, Itay, John, Lauren, Chris, Ploy, Hannah), you have been in the trenches with me and have always been supportive and willing to listen. Special thanks to Kate, for laying all the clumped isotope groundwork, to Tom, who has been an excellent office mate for four years, and to Katie, for making silly signs and joining me on kitchen adventures.

Thanks to many EPS friends: To Emmy and Kathryn, thanks for many great Friday nights and for being great listeners. To Helen and Patrick, you have been with me from the start. To my “book club” ladies (Katie, Katie, Jenny, Shannon, Hannah, Emma), so many fun times but not too many books. To Justin, thank you for making my first field work experience so great. To the current and former 3rd floor residents, thanks for sharing all your birthdays and birthday cakes with me.

Thanks to non-EPS friends: Deepak, it’s hard to believe how long we’ve known each other. Lizzy, June, and Sonia, my geo girls who I hope will be lifelong friends and colleagues. To my many frisbee friends, from Quasar and LPFK, thanks for lots of good times, specifically Aileen and JenX.

Thanks to my family: Mom, Dad, and Conor, you’ve always encouraged me to go where my interests take me, and somehow that ended up with me becoming the first Dr. Petersen. To the Kort family, thank you so much for welcoming me into your lives over these past years.

Finally, I cannot say enough thanks to Eric, who I first met at the EPS holiday party, and who has never left my side since (figuratively of course). Thank you for blazing the trail and passing down everything you learned, for always listening, and really just for everything. I look forward to many future Doctor-Doctor adventures with you.

Chapter 1. Introduction

1.1 The Study of Past Climate

The Earth System is made up of many components – the atmosphere, oceans, cryosphere, biosphere, and solid earth. The timescales on which these different components respond to changes in forcing can vary from days (biosphere response to a heat wave) to weeks (atmospheric weather patterns) to months (seasonal cycle in temperature) on the shorter end to decades (growth of new forests) to centuries (sea level rise from global warming) to millennia (ocean circulation timescales) on the longer end, to thousands to millions of years at the longest (ocean crust creation and subduction). Compared to a human lifetime, most of these timescales are beyond the limit of what one person, or even one civilization can observe. To learn about the climate feedbacks and responses occurring on longer timescales, we can study how the relationships between different components of the climate system have evolved over Earth history.

Over the past few hundred years, humans have been recording their observations of climate conditions. The longest continuous record of temperature is the Central England temperature record, which gives monthly mean temperatures dating back to 1659 [Manley, 1974] and daily mean temperatures back to 1772 [Parker *et al.*, 1992]. Tide gauges have recorded sea level changes in Amsterdam since 1700 [van Veen, 1945]. Beyond the range of these direct climate observations, scientists have come up with creative ways to extract climate data from other historical records. Indication of the effects of the Little Ice Age, a colder period in Northern Europe spanning 1550 to 1850 C.E., was famously found in Dutch paintings of ice skaters, and in increased depictions of

wintry scenes in paintings from across northern Europe [*Neuberger, 1970*]. Roman records of Nile River delta flooding events document past precipitation changes over northeastern Africa, and writings describing extremely harsh winters can be connected to volcanic activity [*McCormick et al., 2012*]. Archives such as these only extend as far back as advanced civilization – maybe a few thousand years at most. In order to go farther back in time, scientists look to natural recorders of climate – tree rings, ice cores, sediment composition, fossil species, and speleothems, to name a few.

1.2 Geochemical Proxies

In order to reconstruct past climate, a known relationship must exist between a certain measurable parameter and climate in the modern world. Trees grow one ring per growing season, with the width of the ring increasing with temperature. Therefore, the size of fossil tree rings can record temperature variations over the lifetime of that tree. By overlapping and correlating sequential records from many trees, a 12,460 year long record of temperature in Europe has been created using this proxy [*Freidrich et al., 2004*].

This philosophy of correlating measurable parameters recorded in nature to climate conditions has been applied to many chemical quantities as well, creating what are known as “geochemical proxies”. When a chemical property is related to temperature, the proxy becomes known as a “paleothermometer”. Many geochemical proxies rely on the measurement of stable isotope ratios in natural materials, which can record

information about such things as temperature, aridity, salinity, or biological activity in the past.

1.2.1 Stable isotopes and notation

Oxygen has three stable isotopes, ^{16}O , ^{17}O , and ^{18}O , defined by their mass. ^{16}O is by far the most abundant, making up 99.75% of all oxygen atoms. ^{18}O is the second most abundant, at 0.21% of atoms, and ^{17}O makes up the remaining 0.04%. Carbon has two stable isotopes, ^{12}C and ^{13}C (^{14}C is a radioactive isotope), with approximate abundances of 98.9% and 1.1%. In isotope geochemistry, the ratio of a rare to abundant isotope (e.g. $R^{18} = ^{18}\text{O}/^{16}\text{O}$) is measured using the delta notation ($\delta^{18}\text{O}$), which converts a small decimal into a round number. Delta notation, by definition, relates the isotope ratio in a sample material (R_{SA}) to the known ratio in a standard (R_{STD}), as shown in Equation 1.1.

$$\delta^{18}\text{O} = \left(\frac{R_{SA}^{18}}{R_{STD}^{18}} - 1 \right) * 1000 \quad [\text{Eq. 1.1}]$$

The two most common standard materials for oxygen isotope measurements are SMOW and PDB. SMOW, or Standard Mean Ocean Water, (updated to VSMOW), has a composition of $R^{18} = 0.0020052$ and $R^{17} = 0.0003799$, and is meant to approximate average ocean water composition. PDB (updated to VPDB) is a belemnite fossil made of calcium carbonate, which has a composition of $R^{18} = 0.0020672$ and $R^{13} = 0.0112372$. For carbonate materials, VPDB is the standard of choice for both oxygen and carbon isotope ratios, whereas VSMOW is the more common reference material for oxygen isotope ratios of water.

1.2.2 The oxygen isotope paleothermometer

The oxygen isotope paleothermometer is based on the observed relationship between $\delta^{18}\text{O}$ of carbonate materials ($\delta^{18}\text{O}_{\text{carb}}$) and the temperature at which they formed [Urey *et al.*, 1951; Epstein *et al.*, 1951]. In addition to temperature, $\delta^{18}\text{O}_{\text{carb}}$ is also influenced by the isotopic composition of the water in which the carbonate formed ($\delta^{18}\text{O}_{\text{w}}$), which in the modern ocean can be controlled by the local evaporation-precipitation balance, ocean currents, and the volume of isotopically light ice trapped on land in ice sheets. The relationship between these three quantities ($\delta^{18}\text{O}_{\text{carb}}$, $\delta^{18}\text{O}_{\text{w}}$, and Temperature) has been defined by many studies. A common formulation, based on work by Kim and O'Neil [1997], is shown below in two forms (Equations 1.2 and 1.3).

$$1000 * \ln(\alpha_{\text{Calcite-H}_2\text{O}}) = 18.03 * (10^3 T^{-1}) - 32.42 \quad [\text{Eq. 1.2}]$$

where T is temperature in Kelvin and $\alpha_{\text{Calcite-H}_2\text{O}}$ is the fractionation factor between calcite and water, or $R^{18}_{\text{calcite}}/R^{18}_{\text{water}}$. This equation can be re-expressed as in Equation 1.3 [Leng and Marshall, 2004], where T is in degrees Celsius, δ_c is the isotopic composition of the carbonate, $\delta^{18}\text{O}_{\text{carb}}$, expressed relative to the PDB scale and δ_w is the isotopic composition of the water, $\delta^{18}\text{O}_{\text{w}}$, expressed relative to the SMOW scale. This formulation is more convenient for many calculations because each of the parameters is reported relative to the scale most commonly used for that material (PDB for carbonate, SMOW for water, Celsius for T).

$$T(^{\circ}C) = 13.8 - 4.58(\delta_c - \delta_w) + 0.08(\delta_c - \delta_w)^2 \quad [\text{Eq. 1.3}]$$

Early applications of the oxygen isotope paleothermometer attempted to reconstruct the glacial-interglacial change in ocean temperatures by measuring the oxygen isotopic composition of foraminifera (microscopic marine organisms) and calculating a temperature using educated guesses about the influence of changing $\delta^{18}\text{O}_w$ [Emiliani, 1956]. Later alternative interpretations called, instead, on a large change in $\delta^{18}\text{O}_w$ due to ice sheet build up during the glacial stage and almost no change in temperature [Shackleton, 1967]. The puzzle of the glacial-interglacial temperature and ice volume changes was only solved by directly measuring the isotopic composition of glacial seawater trapped in the pore-space of ocean sediments [Schrag *et al.*, 2002; Adkins *et al.*, 2002]. Beyond the most recent glacial maximum, however, it is not possible to use this approach. Without independently knowing $\delta^{18}\text{O}_w$, the oxygen isotope paleothermometer will be forever under-constrained as a temperature proxy.

1.2.3 The clumped isotope paleothermometer

In addition to $\delta^{18}\text{O}$, another isotopic quantity of carbonate has been discovered to relate to temperature. Within the carbonate lattice, the heavy isotopes ^{13}C and ^{18}O are observed to “clump” together into the same molecule at a level above that expected by a random (stochastic) distribution of these isotopes, and is temperature dependent. A carbonate material is converted to CO_2 through acid digestion and the amount of doubly-substituted CO_2 having a mass of 47amu ($^{13}\text{C}^{18}\text{O}^{16}\text{O}$, predominantly) is quantified. The amount of clumping is denoted by Δ_{47} and is defined as the amount of mass-47 CO_2

(R^{47}_{measured}) relative to the expected stochastic distribution ($R^{47}_{\text{stochastic}}$) for a sample based on its bulk isotopic composition (Equation 1.4) [Eiler & Schauble, 2004; Wang et al., 2004]. Just like R^{18} defines the ratio between the rare heavy isotope and the more common lighter isotope of oxygen, R^{47} relates the rare doubly-substituted CO₂ to the most common CO₂ isotopologue ($^{12}\text{C}^{16}\text{O}^{16}\text{O}$), having a mass of 44amu.

$$\Delta_{47} = \left(\frac{R^{47}_{\text{measured}}}{R^{47}_{\text{stochastic}}} - 1 \right) * 1000 \quad [\text{Eq. 1.4}]$$

In practice, this equation is rewritten to include terms that are measurable in the laboratory (Equation 1.5). In this formulation, R^{47} , R^{46} , and R^{45} are measured quantities, and R^{47*} , R^{46*} , and R^{45*} are stochastic distributions calculated from raw single-isotope ratios R^{13} , R^{17} , R^{18} [Wang et al., 2004; Affek and Eiler, 2006].

$$\Delta_{47} = \left[\left(\frac{R^{47}}{R^{47*}} - 1 \right) - \left(\frac{R^{46}}{R^{46*}} - 1 \right) - \left(\frac{R^{45}}{R^{45*}} - 1 \right) \right] * 1000 \quad [\text{Eq. 1.5}]$$

Δ_{47} is defined to be between 0 and 1, and is restricted to 0.55 to 0.8 for normal Earth surface temperatures [Eiler, 2011]. The temperature dependence of Δ_{47} has been demonstrated for a variety of carbonate materials including synthetic, biogenic, and inorganic carbonates [Ghosh et al., 2006; Dennis and Schrag, 2010; Eiler, 2011 and references therein], as well as by theoretical calculations [Schauble et al., 2006; Guo et al., 2009].

As a paleothermometer, the clumped isotope proxy has a benefit over the traditional oxygen isotope paleothermometer in that it does not require prior knowledge of $\delta^{18}\text{O}_w$. In fact, by combining the temperature and $\delta^{18}\text{O}_{\text{carb}}$ values acquired from the clumped isotope measurement in Equation 1.3, $\delta^{18}\text{O}_w$ can be directly calculated [Eiler, 2011]. This makes the clumped isotope paleothermometer a very powerful tool for paleoclimate reconstructions.

1.3 Cenozoic Climate Change

Within the Cenozoic (66Ma-Present), climate has changed dramatically from the “hothouse” Paleocene and Eocene to the Plio-Pleistocene “icehouse”. These changes are well recorded in the oxygen isotopic composition of benthic foraminifera, bottom-dwelling marine microorganisms, the skeletons of which are preserved in ocean sediments. Although benthic $\delta^{18}\text{O}$ is controlled by both temperature and ice volume changes, these two quantities act in the same direction to change $\delta^{18}\text{O}$ (heavier benthic $\delta^{18}\text{O}$ when there is more ice and when climate is colder), so trends in $\delta^{18}\text{O}$ still record overall climate change. Figure 1.1 shows a composite record of benthic $\delta^{18}\text{O}$ over the past 66 million years. Within the Cenozoic, $\delta^{18}\text{O}$ increases towards the present, changing from a minimum around -0.3‰ during the Eocene Climatic Optimum (~50Ma) to maximum of ~5‰ during the Pleistocene glacial cycles (~0.01Ma) [Zachos *et al.*, 2001]. This represents an overall cooling trend since the Eocene. Prior to the Eocene-Oligocene boundary, changes in benthic $\delta^{18}\text{O}$ are interpreted mainly as changes in temperature, because there is little evidence documenting significant continental ice growth at this

time. After the appearance of ice sheets on Antarctica and the northern continents in the late Eocene and Pliocene, respectively, $\delta^{18}\text{O}$ began to be influenced by both temperature and $\delta^{18}\text{O}_w$.

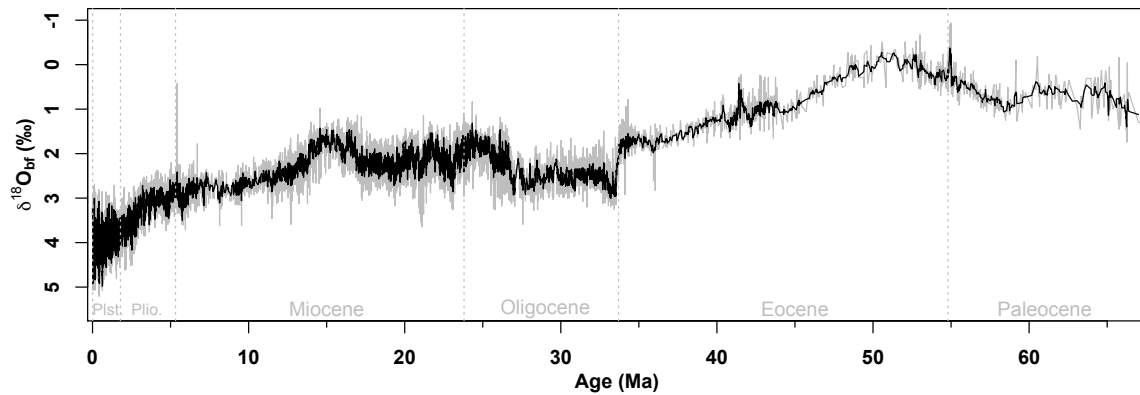


Figure 1.1 Oxygen isotopic composition of benthic foraminifera ($\delta^{18}\text{O}_{br}$) (relative to PDB) across the Cenozoic, combining many sites worldwide (grey) with 5pt. running average (black). Data from *Zachos et al.* [2001].

1.3.1 The Eocene-Oligocene transition

The Eocene-Oligocene transition marked a fundamental shift in global climate, from an ice-free world to one with continental ice sheets on Antarctica. Over a period of less than one million years, the benthic $\delta^{18}\text{O}$ increased by $\sim 1.5\%$, indicating relatively rapid cooling and/or ice growth (Figure 1.2, right). If this entire shift were due to temperature change, it would represent $>6^\circ\text{C}$ of global cooling. If this shift were due to ice volume changes alone, assuming an average isotopic composition of -35% to -45% for the new Antarctic ice sheet [*DeConto et al.*, 2008], this would be equivalent to 165-215% of the modern East Antarctic Ice Sheet, far too much ice to be contained on the Antarctic continent [*Bohaty et al.*, 2012]. The true explanation for this large shift in $\delta^{18}\text{O}$ is therefore most likely a combination of temperature change and ice growth. Attempts to

independently estimate the temperature component of this climate shift using the clumped isotope paleothermometer is discussed in Chapter 5.

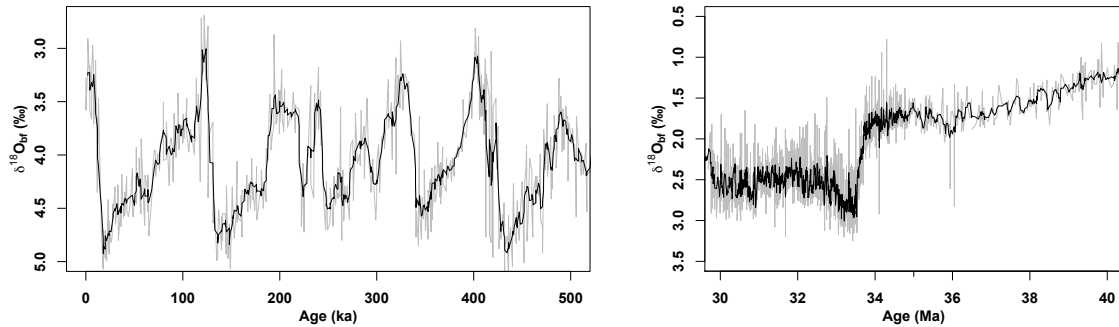


Figure 1.2 Benthic $\delta^{18}\text{O}$ (relative to PDB) (grey) across the last 500kyr, covering four glacial-interglacial cycles (left) and across the Eocene-Oligocene transition (right), with 5pt. running average. Data from *Zachos et al.* [2001].

1.3.2 Millennial-scale variability within Pleistocene glacial climate

Around the beginning of the Pliocene, ice sheets began to appear in the northern hemisphere, driving $\delta^{18}\text{O}_w$ and benthic $\delta^{18}\text{O}$ heavier still. Within the Pliocene and Pleistocene, ice sheets fluctuated through ice age cycles, which appear in benthic $\delta^{18}\text{O}$ due to a combination of changing temperature and ice volume (Figure 1.2, left). In addition to sediment records, climate of the most recent few glacial cycles is also recorded in the ice sheets of Greenland and Antarctica.

Ice cores drilled from the Greenland Ice Sheet in particular cover the most recent glacial period at high resolution, with countable annual layering in the ice [*Grootes et al.*, 1993; *Svensson et al.*, 2008]. This record reveals that glacial climate was not continuously cold, but fluctuated many times between very cold glacial (stadial) climate and intermediate (interstadial) climate on 1-2kyr time scales (Figure 1.3) [*Wolff et al.*,

2010]. Possible explanations for these rapid temperature changes, known as Dansgaard-Oeschger cycles, can be found in Chapter 2.

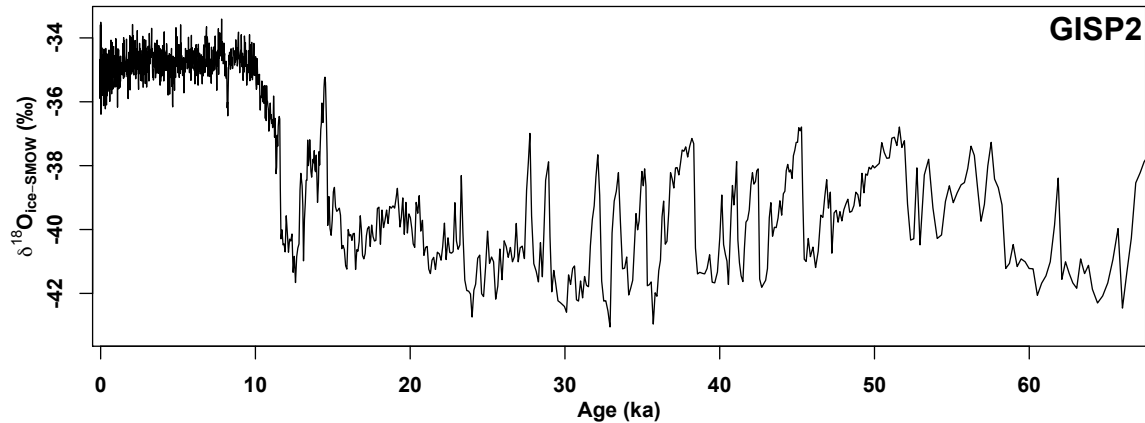


Figure 1.3 $\delta^{18}\text{O}$ of ice in the GISP2 ice core from Greenland, showing many stadial-interstadial fluctuations known as Dansgaard-Oeschger cycles. Data from [Grootes *et al.*, 1993; Meese *et al.*, 1994; Steig *et al.*, 1994; Stuiver *et al.*, 1995; Grootes *et al.*, 1997].

1.4 Summary of Thesis Chapters

This thesis has four body chapters and is broken into two parts. Chapters 2 and 3 deal with climate changes in the most recent glacial period, from two different perspectives. Chapter 2 summarizes the state of knowledge on Dansgaard-Oeschger cycles, the millennial-scale climate fluctuations observed in Greenland ice core records (Figure 1.3), and presents a new hypothesis to explain these unusual temperature changes. Chapter 3 looks to sediment records from the North Atlantic to find evidence in support of the new hypothesis and presents data from a suite of cores using a variety of geochemical proxies.

Chapters 4 and 5 relate to the clumped isotope paleothermometer. Chapter 4 describes a new method for measuring smaller samples, and presents data from many

carbonate standards to document the capabilities of this new measurement technique.

Chapter 5 applies the clumped isotope proxy to foraminifera samples from the Southern Ocean to measure the temperature change across the Eocene-Oligocene transition.

Climate during the Cenozoic changed on a range of timescales, from the gradual cooling trend over the past 50 million years to the more abrupt transition at the end of the Eocene, and from the 100kyr glacial cycles of the Pleistocene to the ~1-2kyr Dansgaard-Oeschger cycles. This thesis documents my work over the past 5 years and details the application of a range of geochemical proxies to study climate change over these different time periods and time scales.

References

- Adkins, J. F., K. McIntyre, and D. P. Schrag (2002), The salinity, temperature, and $\delta^{18}\text{O}$ of the glacial deep ocean, *Science*, 298(5599), 1769-1773.
- Affek, H. P. and J. M. Eiler (2006), Abundance of mass 47 CO_2 in urban air, car exhaust, and human breath, *Geochimica et Cosmochimica Acta*, 70, 1-12.
- Bohaty, S. M., J. C. Zachos, and M. L. Delaney (2012), Foraminiferal Mg/Ca evidence for Southern Ocean cooling across the Eocene-Oligocene transition, *Earth and Planetary Science Letters*, 317-318, 251-261.
- DeConto, R. M., D. Pollard, P. A. Wilson, H. Palike, C. H. Lear, and M. Pagani (2008), Thresholds for Cenozoic bipolar glaciation, *Nature*, 455, 652-657.
- Dennis, K. J. and D. P. Schrag (2010), Clumped isotope thermometry of carbonatites as an indicator of diagenetic alteration, *Geochimica et Cosmochimica Acta*, 74(14), 4110-4122.
- Eiler, J.M. (2011), Paleoclimate reconstruction using carbonate clumped isotope thermometry, *Quaternary Science Reviews*, 30(25-26), 3575-3588.
- Eiler, J.M. and E. A. Schauble (2004), $^{18}\text{O}^{13}\text{C}^{16}\text{O}$ in Earth's atmosphere, *Geochimica et Cosmochimica Acta*, 68(23), 4767-4777.

- Emiliani, C. (1955), Pleistocene Temperatures, *The Journal of Geology*, 63(6), 538-578.
- Epstein, S., R. Buchsbaum, H. Lowenstam, and H. C. Urey (1951), Carbonate-water isotopic temperature scale, *Geological Society of America Bulletin*, 62, 417-426.
- Freidrich, M., S. Remmele, B. Kromer, J. Hofmann, M. Spurk, K. F. Kaiser, C. Orcel, and M. Koppers (2004), The 12,460-year Hohenheim oak and pine tree-ring chronology from central Europe – A unique annual record for radiocarbon calibration and paleoenvironmental reconstructions, *Radiocarbon*, 46(3), 1111-1122.
- Ghosh, P., J. Adkins, H. P. Affek, B. Balta, W. Guo, E. A. Schauble, D. P. Schrag, and J. M. Eiler (2006), ^{13}C - ^{18}O bonds in carbonate minerals: A new kind of paleothermometer, *Geochimica et Cosmochimica Acta*, 70(6), 1439-1456.
- Grootes, P. M. and M. Stuiver (1997), Oxygen 18/16 variability in Greenland snow and ice with 10^3 - to 10^5 -year time resolution, *Journal of Geophysical Research*, 102(C12), 26455-26470.
- Grootes, P. M., M. Stuiver, J. W. C. White, S. Johnsen and J. Jouzel (1993), Comparison of oxygen isotope records from the GISP2 and GRIP Greenland ice cores, *Nature*, 366(6455), 552-554.
- Guo, W., J. L. Mosenfelder, W. A. Goddard III, and J. M. Eiler (2009), Isotopic fractionations associated with phosphoric acid digestion of carbonate minerals: Insights from first-principles theoretical modeling and clumped isotope measurements, *Geochimica et Cosmochimica Acta*, 73(24), 7203-7225.
- Kim, S-T. and J. R. O'Neil (1997), Equilibrium and nonequilibrium oxygen isotope effects in synthetic carbonates, *Geochimica et Cosmochimica Acta*, 61(16), 3461-3475.
- Leng, M. J., and J. D. Marshall (2004), Palaeoclimate interpretation of stable isotope data from lake sediment archives, *Quaternary Science Reviews*, 23, 811-831.
- Manley, G. (1974), Central England temperatures: monthly means 1659 to 1973, *Quarterly Journal of the Royal Meteorological Society*, 100, 389-405.
- McCormick, M., U. Buntgen, M.A. Cane, E.R. Cook, K. Harper, P. Hubers, T. Litt, S. W. Manning, P. A. Mayewski, A. F. M. More, K. Nicolussi, and W. Tegel (2012), Climate Change during and after the Roman Empire: Reconstructing the Past from Scientific and Historical Evidence, *Journal of Interdisciplinary History*, XLIII:2, 169-220.
- Meese, D. A., R. B. Alley, R. J. Fiacco, M. S. Germani, A. J. Gow, P. M. Grootes, M. Illing, P. A. Mayewski, M. C. Morrison, M. Ram, K.C. Taylor, O. Yang, and G. A

- Zielinski (1994), Preliminary depth-age scale of the GISP2 ice core, *Special CRREL Report*, 94-1, US.
- Neuberger, H (1970), Climate in Art, *Weather*, 25(2), 46-56.
- Parker, D. E., T. P. Legg, and C. Folland (1992), A new daily Central England Temperature series 1772-1991, *International Journal of Climatology*, 12, 317-341.
- Schauble, E. A., P. Ghosh, and J. M. Eiler (2006), Preferential formation of ^{13}C - ^{18}O bonds in carbonate minerals, estimated using first-principle lattice dynamics, *Geochimica et Cosmochimica Acta*, 70(10), 2510-2529.
- Schrag, D. P., J. F. Adkins, K. McIntyre, J. L. Alexander, D. A. Hodell, C. D. Charles, and J. F. McManus (2002), The oxygen isotopic composition of seawater during the Last Glacial Maximum, *Quaternary Science Reviews*, 21, 331-342.
- Shackleton, N (1967), Oxygen Isotope Analyses and Pleistocene Temperatures Re-assessed, *Nature*, 215, 15-17.
- Steig, E. J., P. M. Grootes, and M. Stuiver (1994), Seasonal precipitation timing and ice core records, *Science*, 266, 1885-1886.
- Stuiver, M., P. M. Grootes, and T. F. Braziunas (1995), The GISP2 ^{18}O climate record of the past 16,500 years and the role of the sun, ocean, and volcanoes, *Quaternary Research*, 44, 341-354.
- Svensson, A., K. K. Andersen, M. Bigler, H. B. Clausen, D. Dahl-Jensen, S. M. Davies, S. J. Johnsen, R. Muscheler, F. Parrenin, S. O. Rasmussen, R. Rothlisberger, I. Seierstad, J. P. Steffensen and B. M. Vinther (2008), A 60,000 year Greenland stratigraphic ice core chronology, *Climate of the Past*, 4(1), 47-57.
- Urey, H. C., H. A. Lowenstam, S. Epstein, and C. R. McKinney (1951), Measurement of Paleotemperatures and Temperatures of the Upper Cretaceous of England, Denmark, and the Southeastern United States, *Geological Society of America Bulletin*, 62, 399-416.
- Van Veen, J. (1945), Bestaat ere en geologische bodemdaling te Amsterdam sedert 1700, *Tijdschrift Koninklijk Nederlandsch Aardrijkskundig Genootschap*, 2e reeks, deel LXII.
- Wang, Z., E. A. Schauble, and J. M. Eiler (2004), Equilibrium thermodynamics of multiply substituted isotopologues of molecular gas, *Geochimica et Cosmochimica Acta*, 68(23), 4779-4797.

Wolff, E. W., J. Chappellaz, T. Blunier, S. O. Rasmussen and A. Svensson (2010), Millennial-scale variability during the last glacial: The ice core record, *Quaternary Science Reviews*, 29(21-22), 2828-2838.

Zachos, J., M. Pagani, L. Sloan, E. Thomas, and K. Billups (2001), Trends, Rhythms, and Aberrations in Global Climate 65Ma to Present, *Science*, 292, 686-693.

Chapter 2. A new mechanism for Dansgaard-Oeschger cycles

[Petersen, S. V., Schrag, D. P., and Clark, P. U. (2013) A new mechanism for Dansgaard-Oeschger cycles. *Paleoceanography*, 28, 1-7, doi:10.1029/2012PA002364. Copyright Wiley and Sons]

ABSTRACT

We present a new hypothesis to explain the millennial-scale temperature variability recorded in ice cores known as Dansgaard-Oeschger (DO) cycles. We propose that an ice shelf acted in concert with sea ice to set the slow and fast timescales of the DO cycle, respectively. The abrupt warming at the onset of a cycle is caused by the rapid retreat of sea ice after the collapse of an ice shelf. The gradual cooling during the subsequent interstadial phase is determined by the timescale of ice-shelf regrowth. Once the ice shelf reaches a critical size, sea ice expands, driving the climate rapidly back into stadial conditions. The stadial phase ends when warm subsurface waters penetrate beneath the ice shelf and cause it to collapse. This hypothesis explains the full shape of the DO cycle, the duration of the different phases, and the transitions between them and is supported by proxy records in the North Atlantic and Nordic Seas.

2.1 Introduction

During the last glacial period, the North Atlantic basin experienced a number of large and abrupt millennial-scale fluctuations in climate referred to as Dansgaard-Oeschger (DO) cycles. Ice cores from Greenland reveal that each cycle began with an abrupt warming from stadial to interstadial conditions [Johnsen *et al.*, 1992; Dansgaard *et al.*, 1993; Grootes *et al.*, 1993; Huber *et al.*, 2006]. The effects of this warming extended across much of the northern hemisphere [Voelker *et al.*, 2002; Overpeck and Cole, 2006; Piasias *et al.*, 2010], while a near-simultaneous cooling occurred in Antarctica [EPICA Members, 2006; Wolff *et al.*, 2010]. Greenland ice core records then suggest gradual cooling during the initial stages of each interstadial phase, followed by abrupt cooling back to stadial conditions.

A common explanation for these cycles involves changes in the Atlantic meridional overturning circulation (AMOC), perhaps triggered by freshwater forcing [Clark *et al.*, 2001; Ganopolski and Rahmstorf, 2001], but paleoceanographic evidence for these changes remains elusive [Elliot *et al.*, 2002; Piotrowski *et al.*, 2008; Piasias *et al.*, 2010]. Here we propose a mechanism to explain these millennial-scale climate cycles involving abrupt changes in sea-ice cover, gradual regrowth of ice shelves, and warming of intermediate-depth waters.

2.2 Rapid Climate Change in Greenland Ice Cores

$\delta^{18}\text{O}$ records from Greenland ice cores show that each DO cycle began with an abrupt shift in $\delta^{18}\text{O}_{\text{ice}}$, occurring in as little as a few years [Steffensen *et al.*, 2008;

Thomas et al., 2009], which was associated with a large warming, ranging from 8°C to 16°C [*Severinghaus et al.*, 1998; *Huber et al.*, 2006; *Wolff et al.*, 2010 and references therein]. Other properties of the ice, including electrical conductivity [*Taylor et al.*, 1993a, 1993b], deuterium-excess [*Dansgaard et al.*, 1989, *Steffensen et al.*, 2008], dust content [*Fuhrer et al.*, 1999], and methane concentrations [*Brook et al.*, 1996] changed in less than a decade. At the same time, accumulation rates roughly doubled and proportionally more precipitation fell in winter months [*Alley et al.*, 1993; *Cuffey and Clow*, 1997].

Following the abrupt warming, the interstadial climate gradually cooled before abruptly cooling back to stadial conditions. A stable stadial climate characterized by low $\delta^{18}\text{O}_{\text{ice}}$ values was then maintained for the next hundreds to thousands of years until the next abrupt warming, concluding the DO cycle. This characteristic trapezoid shape in $\delta^{18}\text{O}_{\text{ice}}$ can be seen for all DO cycles, but their duration varies from ~1.1 to 8.6 kyr (Figure 2.1A) [*Andersen et al.*, 2006]. *Grootes and Stuiver* [1997] found a strong peak at 1470 years in the power spectrum of DO cycles 1 through 13, but *Schulz* [2002] showed that most of the power in the 1470-year band came from DO cycles 5-7 only. Due to varying age models and statistical techniques, debate persists over whether a 1470-year periodicity exists in the DO time series [*Wunsch*, 2000; *Rahmstorf*, 2003; *Ditlevsen et al.*, 2007]. Based on multiple proxy records with DO-like cycles, *Pisias et al.* [2010] found a mode of variability with broad spectral power of ~1600 years rather than a sharp spectral peak at 1470 years.

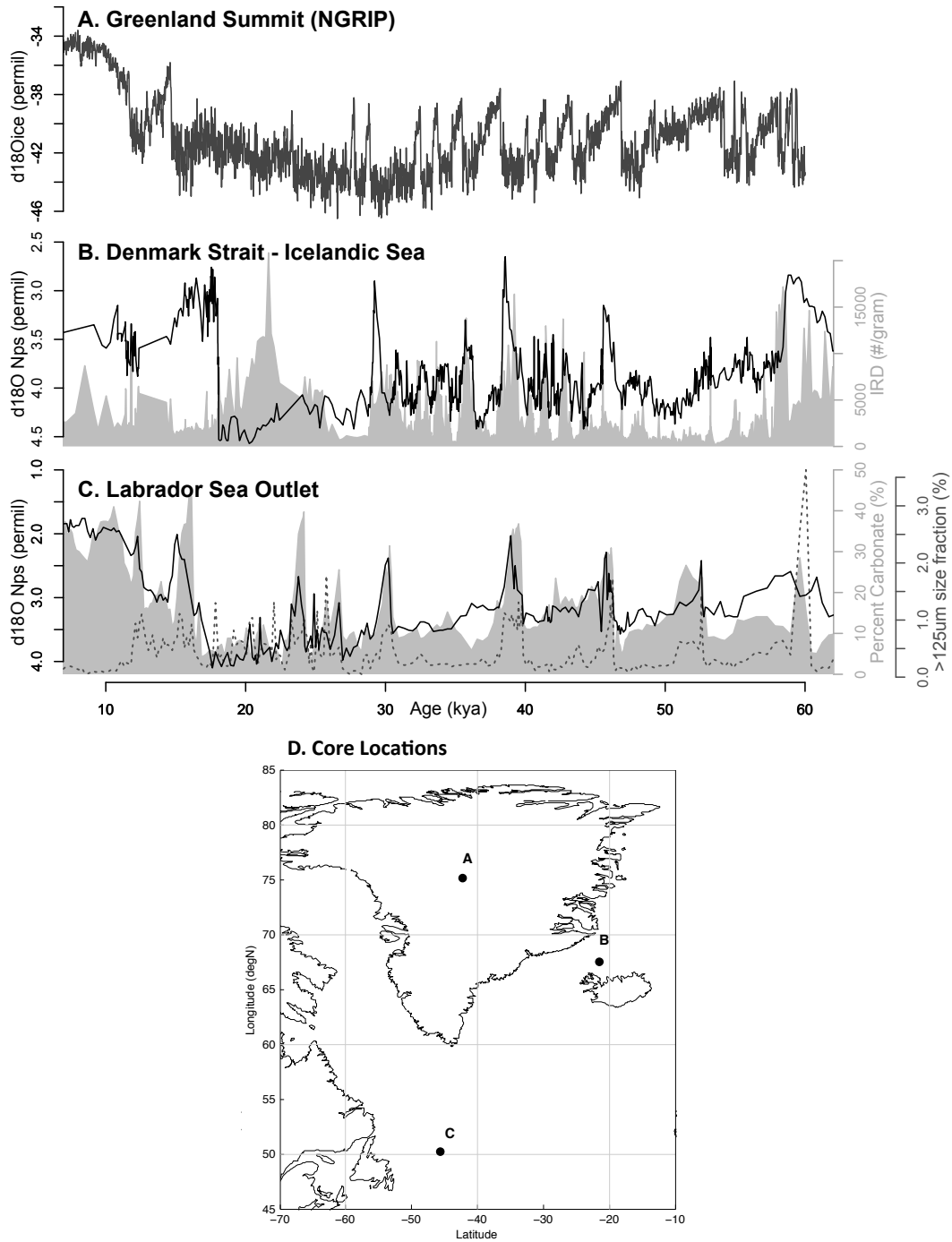


Figure 2.1 Comparison of proxies showing DO variability in the Nordic Seas (B) vs. Heinrich variability in the IRD belt (C). **A.** NGRIP $\delta^{18}\text{O}_{\text{ice}}$ vs. age model GICC05 [Svensson *et al.*, 2008] **B.** Planktonic $\delta^{18}\text{O}$ (black line) and Lithic grain concentration (#/gram) (grey solid) vs. age model from core PS2644-5 [Voelker *et al.*, 1998] **C.** Planktonic $\delta^{18}\text{O}$ (black line), >125 μm size fraction (%) (dotted line), and percent carbonate (%) (grey solid) vs. age from core MD95-2024 [Hillaire-Marcel and Bilodeau, 2000; Weber *et al.*, 2001] **D.** Map showing the location of the proxy records plotted in A-C. Letters on the map correspond to subfigures.

Many climate proxies around the globe show DO-like variability on similar time scales. Proxies from the northern hemisphere show warmer (colder) and wetter (drier) climates during DO interstadials (stadials) [Voelker *et al.*, 2002; Overpeck and Cole, 2006; Piasias *et al.*, 2010]. Climate oscillations in the Antarctic EDML ice core show an inverse relation to Northern Hemisphere climate oscillations (bi-polar seesaw), with a correlation to Greenland stadial duration and the amplitude of the Antarctic temperature warming [EPICA Members, 2006].

Sediment cores from 40-50°N in the North Atlantic (the so-called ice rafted debris (IRD) belt) show IRD from Icelandic and European sources associated with every DO stadial [Bond and Lotti, 1995], but are dominated by larger IRD pulses from the Laurentide ice sheet known as Heinrich events, associated with only every second to fourth stadial (Figure 2.1A, 2.1C) [Hemming, 2004 and references therein]. In contrast, in the Nordic Seas [Voelker *et al.*, 1998; Dokken and Jansen, 1999] and the Irminger Basin [van Kreveld *et al.*, 2000; Elliot *et al.*, 2001], IRD pulses of roughly equal magnitude are visible for every DO stadial, while characteristic Heinrich layers are absent (Figure 2.1B). Planktonic $\delta^{18}\text{O}$ records show large negative excursions associated with Heinrich events in both the Nordic Seas (Figure 2.1B) [Voelker *et al.*, 1998; Rasmussen *et al.*, 1996; Elliot *et al.*, 1998; van Kreveld *et al.*, 2000] and the IRD belt (Figure 2.1C) [Bond *et al.*, 1992; Hillaire-Marcel and Bilodeau, 2000; Hemming, 2004 and references therein], but in the Nordic Seas, weaker negative spikes are also visible for the non-Heinrich stadials (Figure 2.1B).

2.3 Previous Hypotheses for DO Cycles

The origin of DO cycles has commonly been explained by changes in the AMOC, but a mechanism for forcing the AMOC at this timescale remains unknown and existing proxy data do not show corresponding changes in the AMOC for every DO cycle. *Winton* [1993] showed that rapid increases in the overturning rate (“flushing” events) could be produced periodically in models by including a constant atmospheric transport of freshwater from low to high latitudes. This mechanism operates on millennial time scales without the need to dictate a periodicity. The magnitude of warming produced by oscillations of the AMOC alone, however, was substantially less than the warming reconstructed over Greenland during DO events [*Huber et al.*, 2006].

Ganopolski and Rahmstorf [2001] produced a time series of characteristically-shaped DO cycles by forcing an intermediate complexity model with a sinusoidal freshwater flux with a period of 1470 years, which caused large reductions and subsequent resumptions in AMOC strength that resulted in temperature changes over Greenland. We note, however, that there is no known physical mechanism to explain such a sinusoidal fluctuation in the hydrological cycle. Moreover, despite what are likely unrealistically high rates of overturning (~50 Sv) reached by this model, the simulated warming was again considerably less than the reconstructed Greenland temperatures [*Huber et al.*, 2006].

Although benthic $\delta^{13}\text{C}$ [*Zahn et al.*, 1997; *Shackleton et al.*, 2000; *Elliot et al.*, 2002] and neodymium [*Piotrowski et al.*, 2008; *Gutjahr et al.*, 2010] records from intermediate and deep Atlantic sites indicate substantial changes in the AMOC during DO stadials associated with Heinrich events, no significant changes are seen during non-

Heinrich stadials. This indicates that large changes in the AMOC could not have been the primary mechanism behind all the DO cycles.

An alternative mechanism for causing abrupt DO warming involves changes in sea-ice cover [Li *et al.*, 2005; Gildor and Tziperman, 2003]. By removing winter sea-ice cover over a large part of the North Atlantic, Li *et al.* [2005] simulated an annual average warming of up to 5-7°C over Greenland, consistent with the lower end of DO warming reconstructed from $\delta^{15}\text{N}$ of gases trapped in the ice [Huber *et al.*, 2006]. In addition, the simulation produced a doubling of accumulation rate and a shift to more wintertime precipitation, also in agreement with observations from ice cores [Alley *et al.*, 1993; Cuffey and Clow, 1997; Svensson *et al.*, 2008]. Li *et al.* [2010] also found that a reduction in sea-ice cover in the Nordic Seas alone produced significantly more warming (especially in winter) over Greenland's summit than removing sea-ice cover in the western and central North Atlantic, suggesting that the Nordic Sea region may be critical in terms of influencing the air temperature over Greenland.

Li *et al.* [2010] proposed that rapid sea-ice retreat from the Nordic Seas, possibly in response to small changes in wind stress or heat transport, could explain the rapid warming at the onset of a DO cycle. However, this same property of sea ice cannot explain much of the remainder of the DO cycle, which includes the intervals of gradual cooling during the interstadial phase and the sustained cold stadial climate, each of which lasted hundreds of years. This suggests that some other mechanism is needed to set these longer timescales in the DO cycle.

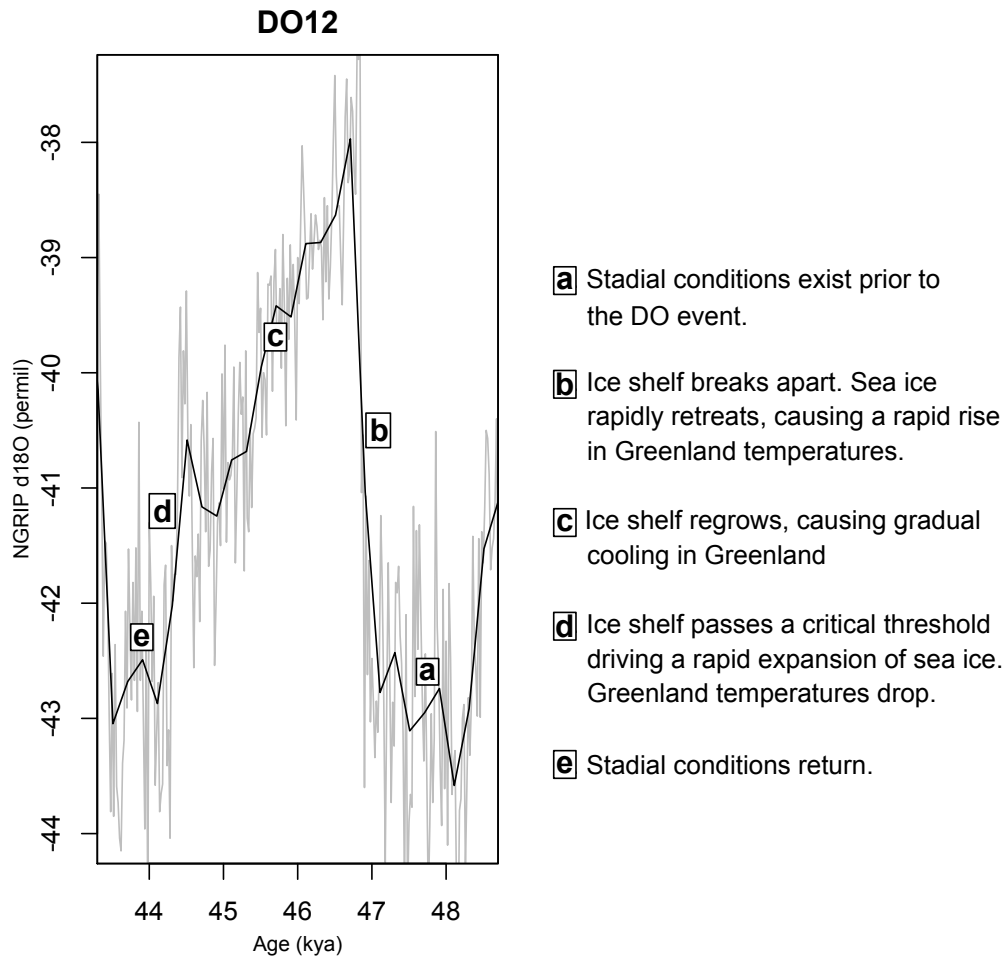


Figure 2.2 Schematic of proposed DO oscillation mechanism. Phases of the DO cycle labeled **a-e** with corresponding description of changes in cryosphere and Greenland temperature occurring during each phase. 20-year resolution $\delta^{18}\text{O}_{\text{ice}}$ from NGRIP ice core (grey line) [Svensson *et al.*, 2008] over the period 43-49 ka showing DO 12, with a 10-point smoothing of the data (black line).

2.4 A New Hypothesis for DO Cycles

We propose a conceptual model for DO cycles that explains their characteristic temporal evolution and is supported by existing proxies of ice-sheet, climate and AMOC variability. In particular, we adopt the sea-ice mechanism of *Li et al.* [2005; 2010] to explain the fast-changing intervals of the DO cycles (Figure 2.2b, 2.2d). We then invoke an ice shelf to explain the slower-changing phases of the DO cycles (Figure 2.2a, 2.2c, and 2.2e). From the perspective of the atmosphere, an ice shelf looks the same as sea ice in terms of its albedo and its insulating effects, which reduce the release of heat from the ocean. However, because ice shelves are much thicker than sea ice (100s of m vs. <10 m), they are largely insensitive to small changes in heat transport or wind stress.

We first consider the influence of an ice shelf covering a large region of the ocean east of Greenland in the Nordic Seas. Given the sensitivity analysis by *Li et al.* [2010] and the number of proxies showing variability of the cryosphere on DO timescales in the Nordic Seas (e.g. Figure 2.1B and others) [*Voelker et al.*, 1998; *Rasmussen et al.*, 1996; *Elliot et al.*, 2002; *Dokken and Jansen*, 1999], we focus on an ice shelf along the eastern Greenland margin that could influence sea-ice cover in this region. We propose that the cooling effect of a large ice shelf combined with extensive sea-ice cover would result in regionally cold surface temperatures due to the insulating properties of the ice shelf and sea ice, as well as their effect on local albedo [*Li et al.*, 2005; 2010]. This stadial climate would be maintained for as long as the ice shelf was present.

In the event of the ice shelf's collapse, potentially caused by warming of subsurface waters (discussed below), the only remaining ice cover would be sea ice and floating icebergs. A small change in wind stress or heat transport could quickly export or

melt this ice, resulting in a large increase in open-ocean area and a corresponding large and abrupt warming over Greenland marking the start of a new DO cycle [Li *et al.*, 2005; 2010].

During the interstadial phase of a DO cycle, the near doubling of accumulation over the Greenland Ice Sheet that accompanies the warmer climate [Alley *et al.*, 1993; Cuffey and Clow, 1997; Svensson *et al.*, 2008] would induce a more positive mass balance, causing the ice shelf to begin reforming along the coast. Expansion of the ice shelf to cover increasingly more ocean surface area would cause air temperatures to gradually cool over Greenland. Once the shelf reached a critical size, it would cause sea ice to rapidly expand through the sea-ice-albedo feedback [Gildor and Tziperman, 2003], driving climate back to stadial conditions and completing the DO cycle. The same cycle could not be achieved with multi-year sea ice because its regrowth time-scale is inconsistent with the gradual decline of climate over the duration of the interstadial phase.

In summary, our hypothesis combines the ability of sea ice in the Nordic Seas to explain the rapid transition into and out of the interstadial phase [Li *et al.*, 2010] with a gradually expanding ice shelf derived from eastern Greenland to (i) explain the progressive cooling during the interstadial (Figure 2.2c), (ii) provide the mechanism to trigger sea-ice growth to cause the rapid cooling (Figure 2.2d), and (iii) sustain the stadial climate once the ice shelf reaches steady state (Figure 2.2a, 2.2e). The duration of the interstadial phase is determined by the time required to regrow the ice shelf to a threshold size, beyond which the local ice-albedo effect causes the rapid expansion of sea ice and the corresponding switch to a stadial climate. After a time, ice-shelf collapse, potentially

due to subsurface warming, along with an associated rapid loss of sea ice causes the abrupt warming that starts a new DO cycle.

2.5 Discussion

We summarize here proxy records, model results, and modern observations that support key elements of our hypothesis for DO cycles. Multiple lines of evidence support the presence of ice shelves in the northern high latitudes during the last glaciation. Reconstructions of seawater salinity during the LGM show that the ocean was saltier than expected from ice-sheet build-up alone [Adkins *et al.*, 2002]. Reconciling these observations requires either a large change in the volume of groundwater or additional ice shelves equivalent to seven times the volume of the modern Antarctic ice shelves [Adkins *et al.*, 2002]. In addition, there is widespread evidence on the continental shelves surrounding the Nordic Seas, including off eastern Greenland, of fast-flowing ice extending to the shelf edge that may have fed ice shelves [Vorren *et al.*, 1998; Stokes and Clark, 2001; Svendsen *et al.*, 2004; Evans *et al.*, 2009; Dowdeswell *et al.*, 2010].

Proxy records suggest substantial variability of the cryosphere in the Nordic Seas on DO timescales. IRD records and planktonic $\delta^{18}\text{O}$ anomalies in the Nordic Seas [Voelker *et al.*, 1998; Dokken and Jansen, 1999] and in the Irminger Basin [van Kreveld *et al.*, 2000; Elliot *et al.*, 1998, 2001] suggest an increase in ice-rafting during each DO stadial (Figure 2.1B). As discussed previously, these records showing similar-scale variability for every DO stadial differ from those found further south in the IRD belt, where the most prominent IRD and $\delta^{18}\text{O}$ signals are associated with Heinrich events

derived from the Laurentide Ice Sheet, and the signals during non-Heinrich DO stadials, particularly in $\delta^{18}\text{O}$, are weak to absent (Figure 2.1C) [Bond *et al.*, 1992; Cortijo *et al.*, 1997; Labeyrie *et al.*, 1999; Hillaire-Marcel and Bilodeau, 2000].

An ice shelf constricting the Denmark Strait between Greenland and Iceland may have played an important additional role in influencing sea-ice cover in the Nordic Seas. Firstly, proxies of ice rafting in this area show a strong response on DO timescales (Figure 2.1B) [Voelker *et al.*, 1998]. Additionally, during the glaciation, grounded ice extended to the shelf break from both Greenland [Vorren *et al.*, 1998; Dowdeswell *et al.*, 2010] and Iceland [Hubbard *et al.*, 2006], narrowing the strait to a width of only ~150 km [Kosters *et al.*, 2004]. Today, the East Greenland Current passes south through the Denmark Strait and exports substantial sea ice from the Arctic to the North Atlantic. If an ice shelf restricted this outlet, which is an ideal setting for growing an ice shelf due to its shallow shelf bathymetry and proximity to two coastlines, sea-ice export would likely be impeded. A “log jam” of sea ice could build up north of the Denmark Strait, contributing to further sea-ice expansion through the ice-albedo feedback. The removal of the ice shelf would allow the East Greenland Current to resume, increasing sea-ice export southward into the mid-North Atlantic. In this way, the ice shelf could indirectly influence ice cover over a larger area of ocean.

Previously, Hulbe *et al.* [2004] proposed a similar mechanism involving the destruction of an ice shelf in the Labrador Sea to explain Heinrich events, but this hypothesis failed to explain why the ice shelf would collapse only during the cold stadial phases [Alley *et al.*, 2005]. Shaffer *et al.* [2004] explained this relationship by suggesting that warming of intermediate-depth waters associated with a large reduction in the

AMOC, such as that which occurred prior to Heinrich events [*Zahn et al.*, 1997; *Clark et al.*, 2007; *Piotrowski et al.*, 2008; *Pisias et al.*, 2010; *Gutjahr et al.*, 2010], would cause melting of the Hudson Strait ice shelf from below while surface temperatures remained cold. Additional model results and proxy data provide support for this mechanism [*Rasmussen et al.*, 2003; *Clark et al.*, 2007; *Alvarez-Solas et al.*, 2010, 2011; *Marcott et al.*, 2011].

Similarly, we propose that subsurface warming caused the collapse of the hypothesized ice shelf along the eastern Greenland margin. In the Nordic Seas, *Rasmussen and Thomsen* [2004] found changes in benthic fauna that suggest intrusion of warm intermediate waters during stadial phases of DO cycles [*Rasmussen et al.*, 1996; *Rasmussen and Thomsen*, 2004]. Depleted benthic $\delta^{18}\text{O}$ signals during DO stadials in this region are also consistent with warming of intermediate depth waters [*Rasmussen et al.*, 1996; *Dokken and Jansen*, 1999; *Rasmussen and Thomsen*, 2004], with a dominant temperature control on these signals supported by Mg/Ca measurements [*Jonkers et al.*, 2010; *Marcott et al.*, 2011].

Several lines of evidence identify subsurface warming as an effective way to destabilize an ice shelf from below. Modern observations show that warm waters at the base of the ice tongue in front of Jakobshavn Isabrae in western Greenland [*Holland et al.*, 2008] and an ice shelf in front of Pine Island glacier in Antarctica [*Jenkins et al.*, 2010] increased basal melting, causing thinning, retreat, and destabilization of those ice shelves, leading to accelerated ice discharge. Ice shelf-ice stream models forced by subsurface warming produce similar results [*Walker et al.*, 2009; *Joughin et al.*, 2010].

In climate model simulations, warming of intermediate waters in the North Atlantic basin is a robust response to a large reduction in the AMOC [Knutti *et al.*, 2004; Clark *et al.*, 2007; Mignot *et al.*, 2007; Liu *et al.*, 2009; Brady and Otto-Bliesner, 2011]. However, model runs show that subsurface warming can still develop with relatively modest changes in the AMOC [Brady and Otto-Bliesner, 2011; Mahajan *et al.*, 2011] and is accompanied by a southward shift in the site of convection [Brady and Otto-Bliesner, 2011]. In the context of our hypothesis, expansion of the ice shelf as well as increased freshwater fluxes from iceberg calving and melting of sea ice transported southward may have caused a slight reduction in the AMOC and a southward shift in convection, causing subsurface warming to develop locally under the expanded ice shelf fringing Greenland in the Nordic Seas. A decrease in flushing by the AMOC around the ice shelf may have allowed the build-up of atmospherically-derived freshwater in the surface ocean that, in addition to the melting of isotopically depleted icebergs calved off the ice shelf, could have contributed to the light planktonic $\delta^{18}\text{O}$ observed in the region during stadials. During the LGM, the sea ice edge could not have been too far south for the subsurface warming to penetrate beneath the ice shelf, resulting in no DO events except following Heinrich events when the amount and extent of subsurface warming was greater.

Although proxy evidence indicates that large reductions in AMOC strength only occurred during Heinrich stadials [Zahn *et al.*, 1997; Clark *et al.*, 2007; Piotrowski *et al.*, 2008; Pisias *et al.*, 2010], existing ocean proxies may not be sensitive to the modest AMOC reductions that models suggest can still induce subsurface warming. Antarctic ice cores show warming events corresponding to the Heinrich stadials [EPICA Members, 2006], times when the AMOC was significantly reduced and interhemispheric heat

transport was weaker. Between these larger Antarctic warming events, smaller events have been correlated with the non-Heinrich stadials [*Wolff et al.*, 2010], consistent with minor changes in heat transport (and therefore AMOC strength) during these times.

Proxies outside of the Atlantic hint at global changes in intermediate depth circulation occurring during DO stadials prior to the abrupt warming. High-resolution sediment cores from the Santa Barbara basin show decreases in benthic $\delta^{18}\text{O}$ occurring 60-200 years prior to the abrupt decrease in planktonic $\delta^{18}\text{O}$ representing the surface warming of the DO event [*Hendy and Kennett*, 2003]. This phasing was interpreted as a shift in intermediate depth circulation bringing $\delta^{18}\text{O}$ -depleted water from the north Pacific into the basin prior to the large-scale atmospheric reorganizing accompanying the DO event warmed the surface waters [*Hendy and Kennett*, 2003]. In addition, high-resolution ice core studies show that atmospheric N_2O began to rise prior to the rapid DO warmings [*Flückiger et al.*, 2004]. In models, global atmospheric N_2O production, predominantly from the tropical Pacific, has been shown to vary as a result of changes in the AMOC [*Schmittner and Galbraith*, 2008], suggesting the early rise in atmospheric N_2O observed in ice cores could be an indicator of changes in Pacific and Atlantic ocean circulations at intermediate depths prior to the main DO event.

2.6 Conclusions

We describe a new mechanism to explain DO cycles involving the formation and collapse of an ice shelf fringing eastern Greenland, potentially extending across the Denmark Strait. Our hypothesis explains the rapid transitions into and out of the

interstadial using the ability of sea ice to rapidly expand and contract, whereas the slower-changing phases are explained by the presence or absence of an ice shelf. The duration of the interstadial phase is set by the regrowth timescale of the ice shelf, and the duration of the stadial phase is determined by the timing of ice-shelf removal, potentially due to subsurface warming. Existing proxy evidence from the Nordic Seas supports the idea of fluctuating ice volume in the region in time with DO cycles. Further proxy studies could explore the IRD and meltwater fluxes resulting from such an ice-shelf break up. Modeling work using an active sea-ice model could test the response of sea ice to the presence or absence of an ice shelf fringing eastern Greenland. A combination of these and other approaches can test the feasibility of this idea and illuminate the exact location of the proposed ice shelf.

Acknowledgements

This work was supported by the NSF Marine Geology and Geophysics Program through grant OCE-0961372. The authors thank Peter Clark for an excellent collaboration and Eli Tziperman, David Battisti, and Jeff Severinghaus for helpful comments and suggestions.

References

- Adkins, J. F., K. McIntyre, and D. P. Schrag (2002), The salinity, temperature, and $\delta^{18}\text{O}$ of the glacial deep ocean, *Science*, 298(5599), 1769-1773.
- Alley, R. B., J. T. Andrews, D. C. Barber and P. U. Clark (2005), Comment on "Catastrophic ice shelf breakup as the source of Heinrich event icebergs" by C. L. Hulbe et al, *Paleoceanography*, 20(1), PA1009.

- Alley, R. B., D. A. Meese, C. A. Shuman, A. J. Gow, K. C. Taylor, P. M. Grootes, J. W. C. White, M. Ram, E. D. Waddington, P. A. Mayewski and G. A. Zielinski (1993), Abrupt increase in Greenland snow accumulation at the end of the Younger Dryas event, *Nature*, 362(6420), 527-529.
- Alvarez-Solas, J., S. Charbit, C. Ritz, D. Paillard, G. Ramstein and C. Dumas (2010), Links between ocean temperature and iceberg discharge during Heinrich events, *Nature Geoscience*, 3(2), 122-126.
- Alvarez-Solas, J., M. Montoya, C. Ritz, G. Ramstein, S. Charbit, C. Dumas, K. Nisancioglu, T. Dokken and A. Ganopolski (2011), Heinrich event 1: an example of dynamical ice-sheet reaction to oceanic changes, *Climate of the Past*, 7(4), 1297-1306.
- Andersen, K. K., A. Svensson, S. J. Johnsen, S. O. Rasmussen, M. Bigler, R. Röthlisberger, U. Ruth, M.-L. Siggaard-Andersen, J. R. Peder Steffensen, D. Dahl-Jensen, B. M. Vinther and H. B. Clausen (2006), The Greenland Ice Core Chronology 2005, 15-42ka. Part 1: constructing the time scale, *Quaternary Science Reviews*, 25(23-24), 3246-3257.
- Bond, G., H. Heinrich, W. Broecker, L. Labeyrie, J. McManus, J. Andrews, S. Huon, R. Jantschik, S. Clasen, C. Simet, K. Tedesco, M. Klas, G. Bonani and S. Ivy (1992), Evidence for massive discharges of icebergs into the North Atlantic ocean during the last glacial period, *Nature*, 360(6401), 245-249.
- Bond, G. C. and R. Lotti (1995), Iceberg Discharges into the North Atlantic on Millennial Time Scales During the Last Glaciation, *Science*, 267(5200), 1005-1010.
- Brady, E. and B. Otto-Bliesner (2011), The role of meltwater-induced subsurface ocean warming in regulating the Atlantic meridional overturning in glacial climate simulations, *Climate Dynamics*, 37(7), 1517-1532.
- Brook, E. J., T. Sowers and J. Orchardo (1996), Rapid Variations in Atmospheric Methane Concentration During the Past 110,000 Years, *Science*, 273(5278), 1087-1091.
- Clark, P. U., S. W. Hostetler, N. G. Pisias, A. Schmittner and K. J. Meissner (2007), Mechanisms for an ~7-kyr Climate and Sea-Level Oscillation During Marine Isotope Stage 3, in *Ocean Circulation: Mechanisms and Impacts, Geophysical Monograph Series*, vol. 173, edited by A. Schmittner, J. Chiang, and S. Hemming, pp. 209-246, AGU, Washington, D.C.
- Clark, P. U., S. J. Marshall, G. K. C. Clarke, S. W. Hostetler, J. M. Licciardi and J. T. Teller (2001), Freshwater Forcing of Abrupt Climate Change During the Last Glaciation, *Science*, 293(5528), 283-287.

- Cortijo, E., L. Labeyrie, L. Vidal, M. Vautravers, M. Chapman, J.-C. Duplessy, M. Elliot, M. Arnold, J.-L. Turon and G. Auffret (1997), Changes in sea surface hydrology associated with Heinrich event 4 in the North Atlantic Ocean between 40° and 60°N, *Earth and Planetary Science Letters*, 146(1-2), 29-45.
- Cuffey, K. M. and G. D. Clow (1997), Temperature, accumulation, and ice sheet elevation in central Greenland through the last deglacial transition, *Journal of Geophysical Research*, 102(C12), 26383-26396.
- Dansgaard, W., S. J. Johnsen, H. B. Clausen, D. Dahl-Jensen, N. S. Gundestrup, C. U. Hammer, C. S. Hvidberg, J. P. Steffensen, A. Sveinbjörnsdóttir, J. Jouzel and G. Bond (1993), Evidence for general instability of past climate from a 250-kyr ice-core record, *Nature*, 364, 218-220.
- Dansgaard, W., J. W. C. White and S. J. Johnsen (1989), The Abrupt Termination of the Younger Dryas Climate Event, *Nature*, 339(6225), 532-534.
- Ditlevsen, P. D., K. K. Andersen and A. Svensson (2007), The DO-climate events are probably noise induced: statistical investigation of the claimed 1470 years cycle, *Climate of the Past*, 3(1), 129-134.
- Dokken, T. M. and E. Jansen (1999), Rapid changes in the mechanism of ocean convection during the last glacial period, *Nature*, 401(6752), 458-461.
- Dowdeswell, J. A., J. Evans and C. O Cofaigh (2010), Submarine landforms and shallow acoustic stratigraphy of a 400 km-long fjord-shelf-slope-transect, Kangerlussuaq margin, East Greenland, *Quaternary Science Reviews*, 29(25-26), 3359-3369.
- Elliot, M., L. Labeyrie, T. Dokken and S. Manthé (2001), Coherent patterns of ice-rafted debris deposits in the Nordic regions during the last glacial (10-60 ka), *Earth and Planetary Science Letters*, 194(1-2), 151-163.
- Elliot, M., L. Labeyrie, G. Bond, E. Cortijo, J.-L. Turon, N. Tisnerat and J.-C. Duplessy (1998), Millennial-Scale Iceberg Discharges in the Irminger Basin During the Last Glacial Period: Relationship with the Heinrich Events and Environmental Settings, *Paleoceanography*, 13(5), 433-446.
- Elliot, M., L. Labeyrie and J.-C. Duplessy (2002), Changes in North Atlantic deep-water formation associated with the Dansgaard-Oeschger temperature oscillations (60-10ka), *Quaternary Science Reviews*, 21(10), 1153-1165.
- EPICA Members (2006), One-to-one coupling of glacial climate variability in Greenland and Antarctica, *Nature*, 444, 195-198.

- Evans, J., C. Ó Cofaigh, J. A. Dowdeswell and P. Wadhams (2009), Marine geophysical evidence for former expansion and flow of the Greenland Ice Sheet across the north-east Greenland continental shelf, *Journal of Quaternary Science*, 24(3), 279-293.
- Flückiger, J., T. Blunier, B. Stauffer, J. Chappellaz, R. Spahni, K. Kawamura, J. Schwander, T. F. Stocker and D. Dahl-Jensen (2004), N₂O and CH₄ variations during the last glacial epoch: Insight into global processes, *Global Biogeochemical Cycles*, 18(1), GB1020.
- Fuhrer, K., E. W. Wolff and S. J. Johnsen (1999), Timescales for dust variability in the Greenland Ice Core Project (GRIP) ice core in the last 100,000 years, *Journal of Geophysical Research*, 104(D24), 31043-31052.
- Ganopolski, A. and S. Rahmstorf (2001), Rapid changes of glacial climate simulated in a coupled climate model, *Nature*, 409(6817), 153-158.
- Gildor, H. and E. Tziperman (2003), Sea-Ice Switches and Abrupt Climate Change, *Philosophical Transactions of the Royal Society of London, Series A*, 361(1810), 1935-1944.
- Grootes, P. M. and M. Stuiver (1997), Oxygen 18/16 variability in Greenland snow and ice with 10³- to 10⁵-year time resolution, *Journal of Geophysical Research*, 102(C12), 26455-26470.
- Grootes, P. M., M. Stuiver, J. W. C. White, S. Johnsen, and J. Jouzel (1993), Comparison of oxygen isotope records from the GISP2 and GRIP Greenland ice cores, *Nature*, 366(6455), 552-554.
- Gutjahr, M., B. A. A. Hoogakker, M. Frank and I. N. McCave (2010), Changes in North Atlantic Deep Water strength and bottom water masses during Marine Isotope Stage 3 (45-35 ka BP), *Quaternary Science Reviews*, 29(19-20), 2451-2461.
- Hemming, S. R. (2004), Heinrich events: Massive late Pleistocene detritus layers of the North Atlantic and their global climate imprint, *Review of Geophysics*, 42(1), RG1005.
- Hendy, I. L., and J. P. Kennett (2003), Tropical forcing of North Pacific intermediate water distribution during Late Quaternary rapid climate change?, *Quaternary Science Reviews*, 22(5-7), 673-689.
- Hillaire-Marcel, C., and G. Bilodeau (2000), Instabilities in the Labrador Sea water mass structure during the last climatic cycle, *Canadian Journal of Earth Science*, 37(5), 795-809.
- Holland, D. M., R. H. Thomas, B. De Young, M. H. Ribergaard and B. Lyberth (2008), Acceleration of Jakobshavn Isbrae triggered by warm subsurface ocean waters,

Nature Geoscience, 1(10), 659-664.

Hubbard, A., D. Sugden, A. Dugmore, H. Norddahl and H. R. G. Pétursson (2006), A modelling insight into the Icelandic Last Glacial Maximum ice sheet, *Quaternary Science Reviews*, 25(17-18), 2283- 2296.

Huber, C., M. Leuenberger, R. Spahni, J. Flückiger, J. Schwander, T. F. Stocker, S. Johnsen, A. Landais and J. Jouzel (2006), Isotope calibrated Greenland temperature record over Marine Isotope Stage 3 and its relation to CH₄, *Earth and Planetary Science Letters*, 243(3-4), 504-519.

Hulbe, C. L., D. R. MacAyeal, G. H. Denton, J. Kleman and T. V. Lowell (2004), Catastrophic ice shelf breakup as the source of Heinrich event icebergs, *Paleoceanography*, 19(1), PA1004.

Jenkins, A., P. Dutrieux, S. S. Jacobs, S. D. McPhail, J. R. Perrett, A. T. Webb and D. White (2010), Observations beneath Pine Island Glacier in West Antarctica and implications for its retreat, *Nature Geoscience*, 3(7), 468-472.

Johnsen, S. J., H. B. Clausen, W. Dansgaard, K. Fuhrer, N. Gundestrup, C. U. Hammer, P. Iversen, J. Jouzel, B. Stauffer and J. P. Steffensen (1992), Irregular glacial interstadials recorded in a new Greenland ice core, *Nature*, 359(6393), 311-313.

Jonkers, L., M. Moros, M. A. Prins, T. Dokken, C. A. Dahl, N. Dijkstra, K. Perner and G.-J. A. Brummer (2010), A reconstruction of sea surface warming in the northern North Atlantic during MIS 3 ice-rafting events, *Quaternary Science Reviews*, 29(15-16), 1791-1800.

Joughin, I., B. E. Smith and D. M. Holland (2010), Sensitivity of 21st century sea level to ocean-induced thinning of Pine Island Glacier, Antarctica, *Geophysical Research Letters*, 37(20), L20502.

Knutti, R., J. Flückiger, T. F. Stocker and A. Timmermann (2004), Strong hemispheric coupling of glacial climate through freshwater discharge and ocean circulation, *Nature*, 430(7002), 851-856.

Kosters, F., R. Kase, K. Fleming and D. Wolf (2004), Denmark Strait overflow for Last Glacial Maximum to Holocene conditions, *Paleoceanography*, 19(2), PA2019.

Labeyrie, L., H. Leclaire, C. Waelbroeck, E. Cortijo, J.-C. Duplessy, L. Vidal, M. Elliot, B. Le Coat (1999), Temporal Variability of the Surface and Deep Waters of the North West Atlantic Ocean at Orbital and Millennial Scales, in *Mechanisms of Global Climate Change at Millennial Time Scales*, *Geophysical Monograph Series*, vol. 112, edited by P.U. Clark, R.S. Webb, and L.D. Keigwin, p. 77-98, AGU, Washington, D.C.

- Li, C., D. S. Battisti and C. M. Bitz (2010), Can North Atlantic Sea Ice Anomalies Account for Dansgaard-Oeschger Climate Signals?, *Journal of Climate*, 23(20), 5457-5475.
- Li, C., D. S. Battisti, D. P. Schrag and E. Tziperman (2005), Abrupt climate shifts in Greenland due to displacements of the sea ice edge, *Geophysical Research Letters*, 32(19), L19702.
- Liu, Z., B. L. Otto-Bliesner, F. He, E. C. Brady, R. Tomas, P. U. Clark, A. E. Carlson, J. Lynch-Stieglitz, W. Curry, E. Brook, D. Erickson, R. Jacob, J. Kutzbach and J. Cheng (2009), Transient Simulation of Last Deglaciation with a New Mechanism for Bølling-Allerød Warming, *Science*, 325(5938), 310-314.
- Mahajan, S., R. Zhang, T. L. Delworth, S. Zhang, A. J. Rosati and Y.-S. Chang (2011), Predicting Atlantic meridional overturning circulation (AMOC) variations using subsurface and surface fingerprints, *Deep Sea Research, Part II*, 58(17-18), 1895-1903.
- Marcott, S. A., P. U. Clark, L. Padman, G. P. Klinkhammer, S. R. Springer, Z. Liu, B. L. Otto-Bliesner, A. E. Carlson, A. Ungerer, J. Padman, F. He, J. Cheng and A. Schmittner (2011), Ice-shelf collapse from subsurface warming as a trigger for Heinrich events, *Proceedings of the National Academy of Sciences*, 108(33), 13415-13419.
- Mignot, J., A. Ganopolski and A. Levermann (2007), Atlantic subsurface temperatures: Response to a shutdown of the overturning circulation and consequences for its recovery, *Journal of Climate*, 20(19), 4884-4898.
- Overpeck, J. T., and J. E. Cole (2006), Abrupt Change in Earth's Climate System, *Annual Review of Environment and Resources*, 31(1), 1-31.
- Piotrowski, A. M., S. L. Goldstein, H. S. R., R. G. Fairbanks and D. R. Zylberberg (2008), Oscillating glacial northern and southern deep water formation from combined neodymium and carbon isotopes, *Earth and Planetary Science Letters*, 272(1-2), 394-405.
- Pisias, N. G., P. U. Clark and E. J. Brook (2010), Modes of Global Climate Variability during Marine Isotope Stage 3 (60 ka), *Journal of Climate*, 23(6), 1581-1588.
- Rahmstorf, S. (2003), Timing of abrupt climate change: A precise clock, *Geophysical Research Letters*, 30(10), 1510.
- Rasmussen, T. L., D. W. Oppo, E. Thomsen and S. J. Lehman (2003), Deep sea records from the southeast Labrador Sea: Ocean circulation changes and ice-rafting events during the last 160,000 years, *Paleoceanography*, 18(1), 1018.

- Rasmussen, T. L., and E. Thomsen (2004), The role of the North Atlantic Drift in the millennial timescale glacial climate fluctuations, *Palaeogeography, Palaeoclimatology, Palaeoecology*, 210(1), 101-116.
- Rasmussen, T. L., E. Thomsen, T. C. E. van Weering and L. Labeyrie (1996), Rapid Changes in Surface and Deep Water Conditions at the Faeroe Margin During the Last 58,000 Years, *Paleoceanography*, 11(6), 757-771.
- Schmittner, A., and E. D. Galbraith (2008), Glacial greenhouse-gas fluctuations controlled by ocean circulation changes, *Nature*, 456(7220), 373-376.
- Schulz, M. (2002), On the 1470-year pacing of Dansgaard-Oeschger warm events, *Paleoceanography*, 17(2), 1014.
- Severinghaus, J. P., T. Sowers, E. J. Brook, R. B. Alley and M. L. Bender (1998), Timing of abrupt climate change at the end of the Younger Dryas interval from thermally fractionated gases in polar ice, *Nature*, 391(6663), 141-146.
- Shackleton, N. J., M. A. Hall and E. Vincent (2000), Phase Relationships Between Millennial-Scale Events 64,000-24,000 Years Ago, *Paleoceanography*, 15(6), 565-569.
- Shaffer, G., S. M. Olsen and C. J. Bjerrum (2004), Ocean subsurface warming as a mechanism for coupling Dansgaard-Oeschger climate cycles and ice-rafting events, *Geophysical Research Letters*, 31(24), L24202.
- Steffensen, J. r. P., K. K. Andersen, M. Bigler, H. B. Clausen, D. Dahl-Jensen, H. Fischer, K. Goto-Azuma, M. Hansson, S. s. J. Johnsen, J. Jouzel, V. r. Masson-Delmotte, T. Popp, S. O. Rasmussen, R. Röthlisberger, U. Ruth, B. Stauffer, M.-L. Siggaard-Andersen, Á. E. Sveinbjörnsdóttir, A. Svensson and J. W. C. White (2008), High-Resolution Greenland Ice Core Data Show Abrupt Climate Change Happens in Few Years, *Science*, 321(5889), 680-684.
- Stokes, C. R., and C. D. Clark (2001), Palaeo-ice streams, *Quaternary Science Reviews*, 20(13), 1437-1457.
- Svendsen, J. I., H. Alexanderson, V. I. Astakhov, I. Demidov, J. A. Dowdeswell, S. Funder, V. Gataullin, M. Henriksen, C. Hjort, M. Houmark-Nielsen, H. W. Hubberten, O. Ingolfsson, M. Jacobsson, K. Kjaer, E. Larsen, H. Lokrantz, J. P. Lunkka, A. Lysa, J. Mangerud, A. Matioushkov, A. Murray, P. Möller, F. Niessen, O. Nikolskaya, L. Polyak, M. Saarnisto, C. Siegert, M. J. Siegert, R. F. Spielhagen and R. Stein (2004), Late Quaternary ice sheet history of northern Eurasia, *Quaternary Science Reviews*, 23 (11-13), 1229-1271.
- Svensson, A., K. K. Andersen, M. Bigler, H. B. Clausen, D. Dahl-Jensen, S. M. Davies, S. J. Johnsen, R. Muscheler, F. Parrenin, S. O. Rasmussen, R. Rothlisberger, I.

- Seierstad, J. P. Steffensen and B. M. Vinther (2008), A 60,000 year Greenland stratigraphic ice core chronology, *Climate of the Past*, 4(1), 47-57.
- Taylor, K. C., C. U. Hammer, R. B. Alley, H. B. Clausen, D. Dahl-Jensen, A. J. Gow, N. S. Gundestrup, J. Kipfstuh, J. C. Moore and E. D. Waddington (1993b), Electrical conductivity measurements from the GISP2 and GRIP Greenland ice cores, *Nature*, 366(6455), 549-552.
- Taylor, K. C., G. W. Lamorey, G. A. Doyle, R. B. Alley, P. M. Grootes, P. A. Mayewski, J. W. C. White and L. K. Barlow (1993a), The Flickering Switch of Late Pleistocene Climate Change, *Nature*, 361(6411), 432-436.
- Thomas, E. R., E. W. Wolff, R. Mulvaney, S. J. Johnsen, J. P. Steffensen and C. Arrowsmith (2009), Anatomy of a Dansgaard-Oeschger warming transition: High-resolution analysis of the North Greenland Ice Core Project ice core, *Journal of Geophysical Research*, 114(D8), D08102.
- van Krevelend, S., M. Sarnthein, H. Erlenkeuser, P. Grootes, S. Jung, M. J. Nadeau, U. Pflaumann and A. Voelker (2000), Potential links between surging ice sheets, circulation changes, and the Dansgaard-Oeschger cycles in the Irminger Sea, 60-18 kyr, *Paleoceanography*, 15(4), 425-442.
- Voelker, A. H. L. (2002), Global distribution of centennial-scale records for Marine Isotope Stage (MIS) 3: a database, *Quaternary Science Reviews*, 21(10), 1185-1212.
- Voelker, A. H. L., M. Sarnthein, P. M. Grootes, H. Erlenkeuser, C. Laj, A. Mazaud, M. J. Nadeau and M. Schleicher (1998), Correlation of marine C-14 ages from the Nordic Seas with the GISP2 isotope record: Implications for C-14 calibration beyond 25 ka BP, *Radiocarbon*, 40(1), 517-534.
- Vorren, T. O., et al. (1998), The Norwegian-Greenland Sea Continental Margins: Morphology and Late Quaternary Sedimentary Processes and Environment, *Quaternary Science Reviews*, 17(1-3), 273- 302.
- Walker, R. T., T. K. Dupont, D. M. Holland, B. R. Parizek and R. B. Alley (2009), Initial effects of oceanic warming on a coupled ocean-ice shelf-ice stream system, *Earth and Planetary Science Letters*, 287(3-4), 483-487.
- Weber, M. E., L. A. Mayer, C. Hillaire-Marcel, G. Bilodeau, F. Rack, R. N. Hiscott, and A. E. Aksu (2001), Derivation of $\delta^{18}\text{O}$ from Sediment Core Log Data: Implications for Millennial-Scale Climate Change in the Labrador Sea, *Paleoceanography*, 16(5), 503-514.
- Winton, M. (1993), Deep Decoupling Oscillations of the Oceanic Thermohaline Circulation, in *Ice in the Climate System*, edited by W. R. Peltier, pp. 417-432, Springer-Verlag, New York.

- Wolff, E. W., J. Chappellaz, T. Blunier, S. O. Rasmussen and A. Svensson (2010), Millennial-scale variability during the last glacial: The ice core record, *Quaternary Science Reviews*, 29(21-22), 2828-2838.
- Wunsch, C. (2000), On Sharp Spectral Lines in the Climate Record and the Millennial Peak, *Paleoceanography*, 15(4), 417-424.
- Zahn, R., J. Schönfeld, H.-R. Kudrass, M.-H. Park, H. Erlenkeuser and P. Grootes (1997), Thermohaline Instability in the North Atlantic During Meltwater Events: Stable Isotope and Ice-Rafted Detritus Records from Core SO75-26KL, Portuguese Margin, *Paleoceanography*, 12(5), 696-710.

Chapter 3. Evidence for Dansgaard-Oeschger cycles in sediment cores from the northern North Atlantic and Irminger Basin

ABSTRACT

During the last glacial period, millennial-scale fluctuations in climate are recorded globally by proxy records. Greenland ice cores document many stadial-interstadial transitions known as Dansgaard-Oeschger (DO) cycles. Sediment cores record these cycles, as well as less frequent iceberg discharge events called Heinrich events. A new hypothesis points to fluctuations in ice cover (ice shelf + sea ice) off the southeastern coast of Greenland as the driver of DO cycles. In this study, we look for evidence of this fluctuating ice shelf in sediment records. We use a variety of proxies to show that pulses of ice-rafted debris entered sediments in the northeastern Atlantic and Irminger basin during the last glacial period and suggest correlation to climate events.

3.1 Introduction

Within the last glacial period, the North Atlantic experienced millennial scale variability in temperature and ice sheet behavior. Greenland ice cores record a pattern of repetitive temperature changes known as Dansgaard-Oeschger (DO) cycles, involving a rapid initial warming and a gradual cooling back to glacial conditions [*Johnsen et al.*, 1992; *Dansgaard et al.*, 1993; *Grootes et al.*, 1993]. Sediment cores from the North Atlantic document episodes of massive iceberg discharge from the Laurentide Ice Sheet, known as Heinrich events, appearing as distinct layers of ice rafted detritus (IRD) within otherwise fine-grained abyssal sediment [*Hemming*, 2004 and references therein]. Heinrich events occur approximately every 7-10kyr [*Bond et al.*, 1992] and always fall during the stadial phase of Dansgaard-Oeschger (DO) cycles [*Bond et al.*, 1993]. DO cycles occur more frequently, with 1-4 cycles occurring between successive Heinrich events.

In Chapter 2, we put forth a new hypothesis to explain the DO temperature cycles. We suggest that a fluctuating ice shelf off of southeastern Greenland, accompanied by shifts in sea ice cover, can explain the large observed temperature shifts [*Petersen et al.*, 2013]. In this study, we search for physical evidence of such an ice shelf in the sediment record. We use a variety of geochemical tools to study a suite of cores running from 52-67°N in the North Atlantic. The transect of cores begins just north of the “IRD belt”, a swath from 40°N to 50°N in the North Atlantic where Heinrich events are most strongly recorded [*Ruddiman*, 1977], and ends at the southern outlet of the Denmark Strait, near the proposed location of the ice shelf. We aim to expand the number of cores

documenting DO cyclicity in the Nordic Seas region and delineate the spatial range of influence of Heinrich events vs. DO cycles in the sediments.

3.1.1 Identification of Heinrich events and other Dansgaard-Oeschger stadials

Traditionally, Heinrich events are identified by an increase in IRD (# grains per gram of dry sediment in the >63 μ m size fraction), accompanied by a decrease in the oxygen isotopic composition of planktonic foraminifera, typically *N. pachyderma* (sinistral), a cold-water species ($\delta^{18}\text{O}_{\text{Nps}}$) [Bond *et al.*, 1992; Bond and Lotti, 1995]. The decrease in $\delta^{18}\text{O}_{\text{Nps}}$ is attributed to an input of isotopically light water into the surface ocean from the melting of glacial ice (icebergs), as opposed to a warming event, based on the cold surface water temperatures implied by the concurrent high percentage of *N. pachyderma* (sin.), a proxy for temperature [Bond *et al.*, 1992]. Six primary Heinrich layers (H1-H6) have been documented in the IRD belt using these metrics [Bond *et al.*, 1992], with a seventh found in the Labrador Sea between H5 and H6 [Rashid *et al.*, 2003], and four older events (H7-H10) found in longer cores near the mouth of the Labrador Sea [Rasmussen *et al.*, 2003]. A similar event, named H11, coincides with Termination II during the previous glacial period [Rasmussen *et al.*, 2003].

In the IRD belt, Heinrich events stand out very prominently from the background values of $\delta^{18}\text{O}_{\text{Nps}}$ and %IRD, whereas the other DO stadials show little change in either metric [Bond *et al.*, 1992; Hemming, 2004 and references therein]. In comparison, cores from farther north in the Nordic seas show pulses of IRD corresponding to every DO stadial phase, with no apparent difference in magnitude between Heinrich and non-Heinrich stadials [Voelker *et al.*, 1998; Elliot *et al.*, 1998, 2002] (Figure 3.1). $\delta^{18}\text{O}_{\text{Nps}}$ also

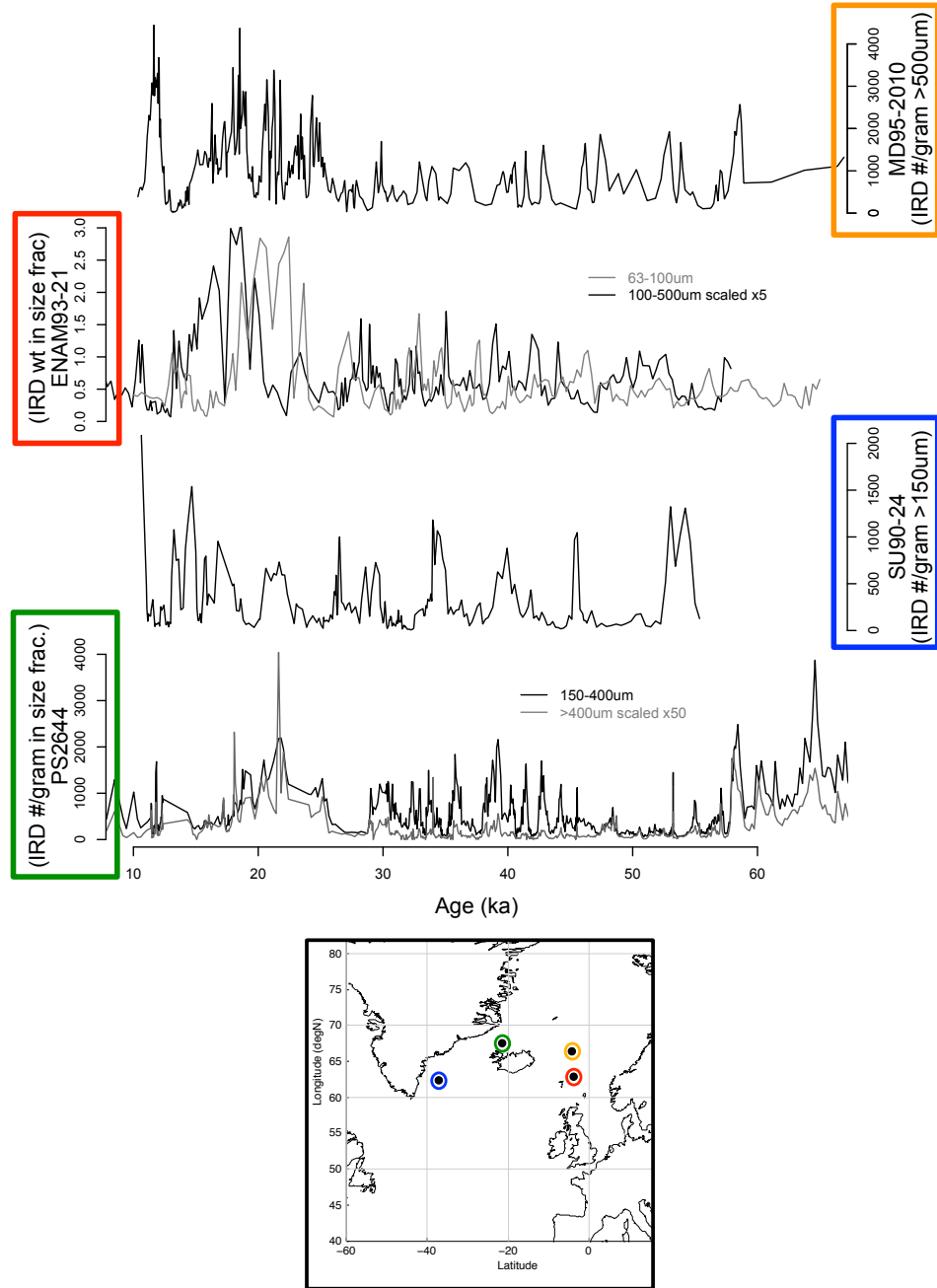


Figure 3.1 Published records of IRD content (# grains per gram dry sediment) from cores MD95-2010 [Dokken and Jansen, 1999], ENAM93-21 [Rasmussen et al., 1996], SU90-24 [Elliot et al., 2002], and PS2644-5 [Voelker et al., 1998] in the Irminger Basin and Nordic Seas region.

For ENAM93-21, IRD content is measured as the weight of IRD over the weight of total sediment in a certain size fraction. Larger size fractions have been scaled for clarity. Map shows locations of cores with the color of the points corresponding to y-axis labels.

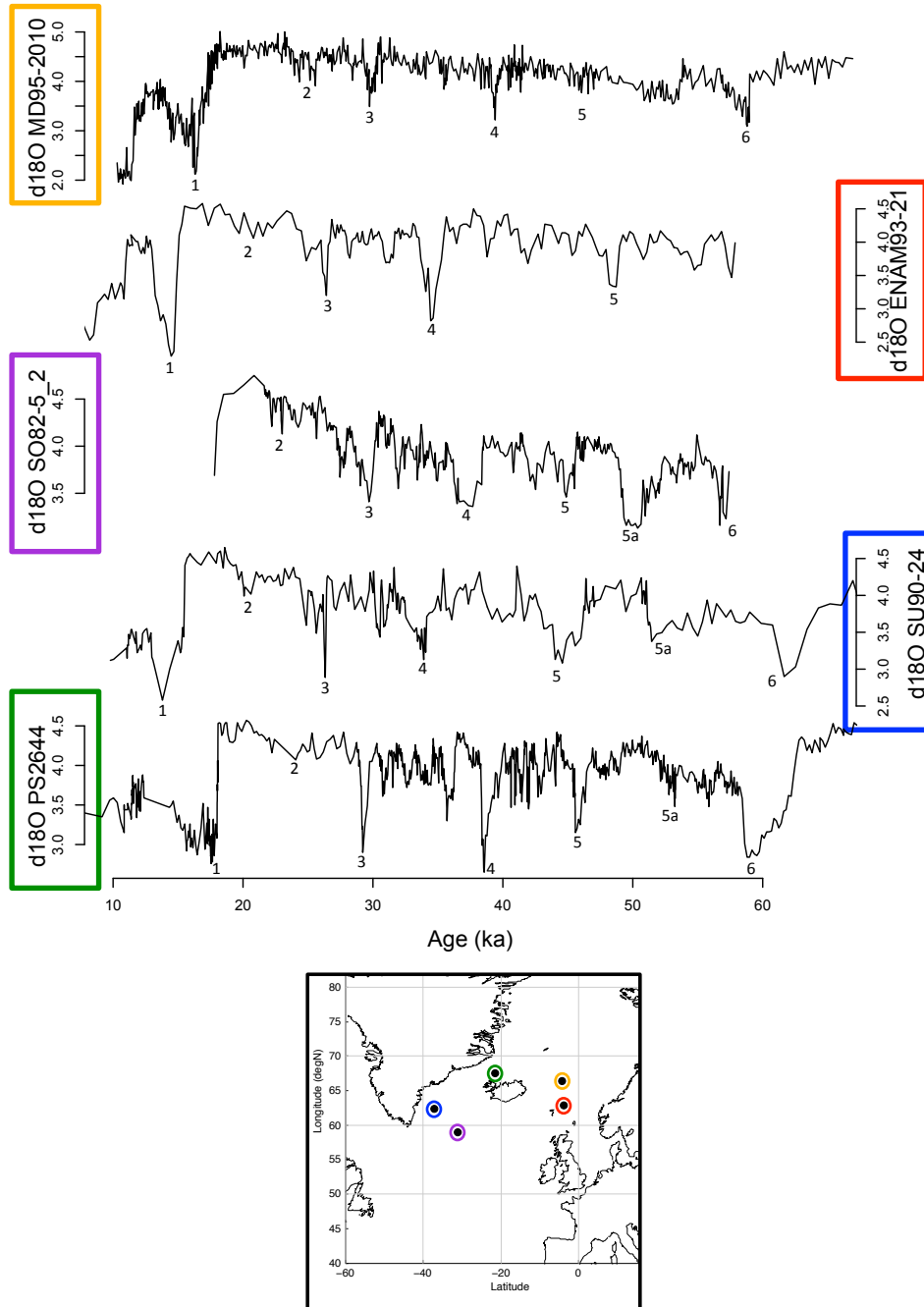


Figure 3.2 Published records of $\delta^{18}\text{O}$ of the planktonic foraminifera *N. pachyderma* from cores MD95-2010 [Dokken and Jansen, 1999], ENAM93-21 [Rasmussen et al., 1996], SO82-5_2 [van Kreveld et al., 2000], SU90-24 [Elliot et al., 2002], and PS2644-5 [Voelker et al., 1998] in the Irminger Basin and Nordic Seas region. Negative excursions are labeled by the number of the corresponding Heinrich event. Map shows locations of cores with the color of the points corresponding to y-axis labels.

becomes more negative for each DO stadial [Voelker *et al.*, 1998; Elliot *et al.*, 1998, 2002], with larger magnitude excursions recorded for Heinrich stadials compared to non-Heinrich DO stadials (Figure 3.2). These larger $\delta^{18}\text{O}_{\text{Nps}}$ anomalies during Heinrich stadials are likely due to the significantly larger volume of icebergs ejected during Heinrich stadials. Such large magnitude shifts observed so far north of the IRD belt have previously been interpreted as a northward propagation of a meltwater lens from icebergs melting in the IRD belt [Elliot *et al.*, 1998].

3.1.2 Motivation for stable isotopes of bulk sediment carbonate

Within the IRD belt, variations in $\delta^{18}\text{O}$ of bulk sediment carbonate ($\delta^{18}\text{O}_{\text{bs}}$) have been shown to strongly correlate with the depths of Heinrich layers [Hodell and Curtis, 2008]. $\delta^{18}\text{O}_{\text{bs}}$ represents the average isotopic composition of all carbonate in the sediment, including both biogenic carbonate (foraminifera, coccolithophores) and detrital carbonate (IRD). Variations in this parameter can represent 1) changes in the relative proportions of biogenic:detrital carbonate; and/or 2) changes in the end-member isotopic value of biogenic, detrital carbonate, or both.

Within Heinrich layers, the sediment is made up of nearly 100% IRD [Bond *et al.*, 1992]. The majority of the IRD in these layers is detrital carbonate derived from Paleozoic carbonate units underlying the Laurentide Ice Sheet [Bond *et al.*, 1992]. In some cores, sediment in Heinrich layers is made up of > 50% carbonate (mainly of detrital origin), a large increase over background values of ~10% carbonate [Hemming, 2004]. Hodell and Curtis [2008] showed that this Laurentide-derived detrital carbonate is much lighter in $\delta^{18}\text{O}$ than the background biogenic carbonate (-5 to -6‰ compared to +3-

4‰), making the IRD-rich layers stand out in $\delta^{18}\text{O}_{\text{bs}}$. In this case, the change in $\delta^{18}\text{O}_{\text{bs}}$ is due mainly to an increase in the proportion of the detrital end-member over the biogenic end-member. The biogenic end-member also becomes lighter during Heinrich events due to meltwater inputs, but this change is swamped by the IRD flux.

In this study, we combined $\delta^{18}\text{O}_{\text{bs}}$ and %CaCO₃ measurements to identify IRD input in cores farther north than the IRD belt. These two parameters can be achieved in a single measurement, and can be accomplished in large quantities using an automated sampler. This allowed us to quickly “scan” through many cores to search for sections of interest, where we then focused more in depth.

IRD in the region of the Irminger Basin and northeastern North Atlantic could be sourced from the Laurentide Ice Sheet via the Hudson Strait, from Eastern Greenland, Iceland, or any of the European ice sheets. IRD from the Laurentide, such as that which makes up the majority of the Heinrich layer material, has a large fraction of detrital carbonate of distinct isotopic composition, making it easy to pick up with this method. Another province of carbonate rocks can be found on southeastern Greenland [*Bond et al.*, 1992], ideally located to contribute to sediment in the Irminger Basin. Proximity would also suggest that IRD from Iceland could contribute significantly to sediments in the target region. However, the majority of IRD from Iceland is basaltic glass, which would not affect $\delta^{18}\text{O}_{\text{bs}}$ values, but may influence %CaCO₃. Much of Greenland is made of metamorphic rocks that would also not affect $\delta^{18}\text{O}_{\text{bs}}$ or $\delta^{13}\text{C}_{\text{bs}}$, but could influence %CaCO₃.

3.2 Materials

3.2.1 Sediment core selection

We sampled 10 sediment cores housed at the Lamont Doherty Earth Observatory Core Repository. The cores came from two cruises – cruise EW93-03 (3 cores) and cruise KN158-4 (7 cores) [*IMLGS database*]. The cores come from water depths varying from 225-2833m, and are all located between 14°W and 31°W and 52°N and 67°N (Table 3.1). This sampling area covers the northeast North Atlantic and the Greenland Sea, and reaches up to the coast of Iceland (Figure 3.3). In the following discussion we will focus on a subset of these cores (KN42, KN55, KN84, EW6, and EW8). A few radiocarbon dates have been previously measured on these cores [*de Menocal, personal communication*]. Ages reported here have been corrected using a 400-year reservoir age and the radiocarbon calibration equation of *Fairbanks et al.* [2005].

3.2.2 Sediment core sampling

Since drilling, sediment cores were stored in refrigerated warehouse rooms at the Lamont Doherty Earth Observatory Core Repository, allowing core material to retain its original moisture. Sediment varied from clay-rich to sandy texture between cores and within each core. Samples were taken from 1cm-wide intervals, and were labeled with the depth at the top of the interval. Most cores were sampled at 2cm-resolution. A few sections were sampled at lower resolution that were known to be outside the glacial period of interest based on magnetic susceptibility scanning data [*de Menocal, personal communication*]. 1-2mg of sediment were sampled for each interval and placed in plastic sample vials for transport back to Harvard University.

Full Core Name	Short Name	Latitude (°N)	Longitude (°W)	Water Depth (m)	Core Length (cm)	Sampled segment (cm)
EW93-03-GGC1	EW1	64.31	25.02	225	204	3-201
EW93-03-JPC6	EW6	64.82	29.93	2080	1189	1-837
EW93-03-JPC8	EW8	63.08	29.40	2118	1317	54-1276
KN158-04-42	KN42	52.55	20.33	2833	450	1-499
KN158-04-53	KN53	55.46	14.71	2184	520	10-519
KN158-04-55	KN55	57.03	17.53	1331	522	1-524
KN158-04-57	KN57	58.66	25.42	2768	554	25-556
KN158-04-63	KN63	61.00	27.08	1443	591	200-592
KN158-04-70	KN70	66.67	24.19	238	484	5-476
KN158-04-84	KN84	63.41	30.94	2484	498	1-491

Table 3.1 List of locations, water depth, and sampled interval for cores measured in this study [IMLGS database].

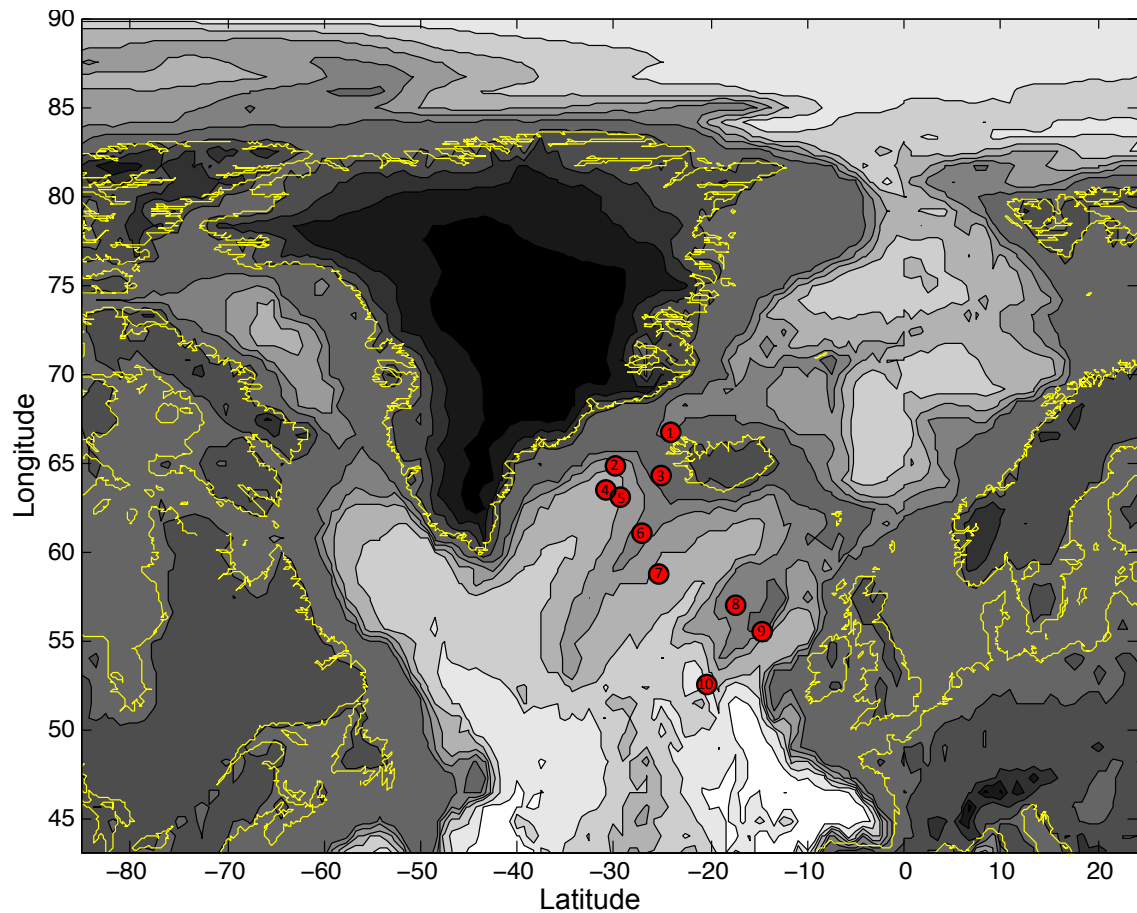


Figure 3.3 Map showing locations of cores measured in this study (red points). Also showing coastlines (yellow) and bathymetry (greyscale). Cores are numbered as follows: 1) KN70; 2) EW6; 3) EW1; 4) KN84; 5) EW8; 6) KN63; 7) KN57; 8) KN55; 9) KN53; 10) KN42.

3.3 Measurement Techniques

3.3.1 Bulk sediment

Aliquots of bulk sediment were dried in an oven and powdered with a mortar and pestle. 5-14mg of powder was weighed into silver boats for analysis. Bulk sediment samples were reacted in a common acid bath at 90°C, and the isotopic composition of the evolved CO₂ was measured on an Optima dual-inlet mass spectrometer. Bulk sediment isotopic values ($\delta^{13}\text{C}_{\text{bs}}$, $\delta^{18}\text{O}_{\text{bs}}$) were acquired with a typical precision of 0.03‰ on $\delta^{13}\text{C}$ and of 0.06‰ on $\delta^{18}\text{O}$. During the transfer of CO₂ into the mass spectrometer, a pressure reading measured the quantity of gas created during the reaction, which was converted to an approximate percent carbonate (%CaCO₃) value based on calibration to pure carbonate standards, to a precision of ~1%.

3.3.2 Sieved size fractions

Aliquots of sediment were wet sieved into four size fractions, dried and weighed. The size fractions were <63µm (fine), 63-150µm (medium), 150-250µm (large), and > 250µm (coarse). The weight percent of sediment in each size fraction was calculated relative to the sum of the four dried size fractions (wt. %_(fine), wt. %_(med), wt. %_(large), wt. %_(coarse)). Material from the smallest two size fractions was measured for its stable isotopic composition ($\delta^{13}\text{C}_{\text{fine}}$, $\delta^{18}\text{O}_{\text{fine}}$, $\delta^{13}\text{C}_{\text{med}}$, $\delta^{18}\text{O}_{\text{med}}$) and percent carbonate (%CaCO_{3-fine}, %CaCO_{3-med}).

3.3.3 Foraminifera

Planktonic foraminifera of the species *N. pachyderma* (sinistral) were picked from the “large” sieved size fraction (150-250 μ m). *N. pachyderma* is a surface dweller that likes cold waters and is common in the North Atlantic. Due to its unique tolerance for cold temperatures, in the highest latitudes it can make up nearly 100% of the foraminifera present in a core. 100-200 specimens were picked per depth horizon. The tests were crushed and sonicated in deionized water to remove any fine-grained carbonate material trapped inside the shells, which can skew isotopic measurements [Hodell and Curtis, 2008]. The resulting clean shell material was split 3 aliquots of 0.3-0.5mg. One to two of these aliquots were measured for stable isotopes ($\delta^{13}\text{C}_{\text{Nps}}$, $\delta^{18}\text{O}_{\text{Nps}}$) and the other one to two were set aside for Mg/Ca analysis [not performed].

3.4 Results – Bulk Sediment Stable Isotopes

3.4.1 KN42, near the IRD belt

Core KN42 (52.55°N, 20.33°W), located just north of the traditional IRD belt region, is the farthest south of all the cores sampled in this study. This core shows six large (3-6‰) negative excursions in $\delta^{18}\text{O}_{\text{bs}}$ (Figure 3.4), similar to those seen in the bulk sediment record from within the IRD belt [Hodell and Curtis, 2008]. In KN42, negative excursions in $\delta^{13}\text{C}_{\text{bs}}$ of 0.6-1.2‰ closely mirror the $\delta^{18}\text{O}_{\text{bs}}$ excursions (Figure 3.4). As in the IRD belt [Hodell and Curtis, 2008], we suggest that these bulk sediment isotope excursions can be correlated to Heinrich events through the influx of detrital carbonate.

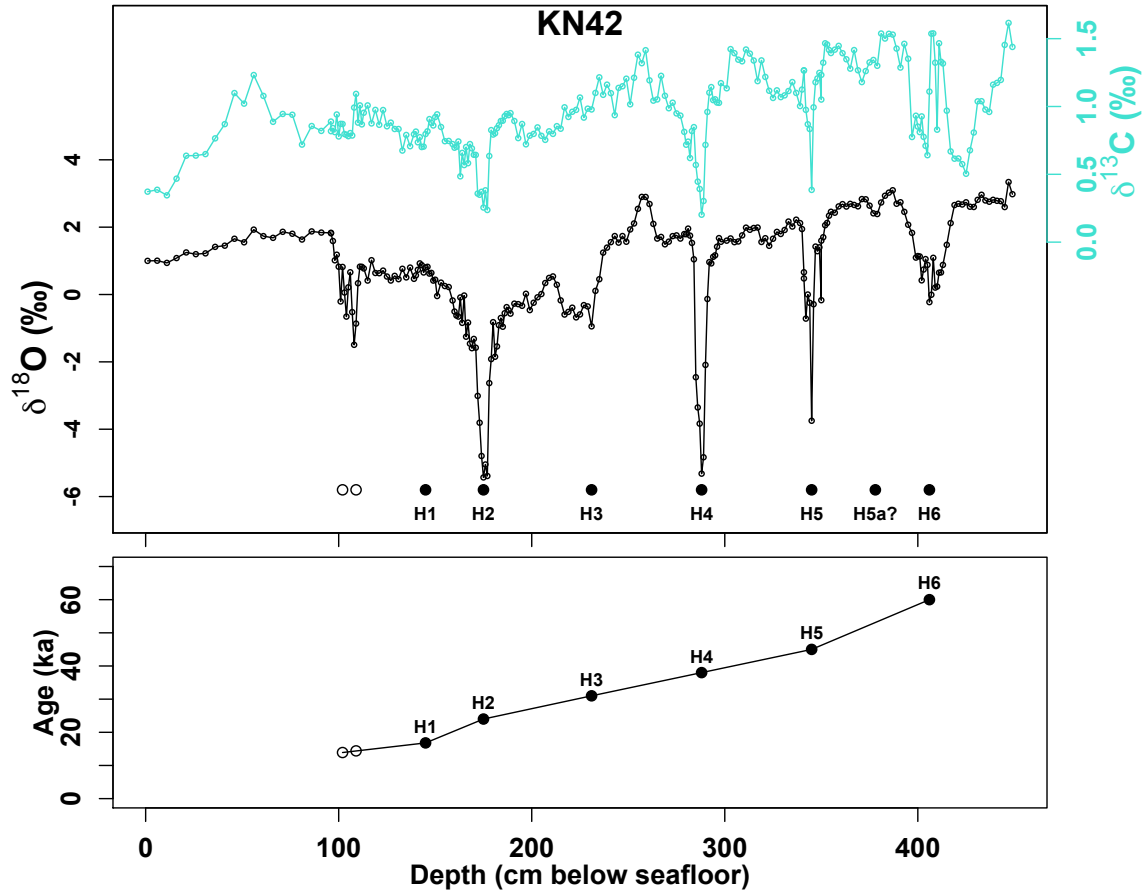


Figure 3.4 Top: $\delta^{18}\text{O}_{\text{bs}}$ (black) and $\delta^{13}\text{C}_{\text{bs}}$ (turquoise) vs. Depth for KN42. Solid black dots mark the depths of excursions, which correlate to H1 through H6, including H5a. Open circles mark the location of two radiocarbon dates (102cm = 13.9ka, 109cm = 14.4ka) [de Menocal, personal communication]. Bottom: Proposed age model, assigning the ages of Heinrich events from Hemming [2004] and including the two radiocarbon dates.

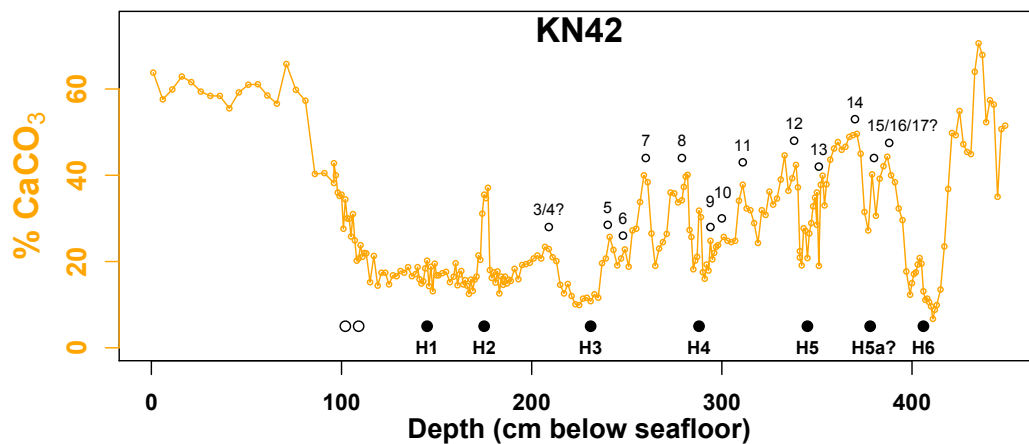


Figure 3.5 %CaCO₃ vs. Depth for KN42. Solid black dots delineate the depths of isotope excursions identified in Figure 3.4. Open circles mark the location of two radiocarbon dates (102cm = 13.8ka, 109cm = 14.4ka) [de Menocal, personal communication]. Potential correlation between maxima in %CaCO₃ and DO events 3-17 are shown in numbered open black circles.

In the IRD belt, *Hodell and Curtis* [2008] found that negative excursions in $\delta^{18}\text{O}_{\text{bs}}$ correlated with the known position of Heinrich layers, defined by an increase in %IRD. The isotope excursions were caused by the presence of detrital carbonate material that was isotopically distinct from the background biogenic carbonate flux. The average isotopic composition of these detrital grains was $-5.32 \pm 1.3\text{‰}$ for $\delta^{18}\text{O}_{\text{bs}}$ and $0.31 \pm 1.3\text{‰}$ for $\delta^{13}\text{C}_{\text{bs}}$ [*Hodell and Curtis*, 2008]. The lowest isotopic composition achieved in the KN42 excursions is -5.4‰ for $\delta^{18}\text{O}_{\text{bs}}$ and 0.2‰ for $\delta^{13}\text{C}_{\text{bs}}$, near the measured end-member value for Laurentide-derived carbonate IRD. If the IRD end-member in KN42 is the same as in the IRD belt, this suggests that Laurentide-derived IRD makes up nearly 100% of the carbonate in many of these excursion intervals.

These isotope excursions match peaks in magnetic susceptibility as well [*de Menocal*, personal communication]. Over the measured section, there are 7 peaks in magnetic susceptibility, whereas there are only 6 isotope excursions. This “missing” isotope excursion would fall at 145cm below seafloor (cmbsf) between the first and second isotope excursion. If these excursions correlate to Heinrich events, the “missing event” likely represents H1. Compared with the other Heinrich events, H1 has a thinner IRD layer in this region [*Hemming*, 2004 – Figure 25], and may have been missed at 2cm sampling resolution or be absent altogether in this core.

Correlating the five later excursions to H2-H6, the two weakest excursions (230 and 405cmbsf) correspond to H3 and H6. This difference between H3/H6 and the other Heinrich events has been noted before, and it has been suggested that these two events are associated with periods of carbonate dissolution as well as IRD influx [*Hemming*, 2004, and references therein]. In KN42, H3 and H6 are associated with the lowest percent

carbonate values seen in the whole core (Figure 3.4), in agreement with this interpretation. This correlation also places the small isotope excursion at ~380cmbsf between H5 and H6. This could be the H5a event identified by *Rashid et al.* [2003] in the Labrador Sea.

Assigning the ages of H1-H6 [*Hemming, 2004*] to the isotope (and magnetic susceptibility) excursions produces a weighted average sedimentation rate of 6.9cm/kyr. This is close to the sedimentation rate of 9.5cm/kyr in nearby core ODP609 over a similar period [*Elliot et al., 1998*], suggesting our correlation of these excursions with Heinrich events is sound. Two radiocarbon dates at 102cmbsf and 109cmbsf produce ages of 13.9ka and 14.4ka, respectively, supporting our age model [*de Menocal, personal communication*]. These ages may be younger than this, due to the increased reservoir age documented during the Younger Dryas interval [*Bard et al., 1994*]. This suggests that the youngest isotope excursion is related to the deglaciation, either representing ice rafting during the Younger Dryas (H0) or melt water influx during the warm Bolling-Allerod.

The %CaCO₃ record shows significant variation throughout the core (Figure 3.5). The down-core drop from high Holocene values (70%) to lower glacial values (20%) around 100cmbsf delineates the glacial/interglacial transition. The lowest %CaCO₃ values in the core (~10%) occur during H3 and H6. The other isotope excursions show differing behavior in %CaCO₃. During the oxygen isotope excursions marking H2 and H4, %CaCO₃ increases to a local maximum, whereas H5 occurs during a decline in %CaCO₃. Between the Heinrich events, there are smaller fluctuations in %CaCO₃ that resemble the DO cycles in their timing and magnitude (Figure 3.5). DO events 8, 12, and 14 stand out as longer intervals of high %CaCO₃ and DO events 9,13, and 15 are shorter,

in line with their relative duration in the Greenland ice cores [Johnsen *et al.*, 1992; Dansgaard *et al.*, 1993; Grootes *et al.*, 1993].

KN42 clearly shows the episodic influx of isotopically light carbonate, which produces large negative spikes in $\delta^{18}\text{O}_{\text{bs}}$ and $\delta^{13}\text{C}_{\text{bs}}$. Correlation of isotopic excursions to known ages of Heinrich events produces a reasonable sedimentation rate. The proposed age model aligns distinct Heinrich events (H3/H6, H5a) with excursions of a slightly different character. Fluctuations in $\%\text{CaCO}_3$ between Heinrich events can potentially be correlated to DO cycles. This core looks very similar to other cores from the IRD belt, despite being outside the traditionally defined IRD belt latitude range, and shows the influence of both Heinrich events and DO cycles.

3.4.2 KN55, moving north of the IRD belt

Four cores were measured from north of the IRD belt between 55°N and 61°N – KN53, KN55, KN57, and KN63. These cores generally show large fluctuations in $\delta^{18}\text{O}_{\text{bs}}$, and $\%\text{CaCO}_3$, but the Heinrich events do not stand out as clearly as in KN42. In this region, we will focus on KN55. Data from cores not discussed here can be found in Appendix A1.

KN55:

KN55 is located at 57.03°N and 17.53°E, on the Rockall Plateau. This core shows $>2\%$ variations in $\delta^{18}\text{O}_{\text{bs}}$, some of which are very rapid. $\%\text{CaCO}_3$ varies between $\sim 20\%$ and $\sim 80\%$ (Figure 3.6). A rough age model for KN55 can be produced by comparing its $\%\text{CaCO}_3$ record to $\%\text{CaCO}_3$ in a nearby well-dated core, ODP982 (57°31'N,

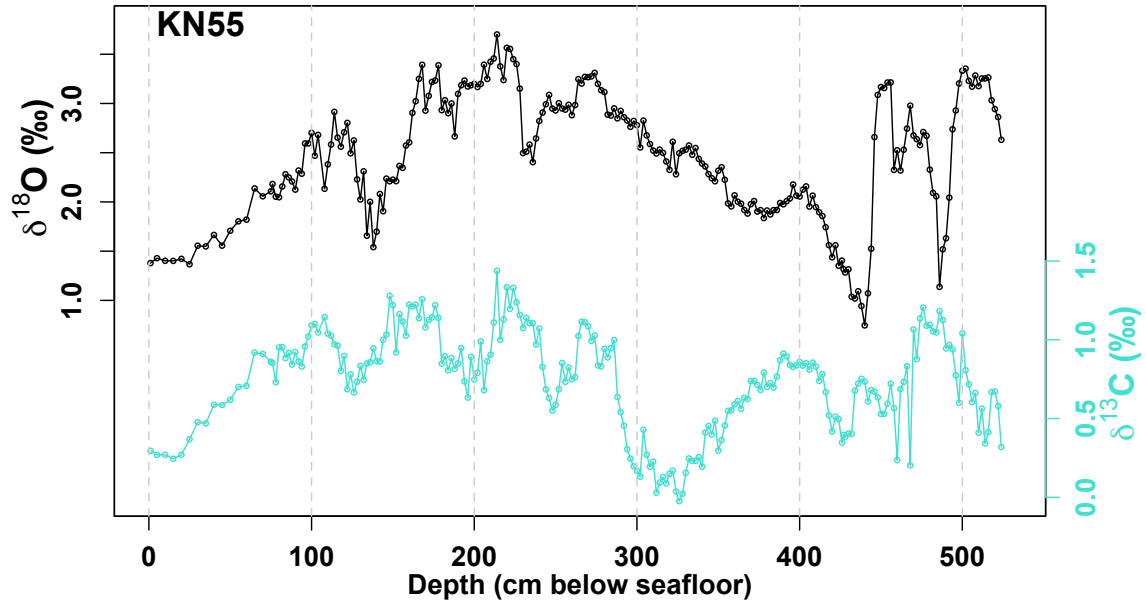


Figure 3.6 $\delta^{18}\text{O}_{\text{bs}}$ (black) and $\delta^{13}\text{C}_{\text{bs}}$ (turquoise) vs. Depth in KN55.

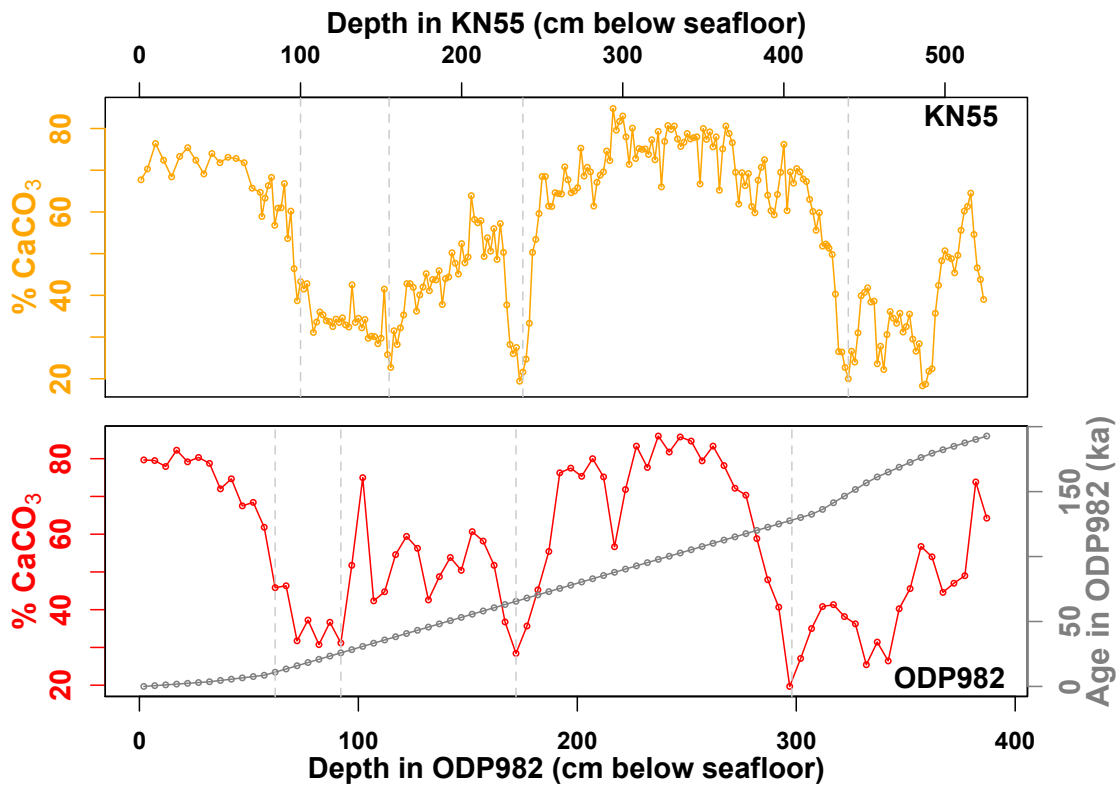


Figure 3.7 Top: %CaCO₃ (orange) vs. Depth for KN55. Bottom: %CaCO₃ (red) and Age (grey) vs. Depth for ODP982 [Venz *et al.*, 1999]. The %CaCO₃ records are highly similar between the two cores, suggesting KN55 covers roughly the same ~190kyr.

15°52'W). The KN55 record looks similar to the first 3.9m of ODP982 (Figure 3.7), which covers the last ~190kyr, spanning two glacial cycles which are clearly seen in the %CaCO₃ variations [Venz *et al.*, 1999]. In KN55, interglacial periods have high %CaCO₃ (>60%) and low magnetic susceptibility [de Menocal, personal communication]. The two glacial periods covered by this core (MIS2-4 and MIS6) have lower and more variable %CaCO₃, and coincide with broad peaks in magnetic susceptibility, likely the result of increased ice-rafted debris diluting the carbonate component of the sediment with terrigenous material. MIS 5 in ODP982 has a dual-peak structure that is not observed in KN55, but is seen in other cores from the area [Ruddiman, 1992].

This age model is corroborated by one radiocarbon date taken at 114cmbsf, which gives an age of 15.6kyr [de Menocal, personal communication]. This date falls in an interval of low %CaCO₃ right before the rise to higher values at the top of the core. In ODP982, the corresponding interval of low %CaCO₃ falls at 72cmbsf and has an age of 15.9kyr (Figure 3.7). This period of low %CaCO₃ therefore likely represents the LGM, and the rise directly afterwards is the deglaciation.

Within the interval that represents the last glacial period (~100-270cmbsf), the strong isotope excursions that were present in KN42 are not seen in KN55. $\delta^{18}\text{O}_{\text{bs}}$ gradually declines into the LGM, with a few negative excursions occurring at 230-235, 188, and 135-140cmbsf. $\delta^{13}\text{C}_{\text{bs}}$ varies between 0.5 and 1.2‰, with the lowest values occurring at 245-250, 180-195, and 120-125cmbsf, offset from the $\delta^{18}\text{O}_{\text{bs}}$ excursions. Based on the age model created from correlation with ODP982, these excursions all occur during the last glacial phase. With the low number of excursions, it is unlikely that they correlate with Heinrich events or Dansgaard-Oeschger cycles.

Although KN55 does not show the same number of negative excursions in $\delta^{18}\text{O}_{\text{bs}}$ as KN42, and the few excursions that are recorded are lower in magnitude and longer in duration, the $\% \text{CaCO}_3$ records show some similarities that can help correlate age in KN55 within the glacial phase. Going down-core, both KN42 and KN55 show 1) the glacial/interglacial transition, 2) a period of low $\% \text{CaCO}_3$ during the LGM, punctuated by a few short spikes, 3) a period of intermediate $\% \text{CaCO}_3$ levels that may correlate to DO interstadials 5-17 in KN42, 4) a large dip down to very low $\% \text{CaCO}_3$ levels that corresponds to H6 in KN42, and 5) a rise to high $\% \text{CaCO}_3$ levels during the previous interglacial, MIS5.

Overall, this core covers the most recent glacial cycle and the penultimate glacial maximum. $\% \text{CaCO}_3$ and magnetic susceptibility track the glacial cycles. $\delta^{18}\text{O}_{\text{bs}}$ and $\delta^{13}\text{C}_{\text{bs}}$ are somewhat correlated and show a few negative excursions during the most recent glacial cycle, but no high-frequency isotope excursions are seen in this core that would suggest IRD or meltwater pulses.

3.4.3 EW1 and KN70, off the coast of Iceland

Two cores, EW1 and KN70, were drilled in less than 300m water depth, both near the coast of Iceland. Despite their proximity to a continental margin that could have produced IRD-rich icebergs, neither of these cores shows the type of fluctuations in $\delta^{18}\text{O}_{\text{bs}}$ that would suggest episodic iceberg discharge events, mainly due to high sedimentation rates restricting the time period covered by the core.

EW1:

The bulk stable isotopes of EW1 are highly variable, with $\delta^{18}\text{O}_{\text{bs}}$ ranging from -11‰ to 4‰ and $\delta^{13}\text{C}_{\text{bs}}$ ranging from -9‰ to 7‰ (Figure 3.8). This variability is also accompanied by poor reproducibility (average $1\sigma = 1.3\text{‰}$ for $\delta^{18}\text{O}_{\text{bs}}$ and 1.0‰ for $\delta^{13}\text{C}_{\text{bs}}$), with some replicates of the same sample varying by as much as 8‰ in $\delta^{18}\text{O}_{\text{bs}}$.

The bulk sediment stable isotope measurement becomes less reproducible at very low %CaCO₃ values (less than 1-2%). In EW1, the majority of the core, except for a short section 0-25cmbsf, has %CaCO₃ values in this range, making the data quality poor overall. The low %CaCO₃ in this core is likely attributable to large inputs of basaltic rock from Iceland. Below the first 15cm, EW1 has a primary composition described as “terrigenous” [IMLGS database].

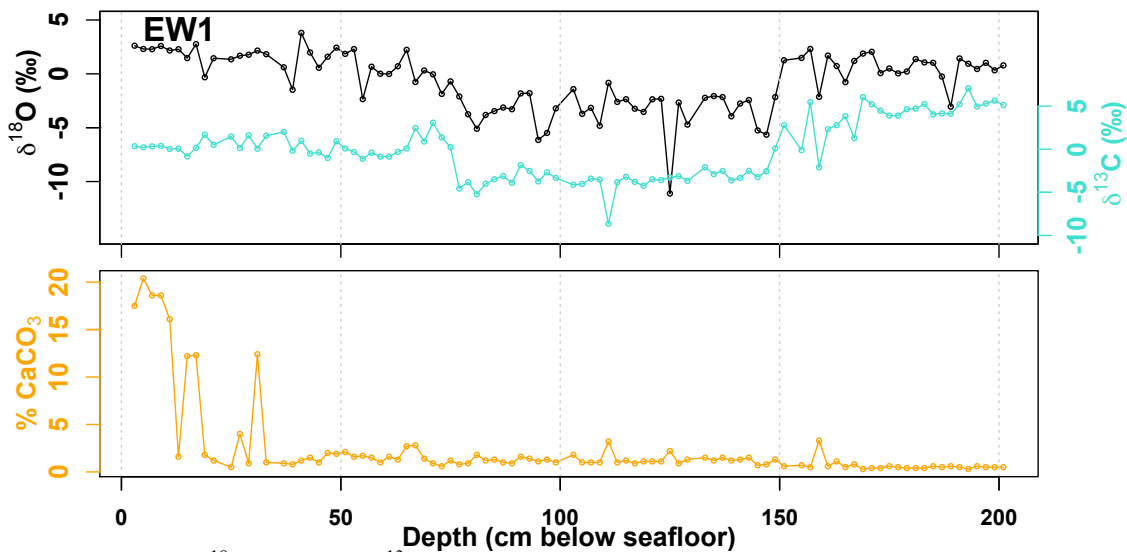


Figure 3.8 $\delta^{18}\text{O}_{\text{bs}}$ (black), $\delta^{13}\text{C}_{\text{bs}}$ (turquoise), and %CaCO₃ (orange) vs. depth for EW1.

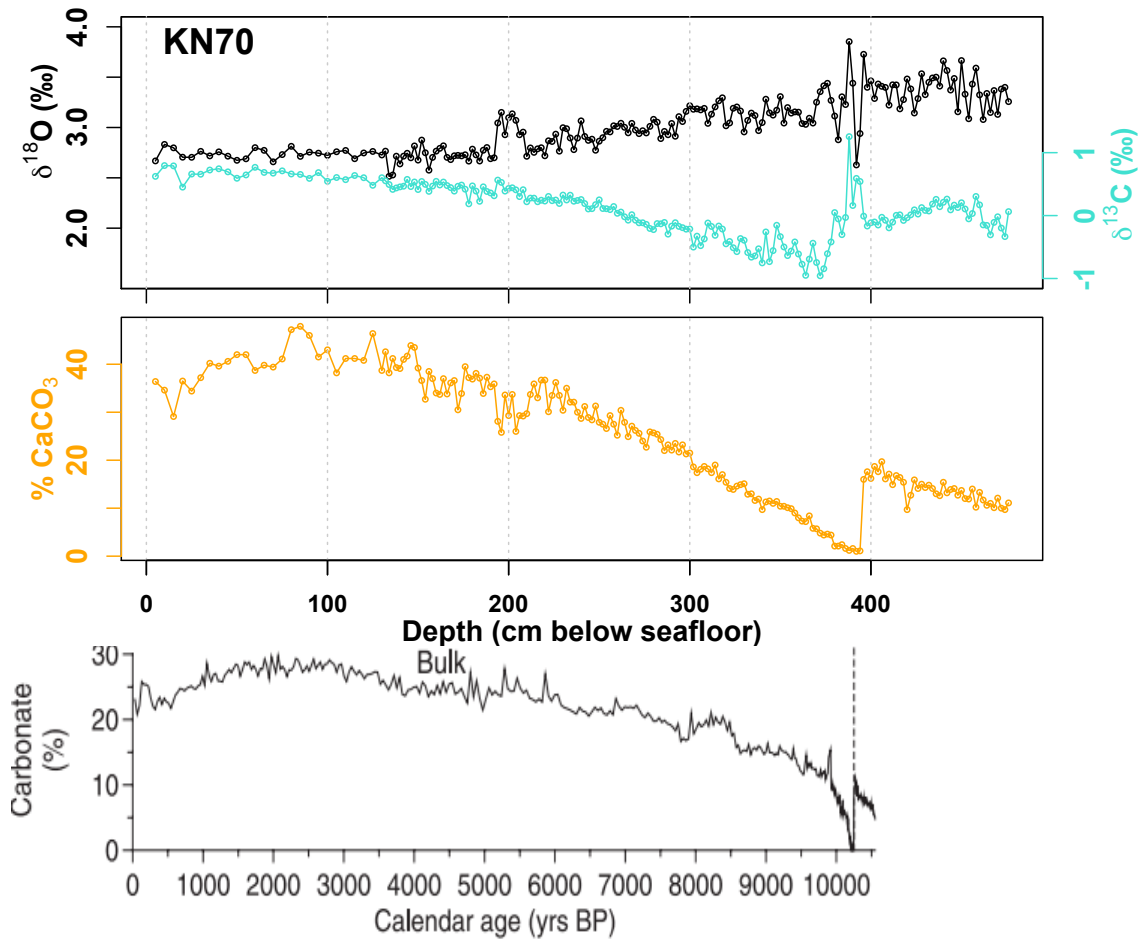


Figure 3.9 $\delta^{18}\text{O}_{\text{bs}}$ (black), $\delta^{13}\text{C}_{\text{bs}}$ (turquoise), and %CaCO₃ (orange) vs. depth for KN70. Bottom: %CaCO₃ vs. calendar age for KN72, drilled 57m away [Andresen *et al.*, 2005].

KN70:

In KN70, the bulk carbonate stable isotopes do not show any strong peaks that would be indicative of episodic iceberg discharges. Sediment composition gradually changes down-core, with $\delta^{18}\text{O}_{\text{bs}}$ increasing and $\delta^{13}\text{C}_{\text{bs}}$ and %CaCO₃ decreasing (Figure 3.9). At ~390cmbsf, %CaCO₃ reaches nearly zero and the isotope values become highly variable as a result. Variability increases dramatically when %CaCO₃ falls below ~2.5% (average 1σ increases from 0.07‰ to 0.5‰ for $\delta^{18}\text{O}_{\text{bs}}$ and from 0.06‰ to 0.7‰ for $\delta^{13}\text{C}_{\text{bs}}$). Due to its proximity to Iceland, KN70 is rich in basalt and is visibly darker in

color than other cores. The primary composition of KN70 from 200-400cmbsf is described as “volcanics” [*IMLGS database*].

%CaCO₃ in KN70 is very similar to %CaCO₃ in neighboring core KN158-4-GGC72 (KN72), which has been well-dated using radiocarbon dating on shell pieces [*Andresen et al.*, 2005]. In KN72, the sharp drop in %CaCO₃ (at 390cmbsf in KN70 and 381cmbsf in KN72) is the result of the presence of a tephra layer, with a composition of nearly 100% basaltic glass [*Andresen et al.*, 2005]. This feature has been dated to 10,200-10,250 calendar years, and is correlated to the Saksunarvatn tephra [*Andresen et al.*, 2005]. Therefore, KN70 is restricted to the Holocene interval. Above the tephra layer, $\delta^{18}\text{O}_{\text{bs}}$ gradually decreases and %CaCO₃ increases, consistent with continued warming during the Holocene.

There is one peak in $\delta^{18}\text{O}_{\text{bs}}$, around 200cmbsf, where $\delta^{18}\text{O}_{\text{bs}}$ shifts from 2.7 to 3.15‰ and %CaCO₃ drops from ~38% to 28% (Figure 3.9). This peak is not observed in KN72, but it must be of mid-Holocene age.

3.4.4 EW6, EW8, and KN84, the Denmark Strait outlet

The best record of Dansgaard-Oeschger cycles in ocean sediments can be found in core PS2644-5, located at the northern inlet to the Denmark Strait [*Voelker et al.*, 1998] (Figure 3.1, 3.2). The proximity to the Greenland Ice Sheet and the shallow bathymetry in this region make it a prime location of the fluctuating ice shelf proposed to drive DO cycles (Chapter 2). Three cores were sampled from the outlet of the Denmark Strait. EW6 and EW8 are both from a depth of ~2100m, whereas KN84 is slightly deeper (~2500m depth). The sedimentation rate in these cores is similar to KN55, such that a ~5m core

covers the last glacial cycle back to Termination II and a bit beyond. Cores EW6 and EW8 are longer (8m and 12m in length), and therefore extend farther back in time. These cores display many large and rapid fluctuations in $\delta^{18}\text{O}_{\text{bs}}$, which may be attributable to ice-rafting events.

KN84:

Core KN84 sits in the center of the outlet of the Denmark Strait at a depth of ~2500m. Multiple negative isotope excursions in $\delta^{18}\text{O}_{\text{bs}}$ are recorded in this core. Each is associated with a minimum in %CaCO₃, and many are also associated with maxima in $\delta^{13}\text{C}_{\text{bs}}$ (Figure 3.10).

The $\delta^{18}\text{O}_{\text{bs}}$ profile has some similarities to that of KN55 – specifically the negative excursion around 300cbsf looks similar in shape to that at 440cbsf in KN55 (rapid decrease, gradual increase). In KN55, this negative $\delta^{18}\text{O}_{\text{bs}}$ event correlated to the last interglacial period based on comparison of the %CaCO₃ record to that of the well-dated core ODP982. The rise in the %CaCO₃ in KN55, KN84, and ODP982 at the onset of the negative excursion in $\delta^{18}\text{O}_{\text{bs}}$ supports assigning this event as Termination II. The dual-peak structure of the interglacial %CaCO₃ record is similar to that seen in ODP982. In KN84, the rise in %CaCO₃ near the top of the core represents the transition from glacial to interglacial, Termination I. The minima in %CaCO₃ around 70cbsf likely represents the glacial maxima.

Two radiocarbon dates on this core were measured at 0 and 100cbsf, giving ¹⁴C ages of 3.2ka and 29.1ka calendar age [*de Menocal*, personal communication], which converts to a sedimentation rate of 3.9cm/kyr over this time. Interpolating between these

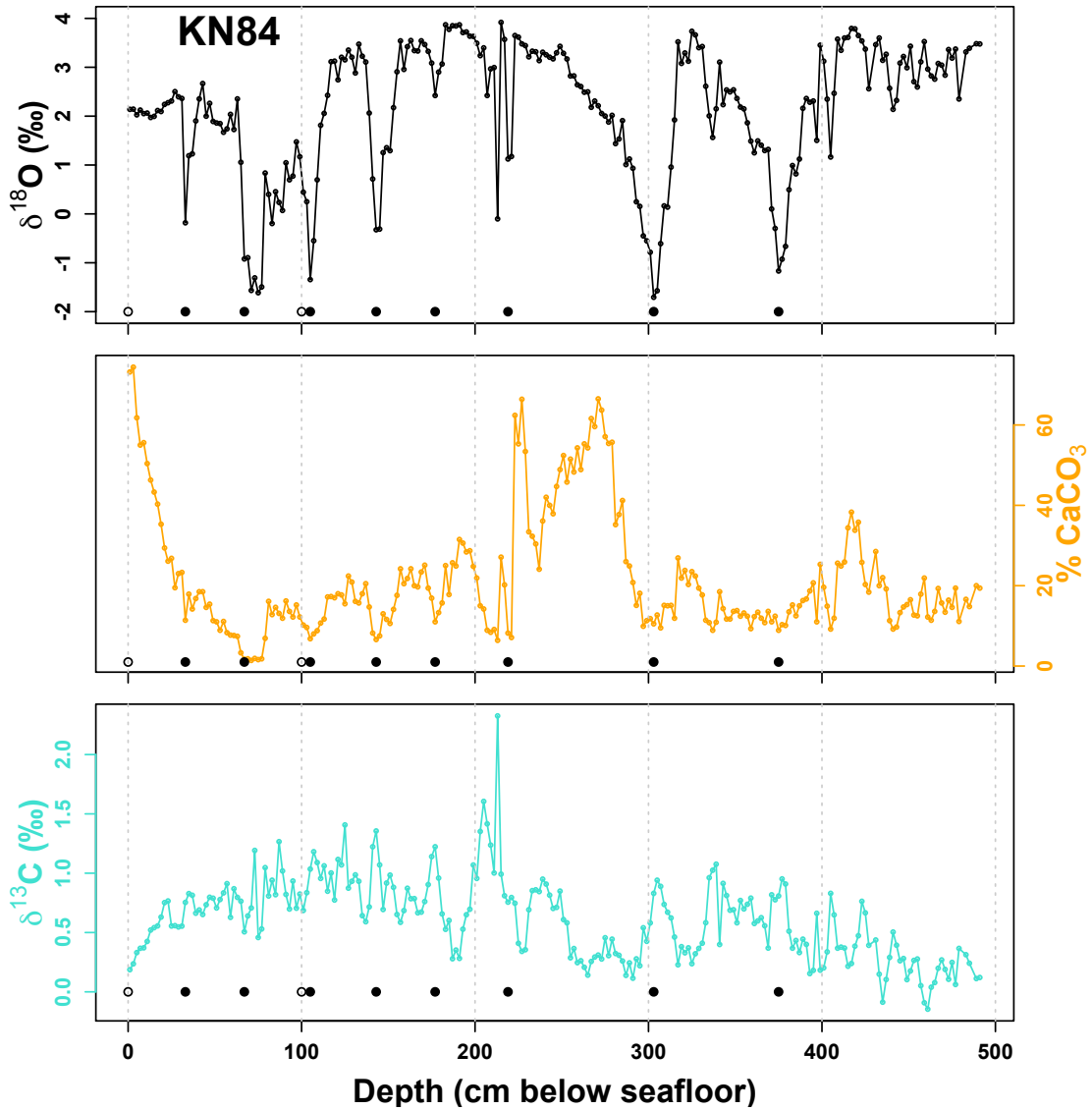


Figure 3.10 $\delta^{18}\text{O}_{\text{bs}}$ (black), %CaCO₃ (orange), and $\delta^{13}\text{C}_{\text{bs}}$ (turquoise) vs. Depth in KN84. Black dots mark the locations of isotope excursions in $\delta^{18}\text{O}_{\text{bs}}$. Open circles mark the location of the two radiocarbon dates (0cmbsf = 3.2ka, 100cmbsf = 29.1ka) [de Menocal, personal communication].

dates, the age of the first two negative $\delta^{18}\text{O}_{\text{bs}}$ excursions (33 and 67-71cmbsf) would be 11.7ka and 20.5-21.6ka. The first excursion likely represents the Younger Dryas, as it is associated with a reversal during the deglacial increase in $\%\text{CaCO}_3$. The second, longer excursion, likely represents the LGM, and is associated with the lowest $\%\text{CaCO}_3$ values and a broad peak in magnetic susceptibility [*de Menocal*, personal communication]. Extrapolating just outside of the dated range, the third excursion, at 105cmbsf, would have an age of 30.4ka. This is close to the age of the third Heinrich event (H3 ~31ka) [*Hemming*, 2004].

This sedimentation rate does not seem to hold for the whole glacial period. Based on a sedimentation rate of 3.9cm/kyr, Termination II would have an age of ~78 ka, much too young, suggesting that sedimentation rate decreased during the glacial period. Therefore, we cannot extrapolate the Holocene sedimentation rate beyond the older of the two dates and cannot determine the ages of the other isotope excursions.

Overall, these excursions are quite rapid and are similar in appearance to the $\delta^{18}\text{O}_{\text{bs}}$ excursions seen in KN42, but they differ in other aspects. In KN42, the excursions in $\delta^{18}\text{O}_{\text{bs}}$ were matched by similar negative excursions in $\delta^{13}\text{C}_{\text{bs}}$, due to the distinctive, light isotopic composition of the detrital end-member. In KN84, the opposite occurs. Negative $\delta^{18}\text{O}_{\text{bs}}$ excursions are associated with maxima in $\delta^{13}\text{C}$. Each excursion is also associated with a clear minimum in $\%\text{CaCO}_3$. In KN42, H3 and H6 were associated with low $\%\text{CaCO}_3$ values, whereas the other Heinrich events had either high or unchanging $\%\text{CaCO}_3$.

A few possibilities exist to explain concurrent negative $\delta^{18}\text{O}_{\text{bs}}$ excursions and $\%\text{CaCO}_3$ minima. First, the $\%\text{CaCO}_3$ minima could be caused by dissolution events

removing carbonate from the deposited sediment. However, this would have to preferentially dissolve away carbonate enriched in $\delta^{18}\text{O}$, while not affecting $\delta^{13}\text{C}$ significantly. A second explanation is that the negative $\delta^{18}\text{O}_{\text{bs}}$ excursions were caused by meltwater pulses. A meltwater pulse with very negative $\delta^{18}\text{O}_{\text{sw}}$ would affect $\delta^{18}\text{O}_{\text{bs}}$ more strongly while leaving $\delta^{13}\text{C}_{\text{bs}}$ mildly affected or unaffected. This does not explain the low $\%\text{CaCO}_3$ accompanying each excursion. All three records could be explained by a flux of icebergs carrying predominantly non-carbonate IRD. The melting of the icebergs could cause more negative biogenic carbonate $\delta^{18}\text{O}$ values without affecting $\delta^{13}\text{C}$. The increase in non-carbonate IRD could drive down $\%\text{CaCO}_3$ to a minimum. Such an event should be recorded by magnetic susceptibility. The magnetic susceptibility record shows intermediate values across the whole glacial period, with a few small peaks at 110, 140, 162, and 180cmbsf, which roughly, but not perfectly, align with the isotope excursions (with the exception of 162cmbsf, which does not have a corresponding isotope excursion). Based on the number of excursions, these cannot represent Dansgaard-Oeschger cycles or Heinrich events. It's possible that they correspond to some Heinrich events and others are missing or unexpressed in this core. If so, the negative $\delta^{18}\text{O}_{\text{bs}}$ could be derived from migration of a $\delta^{18}\text{O}_{\text{sw}}$ anomaly caused by icebergs melting in the IRD belt. Negative excursions in the isotopic composition of foraminifera from this region have previously been attributed to such a traveling $\delta^{18}\text{O}_{\text{seawater}}$ anomaly [Elliot *et al.*, 1998].

EW6 and EW8:

Two cores from cruise EW93-03, EW6 and EW8, are located in the Denmark Strait outlet at a depth of ~2100m. Both are quite long (8 and 13m, respectively), so the deeper portions of the cores likely extend beyond the most recent glacial cycle, and were therefore sampled at lower resolution (deeper than 470 and 610cmbsf respectively). The two cores have many similarities. Both cores show multiple negative excursions in $\delta^{18}\text{O}_{\text{bs}}$ ranging from 1-2‰ up to 6‰ in magnitude, larger in EW6. In addition, both cores have a section of very low %CaCO₃ (denoted by grey bars in Figure 3.11 and 3.12). In these intervals, isotopic measurements become unreliable due to the very low amount of carbonate in the sediment.

The two cores can be correlated using the isotope excursions and coincident changes in %CaCO₃. Similarly to ODP982 and KN84, both cores show a dual-peak maximum in %CaCO₃ around 300-500cmbsf that represents the last interglacial stage (Figure 3.13). The dip in %CaCO₃ in the middle of the interglacial stage is associated with a negative oxygen isotope excursion in both cores (“mid-IG” excursion) (Figure 3.14). Beginning with this correlative excursion, it is possible to work outwards both up- and down-core to correlate other isotope excursions between EW6 and EW8. The mid-IG excursion is bracketed by two smaller excursions. Going deeper in the core, the lower bracketing excursion is followed by a series of three more negative excursions (labeled “a”, “b”, “c” going downwards). Working upwards from upper bracketing excursion, both cores show a W-shaped double-dip excursion (“W”), topped by a segment of very low %CaCO₃. This series of excursions (in order, beginning with the low %CaCO₃ section, they are W, upper bracket, mid-IG, lower bracket, a, b, and c) cover 300-

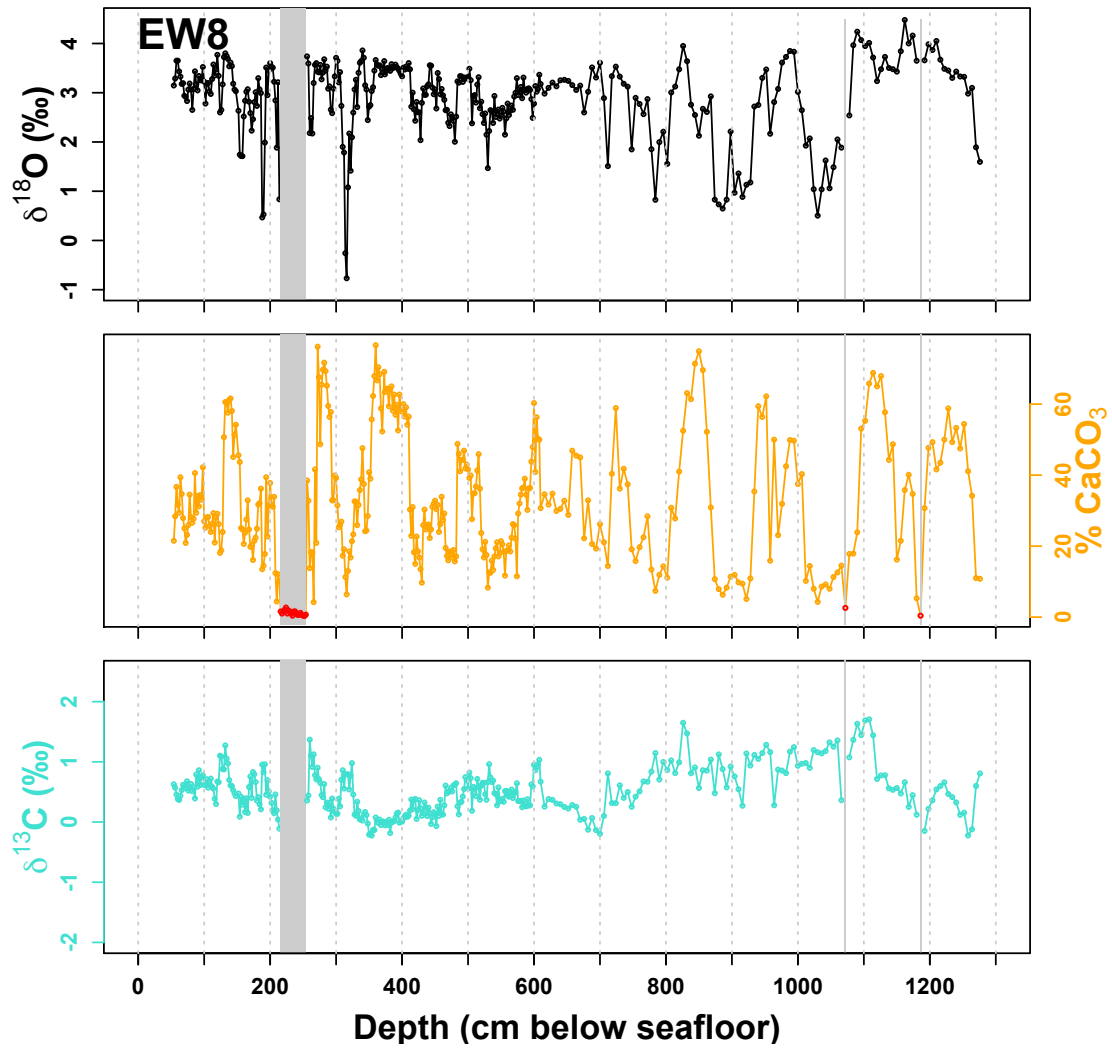


Figure 3.11 $\delta^{18}\text{O}_{\text{bs}}$ (black), % CaCO_3 (orange) and $\delta^{13}\text{C}_{\text{bs}}$ (turquoise) vs. Depth in core EW8. Stable isotope measurements become unreliable when % CaCO_3 is less than ~2-3% (grey bars, red points).

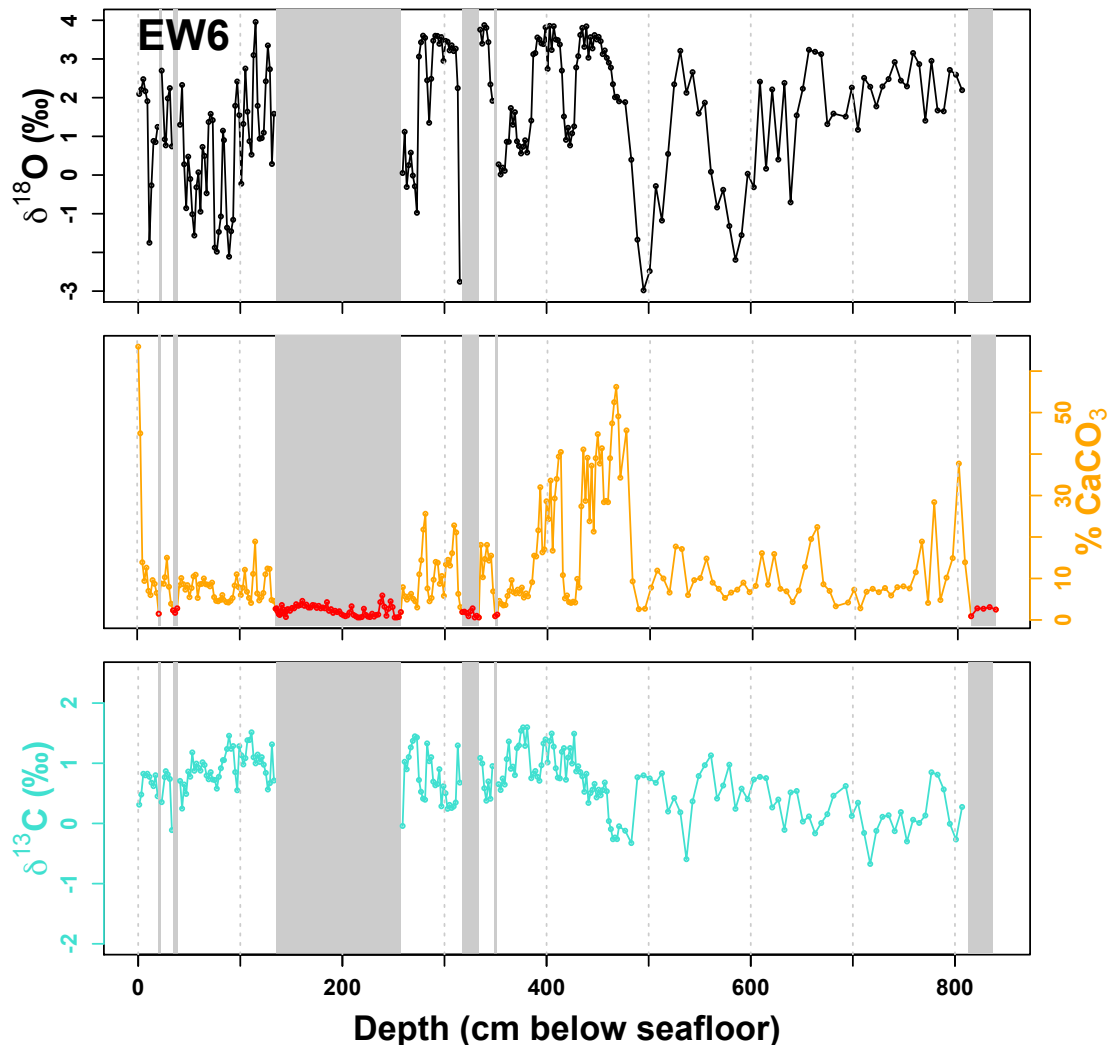


Figure 3.12 $\delta^{18}\text{O}_{\text{bs}}$ (black), %CaCO₃ (orange) and $\delta^{13}\text{C}_{\text{bs}}$ (turquoise) vs. Depth in core EW6. Stable isotope measurements become unreliable when %CaCO₃ is less than ~2-3% (grey bars, red points).

650cmbsf in EW6 and 200-550cmbsf in EW8, suggesting a similar sedimentation rate in the two cores. The deepest three excursions (a, b, and c) occur before Termination II, placing them in the previous glacial phase (MIS6) or earlier. In EW8, %CaCO₃ fluctuates with these three excursions, reaching fairly high levels nearing those of the interglacial period between excursions, suggesting each excursion could be a full glacial/interglacial cycle. However, in EW6 the %CaCO₃ over this interval is similar to glacial values, rather than interglacial values, suggesting the a, b, and c excursions all fall within the previous glacial phase, MIS6.

The top-most 10cm of EW6 record the glacial/interglacial transition, apparent in the rapid rise in %CaCO₃ from ~10% to >60%. EW8 does not record the Termination I. It is likely missing from the top of the core. Because Termination I is not recorded in EW8, the upper boundary of the core must be within the glacial phase (MIS2-4). EW6 records two periods of low %CaCO₃, a shorter and longer period, whereas EW8 only records one shorter period. From the correlations suggested above, we have aligned the two short periods of low %CaCO₃ as the same event. This means that the longer period of low %CaCO₃ seen in EW6 is missing from EW8, potentially also lost off the top of the core. This further restricts the age of the upper 200cm of EW8 as within the early glacial period. Some small fluctuations in $\delta^{18}\text{O}_{\text{bs}}$ can be seen in the top portion of EW8 (54-200cmbsf) that may correspond to similar fluctuations seen between the two low %CaCO₃ zones in EW6.

In the earliest portion of EW6 (1-140cmbsf), $\delta^{18}\text{O}_{\text{bs}}$ fluctuates many times between ~2‰ and -1 or -2‰ (Figure 3.15). These fluctuations fall within the late glacial, up to and including the LGM. They are rapid and large (3-5‰) and many of them are

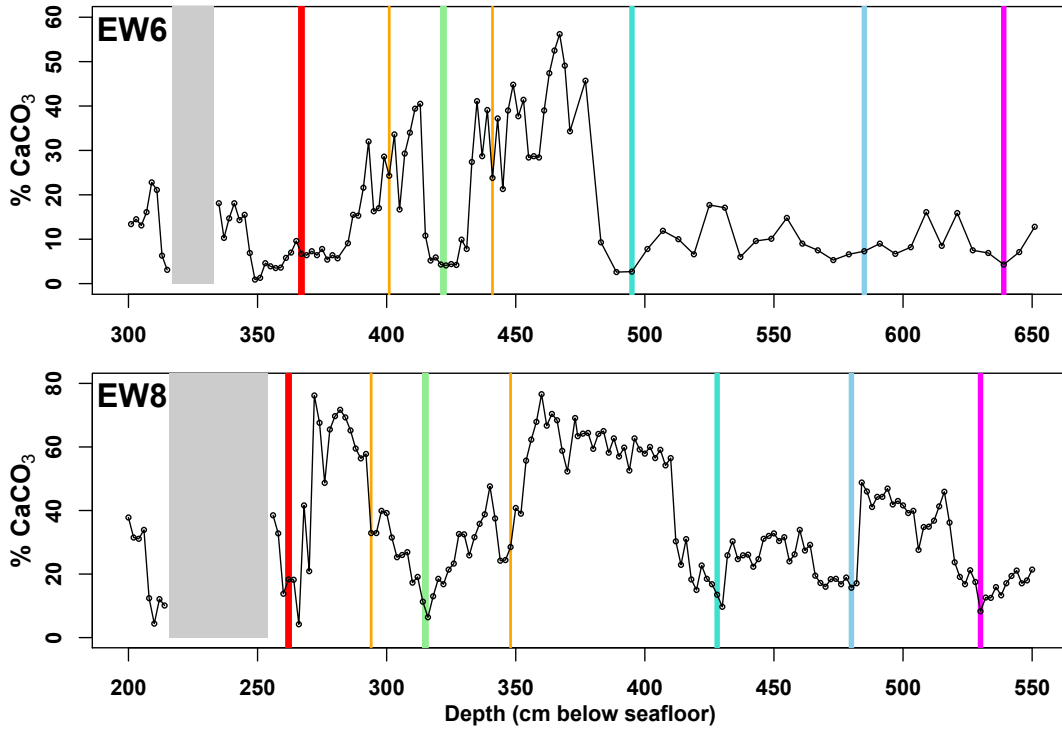


Figure 3.13 %CaCO₃ vs. Depth in cores EW6 (top) and EW8 (bottom) showing correlative negative isotope excursions. Depths of negative excursions marked by colored bars. W=red, bracket excursions = orange, mid-IG = light green, a = turquoise, b = light blue, c = magenta.

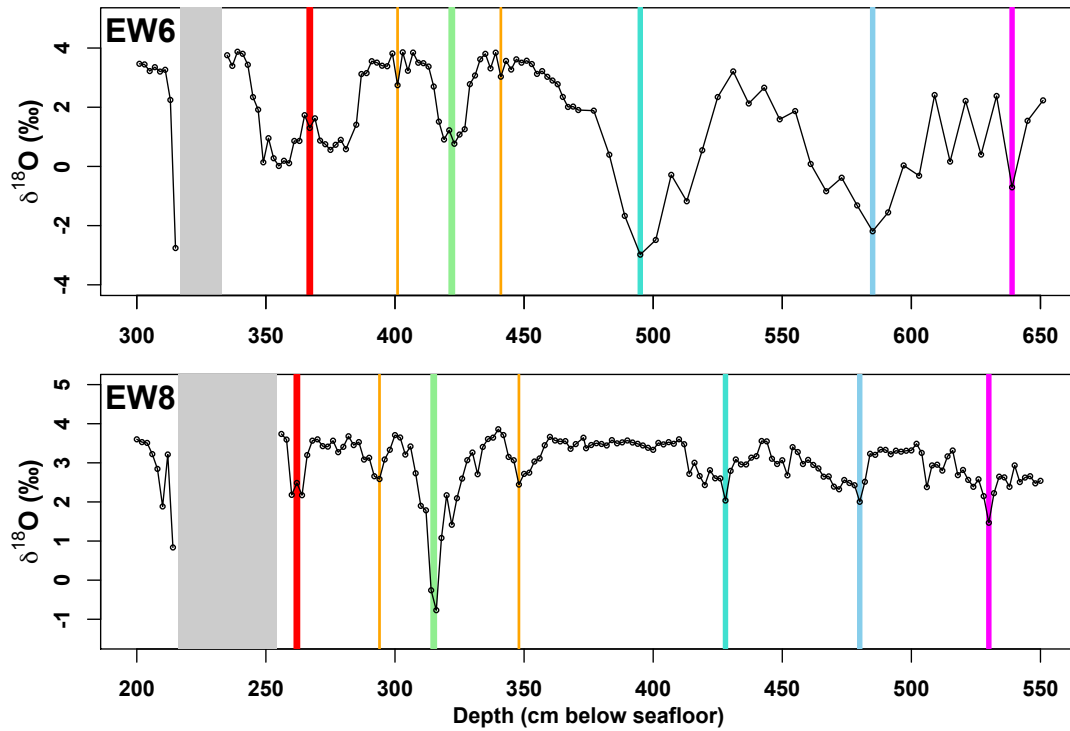


Figure 3.14 $\delta^{18}\text{O}_{\text{bs}}$ vs. Depth in cores EW6 (top) and EW8 (bottom) showing correlative negative isotope excursions. Depths of negative excursions (colored bars) defined in Figure 3.13.

associated with minima in %CaCO₃. The correlation between negative $\delta^{18}\text{O}_{\text{bs}}$, low %CaCO₃, and no change in $\delta^{13}\text{C}_{\text{bs}}$ is similar to the character of excursions in KN84. This suggests periodic influxes of meltwater and non-carbonate IRD. It's possible that these rapid fluctuations in $\delta^{18}\text{O}_{\text{bs}}$ could represent the Dansgaard-Oeschger cycles, based on their timing and number.

Overall, EW6 and EW8 show multiple negative spikes in $\delta^{18}\text{O}_{\text{bs}}$. Much of the most recent glacial period has very low %CaCO₃ and is therefore unusable. The previous glacial period has higher %CaCO₃ and also records excursions. To gain insight into the origin of these excursions, we can look at different components of the sediment such as specific size fractions and the biogenic end-member.

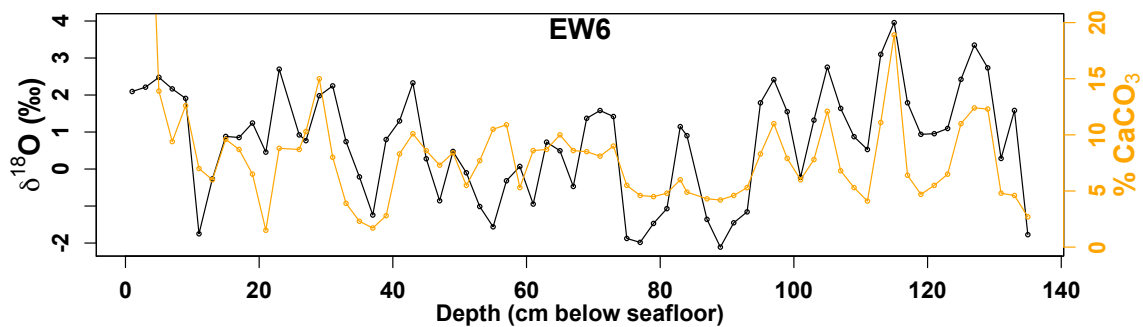


Figure 3.15 $\delta^{18}\text{O}_{\text{bs}}$ (black) and %CaCO₃ (orange) over the first 140cm of EW6, showing many fluctuations in $\delta^{18}\text{O}_{\text{bs}}$, 3-5‰ in magnitude, often correlating to changes in %CaCO₃.

3.5 Results – Sieved Size Fractions

To determine the origin of the isotope excursions and changes in %CaCO₃, sediment samples from the interval spanning the mid-IG through c excursions were sieved into distinct size fractions (see section 3.3.2). The carbonate component in the fine

fraction (particles smaller than 63 μm in size) includes fine carbonate dust, coccoliths, and possibly fragments of foraminifera. The “medium” fraction (63-150 μm) includes smaller IRD as well as many foraminifera. The “large” (150-250 μm) and “coarse” (>250 μm) fractions should include larger IRD and larger foraminifera.

In EW6, $\delta^{18}\text{O}_{\text{fine}}$ and $\delta^{18}\text{O}_{\text{med}}$ track $\delta^{18}\text{O}_{\text{bs}}$ quite closely (Figure 3.16). $\delta^{18}\text{O}_{\text{fine}}$ is sometimes 1-2‰ lower than $\delta^{18}\text{O}_{\text{bs}}$, especially in during some of the negative isotope excursions (mid-IG, b, and c). $\delta^{18}\text{O}_{\text{med}}$ is generally intermediate between $\delta^{18}\text{O}_{\text{fine}}$ and $\delta^{18}\text{O}_{\text{bs}}$. The carbonate content in these size fractions ($\%\text{CaCO}_3\text{-fine}$ and $\%\text{CaCO}_3\text{-med}$) also closely tracks the bulk sediment $\%\text{CaCO}_3$ (Figure 3.16). There is no relation between the isotope excursions and changes in wt. % in any of the size fractions. Most of the mass in the bulk sediment is in the fine fraction (40-60%). All size fractions seem to respond together. If IRD input was causing the isotope excursions, the weight % in the larger size fractions (>63 μm , the threshold definition for IRD) should increase relative to the fine fraction. This is not observed. However, icebergs can carry sediment of all size classes, so the fine fraction may also have been affected, resulting in no change in the relative weight percents.

The same parameters were measured in EW8 over a similar interval. As in EW6, $\delta^{18}\text{O}_{\text{fine}}$ and $\delta^{18}\text{O}_{\text{med}}$ track $\delta^{18}\text{O}_{\text{bs}}$ through all four major isotope excursions (mid-IG, a, b, c), although the magnitude of the excursions differs (Figure 3.17). $\delta^{18}\text{O}_{\text{fine}}$ reaches much more negative values than the bulk sediment, and in three out of four excursions hits a lower bound around -2‰. $\delta^{18}\text{O}_{\text{med}}$ is again intermediate between $\delta^{18}\text{O}_{\text{bs}}$ and $\delta^{18}\text{O}_{\text{fine}}$.

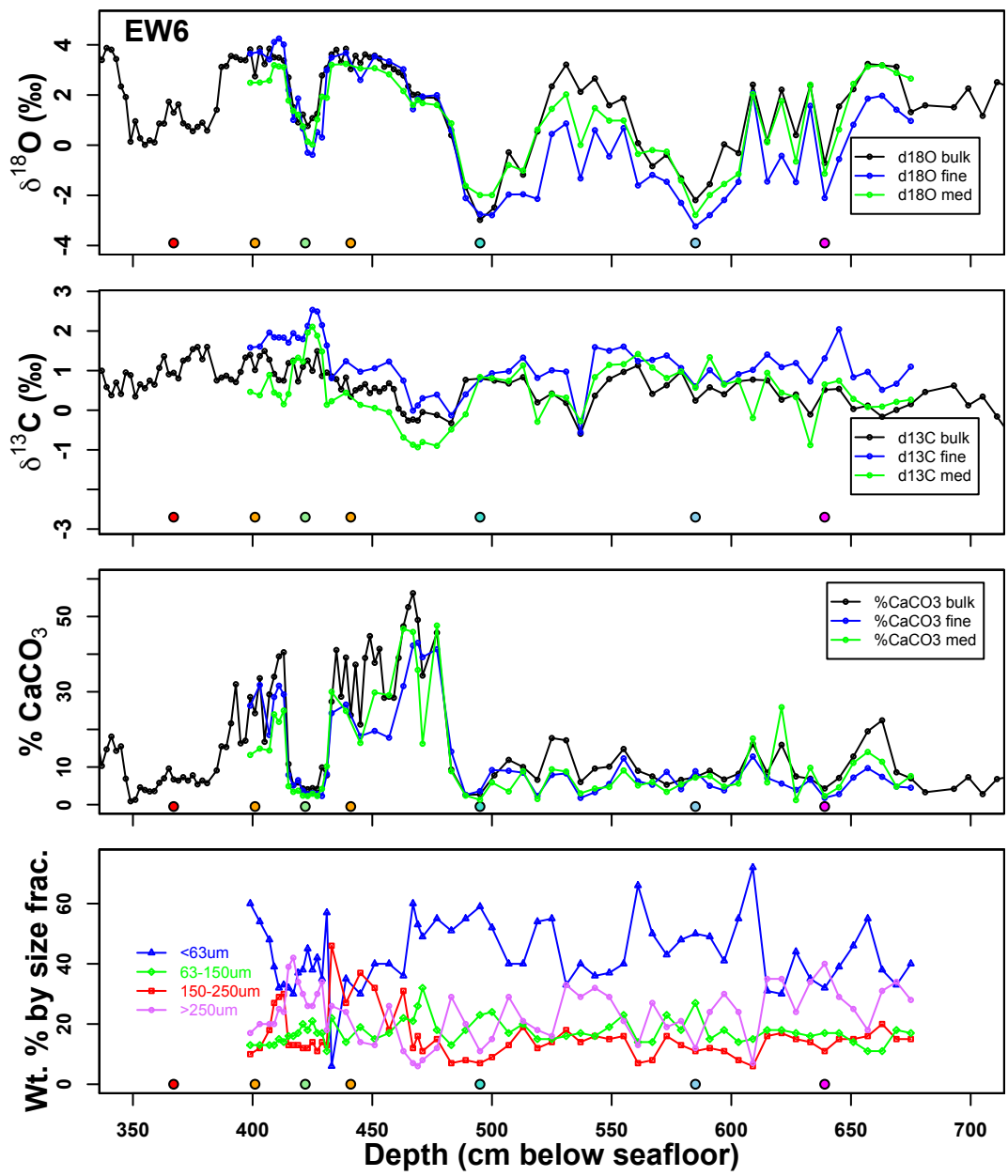


Figure 3.16 $\delta^{18}\text{O}_{\text{bs}}$, $\delta^{13}\text{C}_{\text{bs}}$, and $\% \text{CaCO}_3$ vs. Depth for bulk sediment, fine ($<63\mu\text{m}$) and medium (63-150 μm) size fraction in EW6. Weight % in each size fraction vs. Depth (bottom). Colored dots represent the depths of negative excursions in $\delta^{18}\text{O}_{\text{bs}}$, as shown in Figure 3.14.

Interestingly, the bracketing excursions (orange dots) are not tracked in $\delta^{18}\text{O}_{\text{fine}}$ and $\delta^{18}\text{O}_{\text{med}}$, but this may be due to a sampling bias.

The size-fraction separated $\% \text{CaCO}_3$ measurements also track bulk sediment $\% \text{CaCO}_3$, but not as closely as in EW6. In general $\% \text{CaCO}_{3\text{-fine}}$ and $\% \text{CaCO}_{3\text{-med}}$ are lower than the bulk sediment $\% \text{CaCO}_3$, implying that much of the carbonate in the bulk sediment occurs in the two largest size fractions ($>150\mu\text{m}$). This is especially true during the first part of the interglacial phase (350-420cmbsf). In this interval, the majority of the sediment weight comes from the smallest size fraction, which only has $\sim 20\%$ carbonate, while the bulk sediment has $\sim 60\%$. The mass balance would imply an impossibly high carbonate content in the larger two size classes ($>100\%$). It's possible that some of the carbonate material in the fine and medium size fractions was dolomite, and did not react enough during the 6-8 minute reaction time. In the bulk sediment measurement, the material was powdered using a mortar and pestle before analysis, which would have made dolomite more reactive.

Unlike in EW6, a consistent pattern of increased wt. $\%_{\text{large}}$ (150-250 μm) occurs across all four of the negative $\delta^{18}\text{O}_{\text{bs}}$ excursions scanned. This is at the expense of the fine fraction, which shows a decrease. The percent by mass of the medium and coarse fractions do not change much across excursions. The carbonate in the 150-250 μm size fraction consists mainly of foraminifera, with some contribution of IRD. If these negative excursions were driven by increased influx of IRD, both the large and coarse fractions would be expected to show increased contribution during excursions, whereas only an increase in the large fraction is observed.

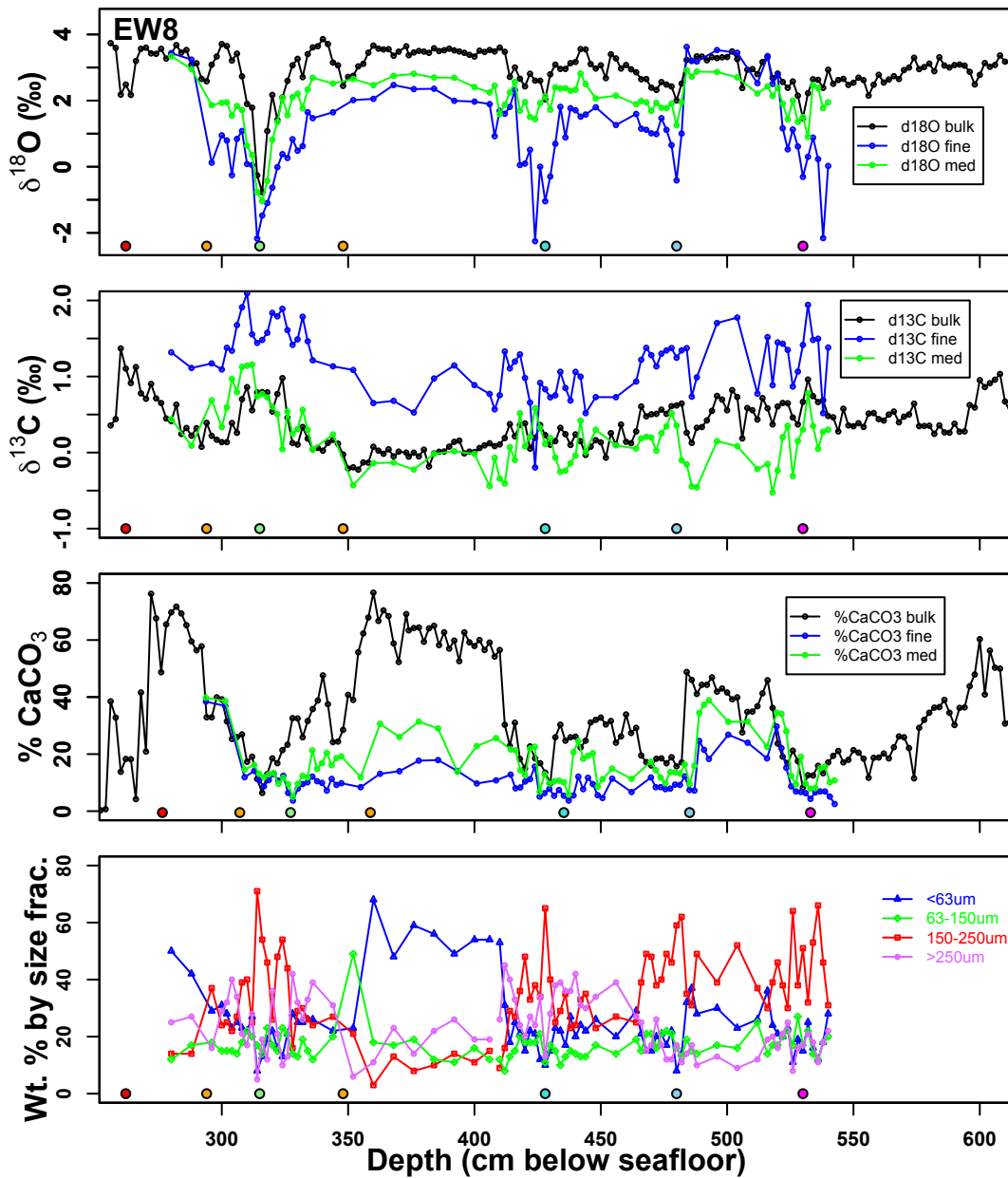


Figure 3.17 $\delta^{18}\text{O}_{\text{bs}}$, $\delta^{13}\text{C}_{\text{bs}}$, and % CaCO_3 vs. Depth for bulk sediment, fine (<63µm) and medium (63-150µm) size fraction in EW8. Weight % in each size fraction vs. Depth (bottom). Colored dots represent the depths of negative excursions in $\delta^{18}\text{O}_{\text{bs}}$, as shown in Figure 3.14.

It's possible that a change in the relative contribution of foraminifera vs. IRD without any change in the end-member values of each could be causing the excursion. Another possibility is that the meltwater pulse decreases $\delta^{18}\text{O}_{\text{sw}}$, changing the composition of the foraminifera while at the same time increasing their prevalence. In order to separate these and other scenarios, the isotopic composition of the biogenic carbonate (foraminifera) end-member must be measured.

3.6 Results – Planktonic Foraminifera

The high-latitude planktonic foraminifera *N. pachyderma* (sinistral) was picked from four intervals across the negative excursions a, b, c, and mid-IG in core EW8. $\delta^{18}\text{O}_{\text{Nps}}$ is generally around 4‰ during this period. Given a range in $\delta^{18}\text{O}_{\text{sw}}$ of 0 to 1‰, this is consistent with temperatures of -2°C to 2°C, in agreement with expected near-freezing temperatures at this latitude. $\delta^{18}\text{O}_{\text{Nps}}$ is heavy relative to $\delta^{18}\text{O}_{\text{bs}}$, $\delta^{18}\text{O}_{\text{fine}}$, and $\delta^{18}\text{O}_{\text{med}}$.

Across excursions a and b, there is essentially no change in $\delta^{18}\text{O}_{\text{Nps}}$, whereas across excursion c, $\delta^{18}\text{O}_{\text{Nps}}$ decreases monotonically by ~1‰. Across the mid-IG excursion, $\delta^{18}\text{O}_{\text{Nps}}$ fluctuates around 4‰ and ends at 4.5‰ post-excursion. $\delta^{13}\text{C}_{\text{Nps}}$ is generally around 0-0.5‰ and is invariant across individual excursions. During the mid-IG excursion, $\delta^{13}\text{C}_{\text{Nps}}$ values are lower around -0.5‰, but are still relatively constant. The small amount of variability in $\delta^{18}\text{O}_{\text{Nps}}$ across these excursions is not enough to explain the magnitude of the excursion.

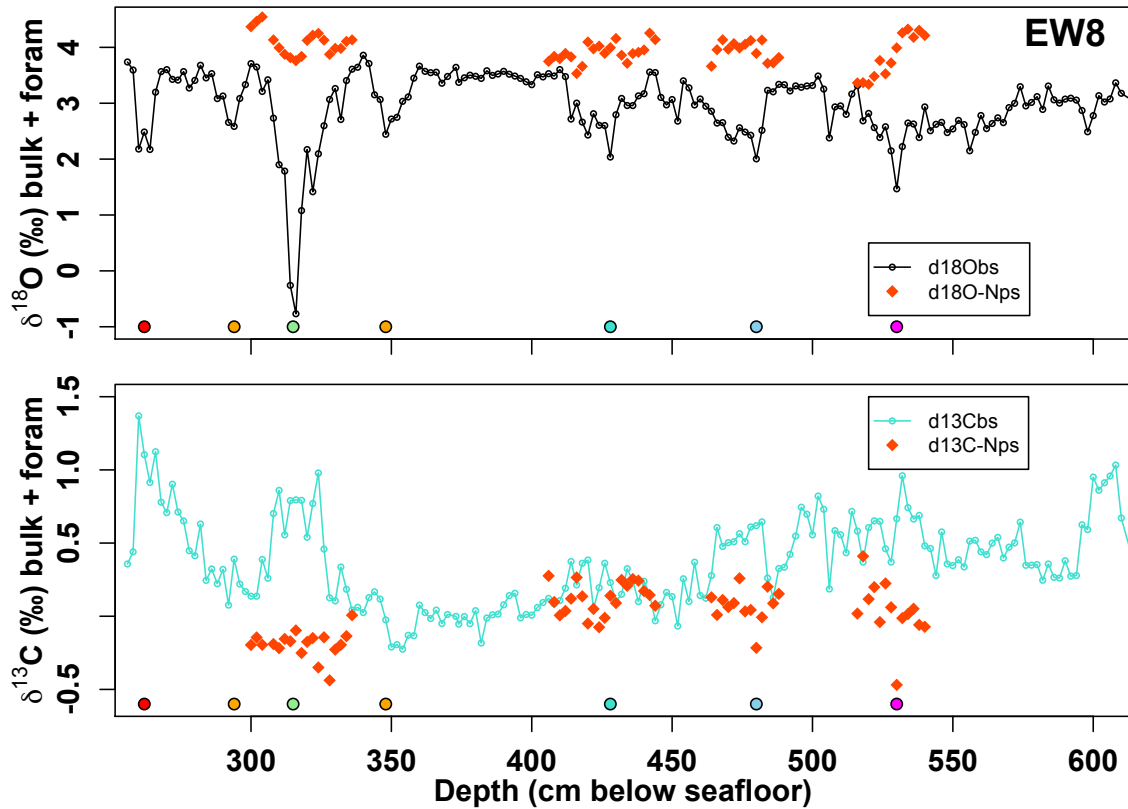


Figure 3.18 $\delta^{18}\text{O}_{\text{bs}}$ (black) and $\delta^{13}\text{C}_{\text{bs}}$ (turquoise) vs. Depth for EW8 across 4 isotope excursions (mid-IG, a, b, and c). $\delta^{18}\text{O}_{\text{Nps}}$ and $\delta^{13}\text{C}_{\text{Nps}}$ shown in red diamonds. Colored dots mark the location of negative isotope excursions in $\delta^{18}\text{O}_{\text{bs}}$, as defined in text.

If a change in temperature occurred during these intervals, the foraminifera do not record it. Either there was no change in temperature, or there was an equal and opposite change in $\delta^{18}\text{O}_{\text{sw}}$. Another possibility is that the detrital carbonate end-member changed composition, bringing in much more depleted carbonate, while the foraminifera remained unchanged. In order for IRD to appear, there must be melt-water from the melting icebergs. This suggests that $\delta^{18}\text{O}_{\text{sw}}$ may have decreased. In order for foraminifera to show no change in $\delta^{18}\text{O}_{\text{Nps}}$, a 0.5‰ decrease in $\delta^{18}\text{O}_{\text{sw}}$ must be accompanied by a 2-3 degree cooling. Based on the temperature from $\delta^{18}\text{O}_{\text{Nps}}$, based on a $\delta^{18}\text{O}_{\text{sw}}$ value of 0 to 1‰, seawater could have cooled a maximum of $\sim 4^{\circ}\text{C}$, which would have caused a $\sim 1\%$

increase in $\delta^{18}\text{O}_{\text{Nps}}$. Since no such change is observed in $\delta^{18}\text{O}_{\text{Nps}}$, $\delta^{18}\text{O}_{\text{sw}}$ must have decreased by 1‰. The magnitude of the excursions (up to 5‰) is much larger than this, meaning changes in $\delta^{18}\text{O}_{\text{sw}}$ could not explain the isotope excursions, given the foraminifera data. This points to an input of isotopically light carbonate material, likely IRD, that affects all size-classes during the excursion intervals. Heinrich-like events have been observed in previous glacial periods [Hodell *et al.*, 2008]. These observed excursions in

3.7 Conclusions

We studied 10 sediment cores from the North Atlantic in search of evidence of ice-rafting events occurring in time with Dansgaard-Oeschger cycles. The farthest south core, KN42 showed clear IRD signals corresponding to the Heinrich events, and potential evidence of DO variability in the %CaCO₃ record. Moving northward, many of our cores had slower sedimentation rates, therefore covering a longer time interval, often including the previous interglacial and beyond. In KN55, KN84, EW6 and EW8, we identified the previous interglacial period based on increased %CaCO₃ levels, and the double-dip structure. In three cores from the outlet of the Denmark Strait, we identified multiple negative excursions in $\delta^{18}\text{O}_{\text{bs}}$ within the most recent and the previous glacial periods. We measured the isotopic composition and weight percent of different sieved size fractions to determine which size class was causing the excursions. In general, all size fractions tracked the bulk sediment record in $\delta^{18}\text{O}$ and %CaCO₃. In EW8 there was an increase in the weight percent in the 150-250 μm size fraction across negative excursions in $\delta^{18}\text{O}_{\text{bs}}$.

We picked the polar planktonic foraminifera *N. pachyderma* (*s*) to isolate changing temperature and $\delta^{18}\text{O}_{\text{sw}}$ effects from variable input of IRD and discovered that the excursions were not caused by changing biogenic carbonate composition, suggesting IRD pulses as the origin, potentially containing dolomite.

Acknowledgements

This work was made possible through collaborations with P. de Menocal, and others at the Core Repository at the Lamont-Doherty Earth Observatory. J. Shakun is thanked for instruction on picking foraminifera. G. Eischeid and V. Shen are thanked for laboratory assistance.

References

- Andresen, C. S., G. Bond, A. Kuijpers, P. C. Knutz, and S. Bjorck (2005), Holocene climate variability at multidecadal time scales detected by sedimentological indicators in a shelf core NW off Iceland, *Marine Geology*, 214(4), 323-338.
- Bard, E., M. Arnold, J. Mangerud, M. Paterne, L. Labeyrie, J. Duprat, M-A. Melieres, E. Sonstegaard, and J-C. Duplessy (1994), The North Atlantic atmosphere-sea surface ^{14}C gradient during the Younger Dryas climatic event, *Earth and Planetary Science Letters*, 126, 175-187.
- Bond, G., W. Broecker, S. Johnsen, J. McManus, L. Labeyrie, J. Jouzel, and G. Bonani (1993), Correlations between climate records from North Atlantic sediments and Greenland ice, *Nature*, 365, 143-147.
- Bond, G., H. Heinrich, W. Broecker, L. Labeyrie, J. McManus, J. Andrews, S. Huon, R. Jantschik, S. Clasen, C. Simet, K. Tedesco, M. Klas, G. Bonani, and S. Ivy (1992), Evidence for massive discharges of icebergs into the North Atlantic ocean during the last glacial period, *Nature*, 360(6401), 245-249.

- Bond, G. C. and R. Lotti (1995), Iceberg Discharges into the North Atlantic on Millennial Time Scales During the Last Glaciation, *Science*, 267(5200), 1005-1010.
- Dansgaard, W., S. J. Johnsen, H. B. Clausen, D. Dahl-Jensen, N. S. Gundestrup, C. U. Hammer, C. S. Hvidberg, J. P. Steffensen, A. Sveinbjörnsdóttir, J. Jouzel and G. Bond (1993), Evidence for general instability of past climate from a 250-kyr ice-core record, *Nature*, 364, 218-220.
- Dokken, T. M., and E. Jansen (1999), Rapid changes in the mechanism of ocean convection during the last glacial period, *Nature*, 401(6752), 458-461.
- Elliot, M., L. Labeyrie, G. Bond, E. Cortijo, J.-L. Turon, N. Tisnerat and J.-C. Duplessy (1998), Millennial-Scale Iceberg Discharges in the Irminger Basin During the Last Glacial Period: Relationship with the Heinrich Events and Environmental Settings, *Paleoceanography*, 13(5), 433-446.
- Elliot, M., L. Labeyrie and J.-C. Duplessy (2002), Changes in North Atlantic deep-water formation associated with the Dansgaard-Oeschger temperature oscillations (60-10ka), *Quaternary Science Reviews*, 21(10), 1153-1165.
- Fairbanks, R. G., R. A. Mortlock, T.-Z. Chiu, L. Cao, A. Kaplan, T. P. Guilderson, T. W. Fairbanks, and A. L. Bloom (2005), Marine Radiocarbon Calibration Curve Spanning 0 to 50,000 years B.P. Based on Paired $^{230}\text{Th}/^{234}\text{U}/^{238}\text{U}$ and ^{14}C Dates on Pristine Corals, *Quaternary Science Reviews*, 24, 1781-1796.
- Hemming, S. R. (2004), Heinrich events: Massive late Pleistocene detritus layers of the North Atlantic and their global climate imprint, *Review of Geophysics*, 42(1), RG1005.
- Hodell, D. A. and J. H. Curtis (2008), Oxygen and carbon isotopes of detrital carbonate in North Atlantic Heinrich Events, *Marine Geology*, 256(1-4), 30-35.
- Hodell, D. A., J. E. T. Channell, J. H. Curtis, O. E. Romero, and U. Ruhl (2008), Onset of "Hudson Strait" Heinrich events in the eastern North Atlantic at the end of the middle Pleistocene transition (~640ka)?, *Paleoceanography*, 23(4), PA4218.
- IMLGS database, Curators of Marine and Lacustrine Geological Samples Consortium: Index to Marine and Lacustrine Geological Samples, National Geophysical Data Center, NOAA, doi: 10.7289/V5H41PB8.
- Grootes, P. M., M. Stuiver, J. W. C. White, S. Johnsen and J. Jouzel (1993), Comparison of oxygen isotope records from the GISP2 and GRIP Greenland ice cores, *Nature*, 366(6455), 552-554.
- Johnsen, S. J., H. B. Clausen, W. Dansgaard, K. Fuhrer, N. Gundestrup, C. U. Hammer, P. Iversen, J. Jouzel, B. Stauffer and J. P. Steffensen (1992), Irregular glacial

- interstadials recorded in a new Greenland ice core, *Nature*, 359(6393), 311-313.
- Rashid, H., R. Hesse, and D. J. W. Piper (2003), Evidence for an additional Heinrich event between H5 and H6 in the Labrador Sea, *Paleoceanography*, 18(4), 1077.
- Rasmussen, T. L., D. W. Oppo, E. Thomsen and S. J. Lehman (2003), Deep sea records from the southeast Labrador Sea: Ocean circulation changes and ice-rafting events during the last 160,000 years, *Paleoceanography*, 18(1), 1018.
- Rasmussen, T. L., E. Thomsen, T. C. E. van Weering and L. Labeyrie (1996), Rapid Changes in Surface and Deep Water Conditions at the Faeroe Margin During the Last 58,000 Years, *Paleoceanography*, 11(6), 757-771.
- Ruddiman, W. F. (1977), Late Quaternary deposition of ice-rafted sand in the subpolar North Atlantic (lat 40° to 65°N), *Geological Society of America Bulletin*, 88, 1813-1827.
- Ruddiman, W. F. (1992), Calcium Carbonate Database. IGBP PAGES/World Data Center – A for Paleoclimatology Data Contribution Series # 92-001, NOAA/NGDC Paleoclimatology Program, Boulder, CO, USA.
- van Kreveld, S., M. Sarnthein, H. Erlenkeuser, P. Grootes, S. Jung, M. J. Nadeau, U. Pflaumann and A. Voelker (2000), Potential links between surging ice sheets, circulation changes, and the Dansgaard-Oeschger cycles in the Irminger Sea, 60-18 kyr, *Paleoceanography*, 15(4), 425-442.
- Voelker, A. H. L., M. Sarnthein, P. M. Grootes, H. Erlenkeuser, C. Laj, A. Mazaud, M. J. Nadeau and M. Schleicher (1998), Correlation of marine C-14 ages from the Nordic Seas with the GISP2 isotope record: Implications for C-14 calibration beyond 25 ka BP, *Radiocarbon*, 40(1).
- Venz, K. A., D. A. Hodell, C. Stanton, and D. A. Warnke (1999), A 1.0 Myr record of Glacial North Atlantic Intermediate Water variability from ODP site 982 in the northeast Atlantic, *Paleoceanography*, 14(1), 42-52.

Chapter 4. Clumped isotope measurements of small (1mg) carbonate samples using a high-efficiency dual-reservoir technique

[Petersen, S. V. and Schrag, D. P. (2014) Clumped isotope measurements of small carbonate samples using a high-efficiency dual-reservoir technique. Rapid Communications in Mass Spectrometry, accepted]

ABSTRACT

The measurement of multiply-substituted isotopologues of CO₂ derived from carbonate has allowed for the reconstruction of paleotemperatures from a single phase (CaCO₃), circumventing uncertainty inherent in other isotopic paleothermometers. Current analytical techniques require relatively large amounts of carbonate (5-8mg per replicate), which limits the applicability of the clumped isotope proxy to certain geological materials such as marine microfossils, commonly used for paleoclimate reconstructions. Clumped isotope measurements of small samples were made on a new, high-efficiency, dual-reservoir sample preparation inlet system attached to a Thermo-Finnegan MAT 253 mass spectrometer. Sample gas produced on the inlet is introduced from a 10mL reservoir directly into the source via a capillary. Reference gas fills an identical 10mL reservoir installed between the reference bellows and capillary. Gas pressures in both reservoirs are initially balanced, and are allowed to decrease together over the run. Carbonate samples from 1mg to 2.6mg produced Δ_{47} values equivalent to

the traditional two-bellows method with identical single-sample precision (1 SE = 0.005-0.015‰) and external standard error (SE = 0.006-0.015‰, n=4-6). The size of sample needed to achieve good precision is controlled by the sensitivity of the mass spectrometer and the size of the fixed reservoirs and adjacent U-trap installed on our inlet. Our demonstration of high-precision clumped isotope measurements of small aliquots of carbonate allows for the application of this proxy to a wider range of geological sample materials, such as marine microfossils, that until now have been near-impossible given sample size limitation.

4.1 Introduction

The measurement of multiply-substituted isotopologues of CO₂ derived from carbonate materials has allowed for the reconstruction of paleotemperatures in a variety of geologic settings. By deriving a temperature from a single phase (CaCO₃), the clumped isotope paleothermometer circumvents the uncertainty inherent to traditional paleothermometers that require information about the isotopic composition of additional phases (H₂O). The carbonate clumped isotope paleothermometer is based on the temperature-dependent ordering of the heavy isotopes ¹³C and ¹⁸O within the carbonate lattice [Eiler, 2011]. At colder temperatures, these heavy isotopes “clump” to produce mass-63 CaCO₃ (Ca¹³C¹⁸O¹⁶O₂) at a level above that expected by a random (stochastic) distribution of these isotopes. When the carbonate is converted to CO₂ via acid digestion, this mass-63 anomaly manifests itself as excess mass-47 CO₂, denoted by the quantity Δ₄₇ (Equation 4.1) [Eiler, 2011]. A Δ₄₇ value of zero indicates a fully random distribution of

isotopes. Over normal Earth surface temperatures, Δ_{47} varies between about 0.55 and 0.8 in the absolute reference frame [Dennis *et al.*, 2011]. Equation 4.1 defines Δ_{47} where the $R^x = {}^x\text{CO}_2/{}^{44}\text{CO}_2$ and R^{x*} is the corresponding stochastic distribution ratio.

$$\Delta_{47} = \left[\left(\frac{R^{47}}{R^{47*}} - 1 \right) - \left(\frac{R^{46}}{R^{46*}} - 1 \right) - \left(\frac{R^{45}}{R^{45*}} - 1 \right) \right] * 1000 \quad [\text{Eq. 4.1}]$$

The temperature dependence of Δ_{47} has been demonstrated for a variety of carbonate materials including synthetic, biogenic, and inorganic carbonates [Eiler, 2011; Ghosh *et al.*, 2006a; Dennis and Schrag, 2010], as well as by theoretical calculations [Schauble *et al.*, 2006; Guo *et al.*, 2009]. Although this is still a new proxy, researchers have already used it to determine paleo-altitude of growing mountains [Ghosh *et al.*, 2006b], reconstruct hydrological and ecological conditions in Africa during the time of early humans [Passey *et al.*, 2010], and measure the body temperature of dinosaurs [Eagle *et al.*, 2011], along with many other applications.

Traditional mass spectrometry practices used to measure stable isotopes ($\delta^{18}\text{O}$ and $\delta^{13}\text{C}$) require micrograms of carbonate material for a single measurement. This facilitates the creation of high-resolution records made up of many measurements of small (<1mg) carbonate samples such as foraminifera. In comparison, the clumped isotope technique requires 5-15mg of carbonate per replicate [Ghosh *et al.*, 2006a], limiting the possible applications of this proxy. In a few cases, this sample size limit has been reduced. Zaarur *et al.* [2011] adjusted the capillary cross section and flow rate and installed a new bellows potentiometer, and were able to measure samples of 3-4mg per replicate. Using a Kiel

device to measure tiny aliquots of carbonate (0.2mg) for a few minutes each and averaging the data from 6-10 aliquots (equivalent to 1.2-2mg), *Schmid and Bernasconi* [2010] were able to calculate a Δ_{47} value with a precision of 0.015-0.040‰ (1 SE), while at the same time producing a high-resolution stable isotope record. By averaging together 5-13 of these runs (equivalent to 6-26mg), they were able to achieve an external precision of 0.005-0.010‰ (1 SE). The total mass of carbonate required for this is similar to ~4 replicates at 3-4mg (equivalent to 12-16mg), and both methods are an improvement over traditional sample requirements (>24mg for 3 replicates) [*Ghosh et al.*, 2006a]. *Meckler et al.* [2014] showed that with additional corrections, an external error of 0.007-0.009‰ (1 SE) could be achieved with 4.5-6mg of total sample.

The clumped isotope proxy has the potential to be very useful in the field of paleoceanography due to its ability to separate the influences of temperature and the isotopic composition of seawater on $\delta^{18}\text{O}$ of marine carbonates [*Eiler*, 2011]. Foraminifera, a commonly used sample material for paleoceanographic studies, have been shown to follow the same temperature- Δ_{47} relationship as other biogenic carbonates [*Tripati et al.*, 2010; *Grauel et al.*, 2013]. However, current analytical techniques make it difficult to acquire enough sample material for replicate analysis of foraminifera due to their small size. A few studies have successfully measured the clumped isotope composition of foraminifera using the traditional large-sample methods [*Tripati et al.*, 2010; *Tripati et al.*, 2014] and the Kiel device method described above [*Grauel et al.*, 2013]. New methods to reduce sample size requirements will make this proxy more widely accessible as a tool for paleoceanography.

Here we present a new method of measuring individual aliquots as small as 1 mg. A high-efficiency dual-reservoir inlet system allows analysis of smaller samples by reducing the “wasted” gas left remaining in the bellows and the sample vial. Gas pressures decrease slowly from a fixed-volume sample reservoir and from an identical reference reservoir installed between the reference bellows and the change-over block. In this study we test the sample size limit of this inlet configuration by measuring carbonate standards from 1.0mg to 2.6mg and demonstrate internal precision of 0.005-0.015‰ (1 SE) and external standard error of 0.006-0.015‰ (1 SE) for 4-6 replicates, in line with the traditional dual-bellows configuration (1 SE = 0.002-0.018‰) [*Dennis and Schrag, 2010; Zaarur et al., 2011; Wacker et al., 2013; Thiagarajan et al., 2011*]

4.2 Methods and Materials

4.2.1 Standard materials

To calibrate the newly constructed sample-preparation inlet, carbonate standards of known composition were measured repeatedly at a range of sizes. Two high-temperature carbonates (CM2, NBS19) with similar Δ_{47} values, but different $\delta^{13}\text{C}$ and $\delta^{18}\text{O}$, were measured. One low-temperature coral (RTG) with a higher Δ_{47} value was measured for comparison. All isotopic compositions are reported relative to V-PDB. All errors on Δ_{47} reported in this section are external standard errors (1 SE) calculated on many measurements, with the number of measurements in parentheses.

- **CM2** – An in-house Carrara Marble standard with isotopic composition $\delta^{13}\text{C} = 2.29\text{‰}$ and $\delta^{18}\text{O} = -1.77\text{‰}$ [Dennis thesis]. Previous analysis of this standard at Harvard using the traditional two-bellows method and large (8 mg) sample sizes yielded a Δ_{47} value of $0.385 \pm 0.005\text{‰}$ (n=40) in the absolute reference frame [Dennis et al., 2011].
- **RTG** – A coral specimen from Raratonga, used as a cooler-temperature in-house standard, with isotopic composition $\delta^{13}\text{C} = -2.20\text{‰}$ and $\delta^{18}\text{O} = -4.11\text{‰}$ [Dennis thesis]. Limited previous analyses of this standard in the two-bellows configuration produced a Δ_{47} value of $0.720 \pm 0.007\text{‰}$ (n=11) [Dennis thesis].
- **NBS-19** – An IAEA Carrara Marble standard with isotopic composition $\delta^{13}\text{C} = 1.95\text{‰}$ and $\delta^{18}\text{O} = -2.20\text{‰}$. Previous analyses at Harvard produced a Δ_{47} value of $0.373 \pm 0.007\text{‰}$ (n=7) in the absolute reference frame [Dennis et al., 2011]. Other labs found similar values ($\Delta_{47} = 0.399 \pm 0.005\text{‰}$ (n=12) at Johns Hopkins [Dennis et al., 2011], $0.404 \pm 0.006\text{‰}$ (n=40) at Yale [Dennis et al., 2011], and $0.373 \pm 0.004\text{‰}$ (n=20) and $0.359 \pm 0.004\text{‰}$ (n=19) at 25°C and 90°C at Goethe-University [Wacker et al., 2013]).

To correct the raw Δ_{47} data to the absolute reference frame [Dennis et al., 2011], heated and equilibrated gases were measured through the same sample-preparation inlet in between carbonate sample runs. A large number of heated and equilibrated gases (10-15) were run at the beginning of each measurement period to establish the calibration lines. During the measurement period, a gas standard was run every 1-2 days (every 3-8 samples). To prepare heated gases, aliquots of four gases (2 tank gases and reacted CM2

and RTG) of distinct composition were transferred into quartz tubes, which were heated to 1000°C for 2 hours. This procedure randomizes the isotope distribution to produce a near-stochastic arrangement, which we measure to correct for a number of mass spectrometer source effects [Huntington *et al.*, 2009]. To prepare equilibrated gases, aliquots of the same four gases were transferred into Pyrex tubes containing ~1mL of deionized water. The tubes were placed in water baths held at 10°C and 35°C and allowed to equilibrate over a minimum of 2 days. Each tube is removed immediately before analysis and the gas is extracted within minutes, before the CO₂ can equilibrate to room temperature (see description below).

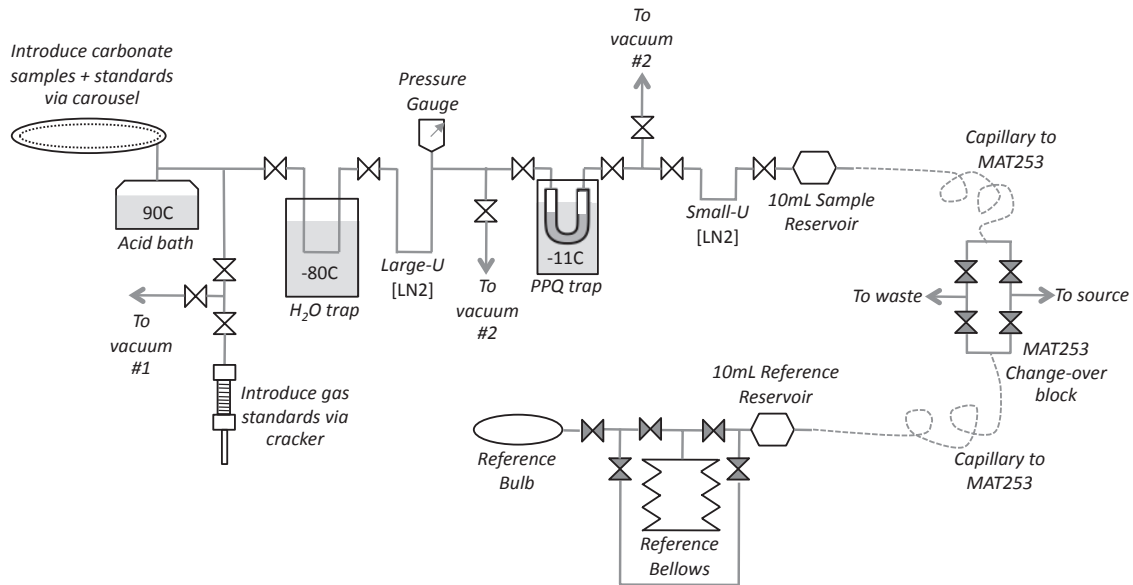


Figure 4.1 Diagram of the new, high-efficiency, dual-reservoir sample preparation inlet. Double triangles represent valves. Shaded valves are controlled by the MAT 253 and white valves are part of the inlet.

4.2.2 Sample preparation

Samples were prepared through a newly constructed high-efficiency dual-reservoir sample preparation inlet (Figure 4.1). This inlet follows the procedure outlined by *Dennis and Schrag* [2010] for creating and cleaning CO₂. Gas is introduced into the inlet in two different ways. For carbonate samples and standards, CO₂ is created by reaction with anhydrous phosphoric acid held at 90°C in a common acid bath and is continuously frozen into a large U-trap submerged in liquid nitrogen (LN₂). Reaction time is 6 minutes, and extends well beyond the point when visible bubble formation ceases. On its way to the U-trap, the gas passes through a trap held at -80°C to remove any trace amounts of water. For gas standards (heated gases and equilibrated gases), CO₂ is introduced into the inlet via a cracker. As with reacted carbonate samples, the CO₂ passes through a -80°C trap to remove water and is frozen into the large U-trap on the far side. For equilibrated gases, within 2-3 minutes of being removed from the water bath (10°C or 35°C), the base of the Pyrex tube is submerged in LN₂, freezing both the water and CO₂ and inhibiting the equilibration of the CO₂ with water at room temperature. LN₂ is then replaced by a -80°C trap before the cracking step to release the CO₂ while the water stays frozen, and is kept at that temperature while the CO₂ is transferred to the U-trap. This whole process takes less than 10-15 minutes and the exposure of CO₂ to water at room temperature is short enough to avoid significant re-equilibration observed in other experiments [*Affek*, 2013]. For all sample types, once the freezing step is complete, the CO₂ is allowed to warm up to room temperature within the large U-trap and the volume of gas created or transferred is roughly determined by an analog pressure gauge.

To remove trace contaminants, the gas is then passed through a Pyrex U-trap (outer diameter ½”) packed with Porapak Q (PPQ) material held at -10 to -12°C by immersion in cooled ethanol. Gas is frozen on the far side into a small U-trap (outer diameter = ¼”, internal volume ~6mL) immersed in LN₂. During this step, the pressure gauge on the large U-trap gradually decreases, demonstrating that the gas is leaving the large U-trap. When the pressure gauge nears baseline and stops decreasing (~4-7 minutes depending on sample size), this step is deemed complete. The small U-trap is closed off and the clean CO₂ is allowed to warm up to room temperature. Finally, the gas is expanded from the small U-trap into the 10mL sample reservoir and allowed to equilibrate for 3 minutes. This completes the sample preparation procedure, which in total takes ~30-40 minutes per sample. While one sample is being analyzed on the mass spectrometer, and before the next sample is processed, the PPQ trap is baked for 20-35 minutes at ~150°C to remove any collected contaminants.

4.2.3 Mass spectrometry

While the CO₂ is equilibrating between the small U-trap and the 10mL sample reservoir, the gas is introduced directly from the reservoir into the source. A more precise determination of yield can be estimated at this point (compared to the rough estimation from the inlet pressure gauge) using the initial beam intensity and the pressure reading off the MAT 253 vacuum gauge. Reference gas from the bellows fills an identical 10mL reference reservoir installed between the bellows and the change-over block (Figure 4.1). The reference bellows are manually adjusted until the intensity on the two *m/z* 47 beams are balanced (on average to within 55 mV, and within 12 mV for samples with initial *m/z*

47 < 1000mV). The reference and sample reservoirs are then closed off from the bellows and the small U-trap, respectively, so the volume from which gas enters the source is identical on both the sample and reference sides. These reservoirs remain closed for the entire run, unlike in the dual-bellows method, where the reservoirs are replenished at the beginning of each acquisition during the pressure adjustment phase.

In order to perfectly balance these volumes, 87 clean glass beads (borosilicate, 3mm diameter, ~1.2mL total volume) were placed permanently in the sample-side reservoir. These beads are necessary to balance the difference between the internal volumes of the adjacent MAT 253 and inlet valves. The inlet valve has a larger internal volume, so the volume of the sample reservoir needs to be decreased accordingly. The specific number of beads was determined by gradually adding beads to the sample side until the beam intensities decreased at the same rate. Any minor offsets between the initial gas pressures set by manual bellows adjustment are eliminated during the course of the run as the reservoir with the higher gas pressure decreases more quickly and eventually matches the other reservoir closely.

The MAT 253 at Harvard is equipped with 5 Faraday cups with resistors of $3 \times 10^7 \Omega$, $3 \times 10^9 \Omega$, and $1 \times 10^{10} \Omega$ for masses 44 through 46 and $1 \times 10^{12} \Omega$ for masses 47 and 48. The capillaries on the mass spectrometer have been changed from the factory-fitted stainless steel variety to a deactivated fused-silica capillary (~1m in length, 110 μ m inner diameter) to prevent the exchange of CO₂ and H₂O within the capillaries. One sample run lasts about 2 hours and 20 minutes and is comprised of 7 acquisitions of 14 cycles each, with an integration time of 26 seconds per cycle and an idle time of 12 seconds, equivalent to 2548 seconds of total integration time on each sample. Raw voltage data is

processed as outlined by *Huntington et al.* [2009] to get raw Δ_{47} values. Carbonate unknowns are then corrected to the absolute reference frame using the heated and equilibrated gas data [*Dennis et al.*, 2011], followed by an additional Δ_{48} correction described below.

In the traditional two-bellows measurement configuration, beam intensities on both the sample and reference side are set to a target value at the beginning of each acquisition (e.g. m/z 47 = 2V or 8V for the Harvard instrument [*Dennis and Schrag*, 2010; *Dennis thesis*]). Over the course of one acquisition, the sample and reference beam intensities decrease somewhat (the amount depends on how many cycles per acquisition and the starting beam intensity), but are returned to the target value at the start of the next acquisition by compressing both the bellows (Figure 4.2). In this set up, all of the cycles are performed at, or closely below, the target voltage (Figure 4.2). By staying near the target voltage, issues of nonlinearities in the source are avoided, and there is no risk of gas fractionating as it decreases to a very low pressure. A 10mL reservoir was installed between the bellows and the capillary on both the reference and sample side of the mass spectrometer to increase the volume from which the gas enters the source, therefore reducing the rate at which the gas pressures (and beam intensities) decrease [*Dennis and Schrag*, 2010]. See Figure A4.1 for detailed set up and part numbers. At m/z 47 = 2V, $\Delta_{47\text{-raw}}$ can be measured to a precision of 0.005-0.010‰ (1 SE) for a single sample run [*Dennis and Schrag*, 2010], reflecting beam stability and shot noise limits [*Merritt and Hayes*, 1994].

In our dual-reservoir configuration, each cycle is measured at progressively lower beam intensity (Figure 4.2). Over the course of a 2-hour 20-minute run, the m/z 47 beam

intensity decreases by 40-60%, at a rate proportional to the gas pressure in the reservoirs (Figure 4.2). While this gas pressure decreases, the beam intensities on the sample and reference sides remain balanced. The ratios between the beams also remain constant, so the calculated isotope ratios do not show a trend with beam intensity. Despite the beam intensity changing significantly over the run, this configuration can achieve similar precision to the dual-bellows configuration for a single measurement, demonstrating isotope-ratio stability over a large voltage range. For a single sample run in this measurement configuration, $\Delta_{47\text{-raw}}$ can be measured to a precision of 0.005‰ to 0.016‰ (1 SE), depending on the sample size, consistent with the shot noise limit [Merritt and Hayes, 1994] (see Appendix A2 for further discussion).

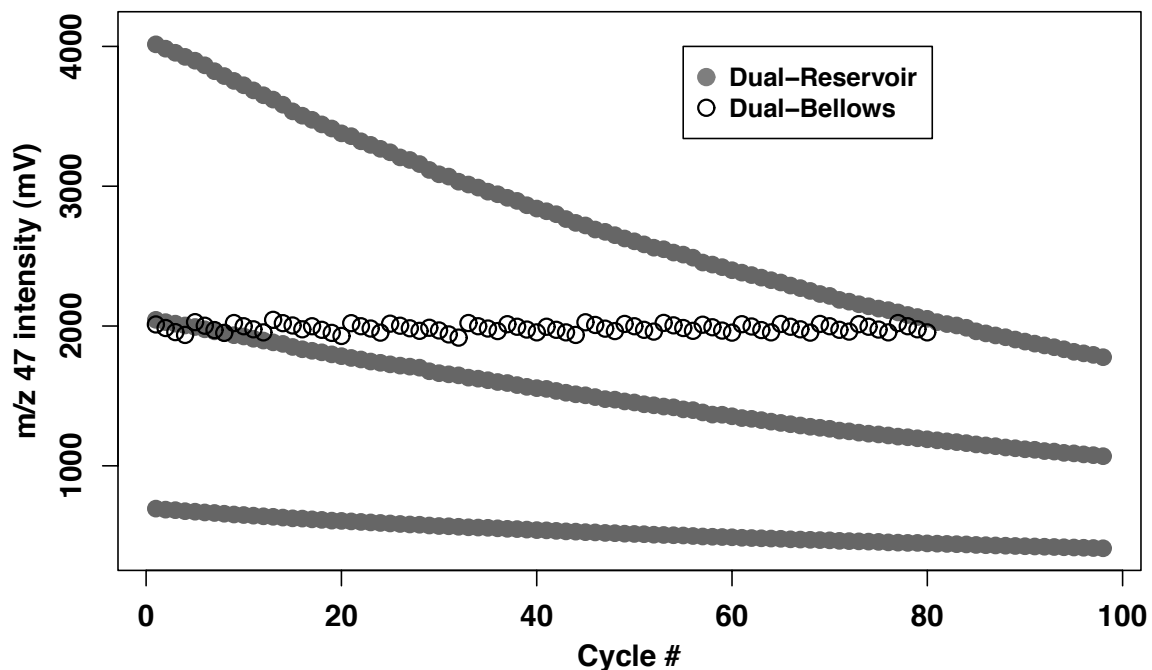


Figure 4.2 m/z 47 beam intensity (mV) over the course of a sample run, shown for one run in the dual-bellows configuration (20 acquisitions x 4 cycles, target voltage = 2V on m/z 47) and three runs in the dual-reservoir configuration (7 acquisitions x 14 cycles, changing m/z 47 voltage) with high, medium, and low starting voltages for m/z 47. m/z 47 beam intensity decreases by 55%, 48%, and 41% for the three cases, respectively.

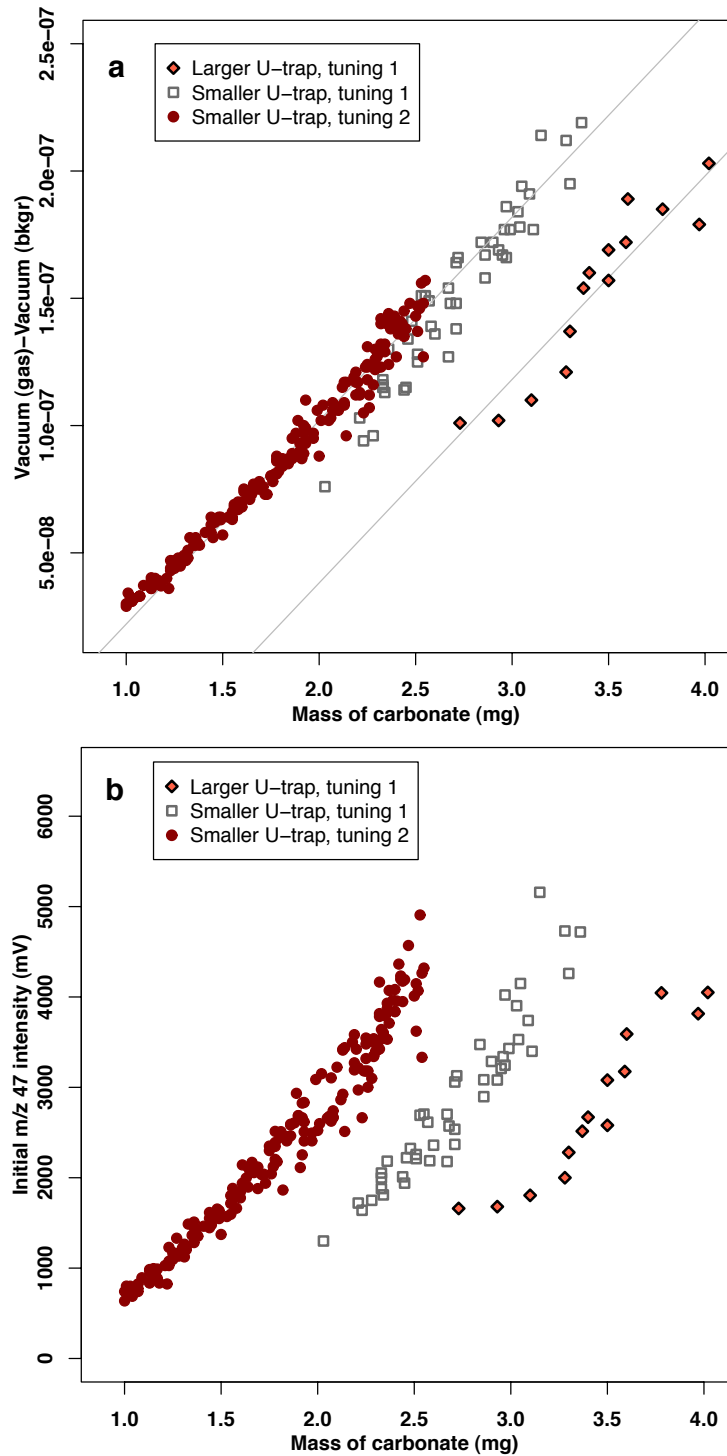


Figure 4.3 Indicators of sample yield. (a) Mass vs. Source Vacuum Pressure above background. Lines are fit through all three data sets and show a consistent yield relationship. (b) Mass vs. Initial m/z 47 beam intensity. Three time periods are plotted. 05/13 – 06/13 – Larger U-trap near the sample reservoir, 1st source tuning configuration; 06/13 – 09/13 – Smaller U-trap near the sample reservoir, 1st source tuning configuration; 10/13 – 03/14 – Smaller U-trap near the reservoir, 2nd source tuning configuration.

4.3 Results

4.3.1 Demonstration of yield at small sample sizes

Sample yield was measured by calculating the increase in pressure recorded by the source vacuum gauge after introducing the sample gas into the source. This yield estimate represents the volume of gas reaching the source per milligram of carbonate reacted, and includes both yield from the acid digestion step and any loss of gas that may have occurred through the cleaning process. The data shows a clear linear relationship between this pressure increase and the mass of carbonate reacted (Figure 4.3a), as is expected from the ideal gas law. In June 2013, installation of a smaller U-trap in front of the sample reservoir decreased the volume of “wasted” gas left in the U-trap and increased the pressure in the source for the same mass of carbonate reacted (Figure 4.3a). Even at the smallest sample sizes, the linear relationship is maintained, indicating good yield is being achieved. This corroborates the inlet pressure gauge, which indicates that nearly all the gas is transferred away from the large U-trap during the PPQ cleaning step.

Sample size can also be compared with the initial m/z 47 beam intensity (Figure 4.3b). For comparison to other instruments, m/z 44 beam intensity is about 5/8 of m/z 47. A source tuning after a power outage in early October 2013 strongly increased the sensitivity (mV beam intensity/mol of gas) of the mass spectrometer, which allowed us to decrease our sample size further, while maintaining the same level of precision (Figure 4.3b, Smaller U-trap, tuning 2). This tuning was done using the Isodat autofocus routine. The increase in sensitivity came mainly from a decrease in the Extraction parameter, and corresponded to a significant decrease in the slope of the gas calibration lines (0.009 to 0.006) but minimal changes in the intercepts (scrambling). After this shift in sensitivity,

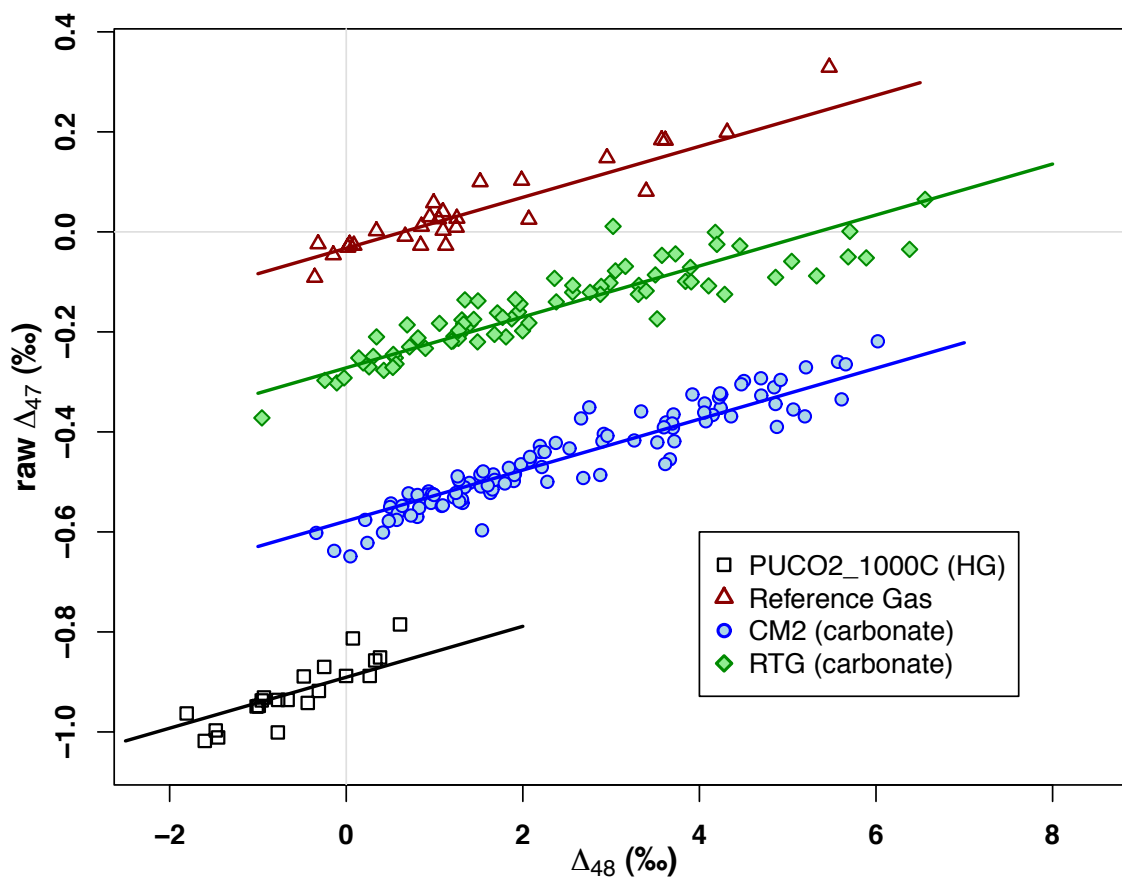


Figure 4.4 Correlation between Δ_{48} and $\Delta_{47\text{-raw}}$ shown for two carbonate standards, one heated gas, and the reference gas run as a sample from the period September 2013 – March 2014. Lines are the result of a group regression to find a common slope and individual intercepts. Error bars are smaller than the symbols.

Sample Type	Number of Data Points	Slope	Error (1SE)
PUCO2_1000C	21	0.0798	0.0098
Reference Gas	29	0.0477	0.0028
CM2 (carbonate)	108	0.0566	0.0017
RTG (carbonate)	76	0.0448	0.0025
All together	234	0.0509	0.0013

Table 4.1 Slopes (and 1SE errors) found from separate regressions of each sample type compared to the slope found using a group regression. Data sets are shown in Figure 4.4. The second column shows the number of replicates in each sample type.

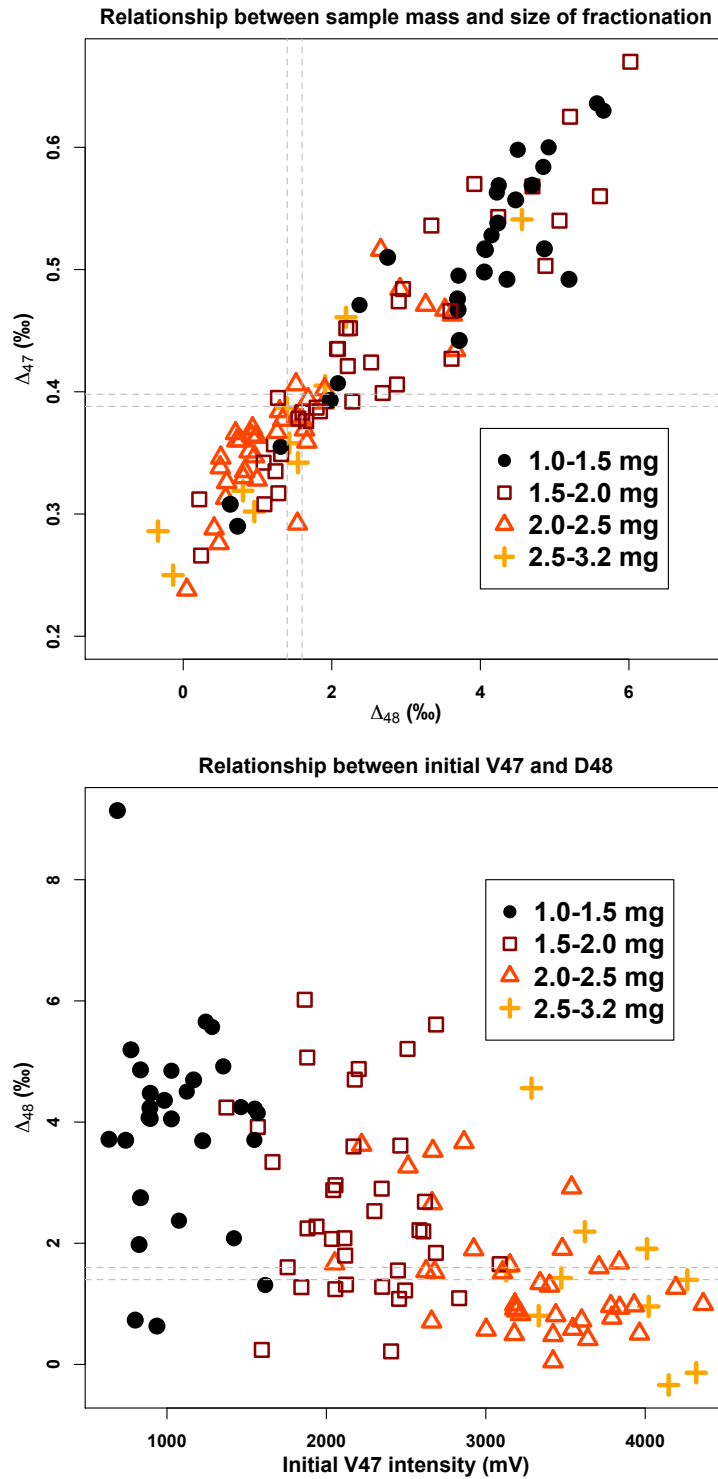


Figure 4.5 Δ_{48} vs. $\Delta_{47\text{-RFAC}}$ (top) and Initial m/z 47 intensity vs. Δ_{48} (bottom), divided by sample size for CM2 runs over all four measurement periods. Smaller sample sizes tend to show higher Δ_{48} , and therefore Δ_{47} , values, whereas larger samples tend to show lower Δ_{48} and Δ_{47} values, although a few points do not follow this. Grey lines delineate “no fractionation”, or $\Delta(\Delta_{48}) = 0$, covering a range of values for the 4 measurement periods.

sample sizes ranging from 1.0mg to 2.5mg produce initial m/z 47 beam intensities between 650mV and 5000mV.

4.3.2 Diagnosing an unknown fractionation

We observe in all our data a strong correlation between Δ_{48} and Δ_{47} , both raw ($\Delta_{47\text{-raw}}$) and fully corrected to the absolute reference frame ($\Delta_{47\text{-RFAC}}$), with Δ_{47} increasing by $\sim 0.05\text{‰}$ for every 1‰ increase in Δ_{48} (Figure 4.4). This relationship is present in carbonate standards and heated gases, and despite varying isotopic compositions and Δ_{47} values, the slope of this relationship is similar among all sample types (Table 4.1). The slope is also nearly unchanged (0.000-0.002) before and after the correction to the absolute reference frame, and across significant changes in source tuning (Figure A4.2, Table A4.1). We observe no significant correlation between Δ_{48} and $\delta^{18}\text{O}$ or $\delta^{13}\text{C}$ (Figure A4.3). Sample size seems to have an influence on the magnitude of the fractionation, with the smallest carbonate samples often (but not always) having higher Δ_{48} and Δ_{47} values (Figure 4.5). The slope of the fractionation is mildly dependent on the average Δ_{47} value of the sample type, with the slope getting slightly steeper (0.04 to 0.08) as the degree of clumping decreases (Table 4.1).

Previously, high Δ_{48} values were interpreted as contamination by hydrocarbons, chlorocarbons, or sulfur compounds, which produce a mass interference on mass-47 and mass-48 [Eiler and Schauble, 2004]. Conventionally, samples should plot within the envelope of calibration gas points in δ^{48} vs. Δ_{48} space. Points outside of this range are thought to be contaminated and would be thrown out in a typical study [Huntington et al., 2009]. In our data, we observe Δ_{48} values both within and outside of the envelope of

calibration gas data (ex. Figure 4.6), for samples we consider to be clean, such as reference gas run through the inlet (Figure 4.4). These high Δ_{48} values have corresponding high Δ_{47} values offset from the known value (zero in the case of reference gas run against itself) and in line with the relationship described above. The result is that we observe a larger range in Δ_{48} for “clean” samples than previously deemed acceptable.

We do not know the cause of this fractionation, but we can rule out some potential explanations. We see the relationship between Δ_{47} and Δ_{48} in heated gases originating from multiple tanks and in the reference gas run as a sample, all of which are pure CO_2 . This suggests our fractionation is not due to sample contamination. The fractionation is also not produced during the acid digestion step because it is observed in standard gases that do not get reacted (and are measured both with and without an acid bath attached to the inlet). Variations in yield also do not cause the fractionation because residuals on this yield do not correlate with Δ_{48} (Figure A4.4).

One possible explanation is that this fractionation is produced in the PPQ cleaning step. Previous studies measuring extremely small samples ($<15\mu\text{mol CO}_2$ equivalent to $<1.5\text{mg CaCO}_3$) observed a fractionation in Δ_{47} associated with the GC cleaning step, producing Δ_{47} values up to 0.2‰ enriched compared to larger samples [Guo and Eiler, 2007]. This is of the same order of magnitude as the fractionation we observe (Figure 4.4). However, the authors observed no correlation between Δ_{47} and either mass-48 or mass-49 excesses [Guo and Eiler, 2007].

We observe different relationships between Δ_{48} and Δ_{47} when gas does or does not pass through the PPQ trap. Reference gas introduced directly into the small U-trap (therefore bypassing the PPQ step) did not show a strong relationship in Δ_{48} vs. Δ_{47}

(Figure A4.5a). However, reference gas frozen directly into the small U-trap (instead of expanded) shows a fairly strong correlation in Δ_{48} vs. Δ_{47} , but with a slope almost twice as steep as when the same gas passed through the whole inlet (Figure A4.5a). Both the amount of gas frozen into the U-trap and the voltage at which the gas was run did not correlate with the magnitude of the fractionation, although none were as small as our smallest samples (Figure A4.5bc). Replacing the PPQ material did not change the slope (Figure A4.2). The duration of baking the PPQ trap before passing a new sample through was observed to have some influence (longer baking = lower Δ_{48}), but it was inconsistent.

The sample size dependence of this fractionation points to a possible influence of the pressure-dependent negative baselines (PBL) observed in many other studies [*He et al.*, 2012; *Yeung et al.*, 2012; *Bernasconi et al.*, 2013], which would have the strongest influence on samples run at the lowest signal intensity. We did not measure PBLs in this study, but the correction to the absolute reference frame implicitly takes the PBL effect into account if reference gases and samples are run at the same voltage. Our calibration gases span a range of sizes that generally overlaps with the range of sample sizes we ran in this study. Some of our smallest samples are outside this range. However, looking at a subset of samples and calibration gases run over a narrow voltage range (m/z 47 = 3300 – 3800mV at the start of the run), we still observe the same relationship, both before and after correction to the absolute reference frame (Figure A4.6, Table A4.2). This suggests that the size (and running voltage) of the reference and sample gases is not causing the observed fractionation.

Heated gases show a smaller range of fractionation than the carbonate samples (Figure 4.4). The volume of CO₂ in each aliquot of heated or equilibrated gas was often

larger than the volume of CO₂ produced by a typical carbonate sample (especially compared to our smallest samples) due to the method of preparation of aliquots from the reference tanks. After passing through our sample preparation inlet (described below), heated and equilibrated gases were chopped down to a volume comparable to the carbonate samples so they could be run at similar beam intensities. This was done by expanding the gas into the T-junction adjacent to the small U-trap (Figure 4.1), or by closing off the reservoir, evacuating the small U-trap, and expanding the gas back into the U-trap. The smaller magnitude of fractionation in the heated gases suggests that the volume of gas passing through the PPQ trap may play a role in setting the magnitude of fractionation.

Another possibility is that this fractionation is caused by our dual-reservoir configuration and the way the beam intensities decrease throughout the run. However, Δ_{48} and Δ_{47} show very little trend over the 2-hour 20-minute run, and the Δ_{48} , whether low or high, is identifiable in the first few cycles, which are no different than the first few cycles of a traditional two-bellows analysis. Regardless of the cause of the fractionation, it is consistent, well defined, and can be corrected.

4.3.3 Correcting for a fractionation in Δ_{47} and Δ_{48}

The observed relationship between increased Δ_{48} and Δ_{47} causes an undesirable, large scatter in the Δ_{47} of measured carbonate samples and standards. If a “true” Δ_{48} value is known for each sample type (e.g. CM2, RTG), the Δ_{47} data can be simply corrected back to this value along the observed slope. In the past, the “true” (uncontaminated) Δ_{48} value has been determined in relation to the behavior of heated and equilibrated gases in

δ^{48} vs. Δ_{48} space [Huntington *et al.*, 2009]. Heated and equilibrated gases show a positive linear relationship between δ^{48} and Δ_{48} , and replicates of a single carbonate sample form an intersecting line of steeper slope (see Figure 4.6a). The deviation between the Δ_{48} of an individual replicate and the line determined by the heated/equilibrated gases is denoted $\Delta(\Delta_{48})$ and is calculated based on Equation 4.2.

$$\Delta(\Delta_{48}) = \Delta_{48} - (\delta^{48} * \text{Slope}_{\text{HG/EG}} + \text{Int}_{\text{HG/EG}}) \quad [\text{Eq. 4.2}]$$

$\text{Slope}_{\text{HG/EG}}$ and $\text{Int}_{\text{HG/EG}}$ are the slope and intercept of the line fitted to all the heated and equilibrated gas points in δ^{48} vs. Δ_{48} space (Figure 4.6a, black points/lines). The “true” Δ_{48} value for each carbonate sample type (CM2, RTG, unknown) is then determined to be the value at which $\Delta(\Delta_{48}) = 0$ (i.e. the point of intersection between the sample line and the heated/equilibrated gas line). This can be calculated for each sample type using Equation 4.3.

$$\text{“true” } \Delta_{48} = (\text{Int}_{\text{CARB48}} * \text{Slope}_{\text{HG/EG}} - \text{Int}_{\text{HG/EG}} * \text{Slope}_{\text{CARB48}}) / (\text{Slope}_{\text{HG/EG}} - \text{Slope}_{\text{CARB48}}) \quad [\text{Eq. 4.3}]$$

$\text{Slope}_{\text{CARB48}}$ and $\text{Int}_{\text{CARB48}}$ are the slope and intercept of the line fitted to all the data of a single carbonate sample type in δ^{48} vs. Δ_{48} space (Figure 4.6a, colored points/lines). $\text{Slope}_{\text{CARB48}}$ and $\text{Int}_{\text{CARB48}}$ can be determined individually for each sample type by fitting a line to all replicates of that sample. The individual δ^{48} vs. Δ_{48} slopes for carbonates agree with each other within error when sample types have enough replicates,

suggesting all carbonates are following the same slope and the lines are parallel. Therefore, data sets of all carbonate sample types can be fitted simultaneously for a common slope and individual intercepts. This is the same as the mathematical procedure done to solve for the slope and intercepts of the heated and equilibrated gases in δ^{47} vs. Δ_{47} space when correcting data to the absolute reference frame [Dennis *et al.*, 2011]. By solving all data sets together, this decreases the influence of any individual outlying point, and improves the fit to a sample for which you have few replicates (e.g. NBS19). Slopes and intercepts resulting from the group fit are the same as those from individual fits for CM2 and RTG within error, but not for NBS19, which only has 2-5 replicates per measurement period. The close agreement between slopes of different sample types, and the benefits when measuring unknowns with few replicates lead us to prefer the group fit for this step. δ^{48} vs. Δ_{48} lines in this study have been calculated using a group fit of CM2, RTG, and NBS19 together. See Appendix A5 for an in-depth discussion of group fit vs. individual fit.

Figure 4.6 Diagram of correction method for RTG data points from February to March 2014. (a) δ^{48} vs. Δ_{48} for three carbonate sample types and for heated and equilibrated gases (HG/EG). The line fitted to the HG/EG (black) gives $\text{Slope}_{\text{HG/EG}}$ and $\text{Int}_{\text{HG/EG}}$ and the lines fitted together to the carbonate data give one $\text{Slope}_{\text{CARB48}}$ value and individual $\text{Int}_{\text{CARB48}}$ values. (b) Δ_{48} vs. Δ_{47} for RTG data corrected ($\Delta_{47\text{-corr}}$) and uncorrected ($\Delta_{47\text{-RF/AC}}$) for the Δ_{48} fractionation. In both panels, the green arrow denotes the “true Δ_{48} ” value. The small black arrow indicates the way in which points are corrected back to the “true Δ_{48} ” along the slope. Bars on the right indicate the full range of points, corrected and uncorrected. Points and error bars on the right indicate the mean and standard error (1 SE) of the corrected and uncorrected data sets. The published value $0.720 \pm 0.007\text{‰}$ is plotted for comparison.

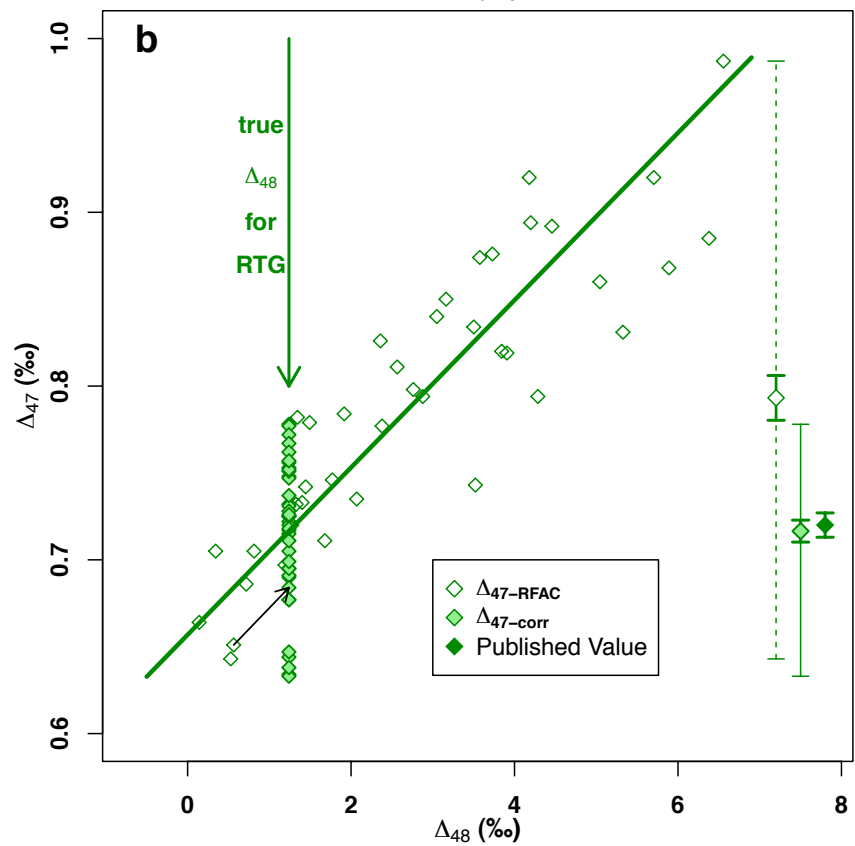
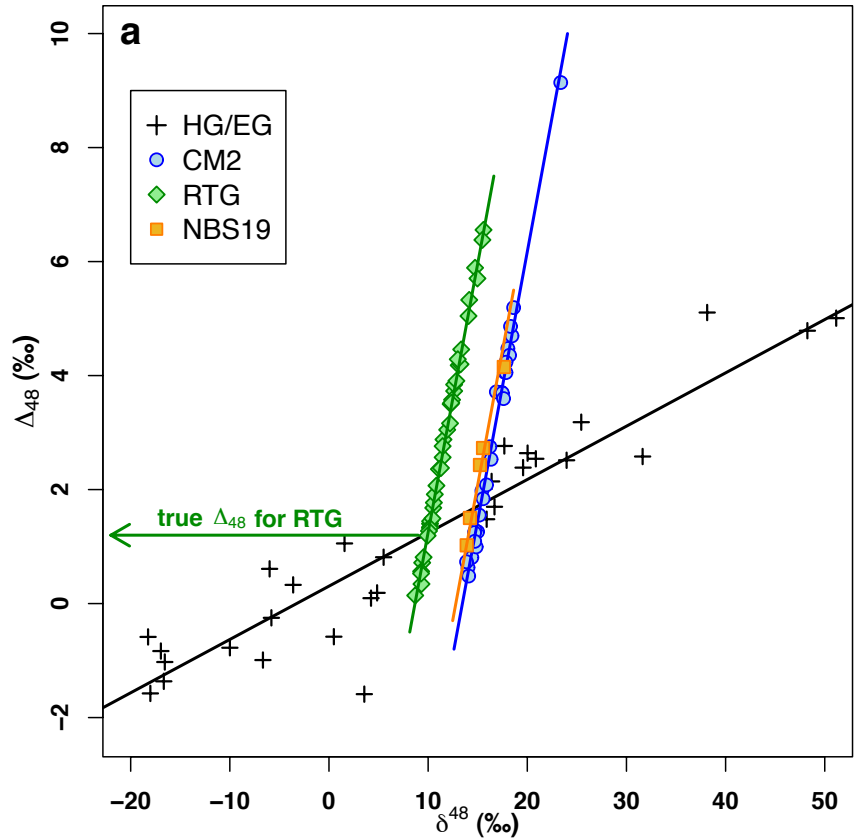


Figure 4.6 [continued]

Once the “true” Δ_{48} value is determined for each sample type, the scattered Δ_{47} data can be corrected to this value using Equation 4.4, following the observed relationship between Δ_{47} and Δ_{48} (see Figure 4.6b).

$$\Delta_{48}\text{-Corrected } \Delta_{47} = \Delta_{47\text{-corr}} = \Delta_{47\text{-RF/AC}} - (\Delta_{48} - \text{“true” } \Delta_{48}) * \text{Slope}_{\text{CARB47}} \quad [\text{Eq. 4.4}]$$

$\Delta_{47\text{-RF/AC}}$ is the Δ_{47} value corrected to the absolute reference frame and adjusted for the acid digestion fractionation [Dennis *et al.*, 2011]. We choose to apply this correction to the data already corrected into the absolute reference frame since any nonlinearities caused by source effects should be removed in the $\Delta_{47\text{-RF/AC}}$ data. However, the slope of the carbonate lines in Δ_{48} vs. Δ_{47} space ($\text{Slope}_{\text{CARB47}}$) are very similar for the reference frame-corrected and raw data (Table A4.1), so the choice of order of operations does not have a large effect (mean difference of 0.001‰).

$\text{Slope}_{\text{CARB47}}$ can be found by fitting replicates of a single sample type in Δ_{48} vs. Δ_{47} space, or by fitting data sets of all carbonate sample types simultaneously for a common slope. When correcting unknown data with a small number of replicates (e.g. NBS19), it is preferable to do the group fit again (see discussion in Appendix A5). When correcting samples or standards with a large (>10-15) number of replicates, the individual fit should accurately capture $\text{Slope}_{\text{CARB47}}$ for that sample type. For carbonate samples, $\text{Slope}_{\text{CARB47}}$ is roughly equal to 0.05 and does not change much through time (Figure A4.2, Table A4.1). We do observe a slight but consistent difference between slopes of CM2 and RTG, which may be Δ_{47} -dependent. To preserve the difference in slope between CM2 and RTG, while still getting the benefits of the group fit for NBS19, we

choose to fit RTG individually and CM2 and NBS19 together for this step. The small number of NBS19 points have a minimal effect on the group fit making the resulting slope identical within error to the CM2 individual fit. A comparison of data corrected using different fit procedures can be found in Appendix A5. For future measurements of unknowns that only have a few replicates each, a group fit is beneficial. Due to the observed difference in slope between carbonate sample types, a group fit of unknowns should only be combined with a carbonate standard of similar Δ_{47} composition, otherwise data may be skewed one way or the other.

4.3.4 Corrected carbonate data

Applying this correction dramatically reduces the scatter in our Δ_{47} data and shifts the mean value to within error of the published values (Table 4.2). (A comparison of corrected and uncorrected data can be found in Figures A4.7 and Table A4.3). For CM2, the correction shifts the mean Δ_{47} from $0.429 \pm 0.010\text{‰}$ to $0.378 \pm 0.003\text{‰}$ (n=108). For RTG, the correction shifts the mean Δ_{47} from $0.773 \pm 0.010\text{‰}$ to $0.723 \pm 0.004\text{‰}$ (n=76). These values compare nicely with the published values of $0.385 \pm 0.005\text{‰}$ (n=40) for CM2 and $0.720 \pm 0.007\text{‰}$ (n=11) for RTG [Dennis *et al.*, 2011]. $\delta^{13}\text{C}$ values agree well with published data, whereas $\delta^{18}\text{O}$ values are consistently too light by 0.15-0.2‰ from known values (Table 4.2). When measuring unknowns in the future, stable isotope data of unknown samples will be corrected for this systematic offset, as has been done in other studies [Price and Passey, 2013].

Sample	$\delta^{13}\text{C}$ (‰)	$\delta^{18}\text{O}$ (‰)	$\Delta_{47\text{-RFAC}}$ (‰)	$\Delta_{47\text{-corr}}$ (‰)
CM2 (n = 108)	2.22 ± 0.004	-1.95 ± 0.008	0.429 ± 0.010	0.378 ± 0.003
<i>CM2 published</i> ^[17]	2.29 ± 0.006	-1.77 ± 0.010		0.385 ± 0.005 (n=40)
RTG (n = 76)	-2.19 ± 0.006	-4.34 ± 0.007	0.773 ± 0.010	0.723 ± 0.004
<i>RTG published</i> ^[16]	-2.2 ± 0.062	-4.11 ± 0.019		0.720 ± 0.007 (n=11)
NBS19 (n = 9)	1.95 ± 0.019	-2.34 ± 0.037	0.372 ± 0.021	0.366 ± 0.007
<i>NBS19 published</i> ^[17]	1.95	-2.2		0.373 ± 0.007 (n=7)

Table 4.2 Summary of all carbonate samples of sizes 1.0-2.6mg measured from September 2013 to March 2014 compared to published values. $\delta^{13}\text{C}$ and corrected Δ_{47} values compare well to published values. $\delta^{18}\text{O}$ values are consistently 0.15-0.2‰ too light. Future analysis of unknown carbonates will be corrected for this fixed offset. All listed errors are 1 standard error (1 SE) estimates on the mean of all points of that sample type, with the number of replicates listed in parentheses.

Date	Sample	Mass (mg)	δ^{47} (‰)	$\Delta_{47\text{-raw}}$ (‰)	$\Delta_{47\text{-RF/AC}}$ (‰)	δ^{48} (‰)	Δ_{48} (‰)	$\Delta_{47\text{-corr}}$ (‰)
12/10/13	NBS19	2.32	17.317	-0.587±0.008	0.307±0.017	12.926	0.235	0.379±0.022
12/13/13	NBS19	2.41	17.494	-0.547±0.007	0.346±0.016	14.026	1.147	0.366±0.021
01/13/14	NBS19	2.37	17.463	-0.564±0.006	0.329±0.040	14.220	1.407	0.327±0.045
02/05/14	NBS19	2.47	17.491	-0.546±0.006	0.348±0.039	13.564	0.658	0.390±0.044
03/25/14	NBS19	1.23	17.497	-0.449±0.012	0.414±0.036	15.537	2.729	0.356±0.039
03/25/14	NBS19	1.36	17.401	-0.484±0.010	0.379±0.037	14.217	1.502	0.387±0.039
03/27/14	NBS19	2.32	17.499	-0.553±0.006	0.327±0.037	13.889	1.022	0.363±0.039
03/27/14	NBS19	1.27	17.480	-0.477±0.011	0.385±0.037	15.229	2.431	0.343±0.040
03/27/14	NBS19	1.33	17.102	-0.345±0.010	0.517±0.034	17.634	4.151	0.380±0.037
ALL				-0.504±0.025	0.372±0.021			0.366±0.007
Group 1 (1.2-1.4mg, n=4)				-0.439±0.032	0.331±0.007			0.367±0.010
Group 2 (2.3-2.5mg, n=5)				-0.555±0.009	0.424±0.032			0.365±0.011
<i>Published Value</i>								0.373±/±0.007 (n=7)

Table 4.3 Raw data used in the correction of NBS19 data points measured from September 2013 to March 2014. Errors on $\Delta_{47\text{-raw}}$ are 1 SE on all cycles measured for an individual run. Errors on $\Delta_{47\text{-RF/AC}}$ and $\Delta_{47\text{-corr}}$ have taken the raw error and propagated it through the reference frame and Δ_{48} correction, respectively. Average errors (1 SE) on δ^{47} , δ^{48} , and Δ_{48} are 0.011‰, 0.053‰, and 0.052‰, respectively. Errors reported on mean values represent 1 SE of that sample group.

Figure 4.7 shows all the corrected data for CM2 and RTG. The data is separated into 0.1mg bins and samples in each bin are treated as replicates of one sample. In each bin, the average and standard error are computed. For both CM2 and RTG, there is no systematic increase in scatter of individual points or in the external standard error of the binned groups as the sample size is reduced. The RTG data points show more scatter than the CM2 data points ($\Delta_{47\text{-corr}}$ 1 s.d. = 0.036 vs. 0.031, all replicates). This might be explained by increased heterogeneity of samples material between replicates. The RTG coral material was more coarsely ground than the CM2 marble, and shallow-water corals are known to be heterogeneous in Δ_{47} [Ghosh *et al.*, 2006a; Saenger *et al.*, 2012]. In addition, fewer replicates of RTG were run in many of the mass bins compared to CM2 (Table A4.3), leading to larger standard errors for the same mass bins.

A smaller number of replicates of NBS19 were run, producing a mean Δ_{47} value of $0.366 \pm 0.007\text{‰}$ (n=9). This compares well with the value of $0.373 \pm 0.005\text{‰}$ calculated from previous measurements of this standard at Harvard [Dennis *et al.*, 2011]. Replicates of NBS19 fall into two mass groups – a larger group (2.3-2.5mg) and a smaller group (1.2-1.4mg). The means of these two groups ($0.365 \pm 0.011\text{‰}$ and $0.367 \pm 0.010\text{‰}$, respectively) were within error of each other and of the published value (Table 4.3).

Errors (1 SE) on raw Δ_{47} of individual samples increase as the sample size decreases following the shot noise limit (see Appendix A2). At 1mg, error bars on $\Delta_{47\text{-raw}}$ for individual replicates are 0.014-0.016‰ for both CM2 and RTG. At 1.5mg, the same error bars are 0.009-0.011‰. When these raw 1 SE errors are fully propagated through the reference frame and Δ_{48} corrections, they get significantly larger and the influence of

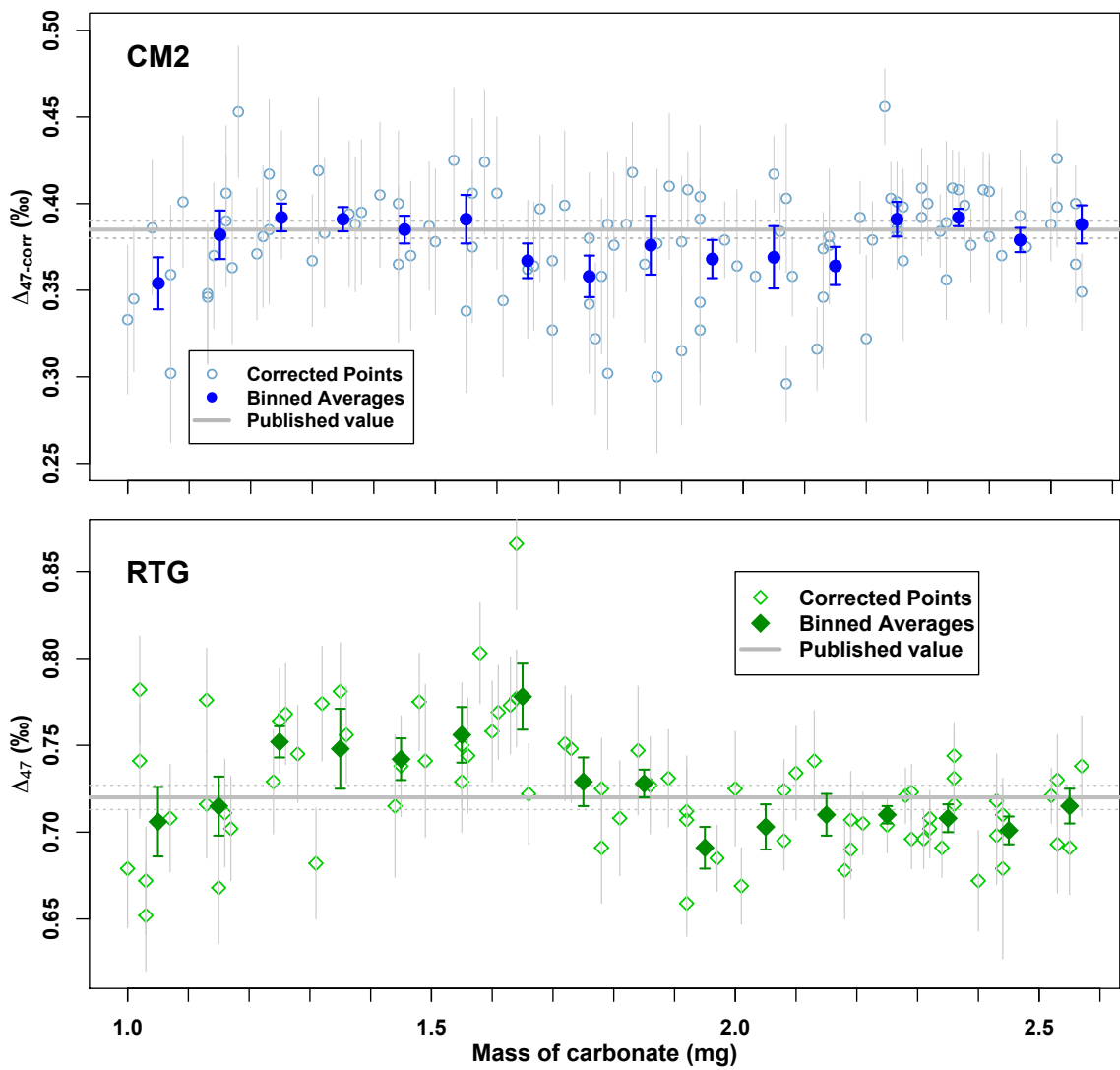


Figure 4.7 (a) Fully corrected $\Delta_{47\text{-corr}}$ vs. Mass for all CM2 points. Individual points are shown with error bars representing the original shot noise error fully propagated through all corrections. Binned averages (0.1mg bins) are shown in filled symbols. Grey horizontal lines indicate the published value and error. (b) Same as (a) but for RTG. Mean values for each bin are summarized in Table A4.3.

sample size disappears (see Appendix A3 for details on error propagation calculations). The average error increases from 0.009‰ to 0.034‰. The majority of this increase comes from the reference frame correction, which is responsible for 0.019‰ of the 0.025‰ increase, whereas the Δ_{48} correction contributes only 0.007‰ on average. The Δ_{48} correction had the largest impact during measurement period #1, where it contributed a 0.013‰ increase to average error, due to the limited number of carbonate samples run during this period (n=15), causing greater uncertainty in the carbonate slopes and intercepts needed for the correction. The reference frame correction is smallest in measurement period #2 (only 0.006‰), where the most standard gases were run. Other measurement periods (#1, #3) were cut short due to mechanical issues (e.g. power outage) before the desirably number of gas standards were run, resulting in larger uncertainties in the heated and equilibrated gas lines and the empirical transfer function.

4.4 Discussion

4.4.1 Precision and sample size

The benefit of this technique is the ability to measure Δ_{47} on small aliquots of carbonate. All applications of clumped isotopes require at least 3 replicates per unknown to reduce the uncertainty on the mean. For geologic applications, errors on the order of 0.010‰ are needed to get meaningful results. To improve the overall sample requirements (combined mass of all replicates), it's necessary to balance the sample size per replicate and the number of replicates needed to achieve the necessary precision.

In applying this method, we recommend 5-6 replicates of mass 1.2-1.4mg per unknown (equivalent to 6 to 8.4 mg of CaCO₃) to minimize the total amount of sample material needed while achieving acceptable precision. For CM2, mass bins in this range give standard errors of 0.007-0.008‰ for 5 or 6 replicates (Table A4.3). The smaller NBS19 mass bin (1.2-1.4mg) has a standard error of 0.010‰ for 4 replicates (Table 4.3). For RTG, the 1.2-1.3mg mass bin has a standard error of 0.009‰ for 4 replicates. The other mass bin in this range (1.3-1.4mg) has a higher error (0.023‰). The addition of 1-2 more replicates would also improve the error in the RTG and NBS19 mass bin. Even with a larger number of replicates, this is about half the mass required for the best existing traditional techniques (~4 replicates at 3-4mg [Zaarur *et al.*, 2011]) and is similar to the lower limit of measurements made with the Kiel device technique (6-26mg) [Schmid and Bernasconi, 2010; Meckler *et al.*, 2014].

In addition to running the heated and equilibrated gases for correction to the absolute reference frame, it is necessary to run a number of carbonate standards along with unknowns to better resolve the slope of the carbonates in Δ_{48} vs. Δ_{47} space. Because each unknown may have only a few replicates, having one line with many replicates of the same sample type (a standard material) can greatly improve the group fit to find $\text{Slope}_{\text{CARB47}}$.

4.4.2 Detecting contaminated samples

One issue that arises is how to detect contaminated samples if a perfectly clean sample can have high Δ_{48} due to this unexplained fractionation. We suggest that a contaminant would be unlikely to affect Δ_{47} and Δ_{48} in the exact same ratio as our

fractionation. Contaminated samples would therefore deviate from the observed relationship, likely in the direction of higher Δ_{48} . In this study, we observe 7 samples that significantly deviate from the fractionation line in the direction of high Δ_{48} (Figure A4.8), and believe them to be contaminated. These few points are not included in plots and data reported here.

In practice, a threshold or envelope around the fractionation line should be set and points outside this range should be tossed out, similar to how the heated gas line in δ^{48} vs. Δ_{48} space has been used previously. When measuring unknowns, residuals of the unknown data around the unknown's group fit line can be compared to residuals of carbonate standards. Scatter in excess of the typical carbonate standard (especially in the high Δ_{48} direction) should be deemed contamination. This method of determining contamination has the risk of failing to eliminate some "mildly contaminated" samples. Inclusion of these samples would result in temperatures that were too hot.

4.4.3 A lower limit on sample size

We have shown that for sample sizes as low as 1mg, the average of multiple replicates can faithfully reproduce the mean value and give standard errors within an acceptable range (0.005-0.015‰), similar to that achieved by traditional methods [*Dennis and Schrag, 2010; Zaarur et al., 2011; Wacker et al., 2013; Thiagarajan et al., 2011*].

The sample preparation procedure on the inlet does not seem to limit the sample size that can be run because for all sample sizes we obtain good yields consistent with the ideal gas law (Figure 4.3). Instead, we are limited by the beam intensities at which the sample is run, which are intimately linked to the shot noise limit and the maximum

achievable precision on each replicate. As voltages drop below $\sim 500\text{mV}$ on m/z 47, we observe less stability in the isotope ratios through the run, despite obtaining correct mean values when many replicates of this size are measured. This may indicate the lower limit at which the mass spectrometer can operate. The gas pressure (and therefore beam intensity) produced by a given mass is affected by a few parameters: 1) the size of the small U-trap; 2) the sensitivity of the MAT 253; and 3) the size of the sample and reference reservoirs.

Installing a smaller U-trap in front of the sample reservoir decreased the sample size necessary to achieve an internal precision of 0.010‰ and 0.007‰ from 3.1mg to 1.6mg and from 3.7mg to 2.4mg , respectively. Currently, the internal volume of the small U-trap is about 6mL . If this were cut in half to 3mL , it would further decrease the above sample sizes to 1.4mg and 2.1mg , respectively. In an ideal case, the volume of the U-trap would be as small as possible while still allowing the sample to freeze and expand without fractionating.

After tuning the source using the Isodat autotune function, we observed an increase in average sensitivity from 1.94×10^{10} to 2.66×10^{10} mV on m/z 47 per mbar source vacuum pressure. This is equivalent to an increase from m/z 47 = $\sim 2900\text{mV}$ to $\sim 4100\text{mV}$ at $\sim 35\text{mbar}$ pressure in the bellows. This caused the sample size necessary to achieve an internal precision of 0.010‰ and 0.007‰ to decrease further from 1.6mg to 1.4mg and from 2.4mg to 2.0mg , respectively. An instrument with higher sensitivity could measure even smaller samples and achieve the same level of precision.

Changing the size of the sample (and reference) reservoir(s) could also increase the signal from a given volume of sample gas, by the same mechanism as decreasing the

size of the small U-trap. However, decreasing the reservoir size also increases the rate at which gas depletes. The 10mL reservoir is the smallest available from Swagelok, but this technique should work equally well for a smaller reservoir. For very small reservoir sizes, the gas may deplete away before the 2-hour run completes. In other methods using microvolumes, either the gas is not run for a very long time [*Schmid and Bernasconi, 2010*] or additional corrections for fractionation in stable isotopes were necessary [*Halevy et al., 2011*]. We selected the 10mL reservoir size to balance the sample yield and the depletion rate.

Our high-efficiency dual-reservoir configuration, in its current state, can handle samples as small as 1 mg. At this low limit, we begin to see more instabilities in the isotope ratios. A similar inlet with a smaller U-trap, a slightly smaller reservoir, or higher sensitivity of the mass spectrometer could push the sample size even lower using this measurement technique.

4.5 Conclusions

This study demonstrates that sample sizes as small as 1mg can be measured with good precision using a newly constructed, high-efficiency, dual-reservoir inlet. By eliminating the sample bellows and installing matching fixed reservoirs from which gas gradually enters the source, the volume of “wasted” gas typically left in a sample vial or bellows is reduced and yield is increased. With some adjustments, this measurement configuration could be successful for even smaller sample sizes. This achievement will allow the application of the clumped isotope proxy to sample materials for which it is

difficult to acquire a large amount of material, such as foraminifera, and will expand the usage of this proxy in fields such as paleoceanography.

Acknowledgements

This work was supported by Henry and Wendy Breck. The authors would like to thank G. Eischeid, S. Manley, and F. Chen for laboratory assistance.

References

- Affek, H. P. (2013), Clumped isotopic equilibrium and the rate of isotope exchange between CO₂ and water, *American Journal of Science*, 313(4), 309-325.
- Bernsaconi, S. M., B. Hu, U. Wacker, J. Fiebig, S. F. M. Breitenbach, and T. Rutz (2013), Background effects on Faraday collectors in gas-source mass spectrometry and implications for clumped isotope measurements, *Rapid Communications in Mass Spectrometry*, 27(5), 603.
- Dennis, K. J. Ph.D. (2011), Clumped isotope thermometry and its application to Earth's history, Harvard University (Cambridge, MA).
- Dennis, K. J. and D. P. Schrag (2010), Clumped isotope thermometry of carbonatites as an indicator of diagenetic alteration, *Geochimica et Cosmochimica Acta*, 74(14), 4110-4122.
- Dennis, K. J., H. P. Affek, B. H. Passey, D. P. Schrag, and J. M. Eiler (2011), Defining an absolute reference frame for 'clumped' isotope studies of CO₂, *Geochimica et Cosmochimica Acta*, 75(22), 7117-7131.
- Eagle, R. A., T. Tutken, T. S. Martin, A. K. Tripathi, H. C. Fricke, M. Connely, R. L. Cifelli, and J. M. Eiler (2011), Dinosaur body temperature determined from isotopic (¹³C-¹⁸O) ordering in fossil biominerals, *Science*, 333(6041), 443-445.
- Eiler, J.M. (2011), Paleoclimate reconstruction using carbonate clumped isotope thermometry, *Quaternary Science Review*, 30(25-26), 3575-2588.

- Eiler, J.M. and E. A. Schauble (2006), $^{18}\text{O}^{13}\text{C}^{16}\text{O}$ in Earth's atmosphere, *Geochimica et Cosmochimica Acta*, 68(23), 4767-4777.
- Ghosh, P., C. N. Garzione, and J. M. Eiler (2006b), Rapid uplift of the Altiplano revealed through ^{13}C - ^{18}O bonds in paleosol carbonates, *Science*, 311(5760), 511-515.
- Ghosh, P., J. Adkins, H. P. Affek, B. Balta, W. Guo, E. A. Schauble, D. P. Schrag, and J. M. Eiler (2006a), ^{13}C - ^{18}O bonds in carbonate minerals: A new kind of paleothermometer, *Geochimica et Cosmochimica Acta*, 70(6), 1439-1456.
- Grauel, A.-L., T. W. Schmid, B. Hu, C. Bergami, L. Capotondi, L. Zhou, and S. M. Bernasconi (2013), Calibration and application of the 'clumped isotope' thermometer to foraminifera for high-resolution climate reconstructions, *Geochimica et Cosmochimica Acta*, 108(0), 125-140.
- Guo, W., J. L. Mosenfelder, W. A. Goddard III, and J. M. Eiler (2009), Isotopic fractionations associated with phosphoric acid digestion of carbonate minerals: Insights from first-principles theoretical modeling and clumped isotope measurements, *Geochimica et Cosmochimica Acta*, 73(24), 7203-7225.
- Guo, W. and J. M. Eiler (2007), Temperatures of aqueous alteration and evidence for methane generation on the parent bodies of the CM chondrites, *Geochimica et Cosmochimica Acta*, 71(22), 5565-5575.
- Halevy, I., W. W. Fischer, and J. M. Eiler (2011), Carbonates in the Martian meteorite Allan hills 84001 formed at $18\pm 4^\circ\text{C}$ in a near-surface aqueous environment, *Proceedings of the National Academy of Sciences*, 108(41), 16985-16899.
- He, B., G. A. Olack, and A. S. Colman (2012), Pressure baseline correction and high-precision CO_2 clumped-isotope (Δ_{47}) measurements in bellows and micro-volume modes, *Rapid Communications in Mass Spectrometry*, 26(24), 2837-2853.
- Huntington, K. W., J. M. Eiler, H. P. Affek, W. Guo, M. Bonifacie, L. Y. Yeung, N. Thiagarajan, B. H. Passey, A. K. Tripathi, M. Daeron, and R. Came (2009), Methods and limitations of 'clumped' CO_2 isotope (Δ_{47}) analysis by gas-source isotope ratio mass spectrometry, *Journal of Mass Spectrometry*, 44(9), 1318-1329.
- Meckler, A. N., M. Ziegler, M. I. Millan, S. F. M. Breitenbach, and S. M. Bernasconi (2014), Long-term performance of the Kiel carbonate device with a new correction scheme for clumped isotope measurements, *Rapid Communications in Mass Spectrometry*, 28(15), 1705-1715.
- Merritt, D. A. and J. M. Hayes (1994), Factors controlling precision and accuracy in isotope-ratio-monitoring mass spectrometry, *Analytical Chemistry*, 66, 2336-2347.

- Passey, B. H., N. E. Levin, T. E. Cerling, F. H. Brown, and J. M. Eiler (2010), High-temperature environments of human evolution in East Africa based on bond ordering in paleosol carbonates, *Proceedings of the National Academy of Sciences*, 107(25), 11245-11249.
- Price, G. D. and B. H. Passey (2013), Dynamic polar climates in a greenhouse world: Evidence from clumped isotope thermometry of Early Cretaceous belemnites, *Geology*, 41, 923-926.
- Saenger, C., H. P. Affek, T. Felis, N. Thiagarajan, J. M. Lough, and M. Holbom (2012), Carbonate clumped isotope variability in shallow water corals: Temperature dependence and growth-related vital effects, *Geochimica et Cosmochimica Acta*, 99, 224-242.
- Schauble, E. A., P. Ghosh, and J. M. Eiler (2006), Preferential formation of ^{13}C - ^{18}O bonds in carbonate minerals, estimated using first-principle lattice dynamics, *Geochimica et Cosmochimica Acta*, 70(10), 2510-2529.
- Schmid, T. W. and S. M. Bernasconi (2010), An automated method for ‘clumped-isotope’ measurements on small carbonate samples, *Rapid Communications in Mass Spectrometry*, 24(14), 1955-1963.
- Thiagarajan, N., J. Adkins, and J. M. Eiler (2011), Carbonate clumped isotope thermometry of deep-sea corals and implications for vital effects, *Geochimica et Cosmochimica Acta*, 75(16), 4416-4425.
- Tripati, A. K., R. A. Eagle, N. Thiagarajan, A. C. Gagnon, H. Bauch, P. R. Halloran, and J. M. Eiler (2010), ^{13}C - ^{18}O isotope signatures and ‘clumped isotope’ thermometry in foraminifera and coccoliths, *Geochimica et Cosmochimica Acta*, 74(20), 5697-5717.
- Tripati, A. K., S. Sahany, D. Pittman, R. A. Eagle, J. D. Neelin, J. L. Mitchell, and L. Beaufort (2014), Modern and glacial tropical snowlines controlled by sea surface temperature and atmospheric mixing, *Nature Geoscience*, 7(3), 205-209.
- Wacker, U., J. Feibig, and B. R. Schoene (2013), Clumped isotope analysis of carbonates: comparison of two different acid digestion techniques, *Rapid Communications in Mass Spectrometry*, 27, 1631-1642.
- Yeung, L.Y., E. D. Young, and E. A. Schauble (2012), Measurements of ^{18}O - ^{18}O and ^{17}O - ^{18}O in the atmosphere and the role of isotope-exchange reactions, *Journal of Geophysical Research*, 117(D18), D18306.
- Zaarur, S., G. Olack, and H. P. Affek (2011), Paleo-environmental implication of clumped isotopes in land snail shells, *Geochimica et Cosmochimica Acta*, 75(22), 6859-6869.

Chapter 5. Application of the clumped isotope paleothermometer to foraminifera across the Eocene-Oligocene Transition

ABSTRACT

Across the Eocene-Oligocene transition (EOT), the oxygen isotopic composition of benthic foraminifera increased dramatically (1-1.5‰). This is thought to represent a combination of cooling of bottom waters and growth of a large ice sheet on Antarctica. To determine the contribution of each of these effects on the total change in benthic $\delta^{18}\text{O}$, an independent estimate of temperature is required. Here we use the clumped isotope paleothermometer on planktonic foraminifera from the Southern Ocean to measure the temperature change across the EOT. We measure average temperatures of $\sim 12\text{-}13^\circ\text{C}$ both before and after the transition, which compare well with estimates from nearby cores. A net temperature change of $0.0 \pm 1.1^\circ\text{C}$ is calculated, indicating that the change in $\delta^{18}\text{O}$ seen in planktonic foraminifera at this site is almost exclusively due to changes in ice volume. Based on these temperatures, we calculate absolute $\delta^{18}\text{O}_{\text{sw}}$ values that are much heavier than expected. However, the net change in $\delta^{18}\text{O}_{\text{sw}}$ of $0.8 \pm 0.2\text{‰}$ is within the range of previous estimates. We suggest that vital effects or an offset in the Δ_{47} -calibration could explain the high absolute $\delta^{18}\text{O}_{\text{sw}}$ values.

5.1 Introduction

The Eocene-Oligocene Transition (EOT) stands out as a period of major global climate change, occurring ~34 Ma and marking a shift from a “greenhouse” to “icehouse” conditions and the onset of substantial ice sheet growth on Antarctica. The EOT was first identified as a large increase in the $\delta^{18}\text{O}$ of benthic foraminifera [*Shackleton and Kennett, 1975; Kennett and Shackleton, 1976*]. Since then, isotope excursions have been documented in both benthic and planktonic foraminifera from a number of sites around the world. The magnitude of the benthic transition varies globally, from 1.2-1.7‰, with composite records showing an average of 1.5‰ [*Miller et al., 1987; Zachos et al., 2001; Cramer et al., 2009*]. High-resolution studies show that the transition occurred in two steps of ~40kyr each (named EOT-1 and Oi-1), separated by ~200 kyr of stable $\delta^{18}\text{O}$ values [*Zachos et al., 1996; Coxall et al., 2005; Pusz et al., 2011; Bohaty et al., 2012*].

The isotopic composition of benthic foraminifera is affected by both temperature and the isotopic composition of the water in which the foraminifera grew ($\delta^{18}\text{O}_{\text{sw}}$ in this case). If there were no change in $\delta^{18}\text{O}_{\text{sw}}$, a $\delta^{18}\text{O}$ increase of ~1.5‰ (relative to PDB) in benthic foraminifera would correspond to ~6°C of bottom water cooling. Conversely, if there were no temperature change, the same increase in benthic $\delta^{18}\text{O}$ would correspond to a 1.5‰ (relative to SMOW) increase in $\delta^{18}\text{O}_{\text{sw}}$. To convert this change in $\delta^{18}\text{O}_{\text{sw}}$ to a change in sea level or ice volume requires knowledge of the isotopic composition of the newly formed ice, which is not directly known for the Eocene/Oligocene Antarctic Ice Sheet (AIS). Ice sheets forming in the warmer temperatures of the Eocene/Oligocene would be isotopically heavier than the modern AIS (-56.5‰ (SMOW) for the East AIS and -41-42.5‰ for the West AIS [*Lhomme et al., 2005*]), and would have changed over

the course of ice sheet formation. Modeling studies calculate that initial ice formed at -20 to -25‰, and decreased to -42‰ (SMOW) by the end of ice formation [DeConto *et al.*, 2008]. Regardless of the isotopic composition assumed, a 1.5‰ increase in $\delta^{18}\text{O}_{\text{sw}}$ would require significant ice sheet growth, greater than the modern cryosphere. Therefore, instead of being explained by one or the other, the shift in benthic oxygen isotope values likely represents a combination of cooling and ice growth on Antarctica. In order to determine the relative contributions of these two effects on changing benthic and planktonic $\delta^{18}\text{O}$, temperature or $\delta^{18}\text{O}_{\text{sw}}$ must be independently estimated. In this study, we apply the clumped isotope paleothermometer to foraminifera samples from the Southern Ocean to measure the temperature change across the Eocene-Oligocene transition and use it to estimate changes in $\delta^{18}\text{O}_{\text{sw}}$.

5.1.1 Ice growth on Antarctica during the EOT

Many qualitative proxies suggest increased ice growth on Antarctica around the Eocene-Oligocene transition. In Southern Ocean sediment cores, changes in clay mineralogy and shifts in ϵ_{Nd} towards more continental values coincide with the observed two-step increase in benthic $\delta^{18}\text{O}$, signifying increased physical weathering on Antarctica [Robert and Kennett, 1997; Ehrmann and Mackensen, 1992; Scher *et al.*, 2011]. The appearance of ice-rafted debris in open-ocean sediments during the second step implies that significant continental ice existed on Antarctica by the end of the EOT [Scher *et al.*, 2011].

More direct measures of ice growth across this period can be calculated from sedimentological evidence of changes in sea level near coastal sites. Sedimentological

studies of shallow marine sections in Italy document a drop in sea level of 20m during the first step (EOT-1) and 50-60m during the second step (Oi-1) of the transition [*Houben et al.*, 2012]. Backstripping methods and benthic biofacies changes on the Alabama coast and New Jersey shelf suggested <25m sea level fall for the first step (EOT-1) and 80 ± 25 m for the second step (Oi-1) [*Miller et al.*, 2009; *Kominz and Pekar*, 2001]. Both these indicators of ice growth suggest the first step of the transition was mainly a cooling event and the second was a combination of ice growth and cooling [*Miller et al.*, 2009; *Houben et al.*, 2012].

5.1.2 Temperature change across the EOT

Initial attempts to independently estimate the temperature change across the EOT used the Mg/Ca proxy and showed no change or a small warming of bottom waters [*Lear et al.*, 2000; *Billups and Schrag*, 2003; *Lear et al.*, 2004]. The apparent increase in bottom water temperatures across this transition requires a change in $\delta^{18}\text{O}_{\text{sw}}$ greater than the magnitude of the observed change in benthic $\delta^{18}\text{O}$. The volume of ice growth implied by these estimates is hard to accommodate on Antarctica alone, suggesting northern hemisphere ice accumulation occurred as well. Evidence of ice-rafting in the Nordic Seas prior to the EOT support this hypothesis [*Eldrett et al.*, 2007], but pollen records from Greenland imply minimum temperatures too warm to sustain more than high-elevation mountain glaciers in the northern hemisphere [*Eldrett et al.*, 2009].

To explain the disagreement between the cooling signal of the benthic $\delta^{18}\text{O}$ and the warming signal implied by Mg/Ca, *Billups and Schrag* [2003] suggested that environmental factors in addition to temperature may have been controlling Mg/Ca, such

as primary productivity. It was later determined that the carbonate ion concentration of seawater ($[\text{CO}_3^{2-}]$) has a significant effect on how Mg is incorporated into carbonate [Elderfield *et al.*, 2006]. A $\sim 1\text{km}$ deepening of the CCD, as seen across the EOT, would perturb the saturation state of the oceans, increasing $[\text{CO}_3^{2-}]$ at depths, and would increase Mg/Ca recorded in benthic foraminifera without any change in temperature. To avoid this corrupting effect, authors looked for shallow-water sites that were above the CCD through the whole transition, where the change in $[\text{CO}_3^{2-}]$ would be less dramatic, or attempted to correct for changes in $[\text{CO}_3^{2-}]$ using other elemental ratios. Intermediate water temperatures [Katz *et al.*, 2008; Katz *et al.*, 2011] and surface temperatures [Lear *et al.*, 2008; Wade *et al.*, 2012] from shallow tropical sites showed $\sim 2\text{-}2.5^\circ\text{C}$ cooling across the EOT, mostly occurring in the first step (EOT-1). Thermocline and intermediate-depth waters in the Southern Ocean cooled $2\text{-}3^\circ\text{C}$ [Bohaty *et al.*, 2012], in agreement with estimates of 3°C of cooling in these latitudes from changes in the abundance of cool-water taxa [Wei, 1991], a proxy impervious to changes in $[\text{CO}_3^{2-}]$, but with its own biological uncertainties. Alkenone proxies disagree over whether there was cooling in tropical SSTs, but do show $\sim 3\text{-}5^\circ\text{C}$ cooling in high latitudes [Liu *et al.*, 2009].

In cores that are strongly affected by changes in the CCD, authors attempted to correct for changes in $[\text{CO}_3^{2-}]$ using paired Li/Ca and Mg/Ca measurements [Lear *et al.*, 2010]. Both Li/Ca and Mg/Ca are predominantly controlled by temperature and $[\text{CO}_3^{2-}]$. By measuring both ratios, the influence of each of these factors can be estimated [Lear and Rosenthal, 2006; Lear *et al.*, 2010]. Across the EOT, large shifts in Li/Ca confirm that the changing CCD did indeed affect $[\text{CO}_3^{2-}]$ [Lear and Rosenthal, 2006; Peck *et al.*, 2010]. Correcting for $[\text{CO}_3^{2-}]$ using Li/Ca at two South Atlantic sites caused disagreeing

data (no change and 3°C warming) to come into agreement, both showing 1.5°C cooling across the second step of the transition [Pusz *et al.*, 2011]. However, additional parameters other than temperature and [CO₃²⁻] may affect these elemental ratios (such as growth rate [Rickaby *et al.*, 2002; Thebault *et al.*, 2009]), adding uncertainty to these estimates.

Removing the differing effects of temperature change at many sites from the tropics to the high southern latitudes results in a residual change in benthic δ¹⁸O of ~0.6-0.8‰ to be explained by ice volume (δ¹⁸O_{sw}) changes (Table 5.1). Authors calculated volumes of ice growth anywhere from 40% to 120% of the modern AIS (Table 5.1). The large range in estimates is due both to differences in calculated δ¹⁸O_{sw} change and varying assumptions about the isotopic composition of the new ice sheet. The modern AIS contains 25.4x10⁶ km³ of ice, and is equivalent to 57m of sea level [Lythe *et al.*, 2001], yet because of its light isotopic composition (-56.5‰ (SMOW)), would cause a 0.91‰ change in δ¹⁸O_{sw} if it melted entirely [Lhomme *et al.*, 2005]. By this scaling, a 0.6-0.8‰ shift in δ¹⁸O_{sw} would be equivalent to 1.7-2.3x10⁷ km³ of ice growth at the modern isotopic composition. With the heavier Eocene composition, more ice would be required to explain the same change in δ¹⁸O_{sw}. For comparison, sequence stratigraphy studies estimate ~54m of eustatic sea level (80m apparent sea level) fall at the EOT transition [Pekar *et al.*, 2002], which is nearly equivalent to volume of ice stored in the modern AIS. Ice sheet modeling shows that this range of ice volumes can plausibly grow on Antarctica under late Eocene conditions [DeConto and Pollard, 2003; DeConto *et al.*, 2008; Goldner *et al.*, 2014], eliminating the need for significant ice growth in the northern hemisphere.

Study	Location	Change in $\delta^{18}\text{O}_{\text{sw}}$?	Ice volume estimate
<i>Lear et al.</i> , 2008	Tanzania Drilling Sites (TDP11, 12, 17) (tropical)	0.6‰	70-118% modern AIS
<i>Katz et al.</i> , 2008	Saint Stephens Quarry, Alabama (tropical)	1.2‰	120% modern AIS
<i>Liu et al.</i> , 2009	High latitudes (SH: ODP 511, 277, and 1090; NH: 336 and 913)	0.4-0.85‰	40-120% modern AIS
<i>Peck et al.</i> , 2010	South Atlantic (ODP 1263)	0.6‰	none calculated
<i>Pusz et al.</i> , 2011	South Atlantic (ODP 1090 and 1265)	0.75‰	85-95% modern AIS
<i>Bohaty et al.</i> , 2012	Southern high latitudes (ODP 738, 744, 748)	0.45-0.75‰	60-130% modern EAIS

Table 5.1 Summary of measured temperature changes, calculated $\delta^{18}\text{O}_{\text{sw}}$ increases, and equivalent ice volumes reported in published studies, using a variety of assumptions detailed in each article. AIS= Antarctic Ice Sheet, EAIS = East AIS.

5.1.3 Possible causes of the EOT

Early studies suggested the EOT was caused by the opening of the Drake Passage and the onset of the Antarctic Circumpolar Current (ACC), which thermally isolated the continent and kept it cool enough to sustain significant continental ice [*Kennett and Shackleton, 1976; Kennett, 1977*]. There is controversy over the timing of the opening of the Drake Passage, and a recent review found that it would not have been deep enough to sustain a full ACC until 22 Ma, much too late to explain the EOT [*Barker and Thomas, 2004*]. However, neodymium isotopes suggest that the passage was open to shallow or intermediate depths by 37 Ma, prior to the EOT [*Scher and Martin, 2006*]. A partially-opened Drake Passage could still allow a proto-ACC to form, which would begin to change Southern Ocean circulation and cause some thermal isolation [*Katz et al., 2011*]. Model runs with the Drake Passage open and closed show that this change alone was not

enough to drive ice sheet growth on Antarctica [*DeConto and Pollard, 2003; Goldner et al., 2014*].

The decrease in pCO₂ that occurred across this transition has also been proposed as a driver of cooling and ice growth. The Eocene was characterized by pCO₂ levels above 1000ppm [*Lowenstein and Demicco, 2006; Pagani et al., 2011; Pearson et al., 2009; Breecker et al., 2010*], which declined to ~600-700ppm by the end of the EOT [*Pearson et al., 2009; Pagani et al., 2011*]. These lower levels are consistent with the threshold for Antarctic glaciation produced in models [*DeConto et al., 2008*]. In addition, observations of cooling in both the northern and southern high latitudes is more consistent with declining pCO₂ than opening of the Drake Passage, which would have had stronger local effects [*Liu et al., 2009*]. Orbital configurations during the transition favored cooler summers (decreased seasonality), which likely allowed for ice accumulation on land [*Coxall et al., 2005*]. Feedbacks between ice sheet growth and ocean circulation under decreasing pCO₂ are sufficient to explain the observed ocean temperature pattern without the need for gateway changes [*Goldner et al., 2014*].

The timing of the EOT also coincides with changes in ocean circulation and deepwater formation in the northern hemisphere. A reduction in strength of the Icelandic mantle plume resulted in deepening of the Greenland-Scotland-Faroe Ridge around the EOT and allowed the overflow of dense water from the Norwegian Sea into the North Atlantic for the first time [*Abelson et al., 2008*]. Initiation of sediment deposition at the Feni Drift [*Wold, 1994*] and the Southeast Faroe Drift [*Davies et al., 2001*] document this new deepwater flow, and neodymium isotopes in the South Atlantic indicate increased contribution of northern-sourced waters to deep waters in the Atlantic basin [*Via and*

Thomas, 2006]. These changes in ocean circulation may also have played an indirect role in changing global climate at the EOT, due to the highly coupled nature of the climate system.

5.1.4 Determination of temperature change using clumped isotopes

The clumped isotope proxy is ideally suited to study the EOT, because both temperature and $\delta^{18}\text{O}_{\text{sw}}$ changed together, and large perturbations to the ocean's carbonate chemistry complicate Mg/Ca measurements. Clumped isotopes have been used to reconstruct terrestrial temperature change across this period in northern mid-latitudes [*Hren et al.*, 2013], but have not yet been used to look at ocean temperature changes. Middle to Late Eocene temperatures in high southern latitudes have been measured using clumped isotopes on bivalves, but this record does not extend across the EOT [*Douglas et al.*, 2014].

In this study, we apply the clumped isotope proxy to planktonic foraminifera samples from the Southern Ocean to reconstruct temperature and $\delta^{18}\text{O}_{\text{sw}}$ changes across this transition. A variety of foraminifera species have been shown to follow the same Δ_{47} -T relationship as other biogenic carbonates [*Tripati et al.*, 2010; *Grauel et al.*, 2013]. In order to measure sample-limited materials like foraminifera, a new method that reduces sample size requirements for clumped isotopes was developed and will be employed in this study [*Petersen and Schrag*, in revision].

5.2 Methods and Materials

5.2.1 Site ODP 689B

Site ODP 689B was selected for this study due to its location proximal to Antarctica, and the previous work that has been done on this core [Kennett and Stott, 1990; Mackensen and Ehrmann, 1992; Mead and Hodell, 1995; Billups and Schrag, 2002; 2003; Bohaty *et al.*, 2012]. Core 689B was taken on ODP Leg 113, and is located at 64°N, 3°E [Barker *et al.*, 1988]. Site 689B is located on the Maud Rise in the Weddell Sea, at a modern depth of 2080m and a paleodepth of ~1650m [Kennett and Stott, 1990]. This core has continuous recovery across the EOT, lies above the CCD, and has good carbonate preservation (>75% CaCO₃) [Barker *et al.*, 1988]. Core segments from 689B-12H-7 to 689B-14H-7 were sampled over the depth interval 110.22 – 129.37mbsf, yielding 13 depth horizons with sufficient sample material (Table 5.3). This interval spans 31.6-35.4 Ma and encapsulates the EOT transition itself.

The age model in this core was created using datums selected by Kennett and Stott [1990] and SpeiB [1990] with additional datums from Mead and Hodell [1995]. Seven datums span the depths of the samples in this study (Table 5.2). Chron assignments have been adjusted following Mead and Hodell [1995] and ages of these datums have been adjusted from their originally assigned ages to those published by Berggren *et al.* [1995] to reflect updates to the magnetostratigraphy timescale. Sample ages were calculated by linear interpolation between the adjacent datums. Core segments, sample depths, and interpolated ages are shown in Table 5.3.

In this core, the EOT is marked by a ~1.2‰ increase in both benthic and planktonic $\delta^{18}\text{O}$ [Kennett and Stott, 1990; Mackensen and Ehrmann, 1992; Mead and

Hodell, 1995; Bohaty *et al.*, 2012]. Bulk sediment carbonate also shows an increase in $\delta^{18}\text{O}$ of similar magnitude [Shackleton and Hall, 1989]. Across the study interval, percent carbonate in the sediment decreases from ~90% to ~60% and the non-biogenic fraction, opal fraction, and terrigenous silt fraction increases due to an increased input of ice-rafted debris from Antarctica [Ehrmann and Mackensen, 1992]. Mg/Ca records from planktonic and benthic foraminifera show excursions around the transition itself, but display similar stable values in the intervals before and after the transition period [Billups and Schrag, 2003; Bohaty *et al.*, 2012].

Depth (mbsf)	Datum Description	Age (Ma)
106.87	Base C12n	30.939
116.71	Top C13n	33.058
119.69	Base C13n	33.545
124.09	Top C15n	34.655
125.07	Base C15n	34.940
128.32	Top C16n	35.343
134.02	Base C16n-1	35.536

Table 5.2 Datum levels used for constructing timescale in core ODP 689B. Selected datums span the depth range of samples measured in this study. Depths and assigned chrons from Kennett and Stott [1990] and SpeiB [1990], updated following Mead and Hodell [1995], with chron ages updated to Berggren *et al.* [1995], as described in the text.

Core	Segment	Depth in segment (cm)	Depth below sea floor (mbsf)	Age (Ma)
12H	7	22	110.22	31.660
13H	1	21	110.81	31.787
13H	2	17	112.27	32.102
13H	3	17	113.77	32.425
13H	4	20	115.3	32.754
14H	1	16	120.36	33.714
14H	1	68	120.88	33.845
14H	1	118	121.38	33.971
14H	2	67	122.37	34.221
14H	2	119	122.89	34.352
14H	3	20	123.4	34.481
14H	4	20	124.9	34.891
14H	7	17	129.37	35.377

Table 5.3 Depth horizons of measured samples with core segment information and calculated ages, found using linear interpolation between datums in Table 5.2.

5.2.2 Sample preparation

Wet sediment was prepared for picking foraminifera in the course of a previous study [Billups and Schrag, 2003], and the procedure is described by Billups and Schrag [2002]. Bulk sediment samples were dried in the oven, soaked in a metahexaphosphate solution buffered to a pH of 7.5, and washed through a 63 μ m sieve. In this study, a second step of dry-sieving was performed to capture only the >150 μ m size fraction, from which foraminifera were individually picked.

For each sample, two planktonic species *Subbotina angiporoides* (hereafter *S. ang*) and *Subbotina utilisindex* (hereafter *S. util*) were picked. These species are both thought to have descended from *Subbotina linaperta* in the middle and late Eocene, respectively [Pearson et al., 2006]. All three of these *Subbotina* species have been designated as thermocline-dwellers based on having $\delta^{18}\text{O}$ values intermediate between benthic species and the lightest planktonic species (*Globigerina angiporoides* and *Globigerina utilisindex* [Poore and Matthews, 1984]; *Globigerina angiporoides* and *Subbotina linaperta*, [Keigwin and Corliss, 1986]). This type of “ranking” of foraminifera species based on their $\delta^{18}\text{O}$ values does not account for possible vital effects, which are difficult to judge in extinct species like these. In one depth horizon, the surface-dwelling species *Chiloguembelina cubensis* was prevalent and two samples were measured.

Picked foraminifera were sonicated for 20-30 seconds and rinsed with dI water to remove any caked sediment. This was repeated multiple times until the solute no longer became cloudy after sonication. Cleaned foraminifera were placed in an oven at 35°C to

dry overnight. Dry foraminifera were separated into 1.1-2.5mg aliquots for measurement, with the majority weighing 1.5-2.2mg.

5.2.3 Clumped isotope measurement and data correction

The clumped isotope measurement was made using the high-efficiency sample preparation inlet and the dual-reservoir measurement technique described in Chapter 4 [Petersen and Schrag, in revision]. Foraminifera samples were reacted in phosphoric acid at 90°C in a common acid bath to produce CO₂. CO₂ was then cleaned of contaminants by passing through a U-trap filled with Porapac Q material, held at -11°C. Finally, clean CO₂ was introduced into the mass spectrometer from a fixed reservoir. Reference gas entered the mass spectrometer from an identical reference reservoir filled to an equal pressure by compression of the reference bellows based on matching m/z 47 beam intensity. Both reservoirs were closed off and allowed to decrease in pressure during the measurement period of 2 hours 20 minutes. Measurements were made on a Thermo Finnegan MAT 253, equipped with 5 cups measuring masses 44 to 48 (resistors of 3E7, 3E9, 1E10, 1E12, and 1E12 Ω , respectively). Samples were each run for 7-9 acquisitions of 14 cycles with 26 seconds integration time, at starting voltages between 800mV and 3500mV on m/z 47, depending on sample size and sensitivity of the instrument at the time.

Raw voltages were converted to Δ_{47} using the calculations described by Huntington *et al.* [2009]. Measured Δ_{47} values samples and carbonate standards were corrected to the absolute reference frame using heated gases (1000°C), and gases equilibrated with water at 35°C and 10°C, as described by Dennis *et al.* [2011].

Carbonate standards were also run alongside samples. These included the in-house standards CM2 (Cararra marble, $\Delta_{47} = 0.395 \pm 0.005\text{‰}$) and RTG (tropical coral, $\Delta_{47} = 0.731 \pm 0.007\text{‰}$), and the international standard NBS19 (marble, $\Delta_{47} = 0.384 \pm 0.007\text{‰}$), whose values were determined by previous studies [Dennis *et al.*, 2011; Dennis *thesis*, 2011]. Once in the absolute reference frame, carbonate data was corrected for fractionation during acid digestion using the 90°C acid digestion correction factor of 0.092‰ [Henkes *et al.*, 2013]. $\Delta_{47\text{-RFAC}}$ values of samples and standards were next corrected for a newly-identified fractionation between Δ_{48} and Δ_{47} [Petersen and Schrag, in revision]. Finally, the $\Delta_{47\text{-corr}}$ values of unknowns were corrected for scale compression using a secondary transfer function made up of the carbonate standards, as described in Meckler *et al.* [2014]. This final Δ_{47} value was converted to temperature using the published calibration lines of Ghosh *et al.* [2006] (hereafter GH06) and Dennis and Schrag [2010] (hereafter DS10). Two foraminifera-specific calibration studies exist [Tripathi *et al.*, 2010; Grauel *et al.*, 2013], and show general agreement with the GH06 line. However, these comparisons were made between data from different labs that had not been converted into the absolute reference frame, so this similarity may not hold for reference frame-corrected data. We choose to only use calibration studies that have been corrected to the absolute reference frame, because this facilitates more direct comparison between data measured in different labs and at different times. Oxygen and carbon isotope values of unknowns were adjusted based on the mean offset of measured carbonate standards from known values for each measurement period.

5.3 Results

5.3.1 $\delta^{18}\text{O}$ and $\delta^{13}\text{C}$

Stable isotope values of *S. ang* and *S. util* were acquired in the process of making the clumped isotope measurement. Average precision for $\delta^{18}\text{O}$ and $\delta^{13}\text{C}$ were 0.055‰ and 0.082‰ (1 s.d.), respectively for all samples. The larger error on $\delta^{13}\text{C}$ was caused by two samples that replicated poorly, without which the 1 s.d. error would be 0.065‰. Carbonate standards had precision of 0.103‰ and 0.068‰ (1 s.d.) for $\delta^{18}\text{O}$ and $\delta^{13}\text{C}$, respectively. It is unclear why our samples have better precision than the carbonate standards for $\delta^{18}\text{O}$.

Mean $\delta^{18}\text{O}$ values of *S. ang* and *S. util* are very similar to each other, and agree well with published data from this core in which these two species were combined (Figure 5.1) [Bohaty *et al.*, 2012; Mackensen and Ehrmann, 1992]. The high similarity between the two species supports the decision of these studies to not differentiate between *S. ang* and *S. util*. In our study, each measured aliquot was made up of either *S. ang* or *S. util*, but in later analysis, measurements of both species from a single depth horizon were combined.

Samples record a 1.1‰ increase in $\delta^{18}\text{O}$ across this transition. We have no samples from immediately after the transition, where the published high-resolution data records the heaviest $\delta^{18}\text{O}$ values [Bohaty *et al.*, 2012]. However, our first sample from after the transition (13H4-20cm, 32.754 Ma) has a $\delta^{18}\text{O}$ value of 2.6‰, similar to the lowest values recorded by the high-resolution data immediately after the transition [Bohaty *et al.*, 2012]. After the transition, our samples show a trend towards lighter

values, capturing the “rebound” interval that is also visible in the benthic stack [Zachos *et al.*, 2001].

$\delta^{13}\text{C}$ values gradually decrease from 1.4‰ to 1‰ towards the present (Figure 5.2). Our data display similar trends, but slightly heavier (by $\sim 0.1\text{‰}$) values compared with published data [Mackensen and Ehrmann, 1992]. In addition to planktonic and benthic foraminifera records, the stable isotopic composition of the bulk sediment have also been measured by previous studies (Figure 5.1 and 5.2) [Shackleton and Hall, 1989]. Our stable isotope data differ substantially from the bulk sediment values for both $\delta^{13}\text{C}$ and $\delta^{18}\text{O}$, suggesting our cleaning procedures were sufficient to remove any sediment attached to foraminifera tests.

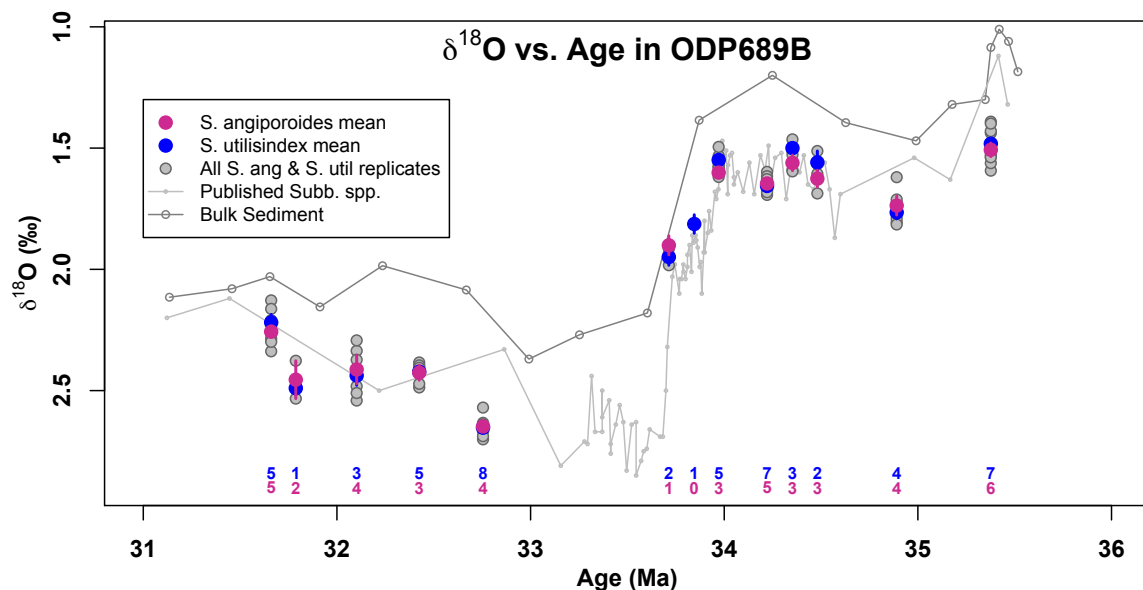


Figure 5.1 $\delta^{18}\text{O}$ of individual replicates (grey filled) and mean values for *S. angiporoides* (purple) and *S. utilisindex* (blue) vs. Age. Published $\delta^{18}\text{O}$ records plotted for comparison using authors age model [Bohaty *et al.*, 2012 (Subb. spp.)] or converted to the age model from this paper [Mackensen and Ehrmann, 1992 (Subb. spp.); Shackleton and Hall, 1989 (bulk sed)]. Number of replicates of *S. ang* and *S. util* are shown in corresponding colors at the bottom. Error bars denote 1SE of mean of the displayed number of replicates. Where only one replicate exists, the internal error on that single point was used.

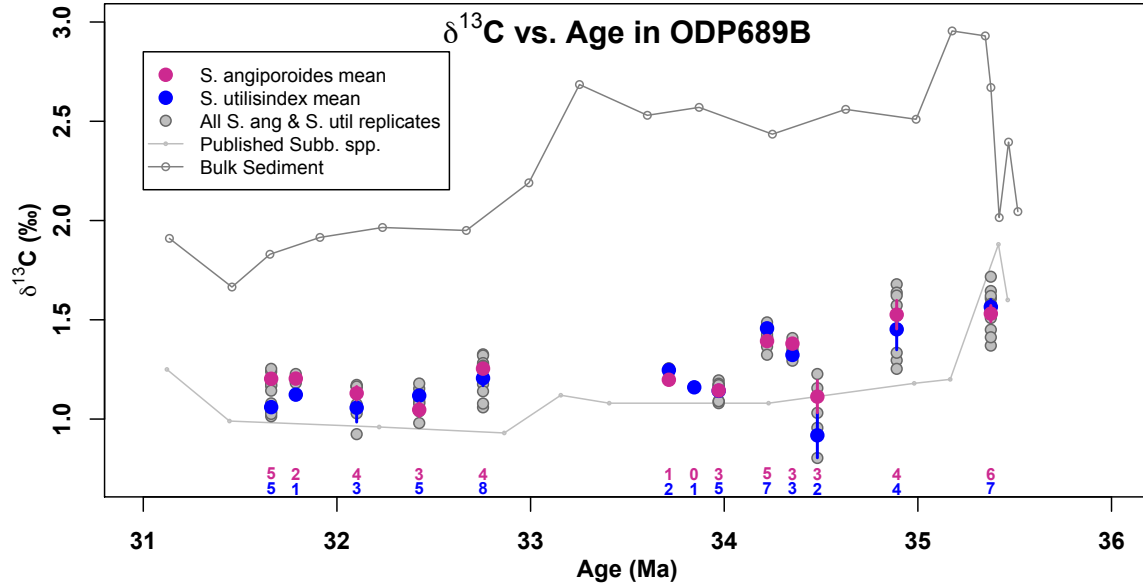


Figure 5.2 δ¹³C of individual replicates (grey filled) and mean values for *S. angiporoides* (purple) and *S. utilisindex* (blue) vs. Age. Published δ¹³C records plotted for comparison [Mackensen and Ehrmann, 1992; Kennett and Stott, 1990; Mead and Hodell, 1995 (Subb. spp.); Shackleton and Hall, 1989 (bulk sed)] plotted on age model from this paper. Number of replicates of *S. ang* and *S. util* are shown in corresponding colors at the bottom. Error bars denote 1SE of mean of displayed number of replicates. Where only one replicate exists, the internal error on that single point was used.

5.3.2 Δ₄₇ across the EOT

Average Δ₄₇ values in our samples range from 0.710 to 0.745‰ (Figure 5.3). The lightest value (0.710), corresponding to the warmest temperature, occurs in sample 14H7-17, from the late Eocene (35.3 Ma). Outside of this oldest sample, all other samples fall within a very narrow Δ₄₇ range, indicating unchanging temperatures across the transition.

Our samples can be divided into four intervals: late-Eocene (1 sample), pre-transition (5 samples), mid-transition (2 samples), and post-transition (5 samples). Due to insufficient foraminifera, we lack data within and immediately following the transition. Of the two samples in the mid-transition interval, only one has sufficient replicates to be reliable. Additionally, these samples only capture the first step of the transition (EOT-1),

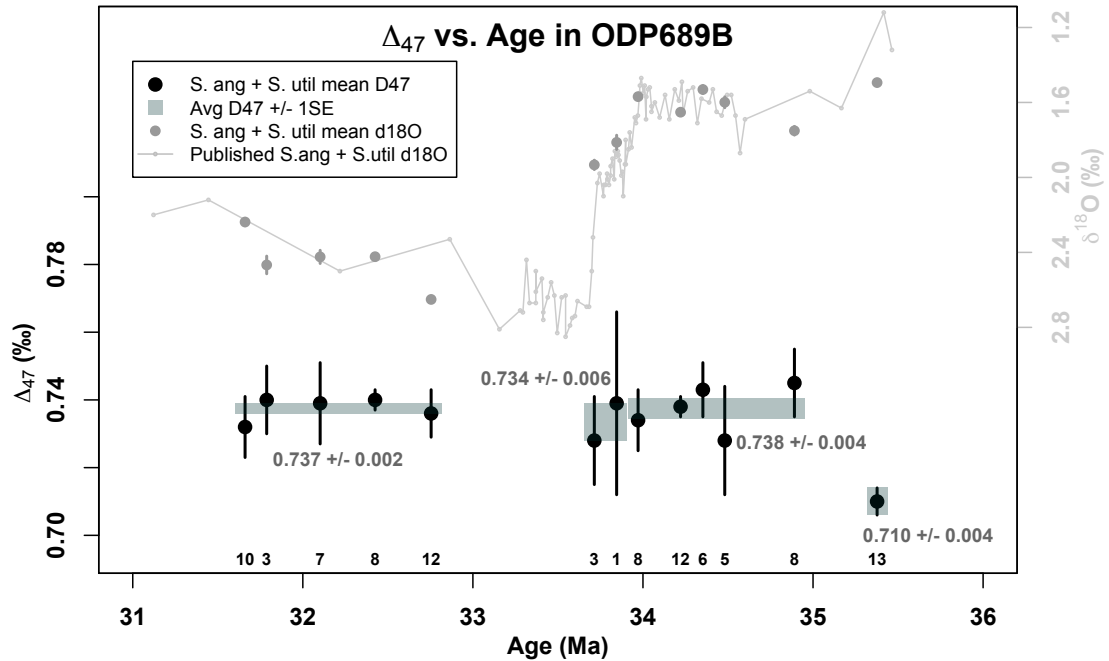


Figure 5.3. Mean Δ_{47} (black circles) and mean $\delta^{18}O$ (grey circles) for each depth horizon vs. Age. Error bars represent external 1 SE errors on the mean. Where only 1 replicate is available, fully-propagated internal 1SE errors are substituted. *S. ang* and *S. util* are combined. Published $\delta^{18}O$ shown for comparison [Bohaty et al., 2012; Mackensen and Ehrmann, 1992]. Grey boxes and numbers show the mean and 1SE of the points in four intervals described in the text. Black numbers at the bottom indicate the number of replicates contained in each depth horizon.

not the larger second step (Oi-1). Therefore, our data do not have the ability to capture the full instantaneous cooling or ice growth. Instead, we attempt to quantify the longer-term shift associated with this transition by comparing the pre- and post-transition intervals, which cover more than one million years each and bracket the transition.

Comparison of the pre- and post-transition mean values reveals negligible change in Δ_{47} (and therefore temperature) across this transition ($-0.001 \pm 0.005\text{‰}$) (Figure 5.3). The only sample that deviates significantly from the others is the late-Eocene sample (14H7-17). This value is made up of 13 analyses, made over two measurement periods. Despite being picked and cleaned at different times and corrected using different standard

gases and carbonates, the mean values from the two measurement periods (n=6 and n=7) only differ by 0.0028‰, well within error of each period's mean value, suggesting that this is not a measurement artifact.

5.3.3 Temperature

Figure 5.4 shows temperatures calculated using the calibrations of *Dennis and Schrag* [2010] (DS10) and *Ghosh et al.* [2006] (GH06), updated into the absolute reference frame [*Dennis et al.*, 2011]. Each individual replicate was converted to temperature, and mean temperatures and 1 SE errors were calculated for each depth horizons. Mean values for depth horizons were combined to calculate average temperatures in each of the four intervals described above. Comparing the pre- and post-transition averages, both calibration lines result in no temperature change across the interval. Combining the errors in quadrature, the GH06 calibration calculates $0.0 \pm 0.7^\circ\text{C}$ of temperature change and the DS10 calibration calculates $0.0 \pm 1.1^\circ\text{C}$ of temperature change. Absolute temperatures differ by 8-9°C between the two studies, with the GH06 calibration calculating warmer temperatures. Excluding the late-Eocene sample, average DS10 temperatures are 12.4°C, whereas average GH06 temperatures are 21.7°C.

5.3.4 $\delta^{18}\text{O}_{\text{sw}}$ across the EOT

Using the measured $\delta^{18}\text{O}$ values and DS10-calculated temperatures, the isotopic composition of seawater can be determined at each depth horizon. This calculation is performed using the $\delta^{18}\text{O}$ -T equilibrium relationship of *Kim and O'Neil* [1997]. Calculated $\delta^{18}\text{O}_{\text{sw}}$ values are in the range of 1‰ to 2‰, and the late-Eocene sample is

~3‰. Although $\delta^{18}\text{O}$ values change dramatically, both through the transition and within the “rebound” interval, Δ_{47} values remain constant, signifying that the large change in foraminiferal $\delta^{18}\text{O}$ is due mainly to changes in $\delta^{18}\text{O}_{\text{sw}}$. The pre-transition mean $\delta^{18}\text{O}_{\text{sw}}$ is $1.2 \pm 0.2\text{‰}$ and the post-transition mean is $2.0 \pm 0.1\text{‰}$. This yields a change in $\delta^{18}\text{O}_{\text{sw}}$ of $0.8 \pm 0.2\text{‰}$ across the whole transition. This falls within the range of estimates determined by previous studies (Table 5.1). Identical calculations done using the GH06-calculated temperatures yield heavier absolute $\delta^{18}\text{O}_{\text{sw}}$ estimates ($3.3 \pm 0.1\text{‰}$ and $4.1 \pm 0.1\text{‰}$ for pre- and post-transition, respectively), but the same net change ($0.8 \pm 0.1\text{‰}$).

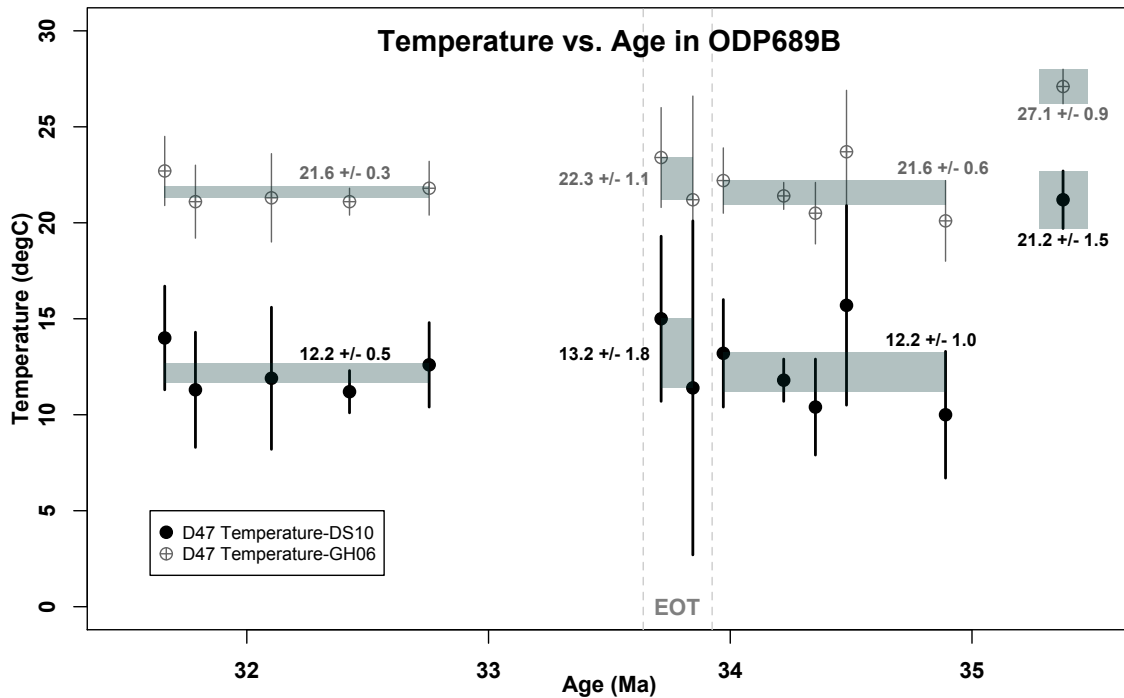


Figure 5.4 Temperature calculated using the *Dennis and Schrag* [2010] and *Ghosh et al.* [2006] calibration lines, both updated to the absolute reference frame [*Dennis et al.*, 2011]. Error bars on each point represent 1SE on the mean of all replicates at that depth horizon. Where only one replicate is available, the internal error (fully propagated) is used. Depth horizons have been combined into 4 intervals (described in the text). Grey boxes show average temperature and 1SE error of the included depth horizons. Where only one depth horizon is included (late-Eocene), the 1SE error from averaging replicates at that depth horizon is used.

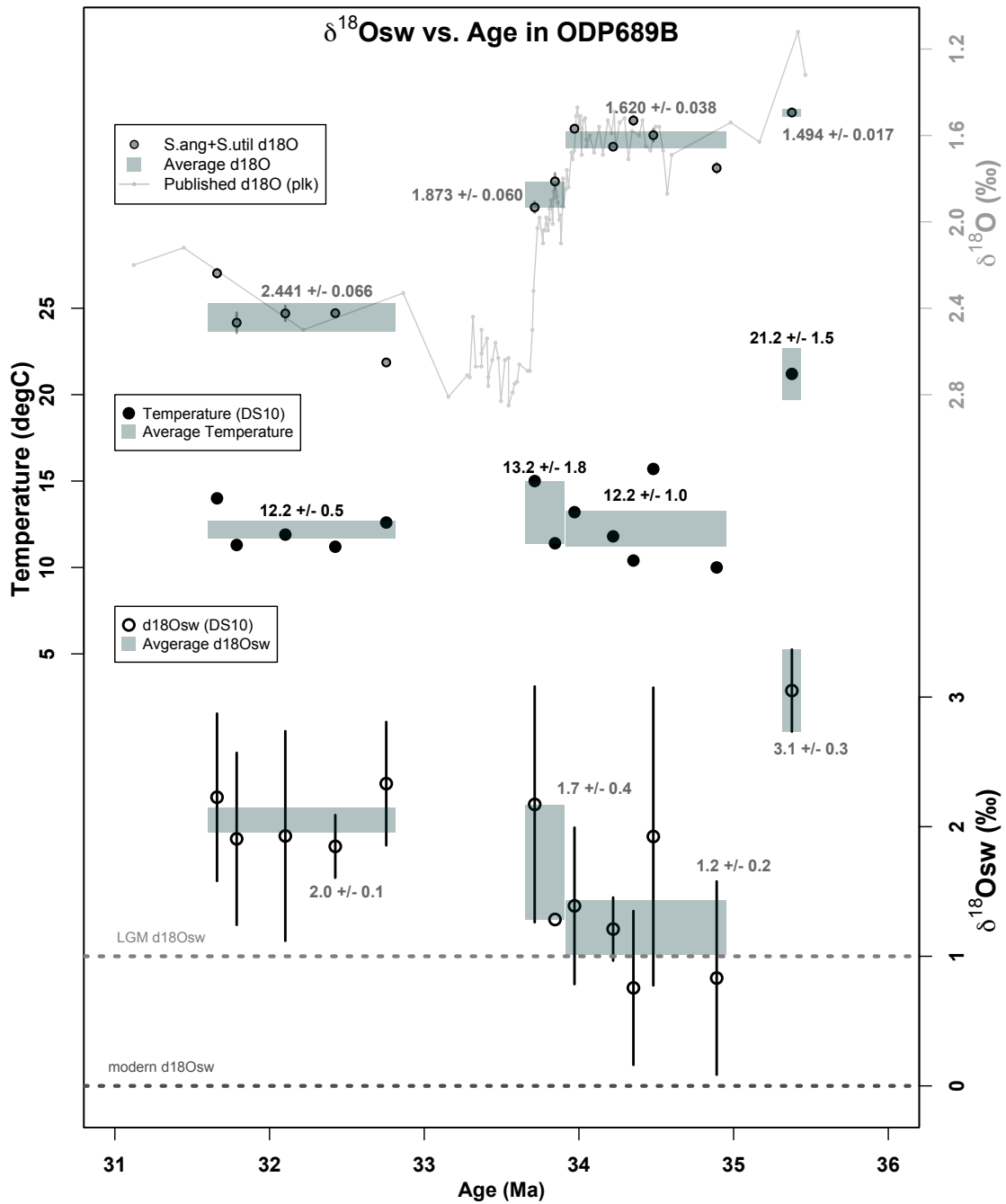


Figure 5.5 Comparison of planktonic $\delta^{18}O$, Δ_{47} -derived temperature (without error bars), calculated using the DS10 calibration, and corresponding $\delta^{18}O_{sw}$. LGM and modern $\delta^{18}O_{sw}$ values are shown for comparison. Grey boxes and text indicate average values for four intervals described in the text.

This change in $\delta^{18}\text{O}_{\text{sw}}$ can be converted to a change in sea level or a volume of ice by assuming an isotopic composition for the growing ice ($\delta^{18}\text{O}_{\text{ice}}$). Modeling studies estimate $\delta^{18}\text{O}_{\text{ice}}$ values ranging from -20 to -25‰ initially, to as light as -42‰ near the end of ice growth [DeConto *et al.*, 2008]. For comparison, the modern West AIS and East AIS have average compositions of -41 to -42.5‰ and -56.5‰, respectively [Lhomme *et al.*, 2005]. Table 5.4 shows calculated volumes of ice for $\delta^{18}\text{O}_{\text{ice}}$ values ranging from -30‰ to -45‰ (SMOW), as well as a comparison to modern AIS volume and an equivalent sea level change. Using the average estimated change in $\delta^{18}\text{O}_{\text{sw}}$ (0.8‰) and an intermediate value for $\delta^{18}\text{O}_{\text{ice}}$ (-35 to -40‰), we estimate 124-140% of modern Antarctic ice volume, or $3.1\text{-}3.5 \times 10^7 \text{ km}^3$ of ice.

5.4 Discussion

5.4.1 Comparison to temperature estimates from other proxies

Temperatures calculated using two calibration lines, DS10 and GH06, differed significantly, with average values of 12.4°C and 21.7°C, respectively (excluding the late-Eocene sample). Other temperature reconstructions from nearby sites compare well with the temperatures calculated by the DS10 calibration, whereas the GH06 temperatures appear too high (Figure 5.6). A multi-proxy study reported temperatures on Seymour Island (current location = 64°S, 56°W, paleolatitude = 67°S) from TEX_{86} and Δ_{47} measurements [Douglas *et al.*, 2014]. At 34 Ma, they measured temperatures of $14.5 \pm 1.4^\circ\text{C}$ and $13.0 \pm 1.5^\circ\text{C}$ from the two proxies [Douglas *et al.*, 2014], in good agreement with our nearest data point at $13.2 \pm 2.8^\circ\text{C}$ and the pre-transition average values of $12.2 \pm$

Average $\delta^{18}\text{O}_{\text{ice}}$	Calculated amount of ice growth	Change in $\delta^{18}\text{O}_{\text{sw}} = 0.6\text{‰}$	Change in $\delta^{18}\text{O}_{\text{sw}} = 0.8\text{‰}$	Change in $\delta^{18}\text{O}_{\text{sw}} = 1.0\text{‰}$
$\delta^{18}\text{O}_{\text{ice}} = -30\text{‰}$	Mass of ice ($\times 10^{19}$ kg)	2.9	3.8	4.7
	Ice Volume ($\times 10^7$ km ³)	3.2	4.1	5.1
	% Modern AIS	128%	164%	204%
	Sea Level equivalent	88m	113m	141m
$\delta^{18}\text{O}_{\text{ice}} = -35\text{‰}$	Mass of ice ($\times 10^{19}$ kg)	2.5	3.2	4.0
	Ice Volume ($\times 10^7$ km ³)	2.7	3.5	4.4
	% Modern AIS	108%	140%	176%
	Sea Level equivalent	75m	97m	122m
$\delta^{18}\text{O}_{\text{ice}} = -40\text{‰}$	Mass of ice ($\times 10^{19}$ kg)	2.1	2.8	3.5
	Ice Volume ($\times 10^7$ km ³)	2.3	3.1	3.8
	% Modern AIS	92%	124%	152%
	Sea Level equivalent	64m	86m	105m
$\delta^{18}\text{O}_{\text{ice}} = -45\text{‰}$	Mass of ice ($\times 10^{19}$ kg)	1.9	2.5	3.1
	Ice Volume ($\times 10^7$ km ³)	2.1	2.7	3.4
	% Modern AIS	84%	108%	136%
	Sea Level equivalent	58m	75m	94m

Table 5.4 Calculated amount of ice growth for different isotopic compositions of new ice ($\delta^{18}\text{O}_{\text{ice}} = -30\text{‰}$ to -45‰) and estimated changes in $\delta^{18}\text{O}_{\text{sw}}$ ($0.8 \pm 0.2\text{‰}$). Calculations use volume estimates of modern ocean (1.33×10^9 km³ [Charette and Smith, 2010]), Antarctic Ice Sheet (2.47×10^7 km³ [Lythe et al., 2001]), and Greenland Ice Sheet (2.93×10^6 km³ [Bamber et al., 2001]), mean isotopic compositions of WAIS (-41.75‰), EAIS (-56.5‰), and Greenland (-35.5‰) relative to SMOW from Lhomme et al. [2005], relative contribution of EAIS and WAIS from sea level estimates, average densities of glacial ice (917 kg/m³) and sea water (1028 kg/m³) from Lythe et al. [2001]. Modern seawater is assumed to have a composition of 0‰ (SMOW). Ice-free ocean is calculated using these values to have a composition of -0.96‰ (SMOW). Conversion to sea level equivalent made using a fixed ocean area of 3.62×10^8 km². Our best estimate of ice volume growth is highlighted.

1.0°C. Seymore Island is currently located at the same latitude as ODP 689 (64°S), and modeling studies of Eocene sea surface temperatures suggest these two sites should have similar temperatures [Douglas *et al.*, 2014].

Another multi-proxy study using TEX₈₆ and U^K₃₇ measured temperatures before and after the EOT at Site 511 (current location, 51°S, 46°W, paleolatitude = 52.5°S) [Liu *et al.*, 2009]. Temperatures from the two proxies combined are 19.3 ± 1.8°C before the transition and 11.4 ± 1.4°C afterwards. This study does not have data coverage immediately prior to or across the actual transition. The pre-transition average agrees with our late-Eocene sample (21.2 ± 1.5°C). The post-transition average agrees very well with our post-transition mean of 12.2 ± 0.5°C. Site 511 is located farther north than ODP 689, but may have been influenced by similar surface waters. Eocene modeling studies produce a gyre in the Weddell Sea circulating clockwise that would have brought waters from ODP689 up the coast to site 511 [Douglas *et al.*, 2014], which may explain the similar temperatures at these two sites.

5.4.2 Lack of temperature change at ODP689

Most recent studies of the EOT record some amount of cooling across the transition, which is needed to account for the large magnitude change in δ¹⁸O without excessive ice growth. Our measurements on thermocline-dwelling *S. ang* and *S. util* record no change in temperature. One possible explanation is that these species have a strong temperature preference and adjusted their depth habitat to maintain the same thermal habitat while the overall ocean was cooling. Compared with surface-dwellers,

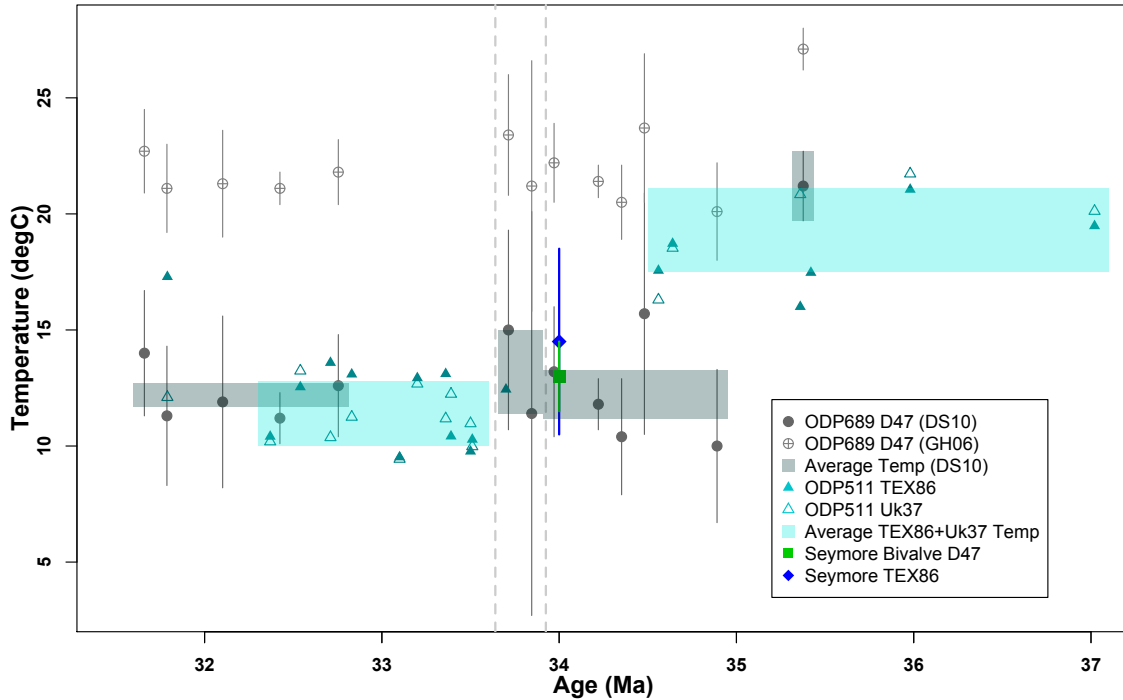


Figure 5.6 A comparison of temperatures calculated with the two calibrations to data from other studies. TEX₈₆ and U^K₃₇ data from ODP511 from *Liu et al.* [2009]. Δ₄₇ and TEX₈₆ data from Seymore Island from *Douglas et al.* [2014].

thermocline-dwelling species would be able to more easily maintain the same temperature environment due to the large thermal gradient without changing the depth (and therefore light conditions) in which they lived. Another study that measured Mg/Ca on *S. util* in the South Atlantic also found no change in temperature across the EOT [*Peck et al.*, 2010]. If these species do change regulate their thermal environment by changing their depth habitat, then changes in δ¹⁸O recorded in their shells should isolate local changes in δ¹⁸O_{sw}.

5.4.3 Extremely high δ¹⁸O_{sw} values

Despite our DS10 temperatures agreeing with nearby sites, the calculated δ¹⁸O_{sw} values are unreasonably high. δ¹⁸O_{sw} values of 1-2‰ require ice volumes in excess of the

Last Glacial Maximum, which are hard to justify, especially for this time period. This implies that the measured temperatures are too warm, even with the DS10 calibration (warmer GH06 temperatures result in even heavier $\delta^{18}\text{O}_{\text{sw}}$ values). $\delta^{18}\text{O}_{\text{sw}}$ values are expected to be between -1 and 0‰ pre-transition, indicating the existence of little continental ice prior to this ice growth event, nearly 2‰ lighter than values calculated in this study.

This discrepancy between calculated and expected $\delta^{18}\text{O}_{\text{sw}}$ values may be due to errors in the absolute $\Delta_{47}\text{-T}$ calibration or possibly to vital effects in this extinct species of foraminifera. Differences in the $\Delta_{47}\text{-T}$ calibration would influence absolute temperatures (and $\delta^{18}\text{O}_{\text{sw}}$) values, but would not have a large impact on the calculated change in temperature, which would be zero regardless of the choice of calibration (as demonstrated by the equivalent change in temperature calculated by the GH06 and DN10 calibrations). Vital effects in foraminifera are generally expressed as a fixed offset from equilibrium values (e.g. +0.64 for *Cibicidoides spp.*), so would also only effect the absolute temperatures and $\delta^{18}\text{O}_{\text{sw}}$ values.

The calculated ice volume increase of 124-140% of the modern Antarctic ice sheet is on the higher end of previous estimates (Table 5.1), but is still plausible. Modeling studies have shown that ice sheets on the order of $2.0\text{-}2.1 \times 10^7 \text{ km}^3$ can be sustained in Eocene-Oligocene conditions [Goldner *et al.*, 2014], which is about 2/3 of our calculated ice volume. At the EOT, the land area of Antarctica was 10-20% larger than today, which, based on the curvature of a growing ice sheet, would scale to an even greater increase in potential ice volume [Wilson and Luyendyk, 2009]. If any ice at all

was growing in the northern hemisphere, the required volume on the Antarctic continent would be reduced.

5.4.4 Choice of clumped isotope calibration line

The absolute $\delta^{18}\text{O}_{\text{sw}}$ values calculated with our Δ_{47} -derived temperatures appear too heavy, indicating the temperature estimates may be too high. This could be due to an offset in the Δ_{47} -T calibration. Published calibration lines that convert Δ_{47} into temperature have been published by a number of authors, and were created by measurement of synthetic carbonates grown in the lab [*Ghosh et al.*, 2006; *Dennis and Schrag*, 2010; *Zaarur et al.*, 2013; *Tang et al.*, 2014] biogenic carbonates with known growth temperatures [*Ghosh et al.*, 2006; *Came et al.*, 2007; *Tripati et al.*, 2010; *Henkes et al.*, 2013; *Grauel et al.*, 2013; *Dennis et al.*, 2013; *Eagle et al.*, 2013; *Came et al.*, 2014], or from theoretical calculations [*Schauble et al.*, 2006; *Guo et al.*, 2009; *Hill et al.*, 2014]. In general, these calibrations tend to fall into two groups – those following a steeper slope similar to the original synthetic + biogenic calibration of *Ghosh et al.* [2006] (GH06) and those that follow a shallower slope similar to the second synthetic calibration study performed by *Dennis and Schrag* [2010] (DS10).

Many possible explanations for these discrepancies have been put forward, such as differences in precipitation methods between the two original synthetic studies, differences in laboratory procedures (e.g. temperature of acid digestion), differences in the Δ_{47} -T relationship for different biogenic carbonate types, etc. Originally, the disparity was attributed to inter-lab differences, but the differences remained even after both the GH06 and DS10 calibration lines were updated into the absolute reference frame [*Dennis*

et al., 2011]. Some correlation exists between the temperature of the acid digestion step (90°C vs. 25°C) and the slope of the calibration lines. Possibly as a result of this, synthetic and biogenic calibrations performed in the same lab tend to agree with each other [*Came et al.*, 2014, and references therein]. Despite this correlation between reaction temperature and calibration line slope, labs using different reaction temperatures (Caltech and Yale at 25°C and Harvard and JHU at 90°C) were able to measure agreeing values in an inter-lab comparison study, once all values were converted to the absolute reference frame [*Dennis et al.*, 2011].

Among the calibrations with the shallower DS10 slope, the intercept values differ by ~0.02-0.04‰ in the Δ_{47} range of interest, with three calibrations coming in lower than DS10 [*Henkes et al.*, 2013; *Schauble et al.*, 2006; *Hill et al.*, 2013] and one coming in higher [*Eagle et al.*, 2013]. A decrease of 0.02‰ in the intercept of the calibration would result in a decrease of ~6.5°C for the mean temperature before and after the transition (from 12.2 to 5.7°C in both periods). At these temperatures, $\delta^{18}\text{O}_{\text{sw}}$ values shift from -0.2‰ before the EOT to 0.6‰ after, showing the same magnitude of change (0.8‰), but absolute values much closer to those expected for a nearly ice-free Eocene.

5.4.5 Comparison to Mg/Ca data

Two studies have measured Mg/Ca on foraminifera from Site ODP 689 [*Billups and Schrag*, 2003; *Bohaty et al.*, 2012]. The conversion of paleo-Mg/Ca values to temperature is complicated by a few factors. First of all, Mg/Ca ratios in seawater have changed through time, and were potentially as low as ~2 at the EOT compared to a modern value of 5.17 [*Evans and Muller*, 2012]. Over short timescales, this influences

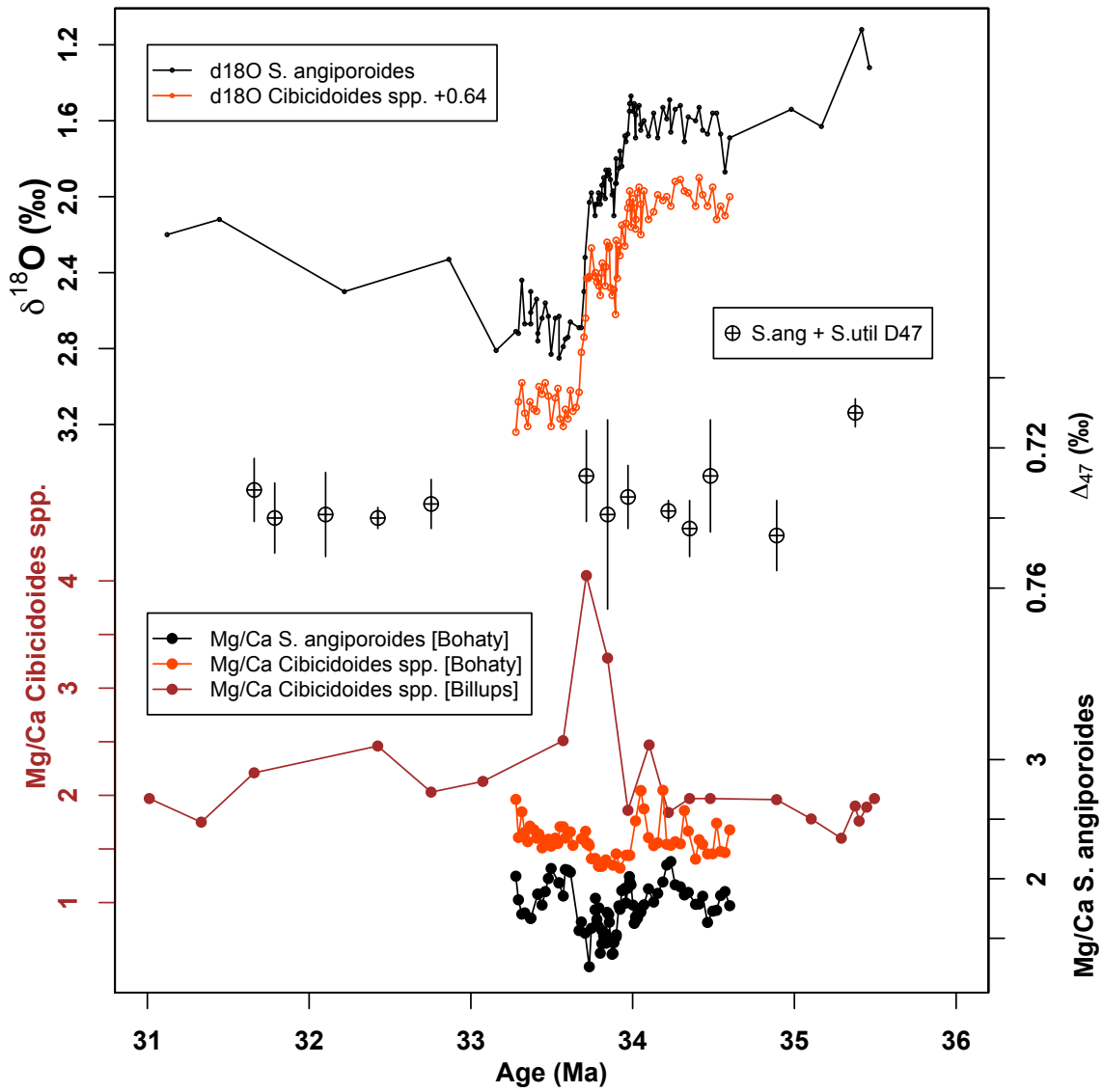


Figure 5.7 Comparison of $\delta^{18}\text{O}$ and Mg/Ca records from *Cibicidoides* spp. (red and brown) and *S. angiporoides* (black) from site ODP689 [Bohaty et al., 2012; Billups and Schrag, 2003] with Δ_{47} data from this study (black crossed circles). All axes are oriented so that the up direction corresponds to warmer temperatures.

absolute temperatures but not relative temperature change because of the long residence time of Mg and Ca in seawater. Second, modern calibration studies have shown interspecies differences in the Mg/Ca-T relationship [Anand *et al.*, 2003], so choosing the right calibration for extinct species is challenging. Finally, it has been shown that changes in carbonate ion concentrations ($[\text{CO}_3^{2-}]$) have a significant effect on the incorporation of Mg into the carbonate lattice [Elderfield *et al.*, 2006], which has the potential to mask the influences of changing temperature. At the EOT, a ~1km deepening of the carbonate compensation depth occurred [Coxall *et al.*, 2005; Palike *et al.*, 2012], which would have increased $[\text{CO}_3^{2-}]$ throughout the water column, but especially at depth. Estimates from paired Li/Ca and Mg/Ca measurements at sites in the South Atlantic [Peck *et al.*, 2010] and equatorial Pacific [Lear *et al.*, 2010] calculate an increase in $[\text{CO}_3^{2-}]$ of 29-36 $\mu\text{mol/kg}$, which has the potential to increase Mg/Ca by 0.25-0.31, the equivalent of a 2-3°C warming signal [Lear *et al.*, 2010].

Both studies show fairly constant Mg/Ca values both before and after the transition, for both benthic and planktonic foraminifera (Figure 5.7) [Billups and Schrag, 2003; Bohaty *et al.*, 2012]. *S. ang*, in particular, shows average values of 1.84 and 1.82 before and after [Bohaty *et al.*, 2012]. This would seem to imply no change in temperature, in agreement with our data, but effects of changing $[\text{CO}_3^{2-}]$ cannot be ruled out. Benthic and planktonic data from Bohaty *et al.* [2012] show similar patterns, whereas benthic data from Billups and Schrag [2003] show an excursion to high Mg/Ca during the transition, implying a warming. The estimated changes in $[\text{CO}_3^{2-}]$ from nearby sites is not enough to explain the magnitude of this shift, and it is curious that it does not appear in the Bohaty *et al* [2012] benthic data. However, the magnitude and timing of changes in

[CO₃²⁻] at site ODP 689 have not been quantified, so these Mg/Ca records are hard to interpret.

The Mg/Ca values of *S. ang* can be converted to temperature using the calibration of *Anand et al.* [2003], which combines many planktonic species. Average temperatures across the whole interval come to 17.0°C using this calibration. However, at the EOT, seawater Mg/Ca was likely around ~2, instead of the modern 5.17 [*Evans and Muller*, 2012]. Scaling the Mg/Ca calibration for this difference, the average temperature increases to 27.5°C. This is warmer than the Δ_{47} -temperatures calculated by both calibrations, and warmer than temperatures from other nearby sites (Figure 5.6). For temperatures calculated from Δ_{47} to be in agreement with Mg/Ca temperatures, Mg/Ca(sw) would have to be ~7.6, which is higher than modern and inconsistent with multiple proxies [*Evans and Muller*, 2012]. This may reflect differences in Mg/Ca-T relationship for this species compared to the modern planktonic species used to generate the calibration [*Anand et al.*, 2003]. These data are therefore hard to reconcile with our and others measurements.

5.4.6 Possible vital effects in *Subbotina* spp.

The $\delta^{18}\text{O}$ -depth “ranking” of *S. ang* and *S. util* as intermediate dwellers due to their heavier $\delta^{18}\text{O}$ values may be incorrect. Instead, these could be surface-dwelling species that fractionate $\delta^{18}\text{O}$ to incorporate more ¹⁸O into their shells than would be expected from equilibrium with seawater. In depth-ranking studies of Eocene-age foraminifera, *S. util* and *S. ang* recorded $\delta^{18}\text{O}$ values 1.39-1.75‰ and 0.04‰ heavier than the lightest $\delta^{18}\text{O}$ recorded by planktonic foraminifera (*Chiloguembelina cubensis*) [*Poore*

and Matthews, 1984]. This is contradictory to what we have observed, which is that $\delta^{18}\text{O}$ values for *S. ang* and *S. util* are nearly identical. None of the samples used by Poore and Matthews [1984] had both *S. ang* and *S. util*, so direct comparison did not occur. At one depth horizon (14H2-67), we measured two replicates of *Chiloguembelina cubensis*, which had $\delta^{18}\text{O}$ values 0.12‰ lighter than the *S. ang* and *S. util* average. The two replicates gave very different Δ_{47} temperatures (14.5 and 37.1°C from DS10), but limited sample material prohibited additional measurements, so we cannot determine whether *C. cubensis* lived in warmer surface waters.

Keigwin and Corliss [1986] use $\delta^{13}\text{C}$ as another metric of depth habitat. $\delta^{13}\text{C}$ in seawater gets lighter with depth, so intermediate-dwelling species should have lighter $\delta^{13}\text{C}$ (because of this gradient) and heavier $\delta^{18}\text{O}$ (because of temperature) than surface-dwelling species. *S. linaperta*, the ancestor of *S. ang* and *S. util* [Pearson et al., 2006], showed $\delta^{18}\text{O}$ values ~1‰ heavier than *C. cubensis* and two other surface-dwelling species, but showed $\delta^{13}\text{C}$ values ~0.75‰ heavier than *C. cubensis* and within error of the other two species, earning it the title of intermediate-depth dweller [Keigwin and Corliss 1986]. In our sample, *C. cubensis* had $\delta^{13}\text{C}$ values ~0.6‰ heavier than the *S. ang* and *S. util* mean, in contradiction with Keigwin and Corliss [1986]. Additional measurements of these two species in ODP689 also show heavier $\delta^{13}\text{C}$ in *C. cubensis* [Kennett and Stott, 1990].

The size of the offset in $\delta^{18}\text{O}$ between *Subbotina* spp. and *C. cubensis* observed by Keigwin and Corliss [1986] and Poore and Matthews [1984] (0-1.75‰), if interpreted as a vital effect, could explain much of the difference in $\delta^{18}\text{O}_{\text{sw}}$ from expected values. If *S. ang* and *S. util* record $\delta^{18}\text{O}$ values 1-2‰ heavier than equilibrium with seawater, the

true $\delta^{18}\text{O}_{\text{sw}}$ would be 1-2‰ lighter than calculated, which would bring estimates in line with a nearly ice-free late Eocene. This also demonstrates the danger of the $\delta^{18}\text{O}$ depth ranking system for determining depth habitat of extinct species, especially using so few samples for comparison [Matthews and Poore 1984; Keigwin and Corliss 1986].

5.4.7 Influence of changing $[\text{CO}_3^{2-}]$ on ice volume estimates

Across the EOT, seawater $[\text{CO}_3^{2-}]$ has been calculated to change on the order of $36\mu\text{mol/kg}$ in the deep Pacific [Lear *et al.*, 2010] and $19\text{-}29\mu\text{mol/kg}$ in the South Atlantic [Lear *et al.*, 2010; Peck *et al.*, 2010] from paired Li/Ca and Mg/Ca measurements. These values agree with a calculated change in $[\text{CO}_3^{2-}]$ of $19\mu\text{mol/kg}$ caused by a 1.2km deepening of the carbonate compensation depth [Lear *et al.*, 2010; Broecker and Peng, 1982]. It has been shown that increases in $[\text{CO}_3^{2-}]$ cause reduced stable isotope values in planktonic foraminifera and other single-celled planktonic organisms with a slope of $-0.0022\text{‰ } \delta^{18}\text{O}/(\mu\text{mol/kg } [\text{CO}_3^{2-}])$ for *Orbulina universa* [Spero *et al.*, 1997], -0.0048 for a coccolithophore species and -0.0243 for a calcareous dinoflagellate [Ziveri *et al.*, 2012]. Based on the above estimates of changes in $[\text{CO}_3^{2-}]$, this could influence $\delta^{18}\text{O}$ values by $0.04\text{-}0.08\text{‰}$ for foraminifera. However, based on the range of slopes observed in various unicellular planktonic calcifying organisms and the single foraminifera species tested, a slope of -0.0022 may not be correct for all foraminifera species. The larger slope for coccolithophores would result in changes in a reduction of post-transition $\delta^{18}\text{O}$ values of $0.09\text{-}0.17\text{‰}$, muting full magnitude of the signal. This influence would differ from site to site, basin to basin, and especially with depth of the core. A site like ODP 1218, which was near the CCD prior to the EOT, saw a large change ($36\mu\text{mol/kg}$ [Lear *et al.*, 2010]),

whereas a shallower site may have seen a smaller impact. These site-to-site and depth-dependent differences may explain some of the range in ice volume estimates, because the calculated changes in $\delta^{18}\text{O}_{\text{sw}}$ may be variably muted according to the local change in $[\text{CO}_3^{2-}]$.

5.5 Conclusions

We have made clumped isotope measurements on foraminifera from the Southern Ocean across the Eocene-Oligocene transition. We observe mean temperatures around 12-13°C using the calibration of *Dennis and Schrag* [2010], both before and after the transition, in line with temperature estimates from nearby sites using other temperature proxies, and with modeled surface ocean circulation before the Drake passage was open [*Douglas et al* 2014; *Liu et al.*, 2009]. We calculate a net change in temperature of $0.0 \pm 1.1^\circ\text{C}$, and a net change in $\delta^{18}\text{O}_{\text{sw}}$ of $0.8 \pm 0.2\text{‰}$ across the transition, resulting in an ice volume increase of $3.1\text{-}3.5 \times 10^7 \text{ km}^3$, equivalent to $\sim 124\text{-}140\%$ of modern AIS. The absolute values of $\delta^{18}\text{O}_{\text{sw}}$ are 1-1.5‰ heavier than expected for this time period. We suggest that this difference could be due to the $\Delta_{47}\text{-T}$ calibration overestimating temperatures, or to vital effects in these species of foraminifera, which was previously mis-identified as an intermediate-depth habitat. Despite high absolute values, the calculated difference in $\delta^{18}\text{O}_{\text{sw}}$ is robust and is within the range of previous estimates.

Acknowledgements

This work was supported by Henry and Wendy Breck and by the GSAS Merit Fellowship. J. Shakun is thanked for instruction on how to pick foraminifera. The authors would like to thank G. Eischeid, S. Manley, and F. Chen for laboratory assistance.

References

- Abelson, M., A. Agnon, and A. Almogi-Labin (2008), Indications for control of the Iceland plume on the Eocene-Oligocene “greenhouse-icehouse” climate transition, *Earth and Planetary Science Letters*, 265 (1-2), 33-48.
- Anand, P., H. Elderfield, and M. H. Conte (2003), Calibration of Mg/Ca thermometry in planktonic foraminifera from a sediment trap time series, *Paleoceanography*, 18(2), 1050.
- Bamber, J. L., R. L. Layberry, and S. P. Gogineni (2001), A new ice thickness and bed data set for the Greenland ice sheet: 1. Measurement, data reduction, and errors, *Journal of Geophysical Research: Atmospheres*, 106(D24), 33773-33780.
- Barker, P. F. and E. Thomas (2004), Origin, signature, and paleoclimatic influence of the Antarctic Circumpolar Current, *Earth Science Reviews*, 66 (1-2), 143-162.
- Barker, PF; Kennett, JP; and Scientific Party (1988), Site 689, *Proceedings of the Ocean Drilling Program, Scientific Results*, 113, 89-181.
- Berggren, W. A., D. V. Kent, C. C. Swisher, and M-P. Aubry (1995), A revised Cenozoic geochronology and chronostratigraphy, *SEPM special papers*, 54, 129-212.
- Billups, K. and D. P. Schrag (2003), Application of benthic foraminiferal Mg/Ca to questions of Cenozoic climate change, *Earth and Planetary Science Letters*, 209(1-2), 181-195.
- Billups, K. and D. P. Schrag (2002), Paleotemperatures and ice volume of the past 27 Myr revisited with paired Mg/Ca and $^{18}\text{O}/^{16}\text{O}$ measurements on benthic foraminifera, *Paleoceanography*, 17 (1), 3-13-11.
- Bohaty, S. M., J. C. Zachos, and M. L. Delaney (2012), Foraminiferal Mg/Ca evidence for Southern Ocean cooling across the Eocene-Oligocene transition, *Earth and Planetary Science Letters*, 317-318, 251-261.

- Breecker, D. O., Z. D. Sharp, and L. D. McFadden (2010), Atmospheric CO₂ concentrations during ancient greenhouse climates were similar to those predicted for A. D. 2100, *Proceedings of the National Academy of Science*, 107(2), 576-580.
- Broecker, W. S. and T-H. Peng (1982), Tracers in the Sea, pp. 169, Lamont-Doherty Geological Observatory of Columbia University, Palisades, New York.
- Came, R. E., J. M. Eiler, J. Veizer, K. Azmy, U. Brand, and C. R. Weidman (2007), Coupling of surface temperatures and atmospheric CO₂ concentration during the Paleozoic era, *Nature*, 449(7159), 198-201.
- Came, R. E., U. Brand, and H. P. Affek (2014), Clumped isotope signatures in modern brachiopod carbonate, *Chemical Geology*, 377(0), 20-30.
- Charette, M. A. and W. H. F. Smith (2010), The Volume of Earth's Ocean, *Oceanography*, 23(2), 112-114.
- Coxall, H. K., P. A. Wilson, H. Palike, C. H. Lear, and J. Backman (2005), Rapid stepwise onset of Antarctic glaciation and deeper calcite compensation in the Pacific Ocean, *Nature*, 433(7021), 53-57.
- Cramer, B. S., J. R. Togweiler, J. D. Wright, M. E. Katz, and K. G. Miller (2009), Ocean overturning since the Late Cretaceous: Inferences from a new benthic foraminiferal isotope compilation, *Paleoceanography*, 24(4), PA4216.
- Davies, R., J. Cartwright, J. Pike, and C. Line (2001), Early Oligocene initiation of North Atlantic Deep Water formation, *Nature*, 410(6831), 917-920.
- DeConto, R. M. and D. Pollard (2003), Rapid Cenozoic glaciation of Antarctica induced by declining atmospheric CO₂, *Nature*, 421(6920), 245-249.
- DeConto, R. M., D. Pollard, P. A. Wilson, H. Palike, C. H. Lear, and M. Pagani (2008), Thresholds for Cenozoic bipolar glaciation, *Nature*, 455, 652-657.
- Dennis, K. J. Ph.D. (2011), Clumped isotope thermometry and its application to Earth's history, Harvard University (Cambridge, MA).
- Dennis, K. J. and D. P. Schrag (2010), Clumped isotope thermometry of carbonatites as an indicator of diagenetic alteration, *Geochimica et Cosmochimica Acta*, 74(14), 4110-4122.
- Dennis, K. J., H. P. Affek, B. H. Passey, D. P. Schrag, and J. M. Eiler (2011), Defining an absolute reference frame for 'clumped' isotope studies of CO₂, *Geochimica et Cosmochimica Acta*, 75(22), 7117-7131.

- Dennis, K. J., J. K. Cochran, N. H. Landman, and D. P. Schrag (2013), The climate of the Late Cretaceous: New insights from the application of the carbonate clumped isotope thermometer to Western Interior Seaway macrofossils, *Earth and Planetary Science Letters*, 362(0), 51-65.
- Douglas, P. M. J., H. P. Affek, L. C. Ivany, A. J. P. Houben, W. P. Sijp, A. Sluijs, S. Schouten, and M. Pagani (2014), Pronounced zonal heterogeneity in Eocene southern high-latitude sea surface temperatures, *Proceedings of the National Academy of Sciences*, 111(18), 6582-6587.
- Eagle, R. A., J. M. Eiler, A. K. Tripathi, J. B. Ries, P. S. Freitas, C. Hiebenthal, A. D. Wanamaker, M. Taviani, M. Elliot, S. Marensi, K. Nakamura, P. Ramirez, and K. Roy (2013), The influence of temperature and seawater carbonate saturation state on the ^{13}C - ^{18}O bond ordering in bivalve mollusks, *Biogeosciences*, 10(7), 4591-4606.
- Ehrmann, W. U. and A. Mackensen (1992), Sedimentological evidence for the formation of an East Antarctic ice sheet in Eocene/Oligocene time, *Palaeogeography, Palaeoclimatology, Palaeoecology*, 93(1-2), 85-112.
- Elderfield, H., J. Yu, P. Anand, T. Kiefer, and B. Nyland (2006), Calibrations for benthic foraminiferal Mg/Ca paleothermometry and the carbonate ion hypothesis, *Earth and Planetary Science Letters*, 250(3-4), 633-649.
- Eldrett, J. S., D. R. Greenwood, I. C. Harding, and M. Huber (2009), Increased seasonality through the Eocene to Oligocene transition in northern high latitudes, *Nature*, 459(7249), 969-973.
- Eldrett, J. S., I. C. Harding, P. A. Wilson, E. Butler, and A. P. Roberts (2007), Continental ice in Greenland during the Eocene and Oligocene, *Nature*, 446(7132), 176-179.
- Evans, D. and W. Muller (2012), Deep time foraminifera Mg/Ca paleothermometry: Nonlinear correction for secular change in seawater Mg/Ca, *Paleoceanography*, 27(4), PA4205.
- Ghosh, P., J. Adkins, H. P. Affek, B. Balta, W. Guo, E. A. Schauble, D. P. Schrag, and J. M. Eiler (2006a), ^{13}C - ^{18}O bonds in carbonate minerals: A new kind of paleothermometer, *Geochimica et Cosmochimica Acta*, 70(6), 1439-1456.
- Goldner, A., N. Herold, and M. Huber (2014), Antarctic glaciation caused ocean circulation changes at the Eocene-Oligocene transition, *Nature*, 511(7511), 574-577.
- Grauel, A.-L., T. W. Schmid, B. Hu, C. Bergami, L. Capotondi, L. Zhou, and S. M. Bernasconi (2013), Calibration and application of the 'clumped isotope' thermometer

- to foraminifera for high-resolution climate reconstructions, *Geochimica et Cosmochimica Acta*, 108(0), 125-140.
- Guo, W., J. L. Mosenfelder, W. A. Goddard III, and J. M. Eiler (2009), Isotopic fractionations associated with phosphoric acid digestion of carbonate minerals: Insights from first-principles theoretical modeling and clumped isotope measurements, *Geochimica et Cosmochimica Acta*, 73(24), 7203-7225.
- Henkes, G. A., B. H. Passey, A. D. Wanamaker, E. L. Grossman, W. G. Ambrose, and M. L. Carroll (2013), Carbonate clumped isotope composition of modern marine mollusks and brachiopod shells, *Geochimica et Cosmochimica Acta*, 106(0), 307-325.
- Hill, P. S., A. K. Tripathi, and E. A. Schauble (2014), Theoretical constraints on the effects of pH, salinity, and temperature on clumped isotope signatures of dissolved inorganic carbon species precipitating carbonate minerals, *Geochimica et Cosmochimica Acta*, 125(0), 610-652.
- Houben, A. J. P., C. A. van Mourik, A. Montanari, R. Coccioni, and H. Brinkhuis (2012), The Eocene-Oligocene transition: Changes in sea level, temperature, or both?, *Palaeogeography, Palaeoclimatology, Palaeoecology*, 335-336, 75-83.
- Hren, M. T., N. D. Sheldon, S. T. Grimes, M. E. Collinson, J. J. Hooker, M. Bugler, and K. C. Lohmann (2013), Terrestrial cooling in Northern Europe during the Eocene-Oligocene transition, *Proceedings of the National Academy of Sciences*, 110(19), 7562-7567.
- Huntington, K. W., J. M. Eiler, H. P. Affek, W. Guo, M. Bonifacie, L. Y. Yeung, N. Thiagarajan, B. H. Passey, A. K. Tripathi, M. Daeron, and R. Came (2009), Methods and limitations of 'clumped' CO₂ isotope (Δ_{47}) analysis by gas-source isotope ratio mass spectrometry. *Journal of Mass Spectrometry*, 44(9), 1318-1329.
- Katz, M. E., B. S. Cramer, J. R. Togweiler, G. Esmay, C. Liu, K. G. Miller, Y. Rosenthal, B. S. Wade, and J. D. Wright (2011), Impact of Antarctic Circumpolar Current Development on Late Paleogene Ocean Structure, *Science*, 332(6033), 1076-1079.
- Katz, M. E., K. G. Miller, J. D. Wright, B. S. Wade, J. V. Browning, B. S. Cramer, and Y. Rosenthal (2008), Stepwise transition from the Eocene greenhouse to the Oligocene icehouse, *Nature Geoscience*, 1(5), 329-334.
- Keigwin, L. D. and B. H. Corliss (1986), Stable isotopes in late middle Eocene to Oligocene foraminifera, *Geological Society of America Bulletin*, 97(3), 335-345.
- Kennett, J. P. (1977), Cenozoic evolution of Antarctic glaciation, the circum-Antarctic Ocean, and their impact on global paleoceanography, *Journal of Geophysical Research*, 82(27), 3843-3860.

- Kennett, J. P. and L. D. Stott (1990), Proteus and Proto-Oceanus: ancestral Paleogene oceans as revealed from Antarctic stable isotope results, ODP Leg 113, *In: Barker, PF; Kennett, JP; et al. (eds.), Proceedings of the Ocean Drilling Program, Scientific Results*, 113, 865-878.
- Kennett, J. P. and N. J. Shackleton (1976), Oxygen isotopic evidence for the development of the psychrosphere 38 Myr ago, *Nature*, 260(5551), 513-515.
- Kim, S-T. and J. R. O'Neil (1997), Equilibrium and nonequilibrium oxygen isotope effects in synthetic carbonates, *Geochimica Cosmochimica Acta*, 61(16), 3461-3475.
- Kominz, M. A. and S. F. Pekar (2001), Oligocene eustasy from two-dimensional sequence stratigraphic backstripping, *Geological Society of America Bulletin*, 113(3), 291-304.
- Lear, C. H., and Y. Rosenthal (2006), Benthic foraminiferal Li/Ca: Insights into Cenozoic seawater carbonate saturation state, *Geology*, 34(11), 985-988.
- Lear, C. H., E. M. Mawbey, and Y. Rosenthal (2010), Cenozoic benthic foraminiferal Mg/Ca and Li/Ca records: Toward unlocking temperatures and saturation states, *Paleoceanography*, 25(4), PA4215.
- Lear, C. H., H. Elderfield, and P. A. Wilson (2000), Cenozoic Deep-Sea Temperatures and Global Ice Volumes from Mg/Ca in Benthic Foraminiferal Calcite, *Science*, 287(5451), 269-272.
- Lear, C. H., T. R. Bailey, P. N. Pearson, H. K. Coxall, and Y. Rosenthal (2008), Cooling and ice growth across the Eocene-Oligocene transition, *Geology*, 36(3), 251-254.
- Lear, C. H., Y. Rosenthal, H. K. Coxall, and P. A. Wilson (2004), Late Eocene to early Miocene ice sheet dynamics and the global carbon cycle, *Paleoceanography*, 19(4), PA4015.
- Lhomme, N., G. K. C. Clarke, and C. Ritz (2005), Global budget of water isotopes inferred from polar ice sheets, *Geophysical Research Letters*, 32(20), L20502.
- Liu, Z., M. Pagani, D. Zinniker, R. DeConto, M. Huber, H. Brinkhuis, S. R. Shah, R. M. Leckie, and A. Pearson (2009), Global Cooling During the Eocene-Oligocene Climate Transition, *Science*, 323(5918), 1187-1190.
- Lowenstein, T. K. and R. V. Demicco (2006), Elevated Eocene Atmospheric CO₂ and its Subsequent Decline, *Science*, 313(5795), 1928.

- Lythe, M. B. and D. G. Vaughan (2001), BEDMAP: A new ice thickness and subglacial topographic model of Antarctica, *Journal of Geophysical Research: Solid Earth*, 106(B6), 11335-11351.
- Mackensen, A. and W. U. Ehrmann (1992), Middle Eocene through Early Oligocene climate history and paleoceanography in the Southern Ocean: Stable oxygen and carbon isotopes from ODP Sites on Maud Rise and Kerguelen Plateau, *Marine Geology*, 108(1), 1-27.
- Mead, G. A. and D. A. Hodell (1995), Controls on the $^{87}\text{Sr}/^{86}\text{Sr}$ composition of seawater from the middle to Eocene to Oligocene: Hole 689B, Maud Rise, Antarctica, *Paleoceanography*, 10(2), 327-346.
- Meckler, A. N., M. Ziegler, M. I. Millan, S. F. M. Breitenbach, and S. M. Bernasconi (2014), Long-term performance of the Kiel carbonate device with a new correction scheme for clumped isotope measurement, *Rapid Communications in Mass Spectrometry*, 28(15), 1705-1715.
- Miller, K. G., J. D. Wright, M. E. Katz, B. S. Wade, J. V. Browning, B. S. Cramer, and Y. Rosenthal (2009), Climate threshold at the Eocene-Oligocene transition: Antarctic ice sheet influence on ocean circulation, *Geological Society of America Special Papers*, 452, 169-178.
- Miller, K. G., R. G. Fairbanks, and G. S. Mountain (1987), Tertiary oxygen isotope synthesis, sea level history, and continental margin erosion, *Paleoceanography*, 2(1), 1-19.
- Pagani, M., M. Huber, Z. Liu, S. M. Bohaty, J. Henderiks, W. Sijp, S. Krishnan, and R. M. DeConto (2011), The Role of Carbon Dioxide During the Onset of Antarctic Glaciation, *Science*, 334(6060), 1261-1264.
- Palike, H. *et al.* (2012), A Cenozoic record of the equatorial Pacific carbonate compensation depth, *Nature*, 488(7413), 609-614.
- Pearson, P. N., *et al.* (2006), Atlas of Eocene planktonic foraminifera, pp.513, Special publication (Cushman Foundation for Foraminiferal Research), Fredericksburg, Virginia.
- Pearson, P. N., G. L. Foster, and B. S. Wade (2009), Atmospheric carbon dioxide through the Eocene-Oligocene climate transition, *Nature*, 461(7267), 1110-1113.
- Peck, V. L., J. Yu, S. Kender, and C. R. Riesselman (2010), Shifting ocean carbonate chemistry during the Eocene-Oligocene climate transition: Implications for deep-ocean Mg/Ca paleothermometry, *Paleoceanography*, 25(4), PA4219.

- Pekar, S. F., N. Christie-Blick, M. A. Kominz, and K. G. Miller (2002), Calibration between eustatic estimates from backstripping and oxygen isotopic records for the Oligocene, *Geology*, 30(10), 903-906.
- Poore, R. Z. and R. K. Matthews (1984), Oxygen isotope ranking of Late Eocene and Oligocene planktonic foraminifers: Implications for Oligocene sea-surface temperatures and global ice-volume, *Marine Micropaleontology*, 9, 111-134.
- Pusz, A. E., R. C. Thunell, and K. G. Miller (2011), Deep water temperature, carbonate ion, and ice volume changes across the Eocene-Oligocene climate transition, *Paleoceanography*, 26(2), PA2205.
- Rickaby, R. E. M., D. P. Schrag, I. Zondervan, and U. Riebesell (2002), Growth rate dependence of Sr incorporation during calcification of *Emiliana huxleyi*, *Global Biogeochemical Cycles*, 16(1), 1006.
- Robert, C. and J. P. Kennett (1997), Antarctic continental weathering changes during the Eocene-Oligocene cryosphere expansion: Clay mineral and oxygen isotope evidence, *Geology*, 25(7), 587-590.
- Schauble, E. A., P. Ghosh, and J. M. Eiler (2006), Preferential formation of ^{13}C - ^{18}O bonds in carbonate minerals, estimated using first-principle lattice dynamics, *Geochimica et Cosmochimica Acta*, 70(10), 2510-2529.
- Scher, H. D., and E. E. Martin (2006), Timing and Climatic Consequences of the Opening of Drake Passage, *Science*, 312(5772), 428-430.
- Scher, H. D., S. M. Bohaty, J. C. Zachos, and M. L. Delaney (2011), Two-stepping into the icehouse: East Antarctic weathering during progressive ice-sheet expansion at the Eocene-Oligocene transition, *Geology*, 39(4), 383-386.
- Shackleton, N. J. and M. A. Hall (1989), Carbon isotope stratigraphy of bulk sediments, ODP sites 689 and 690, Maud Rise, Antarctica, *Proceedings of the Ocean Drilling Program, Scientific Results*, 113, 985-989.
- Shackleton, N. J., and J. P. Kennett (1975), Paleotemperature history of the Cenozoic and the initiation of Antarctic glaciation: oxygen and carbon isotope analyses in DSDP sites 277, 279, and 281. *Initial Reports: Deep Sea Drilling Project*, 29, 743-755.
- SpeiB, V. (1990), Cenozoic Magnetostratigraphy of Leg 113 Drill Sites, Maud Rise, Weddell Sea, Antarctica, *Proceedings of the Ocean Drilling Program, Scientific Results*, Vol. 113, 261-315.
- Spero, H. J., J. Bijma D. W. Lea, and B. E. Bemis (1997), Effect of seawater carbonate concentration on foraminiferal carbon and oxygen isotopes, *Nature*, 390(6659), 497-500.

- Tang, J., M. Dietzel, A. Fernandez, A. K. Tripathi, and B. E. Rosenheim (2014), Evaluation of kinetic effects on clumped isotope fractionation (Δ_{47}) during inorganic calcite precipitation, *Geochimica et Cosmochimica Acta*, 134, 120-136.
- Thebault, J., B. R. Shone, N. Hallmann, M. Barth, and E. V. Nunn (2009), Investigation of Li/Ca variations in aragonitic shells of the ocean quahog *Arctica islandica*, northeast Iceland, *Geochemistry, Geophysics, Geosystems*, 10(12), Q12008.
- Tripathi, A. K., R. A. Eagle, N. Thiagarajan, A. C. Gagnon, H. Bauch, P. R. Halloran, and J. M. Eiler (2010), ^{13}C - ^{18}O isotope signatures and 'clumped isotope' thermometry in foraminifera and coccoliths, *Geochimica et Cosmochimica Acta*, 74(20), 5697-5717.
- Via, R. K. and D. J. Thomas (2006), Evolution of Atlantic thermohaline circulation: Early Oligocene onset of deep-water production in the North Atlantic, *Geology*, 34(6), 441-444.
- Wade, B. S., A. J. P. Houben, W. Quaijtaal, S. Schouten, Y. Rosenthal, K. G. Miller, M. E. Katz, J. D. Wright, and H. Brinkhuis (2012), Multiproxy record of abrupt sea-surface cooling across the Eocene-Oligocene transition in the Gulf of Mexico, *Geology*, 40(2), 159-162.
- Wei, W. (1991), Evidence for an earliest Oligocene abrupt cooling in the surface waters of the Southern Ocean, *Geology*, 19(8), 780-783.
- Wilson, D. S. and B. P. Luyendyk (2009), West Antarctic paleotopography estimated at the Eocene-Oligocene climate transition, *Geophysical Research Letters*, 36(16), L16302.
- Wold, C. N. (1994), Cenozoic sediment accumulation on drifts in the northern North Atlantic, *Paleoceanography*, 9(6), 917-941.
- Zaarur, S., H. P. Affek, and M. T. Brandon (2013), A revised calibration of the clumped isotope thermometer, *Earth and Planetary Science Letters*, 382(0), 47-57.
- Zachos, J. C., T. M. Quinn, and K. A. Salamy (1996), High-resolution (104 years) deep-sea foraminiferal stable isotope records of the Eocene-Oligocene climate transition, *Paleoceanography*, 11(3), 251-266.
- Zachos, J., M. Pagani, L. Sloan, E. Thomas, and K. Billups (2001), Trends, Rhythms, and Aberrations in Global Climate 65Ma to Present, *Science*, 292, 686-693.
- Ziveri, P., S. Thomas, I. Probert, M. Geisen, and G. Langer (2012), A universal carbonate ion effect on stable oxygen isotope ratios in unicellular planktonic calcifying organisms, *Biogeosciences*, 9, 1025-1032.

Appendix A1. Additional Sediment Core Data from Chapter 3

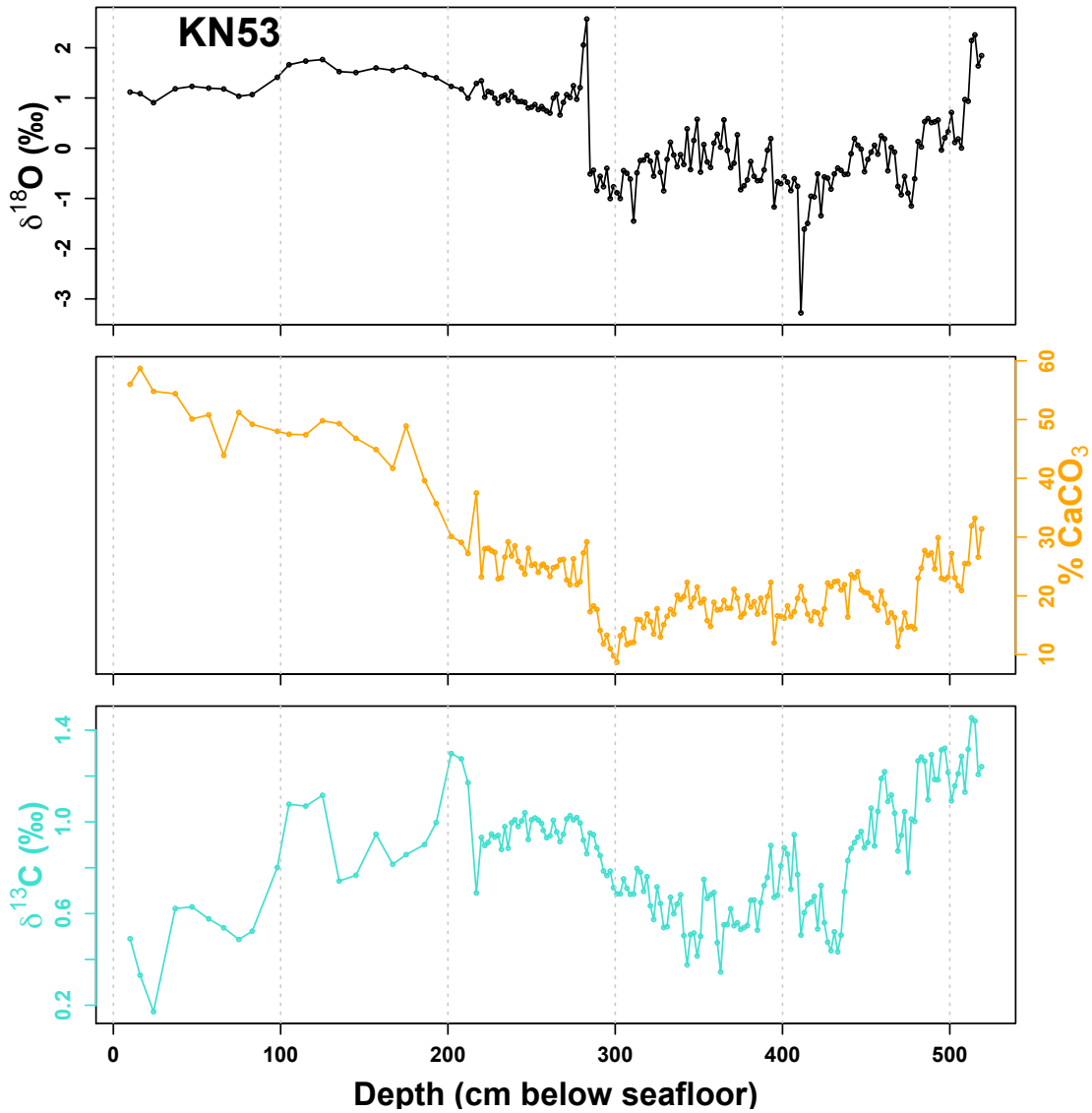


Figure A1.1 $\delta^{18}\text{O}_{\text{bs}}$ (black), % CaCO_3 (orange), and $\delta^{13}\text{C}_{\text{bs}}$ (turquoise) vs. Depth for KN53.

Interpretation:

Covers the glacial/interglacial transition (as seen in % CaCO_3 change). $\delta^{18}\text{O}_{\text{bs}}$ shows a permanent shift to heavier values.

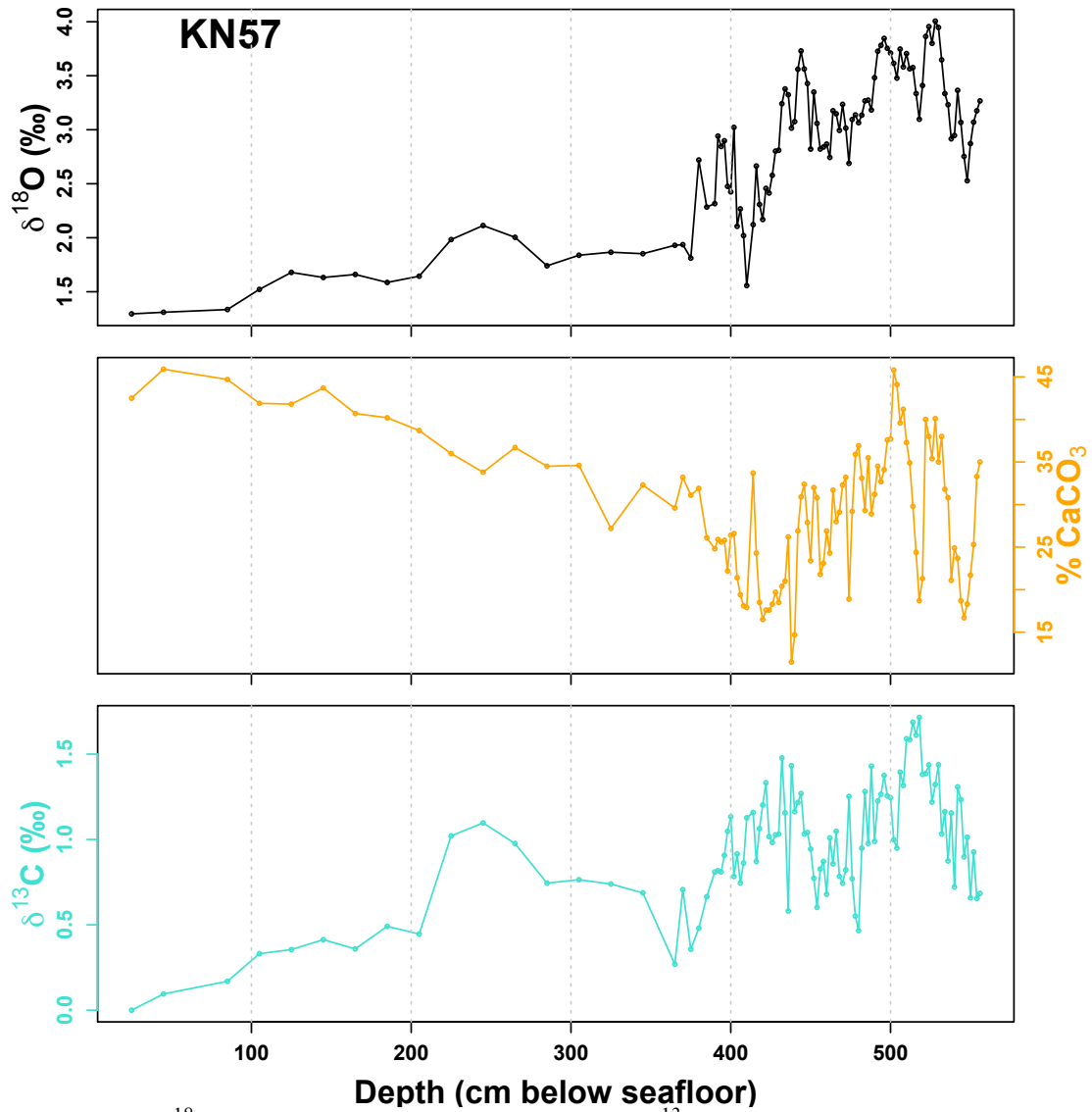


Figure A1.2 $\delta^{18}\text{O}_{\text{bs}}$ (black), %CaCO₃ (orange), and $\delta^{13}\text{C}_{\text{bs}}$ (turquoise) vs. Depth for KN57.

Interpretation:

Radiocarbon dates show that the first portion is all within the Holocene (hence the low-resolution sampling). The portion from 400-600cm likely represents a very compressed glacial period (compare to KN55).

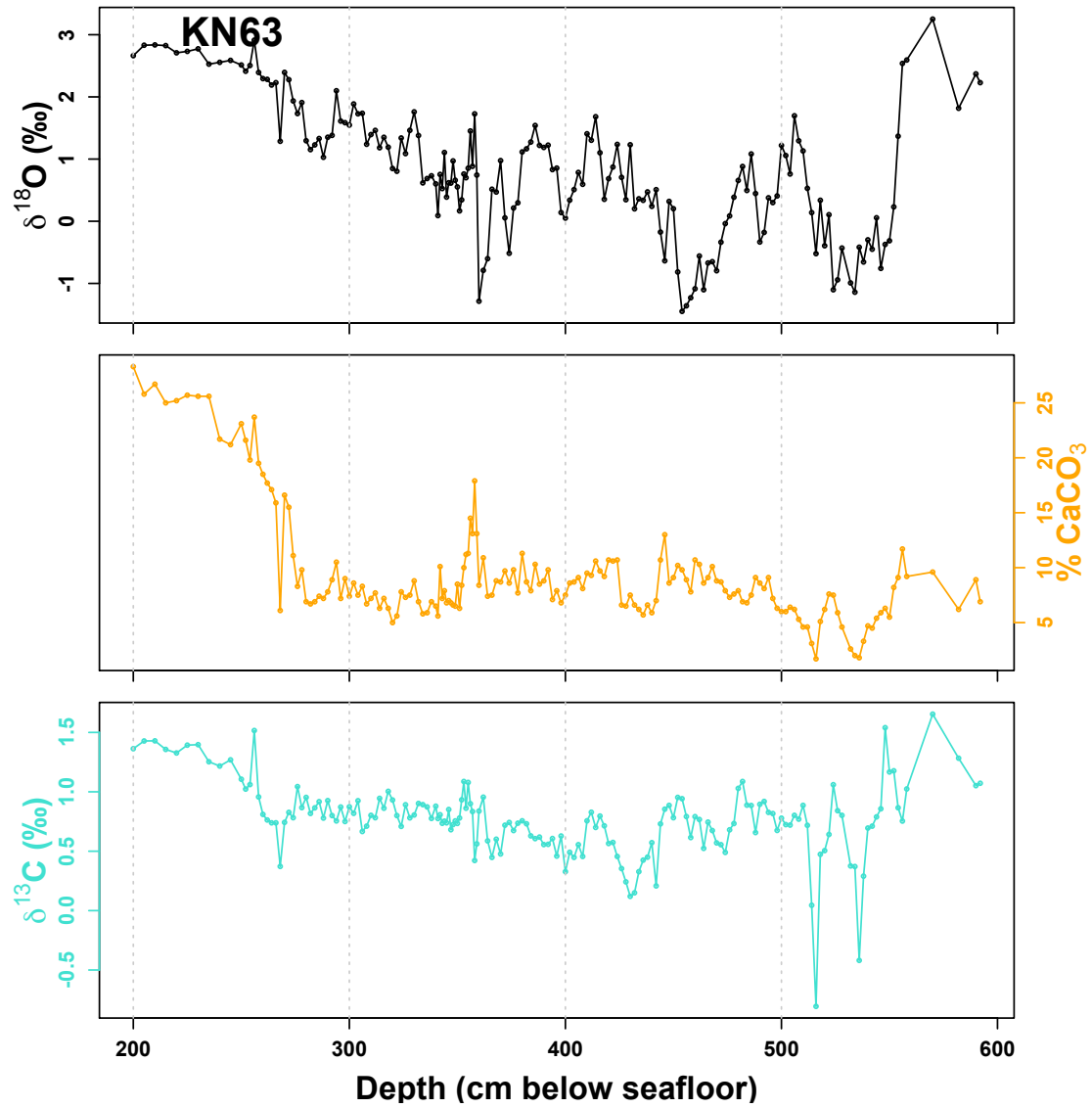


Figure A1.3 $\delta^{18}\text{O}_{\text{bs}}$ (black), %CaCO₃ (orange), and $\delta^{13}\text{C}_{\text{bs}}$ (turquoise) vs. Depth for KN63.

Interpretation:

Covers the glacial/interglacial transition (as seen in %CaCO₃ shift). Lots of excursions in $\delta^{18}\text{O}_{\text{bs}}$, but hard to interpret.

Appendix A2. Discussion of Shot Noise Limit with Decreasing Beam Intensity

Shot noise (σ_δ), or the minimum possible error on a measurement due to instrument noise, is nicely defined by *Merritt & Hayes* [1994] and can be calculated with the following equation:

$$\sigma_\delta^2 = 2 * 10^6 * \left(\frac{\sigma_R}{R} \right)^2 \quad [\text{Eq. A2.1}]$$

This can be rewritten as:

$$\sigma_\delta^2 = 2 * 10^6 * \frac{(1+R)}{R} * \frac{\Omega_{44} * q_e}{t * V_{44}} \quad [\text{Eq. A2.2}]$$

where Ω_{44} is the resistor for the mass-44 beam, which is 3×10^7 ohms for our instrument, and q_e is the charge on each ion (1.6×10^{-19} C). t is the total number of seconds of integration time over all cycles and acquisitions, which can be calculated by multiplying together the number of acquisitions (7), the number of cycles (14), and the integration time per cycle (26s) to get 2548s per sample. R is the ratio of currents between the minor beam of interest and the major beam, or i_{47}/i_{44} in our case. This can be calculated as $(V_{47}/\Omega_{47})/(V_{44}/\Omega_{44})$ using a representative m/z 44 and m/z 47 voltage reading and the mass-47 resistor of 1×10^{12} ohms. In our case, R is approximately 4.8×10^{-5} .

In the traditional dual-bellows measurement configuration, V_{44} is the target voltage for the m/z 44 beam at which every cycle is measured. The quantity $V_{44} * t / q_e$ gives an estimate of the total number of ions collected over the whole measurement period. In our dual-reservoir measurement configuration, the beam intensity (and therefore V_{44}) is constantly changing throughout the run. In order to quantify the total number of ions collected over the measurement period, we “integrate” the beam strength over time. We take V_{44} for each cycle, multiply by 26 seconds, the integration time of a single cycle, and then sum all the cycles. This is computationally equivalent to taking the average V_{44} value over the whole run and inputting that in place of the target voltage V_{44} in Equation A2.2.

We observe a roughly linear relationship between the average V_{44} and the initial V_{47} , which we can relate to sample size by the following two equations:

$$V_{44-average} = 0.4197 * V_{47-initial} + 50.2 \quad [\text{Eq. A2.3}]$$

$$V_{47-initial} = 2231 * (Mass) - 1714 \quad [\text{Eq. A2.4}]$$

where $Mass$ is the mass of carbonate reacted for that sample. We can therefore plot the theoretical shot noise limit against sample size, assuming all samples were run for the same amount of time (7 acquisitions x 14 cycles x 26 second integration time), and compare it to the measured standard errors for samples. We see our measured standard error increasing in line with the predicted shot noise limit at small sample sizes.

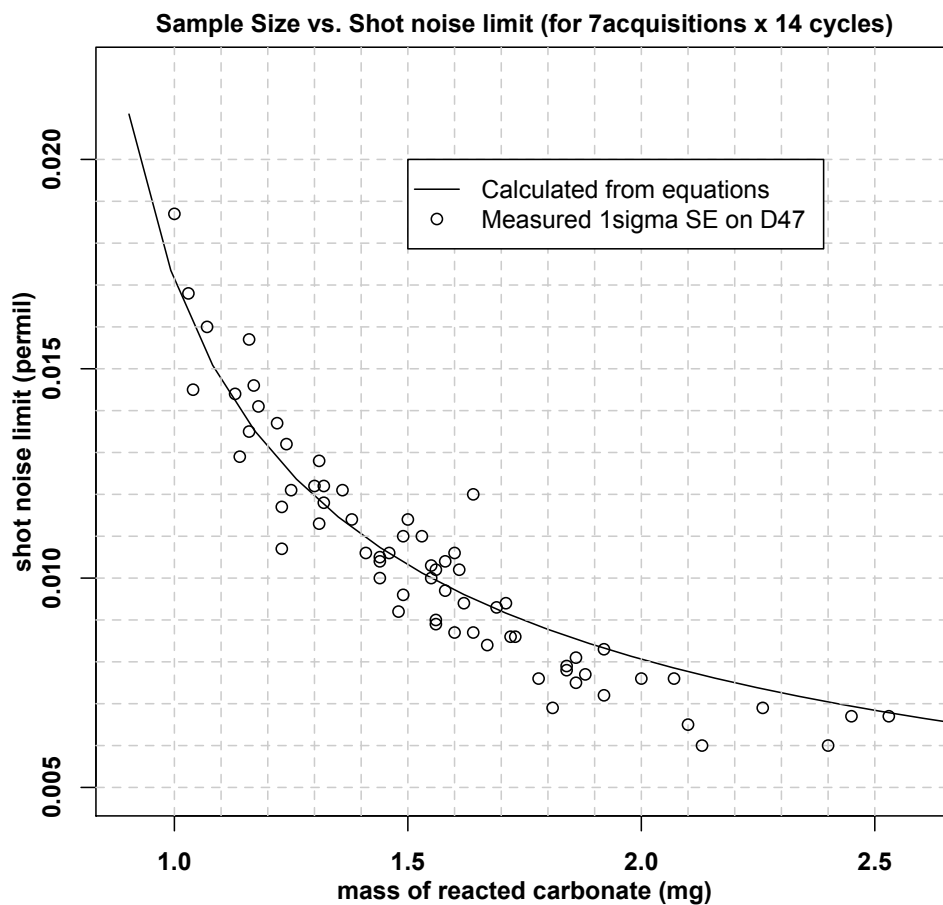


Figure A2.1 Mass of carbonate reacted vs. calculated (line) and observed (points) shot noise limit.

References

Merritt, D .A. and J. M. Hayes (1994), Factors controlling precision and accuracy in isotope-ratio-monitoring mass spectrometry, *Analytical Chemistry*, 66, 2336.

Appendix A3. Error Propagation in the Clumped Isotope Absolute Reference Frame Correction and Δ_{48} Correction

The correction from a raw Δ_{47} value to a fully-corrected Δ_{47} value is made up of a few steps. This includes 3 steps to get from the raw value to a value in the absolute reference frame [Dennis *et al*, 2011], as well as 2 steps to correct for the “unknown fractionation” with Δ_{48} observed in our samples. All of the data and regression outputs that go into these corrections have errors that need to be propagated.

To get from the raw value to the absolute reference frame value takes 3 steps:

$$\text{Step 1: } \Delta_{47\text{-SGvsWG0}} = \Delta_{47\text{-raw}} - \delta_{\text{raw}}^{47} * \text{Slope}_{\text{EGL}} \quad [\text{Eqn. A3.1}]$$

$$\text{Step 2: } \Delta_{47\text{-RF}} = \Delta_{47\text{-SGvsWG0}} * \text{Slope}_{\text{ETF}} + \text{Int}_{\text{ETF}} \quad [\text{Eqn. A3.2}]$$

$$\text{Step 3: } \Delta_{47\text{-RF/AC}} = \Delta_{47\text{-RF}} + \text{Acid Frac. Factor} \quad [\text{Eqn. A3.3}]$$

To correct the absolute reference frame value for the Δ_{48} fractionation takes 2 steps:

$$\text{Step 4: } \text{true}\Delta_{48} = (\text{Int}_{\text{CARB48}} * \text{Slope}_{\text{HG/EG}} - \text{Int}_{\text{HG/EG}} * \text{Slope}_{\text{CARB48}}) * (\text{Slope}_{\text{HG/EG}} - \text{Slope}_{\text{CARB48}}) \quad [\text{Eqn. A3.4}]$$

$$\text{Step 5: } \Delta_{47\text{-corr}} = \Delta_{47\text{-RF/AC}} - (\Delta_{48} - \text{true}\Delta_{48}) * \text{Slope}_{\text{CARB47}} \quad [\text{Eqn. A3.5}]$$

We begin with the raw carbonate data points, containing the following values and errors:

$$\delta^{47} \pm se\delta^{47} \qquad \Delta_{47} \pm se\Delta_{47}$$

$$\delta^{48} \pm se\delta^{48} \qquad \Delta_{48} \pm se\Delta_{48}$$

where the delta values and errors represent the mean and standard error of all cycles and acquisitions in one sample run (7acq x 14 cyc = 98 points to average per sample).

We also have the outputs of two regressions, the equilibrium gas lines (EGL) and the empirical transfer function (ETF). A statistical program such as R will output the standard error of the slope and intercept estimates with the regression information. We also take the published value and error for the acid fractionation factor of your choice (based on reaction temperature).

$$\text{Slope}_{\text{EGL}} \pm se\text{Slp}_{\text{EGL}}$$

$$\text{Slope}_{\text{ETF}} \pm se\text{Slp}_{\text{ETF}} \qquad \text{Int}_{\text{ETF}} \pm se\text{Int}_{\text{ETF}}$$

$$\text{Acid Fractionation Factor} \pm er\text{AcidFr}$$

For the Δ_{48} correction, we also need the slope and intercept of the heated gas (HG/EG) and carbonate (CARB48) data in δ^{48} vs Δ_{48} space, as well as the regression of Δ_{48} vs $\Delta_{47\text{-RF/AC}}$ for carbonates (CARB47). These give us the following additional values:

$$\text{Slope}_{\text{HG/EG}} \pm se\text{Slp}_{\text{HGEG}} \qquad \text{Int}_{\text{HG/EG}} \pm se\text{Int}_{\text{HGEG}}$$

$$\text{Slope}_{\text{CARB48}} \pm se\text{Slp}_{\text{CARB48}} \qquad \text{Int}_{\text{CARB48}} \pm se\text{Int}_{\text{CARB48}}$$

$$\text{Slope}_{\text{CARB47}} \pm se\text{Slp}_{\text{CARB47}}$$

To propagate the errors I will use the two following formulas, which are basic definitions of error propagation.

$$\text{For } z = x + y \quad dz = \sqrt{dx^2 + dy^2} \quad [\text{Eqn. A3.6}]$$

$$\text{For } z = x * y \quad dz = x * y * \sqrt{\left(\frac{dx}{x}\right)^2 + \left(\frac{dy}{y}\right)^2} \quad [\text{Eqn. A3.7}]$$

Step 1: Linearity correction

To propagate the errors through Equation A3.1, we combine the Eqn. A3.6 and A3.7 in the correct order to get:

$$\text{err}\Delta_{47\text{-SGvsWG0}} = \text{SQRT} \left[\text{se}\Delta_{47}^2 + (\delta_{\text{raw}}^{47} * \text{Slope}_{\text{EGL}})^2 * \left(\frac{\text{se}\delta^{47}}{\delta_{\text{raw}}^{47}} \right)^2 + \left(\frac{\text{seSlp}_{\text{EGL}}}{\text{Slope}_{\text{EGL}}} \right)^2 \right] \quad [\text{Eqn. A3.8}]$$

Step 2: ETF correction

To propagate the errors through Equation A3.2, we combine Eqn. A3.6 and A3.7 in the correct order, and input the error calculated in Eqn. A3.8 ($\text{err}\Delta_{47\text{-SGvsWG0}}$). We get:

$$\text{err}\Delta_{47\text{-RF}} = \text{SQRT} \left[\text{seInt}_{\text{ETF}}^2 + (\Delta_{47\text{-SGvsWG0}} * \text{Slope}_{\text{ETF}})^2 * \left(\frac{\text{err}\Delta_{47\text{-SGvsWG0}}}{\Delta_{47\text{-SGvsWG0}}} \right)^2 + \left(\frac{\text{seSlp}_{\text{ETF}}}{\text{Slope}_{\text{ETF}}} \right)^2 \right] \quad [\text{Eqn. A3.9}]$$

Step 3: Acid fractionation correction

To propagate the errors through Equation A3.3, we combine Eqn. A3.6 and A3.7 in the correct order, and input the error calculated in Eqn. A3.9 ($\text{err}\Delta_{47\text{-RF}}$). We get:

$$\text{err}\Delta_{47\text{-RF/AC}} = \text{SQRT} [\text{err}\Delta_{47\text{-RF}}^2 + \text{errAcidFr}^2] \quad [\text{Eqn. A3.10}]$$

Combining equations A3.8, A3.9, and A3.10, we can create one equation for the error on $\Delta_{47\text{-RF/AC}}$ that contains only known quantities. All of the inputs to this equation should be known from original data, regression outputs, or literature values (erAcidFr).

$$\text{err}\Delta_{47\text{-RF/AC}} = \text{SQRT} [(\text{seIntETF}^2 + (\Delta_{47\text{-SGvsWG0}} * \text{Slope}_{\text{ETF}})^2 * ((\text{se}\Delta_{47}^2 + (\delta_{\text{raw}}^{47} * \text{Slope}_{\text{EGL}})^2 * ((\text{se}\delta^{47}/\delta_{\text{raw}}^{47})^2 + (\text{seSlp}_{\text{EGL}}/\text{Slope}_{\text{EGL}})^2)) / \Delta_{47\text{-SGvsWG0}}^2 + (\text{seSlp}_{\text{ETF}}/\text{Slope}_{\text{ETF}})^2)) + \text{errAcidFr}^2] \quad [\text{Eqn. A3.11}]$$

Step 4: Calculate true Δ_{48}

The value $\text{true}\Delta_{48}$ is the y-coordinate (Δ_{48}) of the intersection between the heated gas and carbonate data in δ^{48} vs. Δ_{48} space. Because this is the intersection of two lines with errors on their slopes and intercepts, it is a more complicated calculation to get $\text{errTrue}\Delta_{48}$, and it is discussed below.

Step 5: Correction for Δ_{48} fractionation

To propagate the errors through Equation A3.5, we combine Eqn. A3.6 and A3.7 in the correct order, and input the error calculated in Eqn. A3.10 or A3.11 ($err\Delta_{47-RF/AC}$). We get:

$$err\Delta_{47-corr} = \text{SQRT} [err\Delta_{47-RF/AC}^2 + ((\Delta_{48-raw} - true\Delta_{48}) * Slope_{CARB47})^2 * ((se\Delta_{48}^2 + errTrue\Delta_{48}^2)/(\Delta_{48-raw} - true\Delta_{48})^2 + (seSlp_{CARB47}/Slope_{CARB47})^2)] \quad [\text{Eqn. A3.12}]$$

Combining equations A3.11 and A3.12, we can create an equation for the error on $\Delta_{47-corr}$, the fully corrected value, that contains only known quantities. Everything in this equation should be one of the given values at the start, except for $errTrue\Delta_{48}$.

$$err\Delta_{47-corr} = \text{SQRT} [((seIntETF^2 + ((\Delta_{47-raw} - \delta_{raw}^{47} * Slope_{EGL}) * Slope_{ETF})^2 * ((se\Delta_{47}^2 + (\delta_{raw}^{47} * Slope_{EGL})^2 * ((se\delta^{47}/\delta^{47})^2 + (se_{EGL}/Slope_{EGL})^2))/(\Delta_{47-raw} - \delta_{raw}^{47} * Slope_{EGL})^2 + (seSlp_{ETF}/Slope_{ETF})^2)) + errAcidFr^2) + ((\Delta_{48-raw} - (Int_{CARB48} * Slope_{HG/EG} - Int_{HG/EG} * Slope_{CARB48}) * (Slope_{HG/EG} - Slope_{CARB48})) * Slope_{CARB47})^2 * ((se\Delta_{48}^2 + errTrue\Delta_{48}^2)/(\Delta_{48-raw} - (Int_{CARB48} * Slope_{HG/EG} - Int_{HG/EG} * Slope_{CARB48}) * (Slope_{HG/EG} - Slope_{CARB48}))^2 + (seSlp_{CARB47}/Slope_{CARB47})^2)] \quad [\text{Eqn. A3.13}]$$

Error in the intersection of two fitted lines

We have two lines in δ^{48} vs. Δ_{48} space, one for heated and equilibrated gases (HG/EG) and one for carbonate (CARB48). These are normal regressions, and we get the

standard error on the slope and intercept from the regression output (for example from the summary function in R):

$$\begin{array}{ll} \text{Slope}_{\text{HG/EG}^{\pm}} \text{ seSlp}_{\text{HGEG}} & \text{Int}_{\text{HG/EG}^{\pm}} \text{ seInt}_{\text{HGEG}} \\ \text{Slope}_{\text{CARB48}^{\pm}} \text{ seSlp}_{\text{CARB48}} & \text{Int}_{\text{CARB48}^{\pm}} \text{ seInt}_{\text{CARB48}} \end{array}$$

For now, let's make the notation simpler and say that we have two lines:

$$\begin{array}{ll} \text{Line 1: } y = a*x + c & \text{Line 2: } y = b*x + d \end{array}$$

These lines intersect at the point (X,Y), such that $X = (d-c)/(a-b)$ and $Y = (a*d - b*c)/(a-b)$. The lines are both linear regression fits with errors on the slope and intercept: $\sigma_a, \sigma_b, \sigma_c, \sigma_d$. Each fit also has a covariance coefficient, which is between 0 and 1 and can be calculated as follows:

$$r = \text{cov}(x,y) / [\text{sd}(x) * \text{sd}(y)] \quad [\text{Eqn. A3.14}]$$

x and y in Equation A3.14 are the vectors of data (δ^{48} and Δ_{48}) for either HG/EG or carbonates which were used for the regression. This r is the same as the square root of the R^2 value given by the regression output. We can calculate this for each of the two lines and call them r1 and r2.

We can then write the error matrix (covariance matrix) for the intersection point (X,Y)

$$\begin{bmatrix} \sigma_x^2 & r^* \sigma_x \sigma_y \\ r^* \sigma_x \sigma_y & \sigma_y^2 \end{bmatrix} = N \quad [\text{Eqn. A3.15}]$$

We can write the covariance matrix comparing a, c, b, and d. Note: We are assuming the two lines are independent. Since the lines come from different sample runs (gas standards vs. carbonates), this is a fairly good assumption.

$$\begin{bmatrix} \sigma_a^2 & r1^* \sigma_a^* \sigma_c & 0 & 0 \\ r1^* \sigma_a^* \sigma_c & \sigma_c^2 & 0 & 0 \\ 0 & 0 & \sigma_b^2 & r2^* \sigma_b^* \sigma_d \\ 0 & 0 & r2^* \sigma_b^* \sigma_d & \sigma_d^2 \end{bmatrix} = M \quad [\text{Eqn. A3.16}]$$

We also need a transformation matrix, which calculates the partial derivatives of x and y with each of the parameters a,b,c,d.

$$T = \begin{bmatrix} \frac{\partial x}{\partial a} & \frac{\partial y}{\partial a} \\ \frac{\partial x}{\partial c} & \frac{\partial y}{\partial c} \\ \frac{\partial x}{\partial b} & \frac{\partial y}{\partial b} \\ \frac{\partial x}{\partial d} & \frac{\partial y}{\partial d} \end{bmatrix} = \left(\frac{1}{a-b} \right) \begin{bmatrix} -k & -b^* k \\ -1 & -b \\ k & a^* k \\ +1 & a \end{bmatrix} \quad [\text{Eqn. A3.17}]$$

Where $k = (d-c)/(a-b)$, for simplicity.

We can then use the matrix multiplication $T^T M T = N$ to solve for σ_x and σ_y . They have the following solution, after matrix multiplication and algebra...

$$\sigma_X^2 = 1/(a-b)^2 * [k^2 * (\sigma_a^2 + \sigma_b^2) + 2*k*(r1*\sigma_a*\sigma_c + r2*\sigma_b*\sigma_d) + \sigma_c^2 + \sigma_d^2] \text{ [Eqn. A3.18]}$$

$$\sigma_Y^2 = 1/(a-b)^2 * [k^2 * (b^2*\sigma_a^2 + a^2*\sigma_b^2) + 2*k*(r1*b^2*\sigma_a*\sigma_c + r2*a^2*\sigma_b*\sigma_d) + b^2*\sigma_c^2 + a^2*\sigma_d^2] \text{ [Eqn. A3.19]}$$

If we now translate this back into our clumped isotope calculation, we really care about σ_Y only, which is equal to $\text{errTrue}\Delta_{48}$, or the error on the y-value at the point of intersection. σ_X represents the error in the x-value (δ^{48}) at the point of intersection. Letting Line 1 be the HG/EG line and Line 2 be the CARB48 line, we can make the following substitutions:

$a = \text{Slope}_{\text{HG/EG}}$	$\sigma_a = \text{seSlp}_{\text{HGEG}}$
$c = \text{Int}_{\text{HG/EG}}$	$\sigma_c = \text{seInt}_{\text{HGEG}}$
$b = \text{Slope}_{\text{CARB48}}$	$\sigma_b = \text{seSlp}_{\text{CARB48}}$
$d = \text{Int}_{\text{CARB48}}$	$\sigma_d = \text{seInt}_{\text{CARB48}}$

Finally, we just plug these values into Eqn. A3.19 and solve for σ_Y . This is then plugged into Eqn. A3.13 along with other known quantities to solve for our final product, $\text{err}\Delta_{47\text{-corr}}$, or the error on the fully corrected Δ_{47} value ($\Delta_{47\text{-corr}}$).

References

Dennis, K. J., H. P. Affek, B. H. Passey, D. P. Schrag, and J. M. Eiler (2011), Defining an absolute reference frame for ‘clumped’ isotope studies of CO₂, *Geochimica et Cosmochimica Acta*, 75(22), 7117-7131.

Appendix A4. Supplemental Figures for Chapter 4

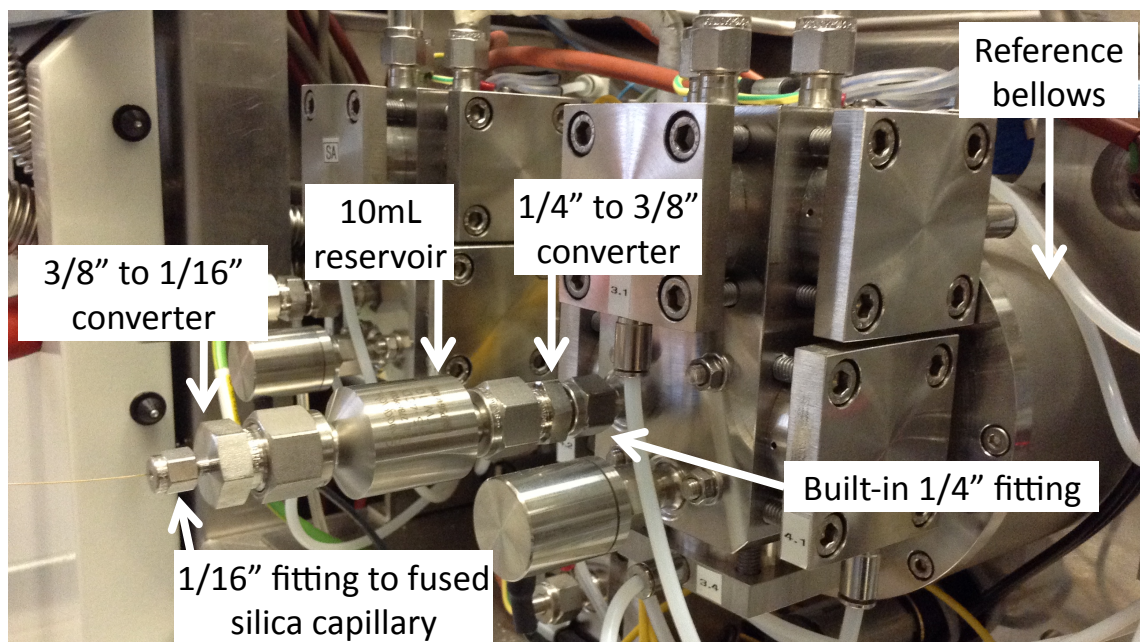


Figure A4.1 Diagram of 10mL reservoir attached to reference bellows. The MAT253 has a built-in 1/4" Swagelok compression fitting as the output to the reference bellows. We attach the 10mL stainless steel reservoir (Swagelok piece # SS-4CD-TW-10) to the fused silica capillaries (~1m length, 110 μ m inner diameter, SGE # 0624459) using two converter pieces (1/4" male to 3/8" female, Swagelok piece # SS-600-R-4, and 3/8" female to 1/16" female, Swagelok piece # SS-600-6-1). The capillaries are connected to the 1/16" Swagelok fitting using a graphite-Vespel composite ferrule (SGE # 072663). On the sample side, the same 2 Swagelok connectors and 10mL reservoir were used to form identical volumes from which the gas bleeds down. However, the internal volume of the inlet valve adjacent to the sample reservoir is larger than the internal volume of the MAT 253 valve adjacent to the reference reservoir, so 87 glass beads (borosilicate, 3mm diameter, similar to VWR#26396-630) were placed inside the sample reservoir to balance this volume difference.

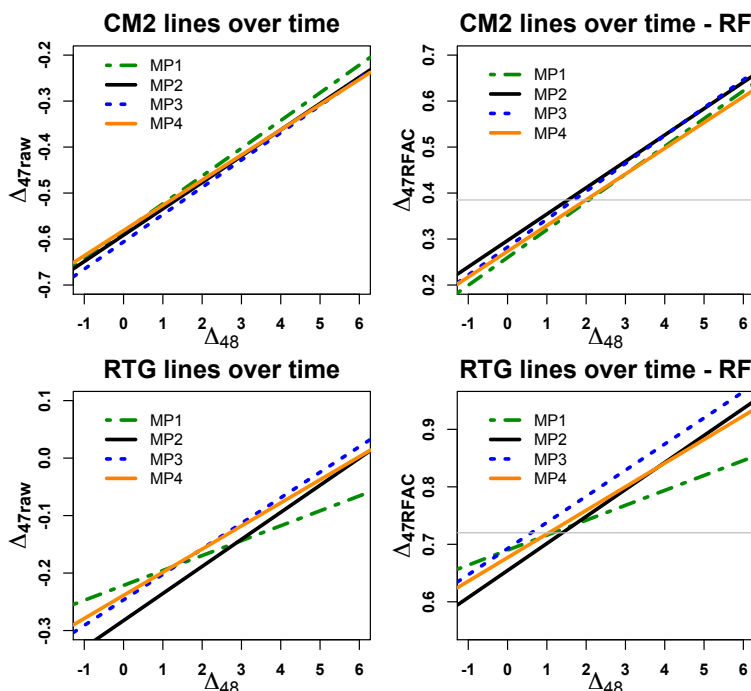


Figure A4.2 Δ_{48} vs. $\Delta_{47\text{-raw}}$ and Δ_{48} vs. $\Delta_{47\text{-RFAC}}$ for both CM2 and RTG for the 4 measurement periods (MP1 = 09/22/13 to 10/03/13; MP2 = 10/07/13 to 12/18/13; MP3 = 01/06/14 to 02/14/14; MP4 = 02/18/14 to 03/28/14). The PPQ trap material was changed during MP3 and did not have a large influence on the slope. Horizontal grey lines indicate published value for each standard. RTG has few replicates in MP1, resulting in a more divergent slope.

Meas. Period	Samp Type	# pts	Raw vs. Ref. Fr.	Slope	Slope Error (1 SE)	Intercept	Intercept Error (1 SE)
1	CM2	10	Raw	0.060	0.003	-0.584	0.009
			Ref. Frame	0.060	0.003	0.260	0.009
2	CM2	36	Raw	0.057	0.004	-0.592	0.008
			Ref. Frame	0.057	0.004	0.297	0.008
3	CM2	41	Raw	0.059	0.003	-0.606	0.011
			Ref. Frame	0.061	0.003	0.282	0.011
4	CM2	29	Raw	0.055	0.003	-0.581	0.010
			Ref. Frame	0.056	0.003	0.273	0.010
1	RTG	5	Raw	0.026	0.023	-0.221	0.029
			Ref. Frame	0.026	0.024	0.690	0.030
2	RTG	20	Raw	0.047	0.003	-0.283	0.006
			Ref. Frame	0.047	0.003	0.654	0.006
3	RTG	13	Raw	0.044	0.011	-0.247	0.028
			Ref. Frame	0.045	0.011	0.693	0.029
4	RTG	40	Raw	0.040	0.003	-0.239	0.011
			Ref. Frame	0.041	0.004	0.677	0.012

Table A4.1 Slopes and intercepts of the lines shown in Figure S3 (Δ_{48} vs. $\Delta_{47\text{-raw}}$ and Δ_{48} vs. $\Delta_{47\text{-RFAC}}$), with errors (1 SE). There is a slight noticeable offset between the slopes fit to CM2 data and that fit to RTG.

Correlations between stable isotopes and D48

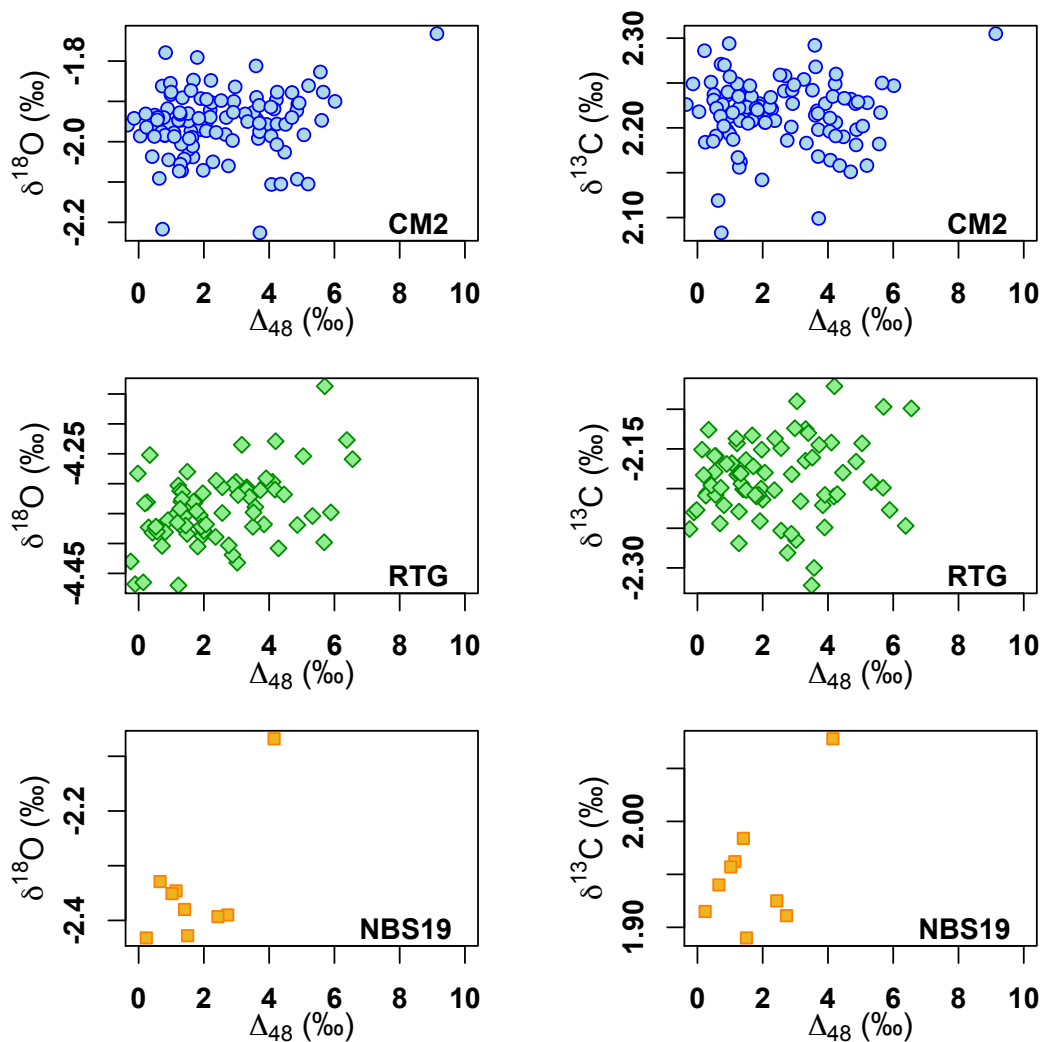


Figure A4.3 $\delta^{18}\text{O}$ (left) and $\delta^{13}\text{C}$ (right) vs. Δ_{48} for all CM2 (blue), RTG (green), and NBS19 (orange) points measured over 4 different measurement periods. No significant correlation is observed between Δ_{48} and the stable isotopes, unlike between Δ_{48} and Δ_{47} . Plots of $\delta^{13}\text{C}$ and $\delta^{18}\text{O}$ vs. $\Delta_{47\text{-RFAC}}$, $\Delta_{47\text{-CORR}}$, and δ^{48} look very similar because of the strong correlation between those quantities and Δ_{48} .

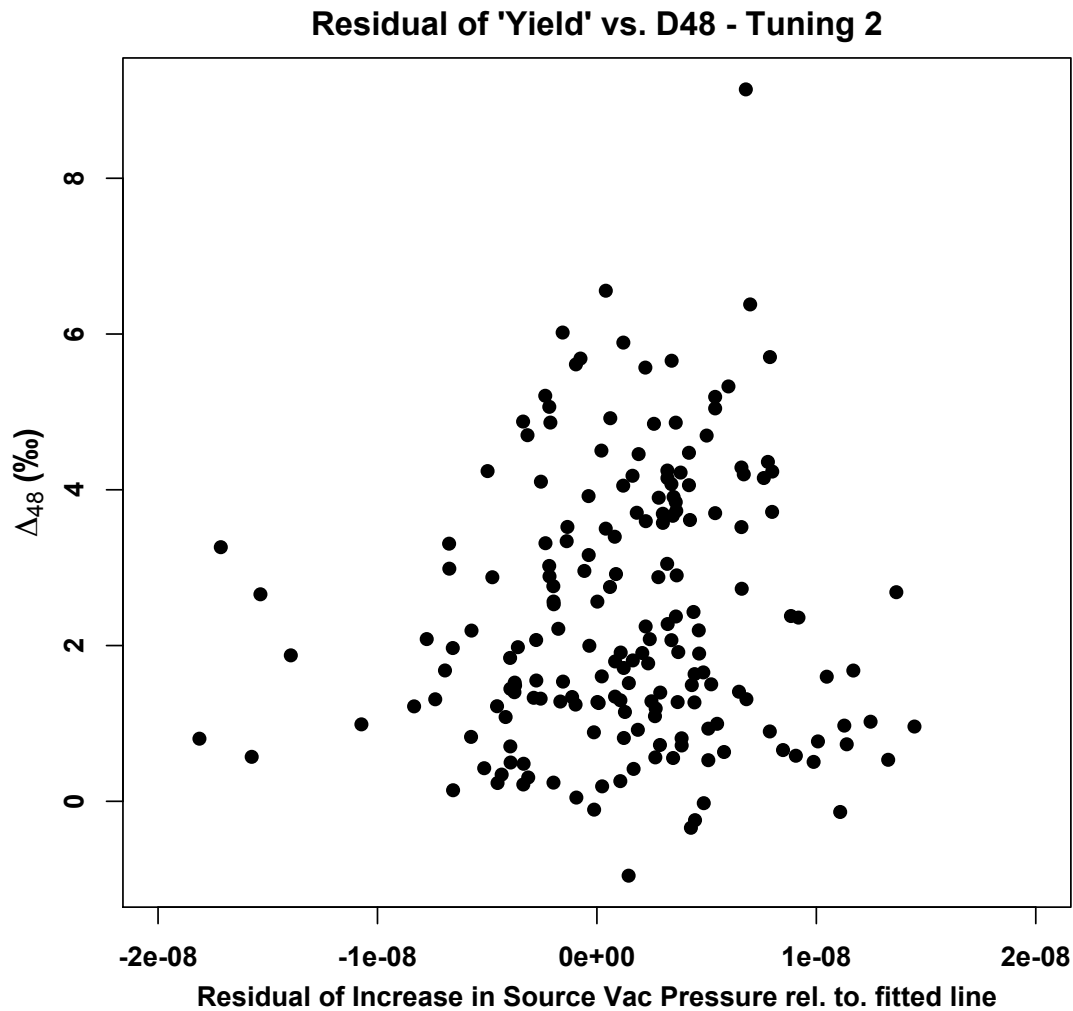


Figure A4.4 Residual yield (difference between observed yield, measured as increase in source vacuum gauge pressure, and fitted line shown in Figure 3a) vs. Δ_{48} for all carbonate data run over all four measurement periods. There is no correlation between residual yield and Δ_{48} , indicating that partial yield is not causing the fractionation. If that were the case, we would expect to see the highest Δ_{48} values occurring either at the highest residual yield (contaminant being added) or the lowest (fractionation occurring during loss of some gas). Instead we see near-zero residual values showing the highest Δ_{48} .

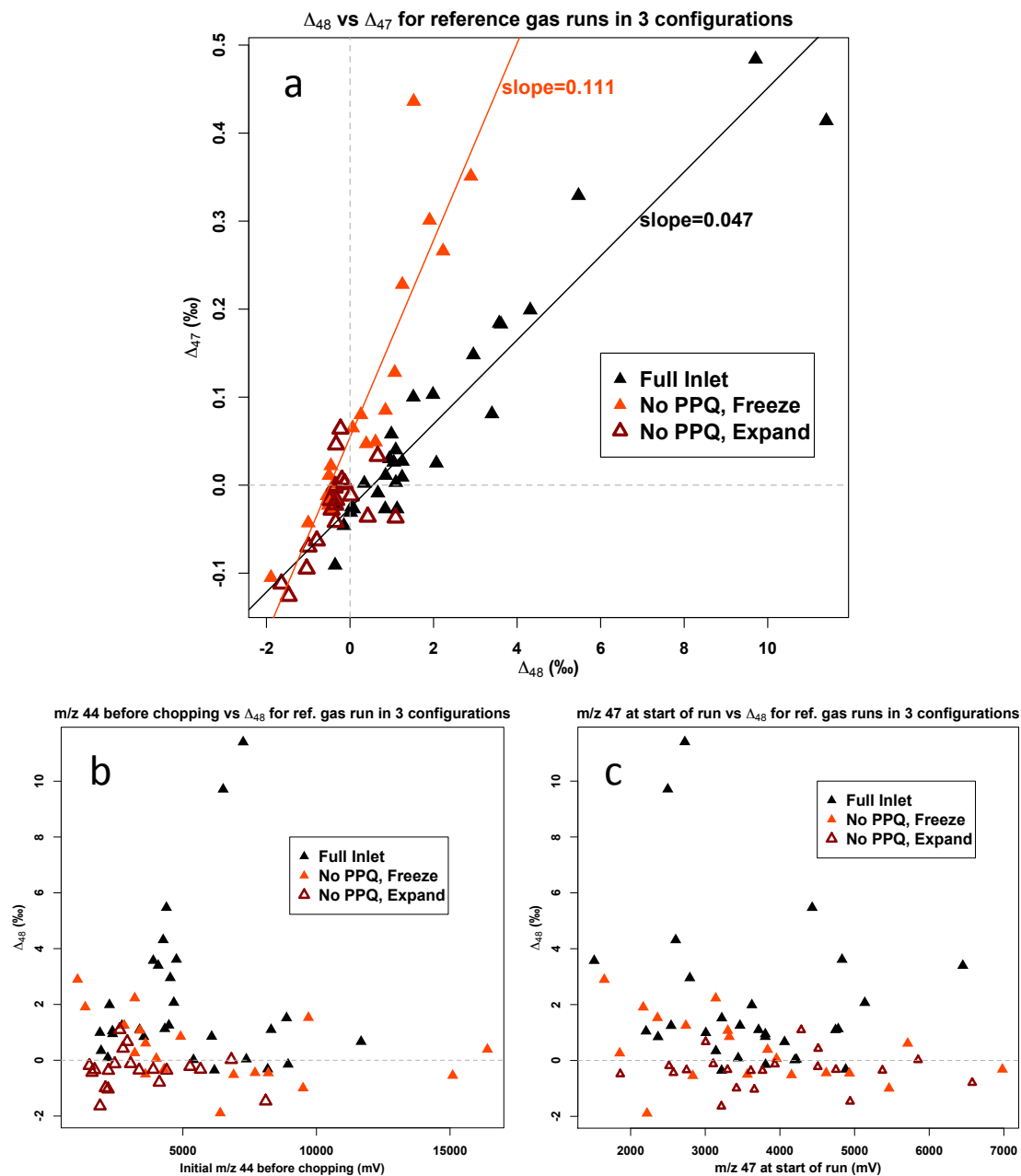


Figure A4.5 Tests of reference gas run as a sample in three different configurations. (a) Δ_{48} vs. Δ_{47} -raw (b) Δ_{48} vs. m/z 44 before chopping (represents the amount of gas entering the U-trap and reservoir initially) (c) Δ_{48} vs. m/z 47 at the start of the run (represents the sample size after chopping). Three configurations are shown - 1) reference gas passed through the full inlet; 2) reference gas frozen into the small U-trap (bypassing the PPQ trap); 3) reference gas expanded into the small U-trap (bypassing the PPQ trap).

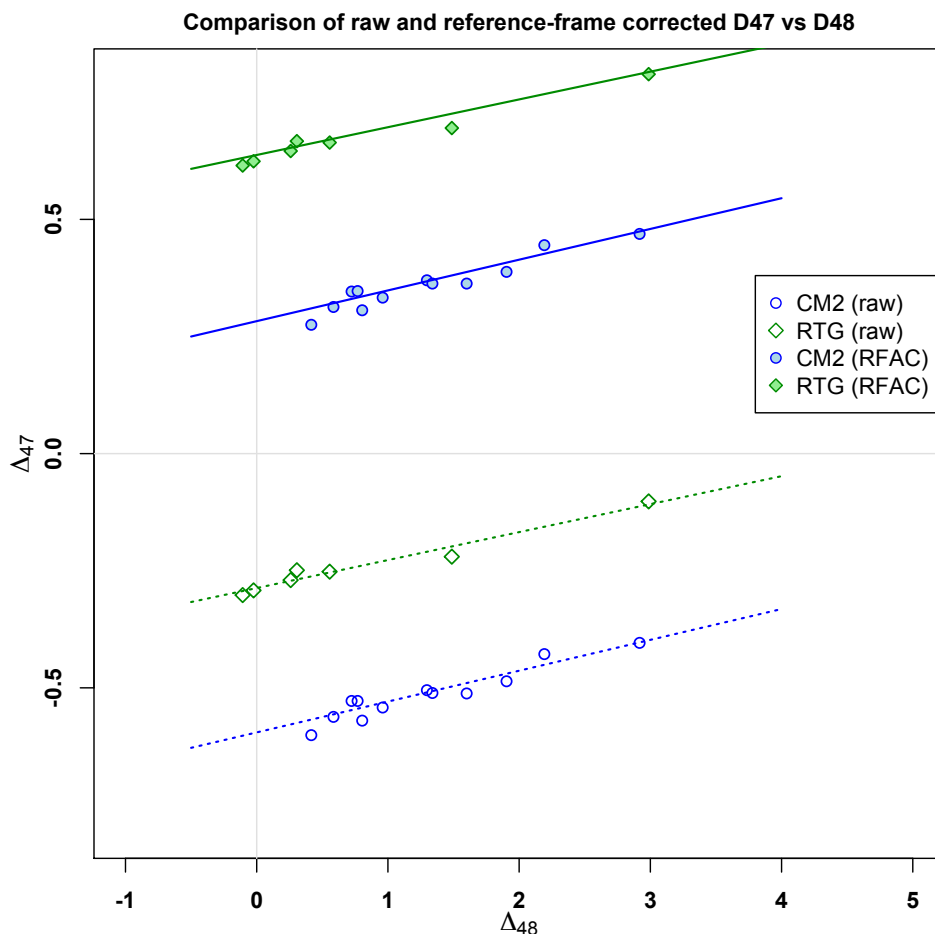


Figure A4.6 Δ_{48} vs. $\Delta_{47\text{-raw}}$ and vs. $\Delta_{47\text{-RFAC}}$. The fractionation relationship is preserved through the correction to the universal reference frame, with essentially no change in slope. The carbonate data shown here are a subset of data from measurement period #2 which were run at a starting voltage of m/z 47 = 3300-3800mV. These carbonates were corrected using only heated and equilibrated gases run within the same voltage range. If the difference in running voltage of the samples and gas standards were causing the observed fractionation, this reference frame correction done with similar-sized carbonates and standard gases should remove the fractionation and flatten out the data in this plot. The fact that the slope is unchanged suggests that differences in running voltage between samples and standards do not cause the observed fractionation.

Line	Slope	Slope error (1 SE)	Intercept	Intercept error (1 SE)	R ²
CM2 ($\Delta_{47\text{-raw}}$)	0.0711	0.0076	-0.6066	0.0112	0.8973
CM2 ($\Delta_{47\text{-RFAC}}$)	0.0700	0.0074	0.2694	0.0109	0.8994
RTG ($\Delta_{47\text{-raw}}$)	0.0596	0.0052	-0.2875	0.0067	0.9632
RTG ($\Delta_{47\text{-RFAC}}$)	0.0582	0.0051	0.6290	0.0066	0.9627

Table A4.2 Fitted slopes and intercepts for the four lines shown in Figure S2. The slope is essentially unchanged by the correction to the universal reference frame, and is statistically different from zero in all cases, suggesting that the reference frame correction does not remove the fractionation slope, even when the gases and carbonates are run at the same voltage.

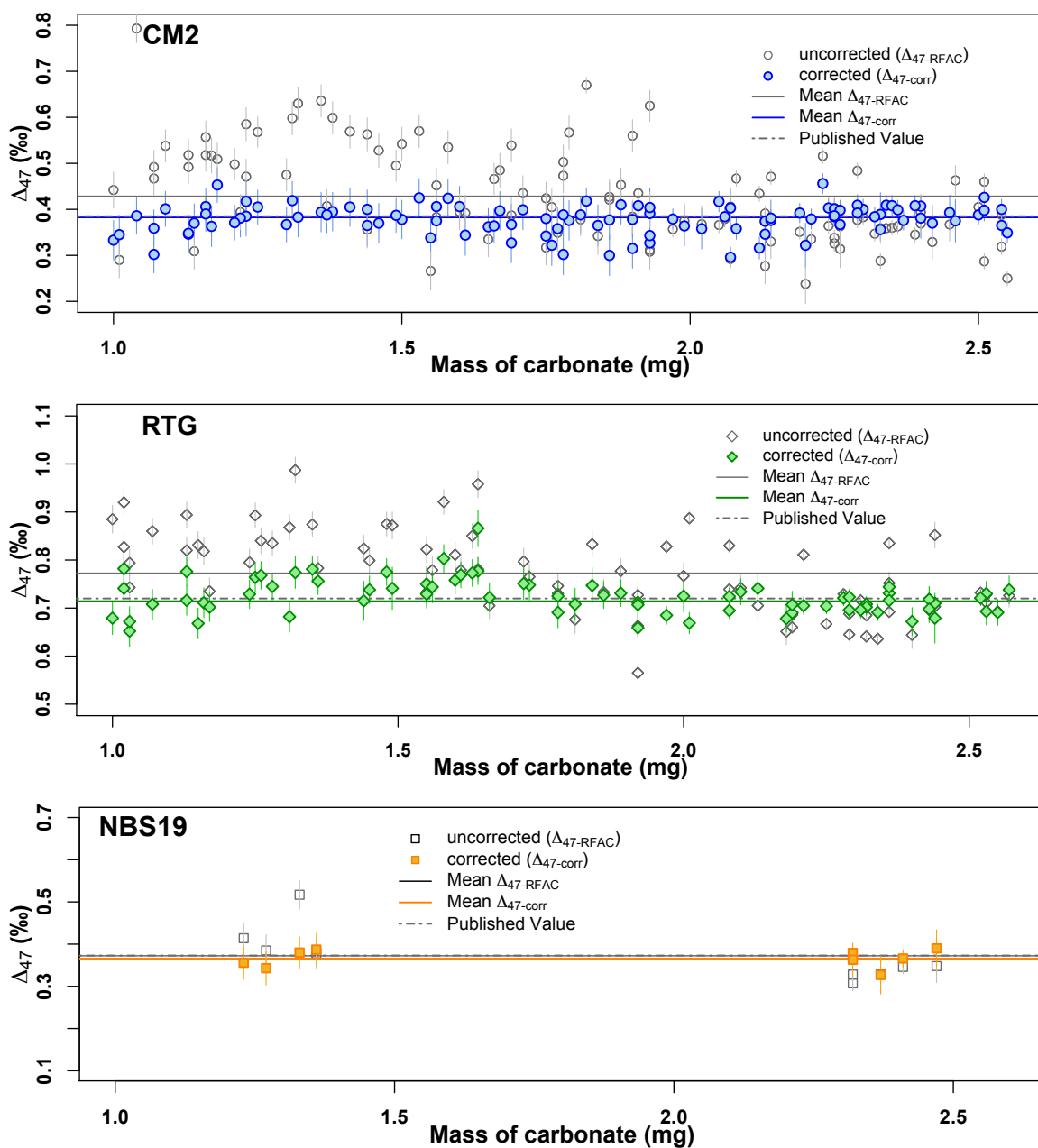


Figure A4.7 $\Delta_{47-RFAC}$ and $\Delta_{47-corr}$ vs. sample size for CM2 (top, blue), RTG (middle, green), and NBS19 (bottom, orange). Filled symbols are the same as open symbols plotted in Figure 6. Correction for the fractionation relationship brings points and mean values closer to published values. Error bars account for full error propagation of original 1 SE on Δ_{47-raw} through all correction steps carried out (Reference frame for $\Delta_{47-RFAC}$ and Reference frame + Δ_{48} correction for $\Delta_{47-corr}$). The majority of the increase above the original shot noise error comes from the Reference frame correction, with a smaller additional increase from the Δ_{48} correction.

Mass Bin	n	Mean $\Delta_{47\text{-RFAC}}$ (‰)	Mean $\Delta_{47\text{-corr}}$ (‰) CM2/NBS19 and RTG fit separately	Mean $\Delta_{47\text{-corr}}$ (‰) All 3 carbonates fit together
CM2 samples				
2.5-2.6mg	5	0.352 ± 0.032	0.388 ± 0.011	0.384 ± 0.012
2.4-2.5mg	4	0.386 ± 0.040	0.379 ± 0.007	0.377 ± 0.007
2.3-2.4mg	10	0.358 ± 0.008	0.392 ± 0.005	0.390 ± 0.005
2.2-2.3mg	11	0.369 ± 0.023	0.391 ± 0.010	0.389 ± 0.011
2.1-2.2mg	7	0.376 ± 0.029	0.364 ± 0.011	0.364 ± 0.011
2.0-2.1mg	6	0.380 ± 0.023	0.369 ± 0.018	0.370 ± 0.017
1.9-2.0mg	7	0.417 ± 0.036	0.368 ± 0.011	0.370 ± 0.011
1.8-1.9mg	8	0.448 ± 0.047	0.376 ± 0.017	0.381 ± 0.019
1.7-1.8mg	8	0.434 ± 0.029	0.358 ± 0.012	0.362 ± 0.012
1.6-1.7mg	6	0.428 ± 0.027	0.367 ± 0.010	0.371 ± 0.010
1.5-1.6mg	6	0.458 ± 0.048	0.391 ± 0.014	0.395 ± 0.015
1.4-1.5mg	6	0.502 ± 0.039	0.385 ± 0.008	0.393 ± 0.009
1.3-1.4mg	5	0.558 ± 0.038	0.391 ± 0.007	0.402 ± 0.006
1.2-1.3mg	6	0.503 ± 0.035	0.392 ± 0.008	0.403 ± 0.009
1.1-1.2mg	7	0.489 ± 0.031	0.382 ± 0.014	0.396 ± 0.014
1.0-1.1mg	6	0.504 ± 0.067	0.354 ± 0.015	0.376 ± 0.019
All CM2s	108	0.429 ± 0.010	0.378 ± 0.003	0.382 ± 0.003
RTG samples				
2.5-2.6mg	5	0.718 ± 0.007	0.715 ± 0.010	0.717 ± 0.012
2.4-2.5mg	4	0.742 ± 0.037	0.701 ± 0.008	0.689 ± 0.020
2.3-2.4mg	8	0.700 ± 0.024	0.708 ± 0.008	0.706 ± 0.006
2.2-2.3mg	5	0.708 ± 0.029	0.710 ± 0.005	0.710 ± 0.006
2.1-2.2mg	4	0.689 ± 0.016	0.710 ± 0.012	0.713 ± 0.012
2.0-2.1mg	4	0.806 ± 0.033	0.703 ± 0.013	0.690 ± 0.016
1.9-2.0mg	5	0.696 ± 0.055	0.691 ± 0.012	0.690 ± 0.012
1.8-1.9mg	4	0.755 ± 0.033	0.728 ± 0.008	0.722 ± 0.002
1.7-1.8mg	4	0.760 ± 0.014	0.729 ± 0.014	0.721 ± 0.014
1.6-1.7mg	5	0.814 ± 0.035	0.778 ± 0.019	0.770 ± 0.016
1.5-1.6mg	5	0.814 ± 0.040	0.756 ± 0.016	0.744 ± 0.013
1.4-1.5mg	4	0.842 ± 0.019	0.742 ± 0.012	0.719 ± 0.015
1.3-1.4mg	4	0.878 ± 0.042	0.748 ± 0.023	0.725 ± 0.026
1.2-1.3mg	4	0.841 ± 0.020	0.752 ± 0.009	0.736 ± 0.008
1.1-1.2mg	5	0.820 ± 0.025	0.717 ± 0.017	0.696 ± 0.018
1.0-1.1mg	6	0.838 ± 0.026	0.706 ± 0.020	0.682 ± 0.021
All RTGs	76	0.773 ± 0.010	0.723 ± 0.004	0.714 ± 0.004

Table A4.3 Binned averages (0.1mg bins) for CM2 and RTG, for data uncorrected ($\Delta_{47\text{-RFAC}}$) and corrected ($\Delta_{47\text{-corr}}$) for the Δ_{48} fractionation using two methods (discussed in later section). Data shown in Figure 6 comes from the 4th column (CM2/NBS19 and RTG fit separately). Comparison of columns 4 and 5 are shown in Figure S20. Column 2 shows the number of replicates per mass bin. Errors are 1 SE of the samples in each bin.

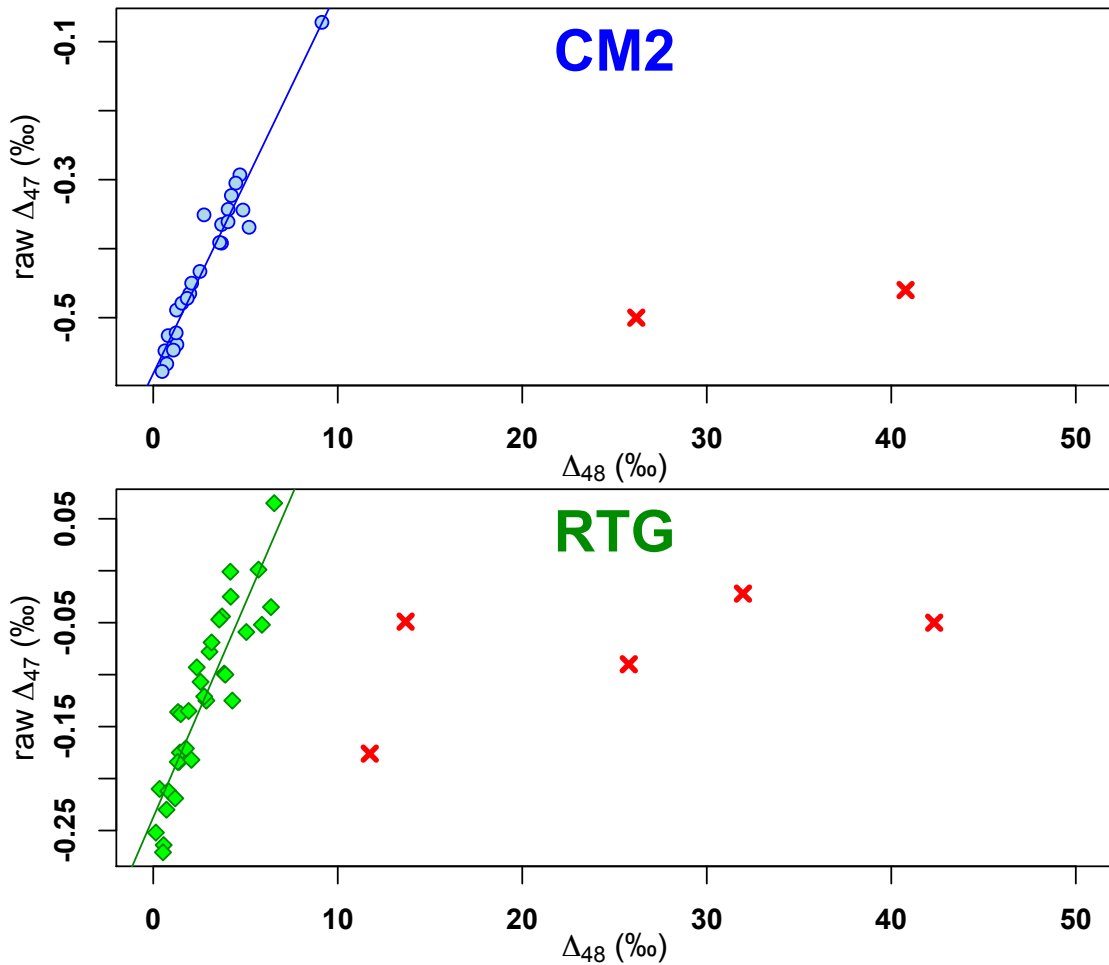


Figure A4.8 Δ_{48} vs. $\Delta_{47\text{-raw}}$ for measurement period 4 showing contaminated samples compared with clean samples. Samples that have significantly elevated Δ_{48} relative to the amount expected for a given Δ_{47} (in other words, fall to the right of the fractionation line), are deemed to be contaminated. These 7 samples were thrown out from further calculations. This method of finding contaminated samples runs the risk of including some “slightly contaminated” samples in the acceptable data. This would result in lighter Δ_{47} values and hotter temperatures.

Appendix A5. Choice of Group Fit vs. Individual Fit for the Δ_{48} Correction

When correcting carbonate data for the Δ_{48} correction, there are two steps in the correction process for which you can choose a group vs. individual fit: 1) solving for the slope and intercepts of carbonate data in δ^{48} vs. Δ_{48} space and 2) solving for the slope of carbonate data in Δ_{48} vs. Δ_{47} space. In the case of most of our data, we have many replicates of each sample type (CM2 and RTG) in each measurement period, giving us more than enough points to get a robust fit for each of these sample types using the individual fit method. However, in many cases where we would be measuring unknowns, we may only have 6 or fewer replicates of each unknown (like NBS19 in this study). Depending on the spread of the data, it may be difficult to fit an individual line that accurately captures the slope of the Δ_{48} vs. Δ_{47} relationship. Below we will show two examples of the group fit vs. the individual fit in the case of having 5 replicates or 2 replicates of an unknown (in this case NBS19) in a given measurement period. We will also discuss the slight but observable difference between the slopes of the CM2 and RTG lines and the choice of group vs. individual fit for future studies.

NBS19 during measurement period #4:

An unknown with a typical number of replicates (5)

First we look at the fit in δ^{48} vs. Δ_{48} space. In this case the two lines are fairly similar, and the important quantity ($\Delta(\Delta_{48}) = 0$) is nearly identical for the two lines. In

general, there tends to be very little scatter around the carbonate lines in δ^{48} vs. Δ_{48} space, meaning the individual fit is usually fairly close to the group fit.

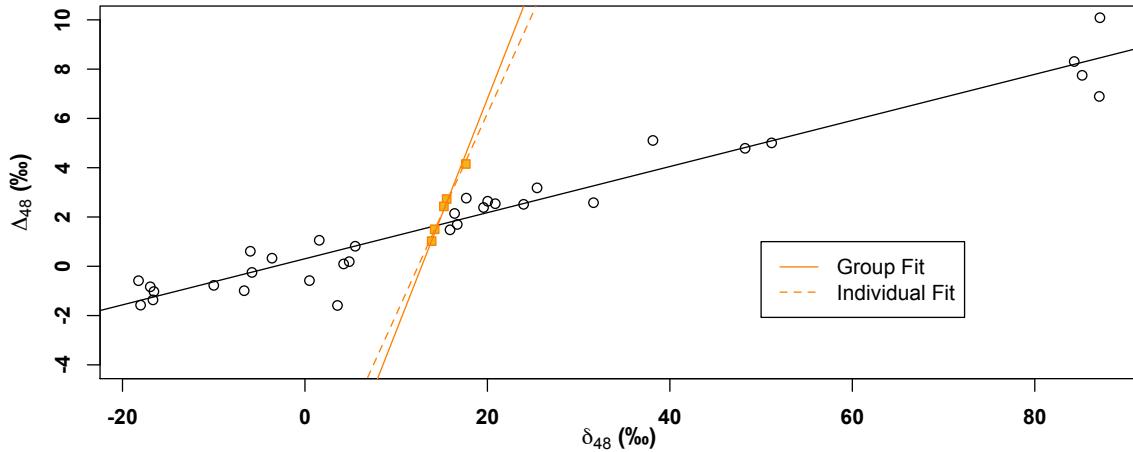


Figure A5.1 δ^{48} vs. Δ_{48} for NBS19 run during measurement period #4 showing two fitted lines – one from an individual fit of just NBS19 data points, and one from the group fit including all CM2 and RTG from measurement period #4. Black points show the heated and equilibrated gases run during this period.

$$\text{HG/EG: } \Delta_{48} = 0.0919 * \delta^{48} + 0.2690$$

$$\text{Individual: } \Delta_{48} = 0.8163 * \delta^{48} - 10.1239, R^2 = 0.9837$$

$$\text{Group: } \Delta_{48} = 0.9432 * \delta^{48} - 12.0647, R^2 = 0.9923 \text{ for all carbonates}$$

These fits in δ^{48} vs. Δ_{48} space are needed to calculate the “true Δ_{48} ” value, aka the intersection with the heated and equilibrated gas line in δ^{48} vs. Δ_{48} space. The different fits correspond to different intersection points, but the “true Δ_{48} ” values only differ by 0.012‰.

$$\text{Individual fit: } (\delta^{48}, \Delta_{48}) = (14.429, 1.655)$$

$$\text{Group fit: } (\delta^{48}, \Delta_{48}) = (14.559, 1.667)$$

The second place where we can compare the group and individual fits is in solving for $\text{Slope}_{\text{CARB47}}$, or the slope of the carbonate samples in Δ_{48} vs. Δ_{47} space. There is much more scatter about the lines in this case, meaning the group fit becomes more important with fewer replicates of the unknown.

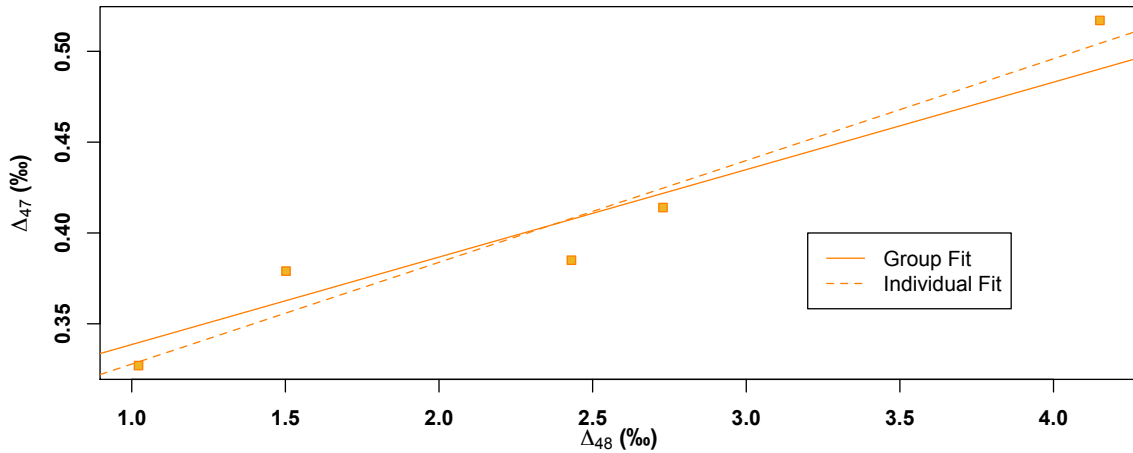


Figure A5.2 Δ_{48} vs. Δ_{47} for NBS19 run during measurement period #4 showing two fitted lines, from the individual and group fits.

Individual: $\text{Slope}_{\text{CARB47}} = 0.0560 \pm 0.0087$

Group: $\text{Slope}_{\text{CARB47}} = 0.0482 \pm 0.0024$

These slopes are not too different, but what matters is how much the final corrected data differs. Using the group and individual $\text{Slope}_{\text{CARB47}}$ values, paired with the intersection points (true Δ_{48}) found for both methods, we can correct the data.

Point #	1	2	3	4	5	Mean	1 SE
Δ_{48}	1.022	1.502	2.431	2.729	4.151		
$\Delta_{47\text{-RFAC}}$	0.327	0.379	0.385	0.414	0.517	0.404	0.031
$\Delta_{47\text{-corr}}$ (Individual Fit)	0.362	0.388	0.342	0.354	0.377	0.365	0.008
$\Delta_{47\text{-corr}}$ (Group Fit)	0.358	0.387	0.348	0.363	0.397	0.371	0.009

Table A5.1 Comparison of raw NBS19 data (Δ_{48} and $\Delta_{47\text{-RFAC}}$) with data corrected with each of the two fits ($\Delta_{47\text{-corr}}$) for measurement period #4.

Although the group fit has a slightly larger error, the mean value is closer to the published values (0.373 +/- 0.007‰ [Dennis *et al.*, 2011]). Other labs found higher values (0.399‰ [JHU] and 0.404‰ [Yale]). This shows that with a typical number of replicates for an unknown (5), the group fit does better than the individual fit. The more replicates of a certain sample type you have, the less the group fit differs from the individual fit.

NBS19 during measurement period #3:

An unknown with a very small number of replicates (2)

Typical clumped isotope measurements have 3-6 replicates of an unknown. However, sometimes not all of these replicates will be conducted in the same measurement period. In this case, we would need to correct a small number of replicates with a given heated gas line. Here we show an example of a case where there were only 2 replicates of NBS19 in a given measurement period.

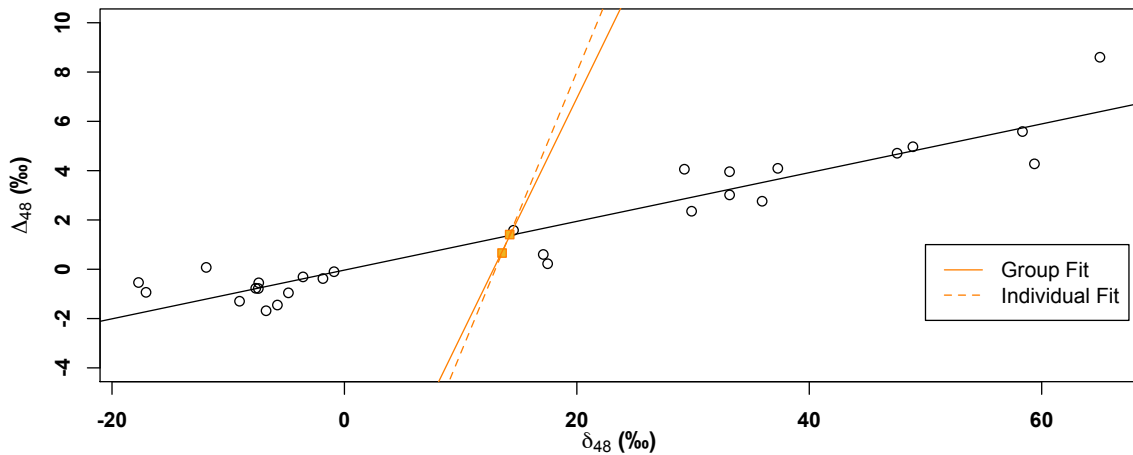


Figure A5.3 δ^{48} vs. Δ_{48} for NBS19 run during measurement period #3 showing two fitted lines – one from an individual fit of just NBS19 data points, and one from the group fit including all CM2 and RTG from measurement period #3. Black points show the heated and equilibrated gases run during this period.

Again, although there are only two points, the lines fitted in δ^{48} vs. Δ_{48} space do not differ very much.

$$\text{HG/EG: } \Delta_{48} = 0.0988 * \delta^{48} - 0.0339$$

$$\text{Individual: } \Delta_{48} = 1.142 * \delta^{48} - 14.829, R^2 = 1$$

$$\text{Group: } \Delta_{48} = 0.9672 * \delta^{48} - 12.4032, R^2 = 0.9941 \text{ for all carbonates}$$

Calculating the intersection points:

$$\text{Individual fit: } (\delta^{48}, \Delta_{48}) = (14.186, 1.368)$$

$$\text{Group fit: } (\delta^{48}, \Delta_{48}) = (14.225, 1.374)$$

In this case the two lines have very similar intersection points, with the “true Δ_{48} ” values differing only by 0.006‰. This is partly because the two points are very close to the heated gas line. In a case where one point has a much higher Δ_{48} (where it could influence the slope of the line more), its possible that the two fits could result in intersection points that are more disparate.

Looking at Δ_{48} vs. Δ_{47} , we will see the real benefit of a group fit.

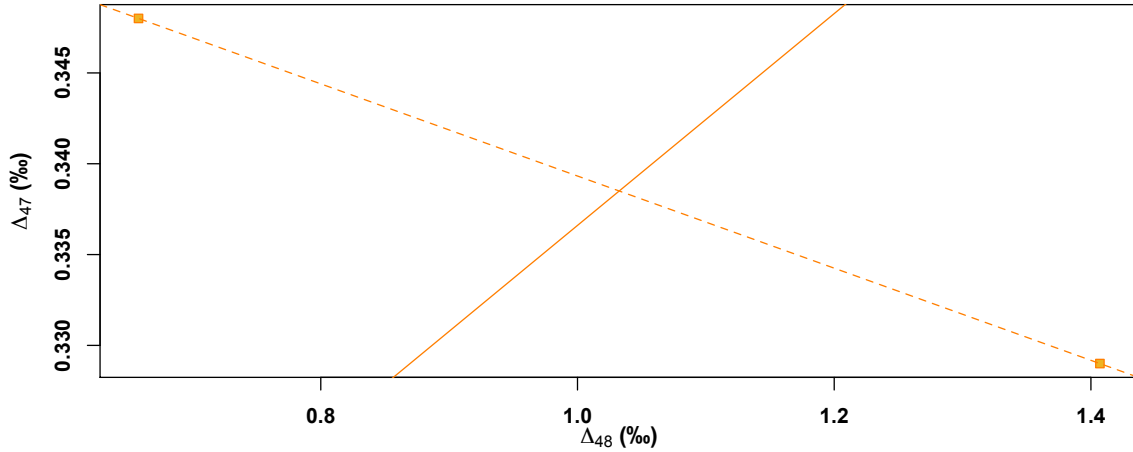


Figure A5.4 Δ_{48} vs. Δ_{47} for NBS19 run during measurement period #3 showing two fitted lines, from the individual and group fits.

Individual: $\text{Slope}_{\text{CARB47}} = -0.0254$ (no error)

Group: $\text{Slope}_{\text{CARB47}} = 0.0583 \pm 0.0035$

In this case, we can see that the two points do not form a line that reflects the fractionation we know occurs (Slope = ~ 0.05). The two points are split on either side of the line calculated by the group fit. In this case, the slope is set by replicates of other carbonate standards (CM2 and RTG), and places the intercept as the average position of the two points.

Point #	1	2	Mean	1 SE
Δ_{48}	0.658	1.407		
$\Delta_{47\text{-RFAC}}$	0.348	0.329	0.329	0.009
$\Delta_{47\text{-corr}}$ (Individual Fit)	0.330	0.330	0.330	0.000
$\Delta_{47\text{-corr}}$ (Group Fit)	0.390	0.327	0.358	0.031

Table A5.2 Comparison of raw NBS19 data (Δ_{48} and $\Delta_{47\text{-RFAC}}$) with data corrected with each of the two fits ($\Delta_{47\text{-corr}}$) for measurement period #3.

The group fit brings the mean value much closer to the published value (0.373 +/- 0.007‰ [Dennis *et al.*, 2011]). The individual fit in this case doesn't correct the data at all. This shows that for a very small number of replicates, the group fit does substantially better than the individual fit. It is possible that you could have a case where two replicates form a line that perfectly matches the true slope, but given the scatter we see around this relationship, it is unlikely that a small number of replicates will properly capture the slope on their own.

We can calculate an individual fit for NBS19 replicates measured during measurement period #2, which had 2 replicates as well. Combining all 9 replicates of NBS19 over three measurement periods, we get a mean value of 0.362 +/- 0.007‰ for the individual fits compared to a mean of 0.368 +/- 0.007‰ for the group fits. In an additional case, we can correct the NBS19 data by doing a group fit with CM2 data only (RTG fit separately). For this case, the mean value is 0.366 +/- 0.007‰.

Choice of individual vs. group fit: CM2 & RTG

We observe a slight but consistent difference between the individual fits of the CM2 and RTG data (see table S3). The slope for RTG is ~0.44, whereas the slope for CM2 is ~0.57. In this paper, we chose to do the group fit for all the data, because in 3 out of 4 measurement periods we had a small number of replicates of NBS19 to correct as well. To test this choice, we also performed an "individual fit" case where we fit RTG with its own line and then did a group fit on CM2 and NBS19 data. This would ideally allow the RTG data to have a more accurate fit, while still giving the benefits of the group fit to the NBS19 data which only had a small number of replicates.

There is very little difference in these two methods. Figure S19 shows a point-by-point comparison for CM2 and RTG data across all measurement periods. The CM2 data shifts slightly downwards, specifically in measurement period #4 (blue X's). RTG data is shifted slightly upwards, with a larger magnitude change than CM2. The largest shifts occur during measurement period #4 as well (blue X's). This likely has to do with the relative number of CM2 vs. RTG during each measurement period (see Table S3). In most cases, the number of CM2 points outweighed the number of RTG points, so the group fit slope was closer to the individual CM2 fit slope, causing little change in CM2 data between the two fit methods. In measurement period #4, RTG points outnumber CM2 points, so we see a larger change in CM2.

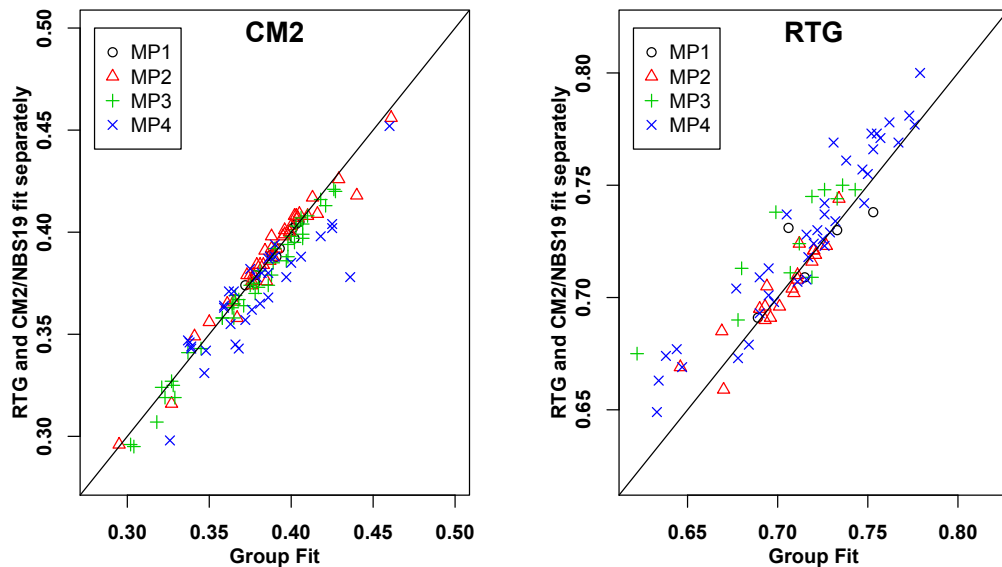


Figure A5.5 Comparison of individual CM2 (left) and RTG (right) data points ($\Delta_{47-corr}$) corrected using the group fit vs. the individual fit described above. Data is separated by color and symbol into the four measurement periods. In both panels, a 1:1 line is plotted for reference. CM2 data shifts slightly downward, whereas RTG shifts slightly upward.

Figure S20 shows the mass-binned averages for each of the two methods. There is a shift in individual averages, but overall there is not much shift in the whole data sets. For CM2, the mean of all points in the group fit is $0.381 \pm 0.003\text{‰}$, whereas in the individual fit this mean is $0.377 \pm 0.003\text{‰}$. For RTG, the group fit mean is $0.713 \pm 0.004\text{‰}$ and $0.723 \pm 0.004\text{‰}$. The individual fit brings the RTG data closer to the published value, while moving the CM2 value slightly lower.

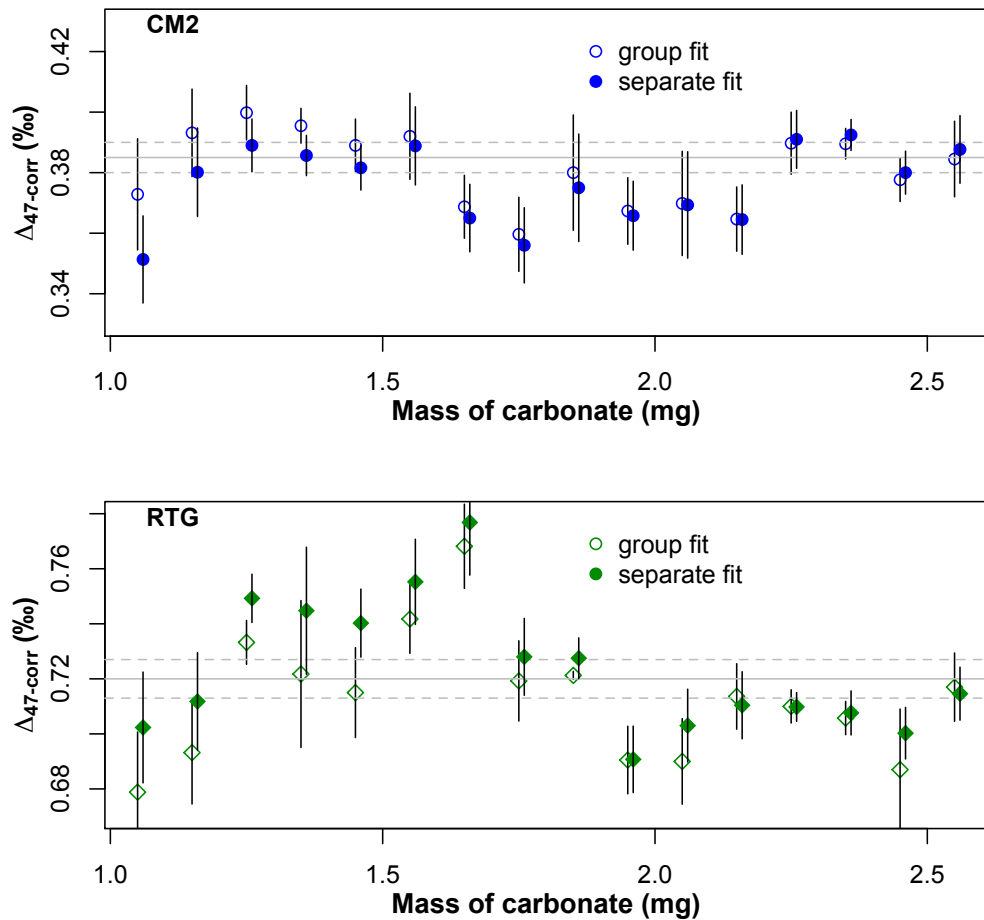


Figure A5.6 Comparison of binned averages for the CM2 and RTG data from all four measurement periods calculated using either the group fit or for the case where RTG and CM2/NBS19 were fit separately. Group fit points are identical to those shown in Fig 6, and listed in Table S4.

In the future, when measuring unknowns, we will opt for the group fit, because there will likely be few replicates of each sample type. Because the observed difference in RTG and CM2 slopes seems to be a constant occurrence, and because most unknowns will have Δ_{47} values more in the range of RTG (aka earth surface temperatures), it may be prudent to use RTG as the primary carbonate standard for the group fit instead of CM2.